

Université du Québec  
Institut National de la Recherche Scientifique  
Énergie, Matériaux et Télécommunications

**Advanced Carbon-Based Materials for Energy Storage and Conversion  
Applications**

Par  
Qiliang Wei

Thèse présentée pour l'obtention du grade de  
Philosophiae doctor (Ph.D.)  
en sciences de l'énergie et des matériaux

**Jury d'évaluation**

Président du jury et examineur interne	Prof. Fiorenzo Vetrone INRS-EMT
Examineur externe	Prof. Oussama Moutanabbir École Polytechnique de Montréal
Examineur externe	Prof. Dominic Rochefort Université de Montréal
Directeur de recherche	Prof. Shuhui Sun INRS-EMT
Codirecteur de recherche	Prof. Ana Tavares INRS-EMT

## ABSTRACT

The development of electrochemical energy storage and conversion systems with high energy density, low cost and good safety have been at the heart of current research on renewable clean energy technologies. To date, lithium-ion batteries (LIBs) have gained the most successful applications ranging from portable electronic devices to electrical vehicles (EVs). However, they are reaching their limitations in energy density and power density, and facing the cost issues of relative shortage of Li resources. New electrochemical energy systems are therefore being actively sought. From the cost issue, sodium-ion batteries (SIBs) have gained increasing research interest all over the world, due to the high abundance and low cost of sodium as well as its suitable redox potential ( $E^0_{(\text{Na}^+/\text{Na})} = -2.71$  V versus the standard hydrogen electrode, SHE), which is only 0.3 V above that of lithium, meaning that there is only a small energy penalty to pay. From the energy density and power density point view, recently, Zn-air batteries (ZABs) and hydrogen-powered proton exchange membrane fuel cells (PEMFCs) are attracting significant attention since the oxygen on the cathode being from air and excluded in the system, which significantly increases the energy densities. In these devices, an efficient oxygen electrocatalyst on the cathode is extremely important for the development of high-performance ZABs and PEMFCs. Up to now, the benchmark catalysts for oxygen reduction reaction (ORR) are noble-metal-based materials; however, the high price and scarcity of these catalysts inhibit their extensive commercial reach. Therefore, developing highly efficient and low-cost non-precious-metal catalysts (NPMCs) to facilitate the sluggish cathodic ORR is a key issue in metal-air batteries and fuel cells. In this thesis, the work is focused on the development of various carbon-based ORR electrocatalysts and their applications in ZABs and PEMFCs. Moreover, we also fabricated highly-ordered microporous carbon (MPC) spheres and applied it as high-performance anodes for SIB.

In the first part of the thesis, we fabricated spherical phenolic resol-F127 monomicelles (SPRMs) by a simple hydrothermal route based on a soft template. A series of 3D microporous Fe/N/C ORR catalysts were then prepared by employing SPRMs as the carbon host for impregnating FeAc and 1,10-Phen, followed by high temperature pyrolysis in Ar and in  $\text{NH}_3$ , consequently. Through the systematic studies, we found that (i) the content of Fe precursor and pyrolysis time under  $\text{NH}_3$  have significant impact on the morphology and structure of the final Fe/N/C catalysts;

(ii) the pyrolysis temperature in Ar, the Brunauer-Emmett-Teller (BET) surface area, and the content of Fe in the catalysts largely affect the ORR activity; (iii) the optimized Fe content of the Fe/N/C catalysts is around 5.5–8 wt% and the optimized porosity is with  $450 \text{ m}^2 \text{ g}^{-1}$  micropore with preferably higher value of mesopores, therefore, only catalysts subjecting within these two ranges exhibit high activity. The optimized 3D Fe/N/C exhibits good ORR performances in both alkaline and acidic conditions. In alkaline solution, it shows excellent activity with a half-wave potential of 0.87 V, excellent stability, and strong methanol tolerance. Moreover, in acidic solution, it also exhibits excellent stability and selectivity. This work provides important reference of key parameters for rational designing high-efficient Fe/N/C electrocatalysts.

From the first work described above, we can see that the microporous structure plays an important role on the electrochemical performance of the Fe/N/C catalysts, therefore, in the second part of the thesis, we employed sulfur (S) as the promoter to tune the pore structures of the Fe/N/C catalyst. We discovered that the addition of S not only affords interpenetrating holes leading to a large surface area and pore volume inside the architecture, but also helps the whole carbon framework keep a perfect 3D spherical shape and uniformly dispersed Fe–N<sub>x</sub> active sites. Moreover, a higher degree of distortion of the local Fe–N<sub>4</sub> structure was observed for the S-treated Fe/N/C sample. Consequently, the optimal S-treated Fe/N/C catalyst shows a litchi-like spherical structure, large surface area ( $982.1 \text{ m}^2 \text{ g}^{-1}$ ) with a huge pore volume ( $1.01 \text{ cm}^3 \text{ g}^{-1}$ ), and excellent ORR/OER (oxygen evolution reaction) activity. Importantly, it achieves a superior performance ( $\sim 250 \text{ mW cm}^{-2}$ , double the power density compared to the untreated sample) as an air cathode for a Zn–air battery device. This work may provide a new strategy to develop high performance carbon-based bifunctional electrocatalysts for low cost metal–air batteries and other electrochemical energy conversion/storage applications.

It is reported that the additional of a second metal (i.e., bimetallic catalyst) could further improve the catalyst performance due to the synergistic effects, therefore in the third part of the thesis, we developed highly porous (Fe-Cu)/N/C based on metal organic framework (MOF). We found that compared with the Fe/N/C, the as-synthesized (Fe-Cu)/N/C possesses higher surface area, longer Fe-N bond, and lower H<sub>2</sub>O<sub>2</sub> yield, which are all favorable for the catalytic activity and stability. Indeed, when applied in a membrane electrode assembly (MEA) in the H<sub>2</sub>-air PEMFC, the (Fe-Cu)/N/C catalyst demonstrates a higher power density ( $0.4 \text{ W cm}^{-2}$ ) than that of the Fe/N/C ( $0.36$

W cm<sup>-2</sup>), and an enhanced stability, i.e., improvement of 3.7% of the current density under a potentiostatic testing at 0.6 V after 40 h.

On the other hand, biomass-derived carbon materials have aroused researchers' much attention, due to their low cost and sustainability. In the fourth part of the thesis, by using the biomass reed stalk which consists of Si and C, we developed an efficient Si-contained Fe/N/C ORR catalyst. Due to the participating of Si in the Fe/N doping process, the Si-Fe/N/C catalyst possesses enhanced graphitic carbon structure with more nitrogen moieties coordinating with Fe, which makes the Si-Fe/N/C catalyst possess good ORR activity. Importantly, Si-Fe/N/C exhibits better stability (with 94.8% retention of the current after 20,000 s under a high voltage of 0.8 V) than the Fe/N/C counterpart (83.3%) and Pt/C (65.5%). In addition, there is only ~12 mV of change at 3 mA cm<sup>-2</sup> for Si-Fe/N/C after 10,000 potential cycles under O<sub>2</sub>-saturated electrolyte (vs. ~19 mV for Fe/N/C and ~40 mV for Pt/C), as well as higher tolerance toward methanol compared with Pt/C. Taking together, using Si-Fe/N/C catalyst as a substitute for commercial Pt/C could provide possibility in fuel cells and other applications with good ORR performance and high stability. We believe that this work will give more insights to design highly stable catalysts for the clean energy related devices and have significant economic and environment effects by making full use of biomass wastes.

More interestingly, we find that even without Fe, the metal-free (Si-N-C) materials derived from biomass reed were demonstrated to be very active for ORR in alkaline media (the fifth part of the thesis). The optimized Si-N-C sample shows an E<sub>onset</sub> of ~1.00 V and E<sub>1/2</sub> of 0.89 V (vs. reversible hydrogen electrode, RHE), which is one of the best among the reported metal-free ORR catalysts. It also displays better stability for ORR than commercial Pt/C in a half-cell test. Moreover, this reed derived Si-N-C metal-free catalyst exhibits excellent performance as an air cathode for a Zn-air battery device. DFT calculation indicates that the Si and N sites (graphitic-N) in the carbon framework could promote the ORR activity. We believe that our work will give more insights to design more efficient catalysts for the clean energy related devices and bring a great significance to the sustainable development of energy.

In addition, during our study of SPRMs materials, we found that the interlayer spacing of the MPC could be well tuned by simply adjusting the heat-treatment temperatures. This phenomena could be very useful for sodium-ion batteries. Therefore, in the last part of the thesis, we did

systematic study on this aspect. In detail, the carbon spheres treated at 700 °C (MPC-700) possess unique features, such as a large interlayer spacing ( $\sim 0.457$  nm), high surface area, structural stability and plenty of micropores, which are favorable for Na insertion, and therefore for high-performance SIB electrode materials. Our results show that the MPC-700 electrode exhibits a high reversible capacity, good cycling stability, and an excellent high-rate performance ( $\sim 160$  mA h  $g^{-1}$  after 500 cycles at 1000 mA  $g^{-1}$ ), making it a promising candidate for SIB anode.

## ACKNOWLEDGEMENTS

Firstly, I would like to express my deepest thanks to my supervisor, Prof. Shuhui Sun, for offering me one of the most valuable opportunities that I ever had in my life. He has been always giving continuous remarkable guidance, mentorship and strong support in all the time of carrying out my research work during my study, without him, this work would not have been possible. More importantly, he conferred me the “group leader” in SUN Group. During the past years, I learned not only the research but also the leadership, how to coordinate the work of the members in the group, and how to communicate with staff at INRS and outside. I would thank my co-supervisor, Prof. Ana Tavares, for her continuous support, I learned a lot from her profound knowledge, excellent organizational ability and kindness. I would also wish to give special thanks to Dr. Gaixia Zhang. She made vital contributions to most of the work and gave me invaluable help and comments on my research and thesis writing. I would like also thank Dr. Régis Chenitz and Dr. Michel Lefèvre for their guidance on the operation of fuel cell stations and data analysis. I thank Dr. Siyu Ye, Dr. Dustin Banham, Dr. Lijun Yang, and Ms Shanna Knights from Ballard Power Systems Co. for the fruitful discussions. I am gratitude to Dr. Ning Chen, Dr. Yongfeng Hu, Dr. Dongniu Wang and Dr. Lucia Zuin from CLS for their strong support for the synchrotron experiment and data analysis.

I appreciate Prof. Ana Tavares, Prof. Mohamed Mohamedi and Prof. Marc Gauthier for kindly allowing me to use their lab facilities. I would like to acknowledge Prof. Ana Tavares, Prof. Daniel Guay, and Prof. Fiorenzo Vetrone at INRS-EMT, for their important comments on my project research during my Pre-doc exam. Also, I sincerely thank Prof. Dominic Rochefort from Université de Montréal, Prof. Oussama Moutanabbir from École Polytechnique de Montréal and Prof. Fiorenzo Vetrone at INRS-EMT to be my thesis defense jury members. I would like to thank Christophe Chabanier and Catalin Harnagea at INRS-EMT, Jean-Philippe Masse at Ecole Polytechnique and Galyna Shul at Université du Québec à Montréal for the excellent training and carrying out XRD, XPS, TEM and BET measurements. Many thanks to Prof. Tsuneyuki Ozaki, Prof. Edward Sacher, Prof. Mohamed Mohamedi, Prof. Vidal François, Prof. Xianyou Wang, Prof. Guowen Meng, and Prof. Xu Li for their strong support during the collaborations. I appreciate the help from the administration staff at INRS: Michelle Marcotte, Hélène Sabourin, Louise Hudon, Sylvain Gingras, Hélène Tanguay, Georges Lamoureux, etc. I am grateful to all

the group members in SUN Group for their significant help throughout my work, including: Xiaohua Yang, Nathan Komba, Xin Tong, Yanqing Fu, Jihai Zhang, Amir Hasanpour, Jiatang Chen, Kunqi Wang, Mingjie Wu, Zhangsen Chen, Jai Prakasha, etc., as well as other collaborators: Willyam R.P. Barros, Youling Wang, Sudipta Mondal, Cherif Mohamed, Almesrati Ali, Juan Carlos, Fangming Han, Haibin Tang, Bin Chen, Kexi Sun, etc. And thanks a million to all the friends who have made my life easy and enjoyable in Canada and gave me a lot of help during my PhD study at INRS: Xin Jin, Fan Yang, Daling Cui, Xin Tong, Yufeng Zhou, Bingyu Sun, Sa Liu, Shun Li, Yue Huang, Maria Joao Paulo, Bruno Guerreiro, Fuyong Yue, Junliang Dong, Jingdan Liu, Ting Cheng, Jianming Zhang, Haiguang Zhao, Chao Wang, Mengyang Fan, Qingzhe Zhang, Xin Chai, Hui Zhang, Jiabin Liu, Shengyun Huang, Zimin Feng, Cybelle Palma, Essen Sokullu, Régis Imbeault, etc., with whom I have built strong friendship and had wonderful memories in my life. Many thanks to Yuting Lei for helping on the French translation of the RÉSUMÉ session in this thesis.

I am in debt to my dear parents and brother, who always gave me unconditional love and support all the time. My gratitude to you for all you have done for me. Words beat me when I want to how to thank my girlfriend, Yanqing Fu, who loves me deeply, shares joys when I was happy, and encourages me when I was down. Without you, I cannot get where I am today. I thank my family and my friends for their continuing love and heartfelt support.

Finally, I wish to acknowledge the following organizations for their research support to my research: the Natural Sciences and Engineering Research Council of Canada (NSERC), Fonds québécois de la recherche sur la nature et les technologies (FQRNT), Canada Foundation for Innovation (CFI), Ballard Power System Co., and Canadian Light Source (CLS). I highly appreciate the support from the China Scholarship Council (CSC) and FQRNT for my graduate fellowships.

# CONTENTS

CHAPTER 1	INTRODUCTION .....	1
1.1	Background.....	1
1.2	Proton Exchange Membrane Fuel Cells .....	3
1.3	Zn-Air Batteries .....	6
1.4	Oxygen Electrochemical Reaction.....	9
1.4.1	Introduction of Oxygen Electrochemical Reaction .....	9
1.4.2	State of Art Oxygen Electrocatalysts.....	11
1.5	Na-Ion Batteries .....	20
1.6	Thesis Objectives and Organization .....	23
1.6.1	Objectives .....	23
1.6.2	Thesis Organization .....	23
CHAPTER 2	EXPERIMENTAL.....	26
2.1	Chemicals and Materials.....	26
2.2	Material Synthesis.....	26
2.2.1	Fe/N/C Catalysts.....	26
2.2.2	Bimetallic (Fe-M)/N/C Catalysts.....	26
2.2.3	Metal-Free Catalyst .....	27
2.3	Physical Characterizations .....	27
2.3.1	Scanning Electron Microscopy (SEM).....	27
2.3.2	Transmission Electron Microscopy (TEM) .....	28
2.3.3	X-Ray Diffraction (XRD).....	29
2.3.4	X-Ray Photoelectron Spectroscopy (XPS).....	30
2.3.5	X-Ray Absorption Spectroscopy (XAS) .....	32

2.3.6	N <sub>2</sub> Adsorption and Desorption.....	33
2.3.7	Raman Spectroscopy .....	34
2.3.8	Neutron Activation Analysis (NAA) .....	34
2.4	Electrochemical Characterizations.....	35
2.4.1	Rotating Ring-Disk Electrode (RRDE) .....	35
2.4.2	Single Cell MEA Tests in PEM Fuel Cells .....	39
2.4.3	Zn-Air Batteries .....	40
2.4.4	Na-Ion Batteries .....	40
CHAPTER 3	RESULTS .....	41
3.1	3D porous Fe/N/C spherical nanostructures as high-performance electrocatalysts for oxygen reduction in both alkaline and acidic media .....	41
3.2	Litchi-like porous Fe/N/C spheres with atomically dispersed FeN <sub>x</sub> promoted by sulfur as highly efficient oxygen electrocatalysts for Zn–air batteries .....	77
3.3	Bio-inspired nonprecious bimetallic (Fe-Cu)/N/C catalyst for oxygen reduction in proton exchange membrane fuel cells .....	110
3.4	An active and robust Si-Fe/N/C catalyst derived from waste reed for oxygen reduction .....	137
3.5	Transforming reed waste into a highly active metal-free catalyst for oxygen reduction reaction .....	168
3.6	Highly-ordered microporous carbon nanospheres: a promising anode for high-performance sodium-ion batteries .....	197
CHAPTER 4	CONCLUSIONS AND PERSPECTIVES .....	211
4.1	Conclusions .....	211
4.2	Perspectives .....	214
Reference	.....	216
RÉSUMÉ	.....	230

## LIST OF FIGURES

**Figure 1.1** Ragone plot comparing the performance of various EESC devices (energy density vs. power density).

**Figure 1.2** Schematic illustration of PEM fuel cell.

**Figure 1.3** Typical polarization curve of a PEM fuel cell.

**Figure 1.4** Theoretical specific energies, volumetric energy densities, and nominal cell voltages for various metal anodes in aqueous and non-aqueous metal-air batteries. Specific energy values account for oxygen uptake in the battery by numeric integration between the fully charged and fully discharged states. Volumetric energy densities were calculated using the density of the anode in the fully discharged state. Refer to the Supporting Information for calculations and further explanations.

**Figure 1.5** Scheme of a rechargeable ZAB and the schematic diagram of the oxygen electrocatalysts in the three-phase air cathode.

**Figure 1.6** ORR pathways in acid and alkaline media.

**Figure 1.7** Side views and top views of the proposed structures of Fe-N<sub>x</sub> species: (Doublet 1): the FeN<sub>4</sub>/C catalytic site in heat-treated, macrocycle-based catalysts. (Doublet 2): the FeN<sub>2+2</sub>-like micropore-hosted site found in the catalyst prepared with iron acetate and heat-treated in ammonia. The distance between the two nitrogen atoms belonging to the graphene planes above and below the FeN<sub>2+2</sub>-plane is similar to that in crystalline iron phthalocyanine. (Doublet 3): the N-FeN<sub>2+2</sub>-like composite site. The iron (II) ion in N-FeN<sub>2+2</sub> is coordinated by five pyridinic nitrogen atoms, one of them belonging to a plane located at the vertical below the N<sub>4</sub>-plane. This axial nitrogen coordination moves the iron (II) ion out of the N<sub>4</sub>-plane towards the fifth coordinating nitrogen atom. Doublet 3 may exist as N-FeN<sub>2+2</sub>/C or as a composite site N-FeN<sub>2+2</sub>·N<sub>prot</sub>/C, where N<sub>prot</sub> is a protonable pyridinic nitrogen atom appearing at the edge of the upper plane in the side view of Doublet 3. In all side views, graphene planes are drawn as lines.

**Figure 1.8** (a) BF-STEM image of a typical (CM+PANI)-Fe-C catalyst showing primary fibrous carbons and secondary graphene sheets. (b) Atomic-resolution HAADF-STEM image of Fe atoms distributed across the surface of fibrous carbon phase showing randomly oriented,

intertwined graphitic domains. (c) HAADF-STEM image of individual Fe atoms (labeled 1, 2, and 3) in a few-layer graphene sheet. (d) EEL spectra of the N k-edge ( $N_{k}$ ) and Fe L-edge ( $Fe_{L}$ ) acquired from single atoms (1 and 2) and few-layer graphene (3), demonstrating the presence of N around the Fe atoms.

**Figure 1.9** (a) Doping of graphitic carbon structure with heteroatoms (e.g., N, B, P). (b) Doping of graphitic carbon structure with heteroatoms (e.g., N) by post-treatment. (c) Periodic table and the corresponding electronegativity of elements.

**Figure 1.10** Scheme of a rechargeable SIB.

**Figure 2.1** Basic principle of a TEM.

**Figure 2.2** Schematic showing the interaction between x-rays and a typical crystalline sample

**Figure 2.3** The XPS equipment at INRS-EMT.

**Figure 2.4** The beamlines at Canadian Light Source.

**Figure 2.5** Rotating ring-disk voltammograms at various rotation rates.

# LIST OF CHEMICAL COMPOUNDS, ABBREVIATIONS AND SYMBOLS

## Chemical Compounds

Al	aluminum
Ar	argon
B	boron
C	carbon
CNT	carbon nanotube
Co	cobalt
CO	carbon monoxide
Cu	copper
F	fluorine
FeAc	iron(II) acetate
FePc	iron(II) phthalocyanine
H <sub>2</sub>	hydrogen
HCl	hydrochloric acid
H <sub>2</sub> O <sub>2</sub>	hydrogen peroxide
H <sub>2</sub> SO <sub>4</sub>	sulfuric acid
K	potassium
K <sub>3</sub> Fe(CN) <sub>6</sub>	potassium ferricyanide
KOH	potassium hydroxide

$\text{KNO}_3$	potassium nitrate
Li	lithium
$\text{Li}_2\text{CO}_3$	lithium carbonate
Mg	magnesium
Mn	manganese
Na	sodium
$\text{NaClO}_4$	sodium perchlorate
$\text{Na}_2\text{CO}_3$	sodium carbonate
NaOH	sodium hydroxide
$\text{N}_2$	nitrogen gas
$\text{NH}_3$	ammonia
Ni	nickel
$\text{O}_2$	oxygen
$\text{OH}^-$	hydroxyl ion
PANI	polyaniline
PC	propylene carbonate
Phen	1,10-phenanthroline
PVDF	polyvinylidene fluoride
Pt	platinum
S	sulfur
$\text{SCN}^-$	thiocyanogen ion

Si	silicon
ZIF	zeolitic imidazolate framework
Zn	zinc
ZnO	zinc oxide
Zn(OH) <sub>4</sub> <sup>2-</sup>	zincate ion

## **Abbreviations**

ADT	accelerated durability test
BE	binding energy
BET	Brunauer, Emmett and Teller
BF-STEM	bright field-scanning transmission electron microscopy
CLS	Canadian Light Source
CV	cyclic voltammetry
DOE	Department of Energy
DFT	density functional theory
EESC	electrochemical energy storage and conversion
EDS	energy dispersive spectroscopy
EIS	electrochemical impedance spectra
EXAFS	extended X-ray absorption fine structure
EV	electrical vehicle
FLY	fluorescent yield
HAADF	high angle annular dark field

HRTEM	high-resolution transmission electron microscope
HXMA	hard X-ray micro analysis
GC	glassy carbon
GDE	gas diffusion electrodes
GDL	gas diffusion layer
GHG	greenhouse gas
LANL	Los Alamos National Laboratory
LIB	lithium ion battery
LSV	linear sweeping voltammetry
Me-N-C	metal-nitrogen-carbon
MEA	membrane electrode assembly
MOF	metal organic framework
MPC	microporous carbon
NAA	neutron activation analysis
NPs	nanoparticles
NPMC	non-precious-metal catalyst
OCV	open circuit voltage
OER	oxygen evolution reaction
ORR	oxygen reduction reaction
PEMFC	polymer electrolyte membrane/proton exchange membrane fuel cell
QSDFT	Quenched solid density functional theory

RHE	reversible hydrogen electrode
RPM	revolutions per minute
RRDE	rotating ring-disk electrode
RSF	relative sensitivity factor
SAC	single-atom catalysts
SCE	saturated calomel electrode
SEM	Scanning Electron Microscopy
SHE	standard hydrogen electrode
SIB	sodium ion battery
SLPM	standard liter per minute
SPRM	spherical phenolic resol-F127 monomicelles
SXRMB	soft X-ray micro characterization beamline
TEM	transmission electron microscope
TEY	total electron yield
UHV	ultra-high vacuum
VLS-PGM	variable line spacing plane grating monochromator
XANES	X-ray absorption near edge structure
XAS	X-Ray Absorption Spectroscopy
XPS	X-ray photoelectron spectroscopy
XRD	X-ray diffraction
ZAB	zinc air battery

## Symbols

A	ampere
$\mu$	micro
cm	centimeter
$^{\circ}\text{C}$	degree
$E^0_a$	equilibrium half-cell potentials
$E_{\text{onset}}$	onset potential
$E_{1/2}$	half-wave potential
$I_d$	disk current
$I_r$	ring current
L	litre
mAh	milliamperere hour
mW	milliwatt
$N_{\text{empirical}}$	empirically measured collection efficiency
$V_{\text{oc}}$	open circuit voltage
Wh	watt hour
$\Omega$	Ohm
$\theta$	diffraction angle
$\lambda$	wave length

# LIST OF PUBLICATIONS AND CONFERENCE CONTRIBUTIONS

## Journal Publications

- 1) Q. Wei, X. Yang, G. Zhang, *et al.* Bio-inspired nonprecious bimetallic (Fe-Cu)/N/C catalyst for oxygen reduction in proton exchange membrane fuel cells. To be submitted.
- 2) Q. Wei, M. Cherif, *et al.* Transforming reed waste into a highly active metal-free catalyst for oxygen reduction reaction. To be submitted.
- 3) Q. Wei, Y. Fu, G. Zhang, *et al.* Rational design of novel nanostructured arrays based on porous AAO templates for electrochemical energy storage and conversion. *Nano Energy*, 2019, **55**, 234-259.
- 4) Q. Wei, X. Yang, G. Zhang, *et al.* An active and robust Si-Fe/N/C catalyst derived from waste reed for oxygen reduction. *Appl. Catal., B.*, 2018, **237**, 85-93.
- 5) Q. Wei, G. Zhang, X. Yang, *et al.* Litchi-like porous Fe/N/C spheres with atomically dispersed FeN<sub>x</sub> promoted by sulfur as highly efficient oxygen electrocatalysts for Zn-air batteries. *J. Mater. Chem. A*, 2018, **6**, 4605-4610.
- 6) Q. Wei, G. Zhang, X. Yang, *et al.* 3D porous Fe/N/C spherical nanostructures as high-performance electrocatalysts for oxygen reduction in both alkaline and acidic media. *ACS Appl. Mater. Interfaces*, 2017, **9**, 36944-36954.
- 7) Q. Wei, Y. Fu, G. Zhang, *et al.* Rational design of carbon-based oxygen electrocatalysts for zinc-air batteries. *Curr. Opin. Electrochem.*, 2017, **4**, 45-59.
- 8) Y. Fu,<sup>†</sup> Q. Wei,<sup>†</sup> G. Zhang, *et al.* High-performance reversible aqueous Zn-ion battery based on porous MnO<sub>x</sub> nanorods coated by MOF-derived N-doped carbon. *Adv. Energy Mater.*, 2018, 1801445.
- 9) Q. Wei, Y. Fu, G. Zhang, *et al.* Highly-ordered microporous carbon nanospheres: a promising anode for high-performance sodium-ion batteries. *RSC Adv.*, 2016, **6**, 84149-84154.
- 10) Q. Wei, X. Tong, G. Zhang, *et al.* Nitrogen-doped carbon nanotube and graphene materials for oxygen reduction reactions. *Catalysts*, 2015, **5**, 1574-1602.
- 11) R. Bavand,<sup>†</sup> Q. Wei,<sup>†</sup> G. Zhang, *et al.* PtRu alloy nanoparticles. 2. chemical and electrochemical surface characterization for methanol oxidation. *J. Phys. Chem. C.*, 2017, **121**, 23120-23128.
- 12) N. Komba, Q. Wei, G. Zhang, *et al.* Controlled synthesis of graphene via electrochemical route and its use as efficient metal-free catalyst for oxygen reduction. *Appl. Catal., B.*, 2019, **243**, 373-380.
- 13) G. Zhang, Q. Wei, X. Yang, *et al.* RRDE experiments on noble-metal and noble-metal-free catalysts: Impact of loading on the activity and selectivity of oxygen reduction reaction in alkaline solution. *Appl. Catal., B.*, 2017, **206**, 115-126.
- 14) Y. Fu, Q. Wei, G. Zhang, *et al.* Advanced phosphorus-based materials for lithium/sodium-ion

- batteries: recent developments and future perspectives. *Adv. Energy Mater.*, 2018, 1703058.
- 15) M. Wu, Q. Wei, G. Zhang, et al. Fe/Co double hydroxide/oxide nanoparticles on N-doped CNTs as highly efficient electrocatalyst for rechargeable liquid and quasi-solid-state zinc–air batteries. *Adv. Energy Mater.*, 2018, 1801836.
  - 16) M. Yu, Q. Wei, M. Wu, et al. Morphology controlled synthesis of SmMn<sub>2</sub>O<sub>5</sub> nanocrystals via a surfactant-free route for Zn-air batteries. *J. Power Sources*, 2018, **396**, 754-763.
  - 17) X. Tong, Q. Wei, X. Zhan, et al. The new graphene family materials: synthesis and applications in oxygen reduction reaction. *Catalysts*, 2017, **7**, 1-26.
  - 18) W. Barros, Q. Wei, G. Zhang, et al. Oxygen reduction to hydrogen peroxide on Fe<sub>3</sub>O<sub>4</sub> nanoparticles supported on Printex carbon and graphene. *Electrochim. Acta*, 2015, **162**, 263-270.
  - 19) Y. Fu, Q. Wei, X. Wang, et al. Porous hollow  $\alpha$ -Fe<sub>2</sub>O<sub>3</sub>@TiO<sub>2</sub> core–shell nanospheres for superior lithium/sodium storage capability. *J. Mater. Chem. A*, 2015, **3**, 13807–13818.
  - 20) S. Mondal, Q. Wei, W. Ding, et al. Aligned copper nanorod arrays for highly efficient generation of intense ultra-broadband THz pulses. *Sci. Rep.*, 2017, **7**, 40058.
  - 21) Y. Fu, Q. Wei, X. Wang, et al. A facile synthesis of Fe<sub>3</sub>O<sub>4</sub> nanoparticles/graphene for high-performance lithium/sodium-ion batteries. *RSC Adv.*, 2016, **6**, 16624-16633.
  - 22) Y. Fu, Q. Wei, B. Lu, et al. Stem-like nano-heterostructural MWCNTs/ $\alpha$ -Fe<sub>2</sub>O<sub>3</sub>@TiO<sub>2</sub> composite with high lithium storage capability. *J. Alloy Compd.*, 2016, **684**, 419-427.
  - 23) G. Zhang, M. Banis, Q. Wei, et al. Pt/TiSi<sub>x</sub>-NCNT novel Janus nanostructure: a new type of high-performance electrocatalyst. *ACS Appl. Mater. Interfaces*, 2018, **10**, 10771-10777.
  - 24) S. Wang, S. Chen, Q. Wei, et al. Bioinspired synthesis of hierarchical porous graphitic carbon spheres with outstanding high-rate performance in lithium-ion batteries. *Chem. Mater.*, 2015, **27**, 336-342.
  - 25) X. Tong, J. Zhang, G. Zhang, Q. Wei, R. Chenitz, et al. Ultrathin carbon-coated Pt/Carbon nanotubes: a highly durable electrocatalyst for oxygen reduction. *Chem. Mater.*, 2017, **29**, 9579-9587.
  - 26) E. Appiah-Hagan, Y. Chen, X. Yu, G.A. Artega, J. Pizarro, L. Mercier, Q. Wei, N. Belzile, Simple and energy-saving modifications of coal fly ash to remove simultaneously six toxic metal cations from mine effluents. *J. Environ. Chem. Eng.*, 2018, **6**, 5498-5509.
  - 27) Y. Chen, X. Yu, E. Appiah-Hagan, J. Pizarro, G.A. Artega, L. Mercier, Q. Wei, N. Belzile, Utilization of coal fly ash and drinking water sludge to remove anionic As(V), Cr(VI), Mo(VI) and Se(IV) from mine waters. *J. Environ. Chem. Eng.*, 2018, **6**, 2470-2479.

### Conference Presentations

- 1) Q. Wei, G. Zhang, et al. Highly-porous Fe/N/C spheres with atomically dispersed FeN<sub>x</sub> promoted by sulfur as high-efficient oxygen electrocatalysts for Zn–air batteries. *Venice International University, International PhD Academy*. 2018, Venice, Italy. (Poster)

- 2) **Q. Wei, G. Zhang, et al.** Graphene supported Fe<sub>3</sub>O<sub>4</sub> nanoparticles as efficient electrocatalyst for H<sub>2</sub>O<sub>2</sub> production and high-performance anode for lithium ion batteries. ***5<sup>th</sup> ECS Montreal Student Symposium***. 2015, Montreal, Canada. (Oral)
- 3) **Q. Wei, W. Barros, et al.** Graphene supported Fe<sub>3</sub>O<sub>4</sub> nanoparticles as efficient electrocatalysts for H<sub>2</sub>O<sub>2</sub> production. ***98<sup>th</sup> Canadian Chemistry Conference***. 2015, Ottawa, Canada. (Poster)
- 4) **Q. Wei, S. Sun.** Nanostructured materials based on anodic aluminum oxides (AAO) for applications in electrochemical energy storage and conversion. ***CQMF annual Symposium***. 2014, Shawinigan, QC. (Oral)
- 5) **Q. Wei, A. Tavares, S. Sun.** Nanomaterials based on anodic aluminum oxides (AAO) template for energy storage and conversion. ***17<sup>th</sup> Annual Chemistry and Biochemistry Graduate Research Conference***. 2014, Montreal, QC. (Oral)

# CHAPTER 1 INTRODUCTION

## 1.1 Background

Today, the major energy source of society still relies on the fossil fuels [1]. Therefore, realizing a secure, economic, environmentally friendly, and sustainable energy future has become one of the greatest scientific and societal challenges in the 21<sup>st</sup> century. To reduce our dependency on fossil fuels, it is particularly urgent and important to develop renewable and sustainable energy sources, such as solar, geothermal, water, tidal, and wind power [2]. However, it is well-known that these energy sources face the challenges of unpredictability, capacity instability, intermittence, and regionalism. To safely and efficiently use these renewable energies, electrochemical energy storage and conversion (EESCs) devices hold great promise for large-scale applications. Of many EESCs, rechargeable lithium-ion batteries (LIBs) have become the most widely used power source that can be seen almost everywhere in daily life, ranging from portable electronics and electric vehicles (EVs) to large-scale smart grids [3-5]. The past decades have witnessed the progress of LIBs from both performance and cost aspects. For example, the specific energy has increased from 90 Wh kg<sup>-1</sup><sub>cell</sub> in the 1990s to over 250 Wh kg<sup>-1</sup><sub>cell</sub> today; meanwhile, the cost of LIB packs has decreased from over 1000 \$ kW h<sup>-1</sup> to ~250 \$ kW h<sup>-1</sup> [6], bringing EV prices down to a reasonable level for the average consumers. However, with the rapid world-wide development, the progress of LIBs technology still cannot adequately meet the continuously surging demand in emerging energy applications that generally require higher power/energy density and longer lifespan, especially in the long-range transportation segment. Besides, limited natural lithium source with its uneven distribution (mainly in South America) in the Earth's crust, and the high costs of its production also exert negative impacts toward meeting large-scale energy storage requirements in our modern society. New electrochemical systems are therefore actively sought [7].

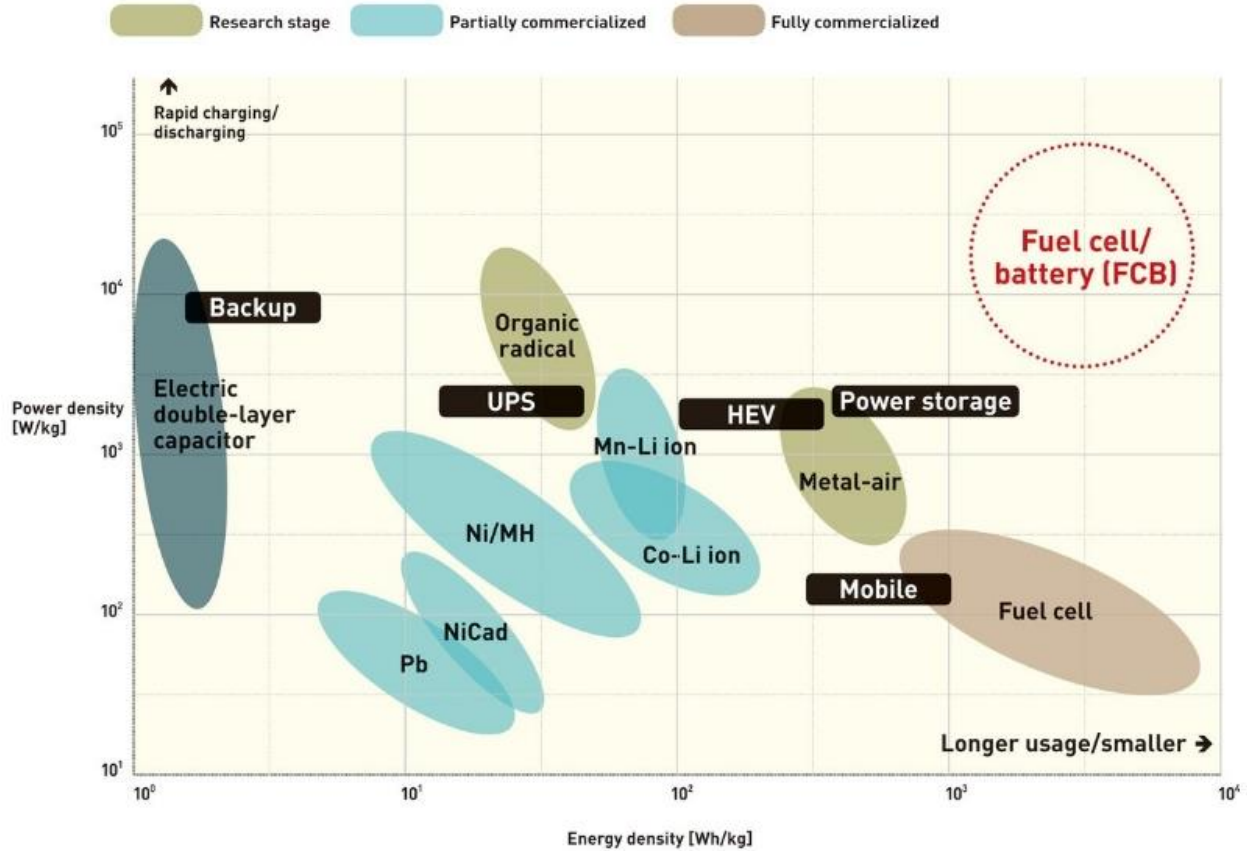


**Figure 1.1** Ragone plot comparing the performance of various EESC devices (energy density vs. power density) [8]

Power density and energy density are the most important metrics for evaluating the performance of EESC devices. The Ragone plot in Figure 1.1 depicts the characteristic power and energy densities of various EESC devices. Consequently, fuel cells [9] and metal-air batteries [10] have aroused great interest among the potential candidate EESC devices, because of their high theoretical power and energy densities. In addition to the electrochemical performance, hydrogen fuel cells and metal-air batteries also have the advantage of being environment-friendly, which makes them among the most promising and attractive technologies for future energy supply.

Cost is also an ineluctable factor of the EESC devices for the wide-spread applications. Given the high abundance and low cost of sodium as well as its very suitable redox potential [11], rechargeable electrochemical cells based on sodium also hold much more promise for large-scale energy storage applications.

## 1.2 Proton Exchange Membrane Fuel Cells

It is generally accepted that fuel cells provide an ultimate energy solution because of their high efficiency, zero emission, quiet operation process and unlimited renewable source of reactants. Stationary power, transportation and portable power are the three major markets for fuel cell technology. The very first fuel cell was invented in 1839 by Sir William Robert Grove (an English lawyer turned scientist), though no practical use was found for another century. General Electric (GE) Company began developing fuel cells in the 1950s and was awarded the contract for the Gemini space mission in 1962. The 1 kW Gemini fuel cell system had a platinum (Pt) loading of  $35 \text{ mg}_{\text{Pt}} \text{ cm}^{-2}$  and performance of  $37 \text{ mA cm}^{-2}$  at  $0.78 \text{ V}$  [12]. In the 1960s, improvements were made by incorporating Teflon in the catalyst layer directly adjacent to the electrolyte, as was done with GE fuel cell at the time. Considerable improvements were made from the early 1970s onward with the adoption of the fully fluorinated Nafion® membrane. However, the research and development in PEMFCs did not receive much attention and funding from the federal government, in particular the US Department of Energy (DOE), and industry, until a couple of decades ago or so when breakthrough methods for reducing the amount of Pt required for PEMFCs were developed and subsequently improved by Los Alamos National Laboratory (LANL) and others. Notably, Raistrick of LANL came up with a catalyst-ink technique for fabricating the electrodes [13]. Among various fuel cells, the proton exchange membrane (PEM) fuel cell [14-16], with the advantages of low operating temperature, quick starting and a compact stack, has attracted much attention worldwide. A recent landmark event in the fuel cell arena is Toyota's launch of its hydrogen fuel cell vehicle "Mirai" at the Los Angeles Auto Show, November 2014. This is one of the first such mass-market vehicles sold commercially [17]. This has given rise to a new tide in fuel cell research.

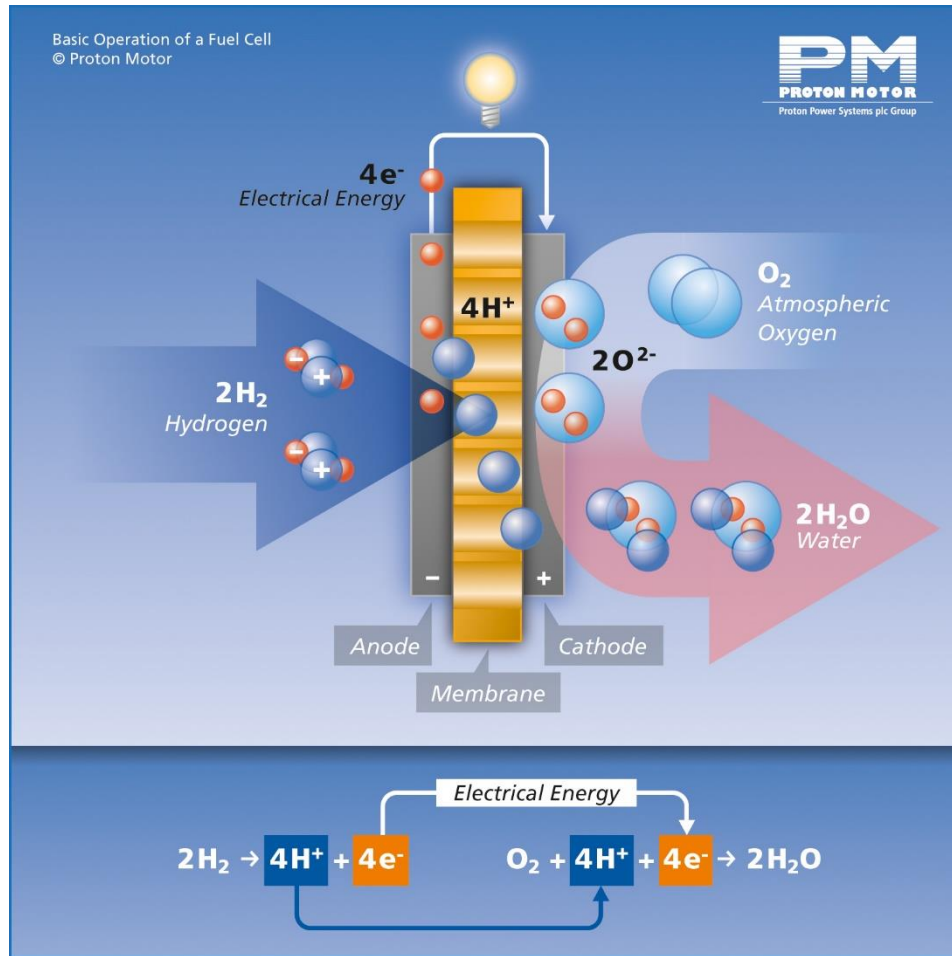


**Figure 1.2** Schematic illustration of a PEM fuel cell [18].

As demonstrated in Figure 1.2, the key component of a PEM fuel cell is the membrane electrode assembly (MEA), which consists of the anode, the Nafion membrane electrolyte, and the cathode. The chemical reactions that happen during working are listed from equation (1) to (3), where their corresponding potentials (vs. Standard hydrogen electrode) are included. As can be seen, the overall reaction generates an open circuit voltage of 1.23 V under standard conditions according to thermodynamic calculations.



However, the theoretically calculated output voltage of PEM fuel cell is compromised during practical application. Such voltage loss includes contribution from kinetic losses, ohmic losses and mass transfer losses at the same time (Figure 1.3). Yet, the dominant part of it comes from the over-potential of the air cathode, owing to the sluggish kinetics of the oxygen reduction reaction (ORR) that happens there.

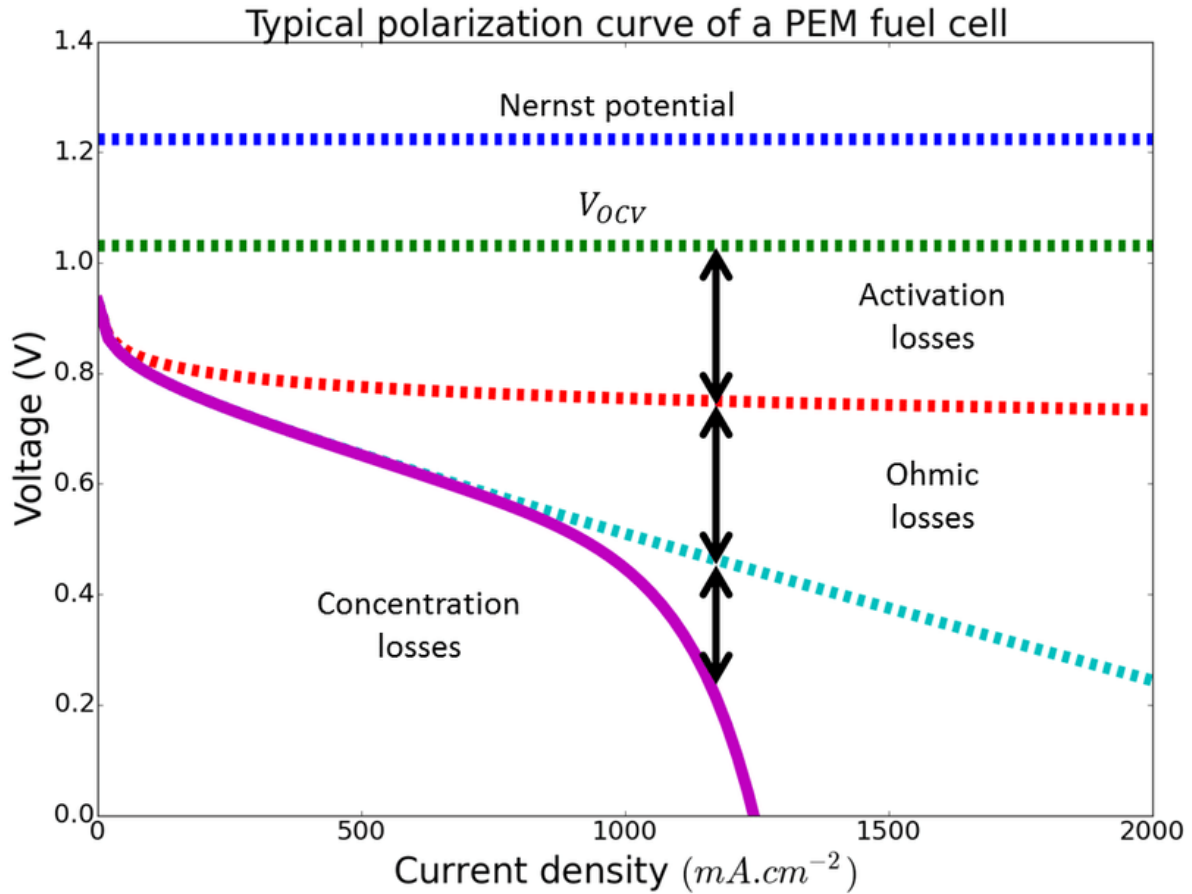


**Figure 1.3** Typical polarization curve of a PEM fuel cell [19].

### 1.3 Zn-Air Batteries

Recently, metal-air batteries have attracted great attention since they possess a unique half-open system that uses the O<sub>2</sub> from ambient air, minimizing the required mass and volume of the air electrode and increasing the energy density. During operation of a metal-air battery, the cathode consumes O<sub>2</sub> continuously from the air as an active material. The anode material is a metal such as Zn, Al, Mg, Li, Na, K or Fe. The theoretical specific energies (i.e., gravimetric energy densities), volumetric energy densities, and nominal cell voltages of various metal anodes in metal-air batteries are displayed in Figure 1.4. Among all metal-air batteries, Li-air batteries have the highest theoretical specific energy [20], but Li in the metallic form is plagued by its inherent instability, when exposed to air and aqueous electrolytes. Mg-air and Al-air batteries are both compatible with aqueous electrolytes and have energy densities comparable to Li-air battery, but suffering from the shortcomings of rapid self-discharge and poor Coulombic charging efficiency [21]. Compared with Li, Zn is inexpensive and more abundant in the earth's crust. More importantly, Zn metal within a metal-air battery has a relative high volumetric energy density (6136 Wh L<sup>-1</sup>), which is particularly desirable for mobile and portable devices (e.g., EVs and personal electronics), because there is a limited volume for mounting the batteries in these applications [22]. Moreover, the inherent safety of Zn means that zinc-air batteries (ZABs) can be placed in the front hood of an automobile, where provision for air access is already well established in today's vehicles.

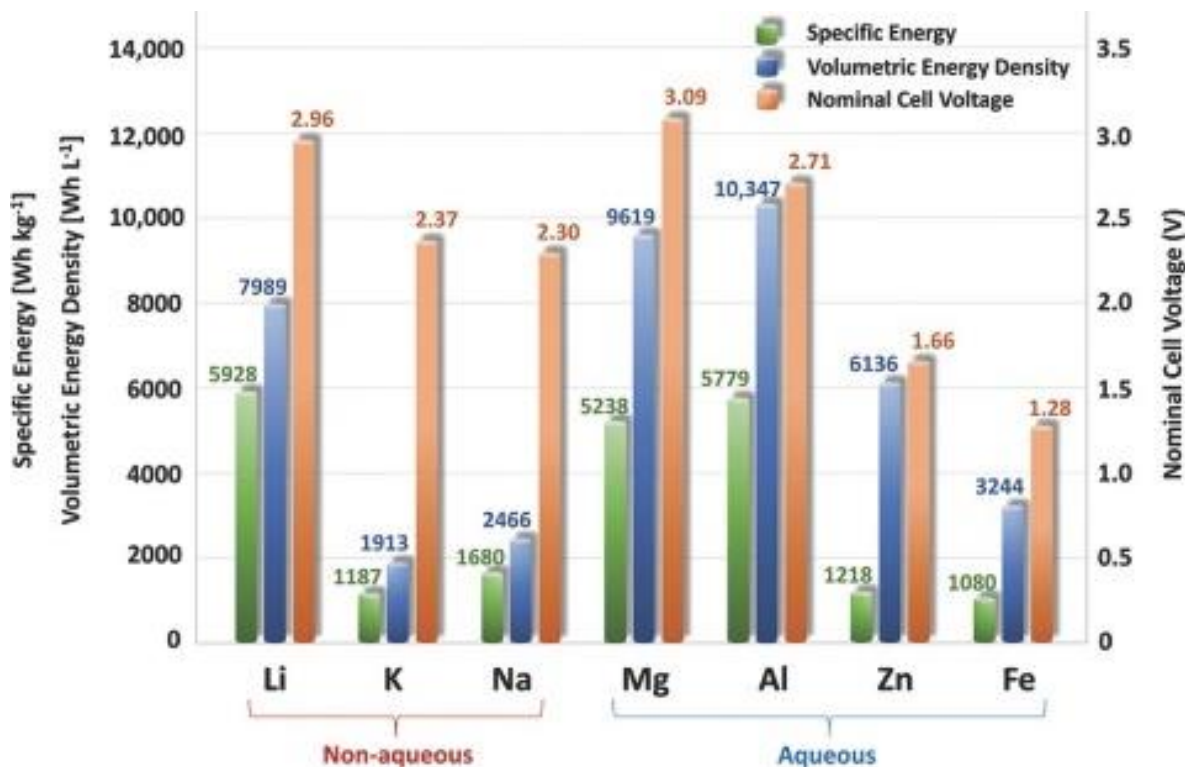
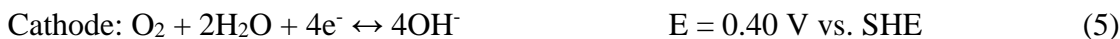


**Figure 1.4** Theoretical specific energies, volumetric energy densities, and nominal cell voltages for various metal anodes in aqueous and non-aqueous metal-air batteries. Specific energy values account for oxygen uptake in the battery by numeric integration between the fully charged and fully discharged states. Volumetric energy densities were calculated using the density of the anode in the fully discharged state [23].

Primary ZABs are most notable for being the predominant energy source for hearing aids, where they provide an impressive volumetric energy density of 1300–1400 Wh L<sup>-1</sup> [23]. Rechargeable ZABs for EVs were heavily investigated between 1975 and 2000 [24-29]. Mechanically rechargeable and electrically rechargeable forms of the battery were both proposed. In mechanically recharged ZABs, the battery was charged by removing spent Zn and re-supplying a fresh Zn anode. This avoided the issues of poor Zn electrode reversibility and unstable bifunctional air electrodes. However, the costs of setting up a network of Zn recharging and supplying stations are quite high, hindering their further development. The most successful electrically rechargeable ZABs employed a flowing electrolyte design, which greatly improved the durability of the Zn electrode. However, their power performance has been a drawback due mainly to fundamental challenges in catalyzing reactions involving O<sub>2</sub> at the air electrode. Moreover, corrosion of the air electrode during the charging reaction was another critical issue,

which, along with the advent of LIBs, slowed down ZAB development at the end of the 20<sup>th</sup> century [30].

Notwithstanding these problems, electrically rechargeable ZABs have gained renewed interest in this decade with the advances in materials science and nanotechnology. A recent economic analysis also found that ZABs being an economically feasible battery technology for smart-grid energy storage. An electrically rechargeable ZAB is typically composed of four main components: an air electrode comprising an ORR/OER (oxygen evolution reaction) bi-functional catalyst-painted gas diffusion layer (GDL), an alkaline electrolyte, a separator, and a Zn electrode. A schematic of a rechargeable ZAB is shown in Figure 1.5. During discharge, the ZAB functions as a power generator through the electrochemical coupling of the Zn metal to the air electrode, in the presence of an alkaline electrolyte, with an inexhaustible cathode reactant (O<sub>2</sub>) from the atmosphere. The electrons liberated at the Zn travel through an external load to the air electrode, while Zn cations are produced at the Zn electrode. At the same time, atmospheric O<sub>2</sub> diffuses into the porous air electrode and is ready to be reduced to OH<sup>-</sup> via ORR (forward Reaction 5) at a three-phase reaction site, which is the interface of O<sub>2</sub> (gas), electrolyte (liquid), and electrocatalysts (solid). The generated OH<sup>-</sup> then migrate from the reaction site to the Zn electrode, forming zincate (Zn(OH)<sub>4</sub><sup>2-</sup>) ions, which then further decompose to insoluble zinc oxide (ZnO) at supersaturated Zn(OH)<sub>4</sub><sup>2-</sup> concentrations. Reaction 6 shows the overall Zn redox reaction. During charging, the ZAB is capable of storing electric energy through the OER (backward Reaction 5), occurring at the electrode-electrolyte interface, whereas Zn is deposited at the cathode surface (backward Reaction 5). The overall reaction (Reaction 6) can be simply shown as Zn combining with O<sub>2</sub> to form ZnO.



Thermodynamically, both reactions are spontaneous and produce a theoretical voltage of 1.66 V. However, the redox reactions of O<sub>2</sub> during the charging and discharging cycles are kinetically slow; thus, an efficient bifunctional catalyst for ORR and OER is extremely important for the development of high-performance electrically rechargeable ZABs.

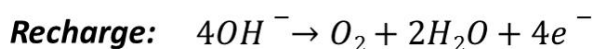
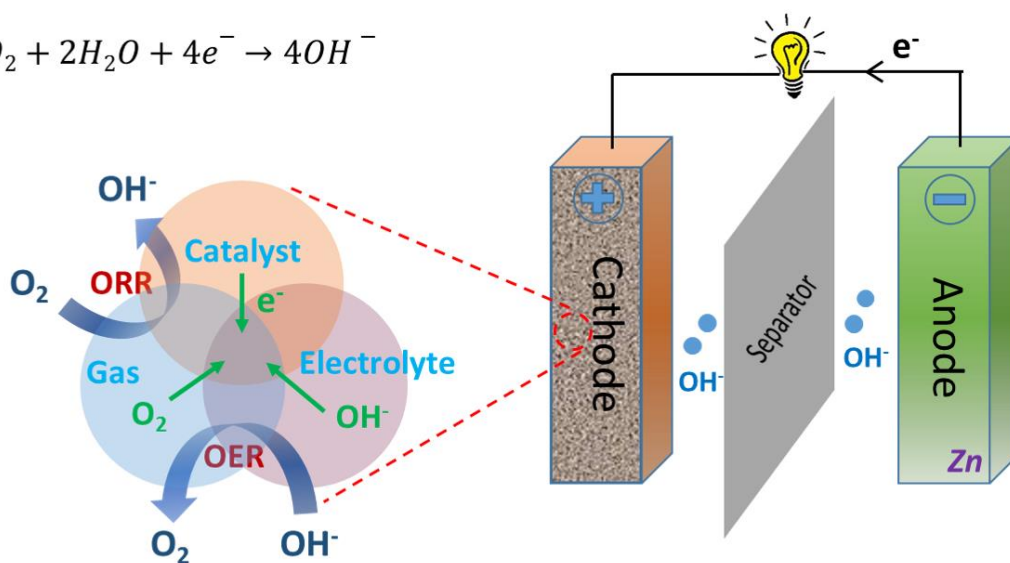


**Figure 1.5** Scheme of a rechargeable ZAB and the schematic diagram of the oxygen electrocatalysts in the three-phase air cathode [31].

## 1.4 Oxygen Electrochemical Reaction

### 1.4.1 Introduction of Oxygen Electrochemical Reaction

From the above, we can see that developing highly efficient electrocatalysts to facilitate sluggish cathodic ORR is a key issue for both ZABs and PEMFCs.

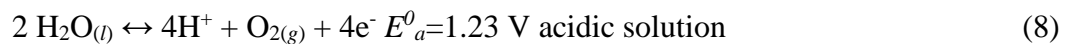
Electrolyte	Reaction pathway	Reaction potential / V (vs. SHE)
Acid medium	4e <sup>-</sup> pathway: $O_2 + 4H^+ + 4e^- \rightarrow 2H_2O$	1.229 V
	Peroxide pathway: $O_2 + 2H^+ + 2e^- \rightarrow H_2O_2$ $H_2O_2 + 2H^+ + 2e^- \rightarrow 2H_2O$ or $2H_2O_2 \rightarrow 2H_2O + O_2$	0.67 V 1.77 V decomposition
	4e <sup>-</sup> pathway: $O_2 + 2H_2O + 4e^- \rightarrow 4OH^-$	0.401 V
Alkaline medium	Peroxide pathway: $O_2 + H_2O + 2e^- \rightarrow HO_2^- + OH^-$ $H_2O + 2HO_2^- + 2e^- \rightarrow 3OH^-$ or $2HO_2^- \rightarrow 2OH^- + O_2$	-0.065 V 0.867 V decomposition
	4e <sup>-</sup> pathway: $O_2 + 2H_2O + 4e^- \rightarrow 4OH^-$	0.401 V

**Figure 1.6** ORR pathways in acid and alkaline medium [32].

It is well known that the ORR can proceed either by a two-step  $2e^-$  pathway with formation of  $H_2O_2$  (in acidic medium) or  $HO_2^-$  (in alkaline medium) as the intermediate specie or by a more efficient  $4e^-$  process to directly reduce  $O_2$  into  $H_2O$  (in acidic medium) or  $OH^-$  (in alkaline medium) (Figure 1.6) [32]. The practical reaction sequences associated with the ORR are rather complicated, involving many intermediates and elementary steps (chemical reaction or electron transfer) depending on the natures of the catalysts and electrolytes.

The selective  $2e^-$  oxygen reduction pathway is a clean and energy-saving route to produce important fine chemical hydrogen peroxide compared to the energy-intensive anthraquinone process [33]. While, the  $4e^-$  pathway that reduces  $O_2$  directly into water is highly preferred for fuel cells and metal-air batteries because of its higher energy-conversion efficiency (Figure 1. 2 and Figure 1.5). The fuel cells directly generate electricity by electrochemically oxidizing fuel and reducing  $O_2$  to produce water as the only by-product on the cathode. Pt and its alloys show the best ORR activity in acidic electrolyte. Today, although tremendous progress has been made, most of the non-precious-metal catalysts (NPMCs) are still far away from satisfaction on the ORR activity in acid medium, let alone the durability for practical PEM fuel cell applications. Comparatively, NPMCs have displayed equivalent or even better electrocatalytic ORR performance than Pt in alkaline electrolytes. The thermodynamic origin of the easier kinetics for ORR in alkaline electrolytes is the lower over-potential (0.7 V @ pH = 14 vs. 1.53 V @ pH = 0) for the first electron transfer to chemisorbed  $O_2$  ( $O_2 \rightarrow O_2^-$ ) [34].

The OER plays a key role in the electrically rechargeable ZABs. In OER, molecular  $O_2$  is produced *via* several proton/electron-coupled procedures [35]. The reaction is highly pH dependent. In acidic and neutral conditions, two water molecules are oxidized into four protons ( $H^+$ ) and oxygen molecule, while in basic environments, hydroxyl groups ( $OH^-$ ) are oxidized and transformed into  $H_2O$  and  $O_2$ . The equilibrium half-cell potentials ( $E^0_a$ ) at 1 atm and 25 °C for OER are shown as follows:



An external current is required to create the potential difference of 1.23 V vs. SHE to drive the OER at pH=0. Thus, a shift in reaction potential *i.e.* ~59 mV per unit pH, occurs theoretically

according to Nernst equation. However, in order to avoid the pH influence on the applied potential and keep the working voltage around 1.23 V for OER, reversible hydrogen electrode (RHE) is commonly used as a reference electrode. The production of O<sub>2</sub> molecule requires transfer of four electrons, and kinetically favorable OER process occurs through multi-step reactions with single-electron transfer at each step. Thus, accumulation of energy at each step makes OER kinetics very sluggish and results in large overpotential. Therefore, a low-cost and highly active electrocatalyst is highly desirable to overcome the energy barrier. Ideally, the OER catalyst must have low overpotential and high stability as well as large earth-abundance and available at low cost for its scalability at industrial scale. Overall, it is important to develop new bifunctional electrocatalysts to fulfil the requirements of high ORR and OER performance, low cost and environmental friendliness.

#### **1.4.2 State of Art Oxygen Electrocatalysts**

##### **a) Pt-Based Catalysts**

Among all of the pure metal ORR catalysts developed to date, Pt is the most widely used electrocatalyst for ORR [36]. It is widely believed that rational optimizing the intrinsic reactivity of Pt-involved active sites and maximizing their utilization based on the understanding of mechanism of ORR are crucial to develop effective Pt-based catalysts for ORR. ORR is very sensitive to the surface electronic properties and electronic surface atomic arrangement or coordination of the catalyst [37-39]. Hence, engineering the surface properties, including the surface electronic structure and atomic arrangement of the catalysts, is believed to be able to effectively tune the catalytic properties of Pt catalyst, enabling enhancement in both activity and durability. Accordingly, altered electronic properties induce a change in the adsorption behavior, specifically a shift of surface-oxide formation to higher potentials. This adsorption behaviour is believed to be the origin of the high activity for ORR. In general, there are four routes to manipulate the surface structure properties of Pt. (i) Controlling the exposed facet (or the shape) of Pt nanocrystals and thus maximizing expression of the facets most active towards ORR [40]. (ii) Combining Pt with another metal to generate multi-metallic nanocrystals with structures in the form of alloys, core-shells, branches or anisotropies [41]. This strategy is attractive and practical, because a bi-metallic system is expected to display, not only a combination of the properties associated with each distinct metal, but also new or unexplored properties, due to a

possible synergistic effect between each metal. Furthermore, the reasonable selection of the alloy metals and the precise control of the size, compositional profile and inner structures of this Pt-based system can boost the final performance. (iii) Modifying Pt nanoparticle surfaces with elaborately selected foreign species, such as metal clusters, molecules, ions, organic or inorganic compounds [42]. Apart from improving the activity or stability of the catalyst, this strategy, in some case, can also render catalysts with specific properties (*e.g.*, hydrophilicity and electronic property) that are beneficial to their operation in ORR system due to the participation of the functional modification species. (iv) Choosing an appropriate catalyst support with high corrosion resistance and with strong interactions with the supported metallic catalyst [43]. It is also recognized that the selection of a robust non-carbon support can improve durability of the catalysts and, in some cases, introduce a synergistic co-catalytic effect between Pt-based nanoparticles and the support *via* support-metal interaction. However, the scarcity and high price of Pt are the key obstacles for the broad deployment in all commercial technologies based on this precious metal [44]. Therefore, developing NPMCs for ORR has been stimulated extensively by the recent push for the commercialization of various EESC systems.

#### b) Me/N/C Catalysts

Among various NPMCs, transition metal-nitrogen-carbon (Me-N-C, Me = Fe, Co, Cu, Ni, Mn, etc.) complexes or composites [45] are the most promising candidates due to their low price, high activity, durability and resistance to the methanol cross-over effect. Research into Me-N-C complexes for ORR started in 1964 when Jasinski *et al.* discovered that cobalt phthalocyanine showed ORR activity [46]. Later Yeager *et al.* reported the first Me-N-C composites for ORR by the pyrolysis of non-N<sub>4</sub>-macrocycles precursors [47]. After that numerous efficient ORR catalysts based on different Me-N-C sources have been developed. Besides Me-N<sub>4</sub> macrocycles [48, 49], inorganic nitrogen sources (ammonia gas, sodium azide) [15, 50-52], small organic molecules (acetonitrile, pyrrole, 1-methylimidazole *etc.*) [53-55] and nitrogen-containing polymers (melamine resin, PANI, poly-dopamine, *etc.*) [56-59] are the commonly used N precursors. Compared with other nitrogen sources, the N-containing polymers, which are more ordered than the small-molecule precursors, could possibly template the formation of a more ordered and thus more stable carbon-based active layer during heat treatment. Polypyrrole was used initially, but it was soon found that polyaniline-derived catalysts were more active and

durable. The intense interest in Me-N-C catalysts and closer shift towards application is the result of important progress made by Dodelet group in 2009, with breakthroughs achieved in the ORR activity reached at high cell voltage in single-cell PEMFC [15]. Based on this very active catalyst, the current density at 0.9 V increases proportionally with the cathode catalyst loading within a certain range (typically  $0.5 \text{ mg cm}^{-2}$  to  $5 \text{ mg cm}^{-2}$ ). But at high current density part, the cell performance is impacted by mass- and charge-transport across the cathode active layer, especially when fed with air. Except the activity at high potential, the power performance (typically operating of 0.6-0.7 V) is a more important target to achieve for practical applications. With this regard, the porous structure plays crucial rule. In 2011, Dodelet group used a metal-organic framework (MOF) consisting of zeolitic Zn imidazolate (ZIF-8) as the host for Fe and N precursors [iron(II) acetate and 1,10-phenanthroline (Phen)]. The prepared Fe/Phen/ZIF-8 catalyst exhibited a peak power density of  $0.91 \text{ W cm}^{-2}$  and a power density of  $0.75 \text{ W cm}^{-2}$  at 0.6 V, the latter comparable with that of a state-of-the-art platinum-based cathode having a loading of  $0.3 \text{ mg}_{\text{Pt}} \text{ cm}^{-2}$ . [16]. In the same year, Zelenay group used polyaniline as a template in the preparation of a catalyst incorporating iron and cobalt. The best-performing FeCo-N-C catalyst exhibited excellent  $4e^-$  selectivity ( $\text{H}_2\text{O}_2$  yield  $<1.0\%$ ), and excellent long-term performance durability with 700 hours test at a fuel cell voltage of 0.4 V [56]. While the test voltage (0.4 V) is too low for the real applications.

However, due to the complex nature, the atomic structure of the active sites and catalytic mechanism of the Me-N-C catalysts remain largely elusive. The likely active-site structures include the following most frequently considered ones: (i) M-N<sub>4</sub> site [60], since the metal macrocycles such as porphyrin and phthalocyanine are catalytically active for ORR, their basic structural motif, *i.e.* Fe-N<sub>4</sub>, has been regarded to be the active centre in the heterogeneous environment; (ii) Me-N<sub>x</sub> sites, which was first proposed by Yeager and co-workers [61, 62] and further developed by the Dodelet group and others [63]; (iii) metal-free carbon structure, as originally proposed by Wiesener (with metal merely serving as a catalyst for the ORR active-site formation). In the case of Fe/N/C catalyst, several Fe-N<sub>x</sub> species have been proposed by Dodelet et al. (Figure 1.7), among which, only FeN<sub>4</sub>/C (D1) and N-FeN<sub>2+2</sub>/C (D3) are catalytically active for ORR, while FeN<sub>2+2</sub>/C (D2) is inactive. This conclusion is based on the electronic population of the 3d orbitals in the iron(II) ion, among which the  $3d_z^2$  orbital is reputed to bind oxygen end-on. This energy level is unoccupied for D1 ( $S = 0$ ) or singly occupied for D3 ( $S = 2$ ), while it is

fully occupied for D2 ( $S = 1$ ). Therefore, D2 is unable to accept one electron from  $O_2$  to form an adduct to the  $FeN_{2+2}/C$  site. Kramm *et al.* attributed the improved ORR kinetics of these Fe- $N_4$  centres to Fe-ion centres with higher electron densities [64]. Koslowski related the current density of ORR to the amount of in-plane  $FeN_4$  centres using Mössbauer spectra and a linear correlation was identified [65]. Wang *et al.* calculated the adsorption energy of ORR species and the energetics (heats of reaction and activation energies) of all of the possible ORR elementary reactions on the modeled Fe- $N_4$  embedded graphene to investigate the reaction pathways for ORR on this catalyst [66]. By using first-principles DFT calculations, they indicated that the  $O_2$  molecule is only chemisorbed to the central transition metal Fe of the Fe- $N_4$  complex embedded in the graphene layer, implying that the existence of an N-chelated transition metal plays a pivotal role to initializing the ORR in this class of catalysts. In 2016, Jiang and co-workers [67] revealed that the coexistence of Fe/ $Fe_3C$  nanocrystals and Fe- $N_x$  sites are the origin of the ORR activity, DFT calculation corroborated this conclusion by indicating that the interaction between Fe/ $Fe_3C$  and Fe- $N_4$  coordination structure favored the adsorption of oxygen molecule. Many other authors proposed a different opinion regarding the possible role of the transition metal towards the ORR active site. Instead of being a part of the active site structure, the metal-ion centres merely catalyze the formation of various nitrogen sites (*e.g.* pyridinic-N, pyrrolic-N) [68-70]. Specifically, the ORR activity is attributed to the formation of graphitic nitrogen and/or pyridinic nitrogen functional groups, or the degree of edge plane exposure the latter represents. This further complicates the understanding of the exact nature of the catalytically active moieties with respect to ORR. Insight into active site formation mechanisms and structures of Me-N-C catalysts is still insufficient at the current technology state. Further investigations of the exact ORR active site as well as the structures of the active site of Me-N-C materials are required in order to boost the ORR performance of this group of catalyst.

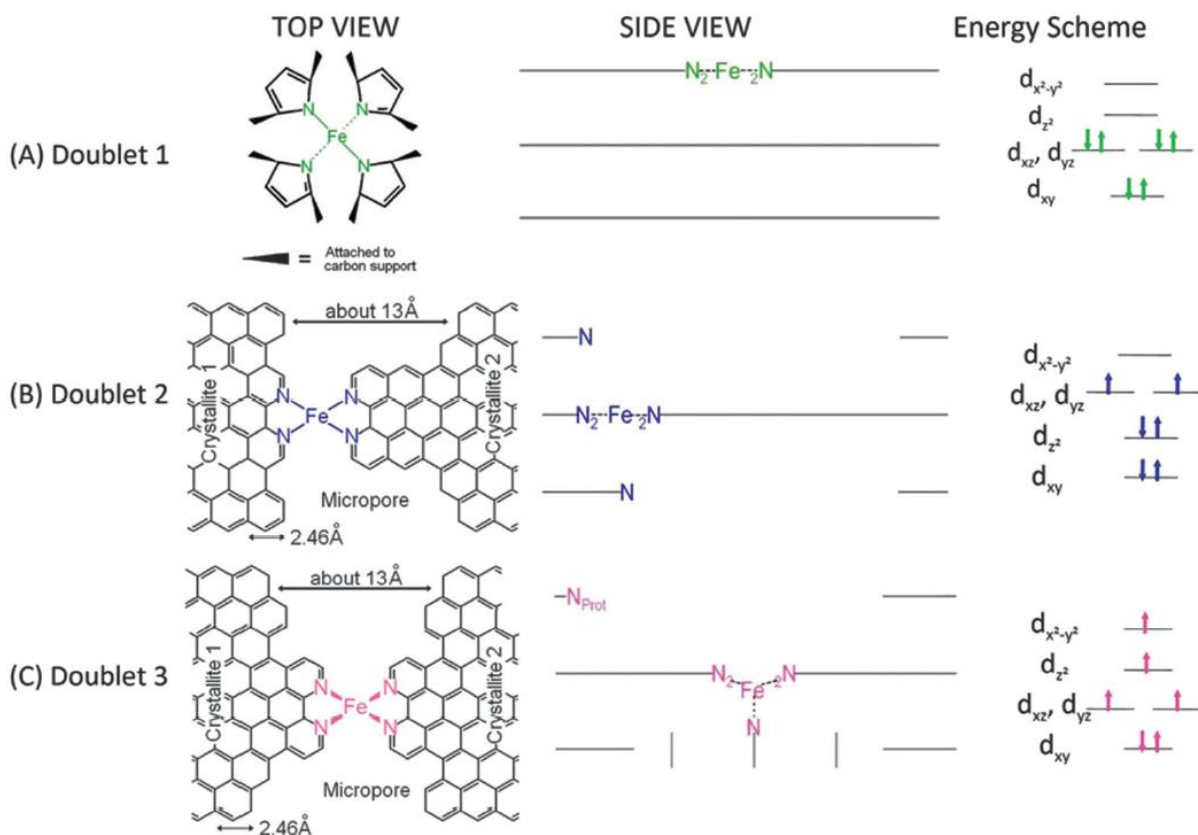


**Figure 1.7** Side views and top views of the proposed structures of Fe-N<sub>x</sub> species: (Doublet 1): the FeN<sub>4</sub>/C catalytic site in heat-treated, macrocycle-based catalysts. (Doublet 2): the FeN<sub>2+2</sub>-like micropore-hosted site found in the catalyst prepared with iron acetate and heat-treated in ammonia. The distance between the two nitrogen atoms belonging to the graphene planes above and below the FeN<sub>2+2</sub>-plane is similar to that in crystalline iron phthalocyanine. (Doublet 3): the N-FeN<sub>2+2</sub>-like composite site. The iron (II) ion in N-FeN<sub>2+2</sub> is coordinated by five pyridinic nitrogen atoms, one of them belonging to a plane located at the vertical below the N<sub>4</sub>-plane. This axial nitrogen coordination moves the iron (II) ion out of the N<sub>4</sub>-plane towards the fifth coordinating nitrogen atom. Doublet 3 may exist as N-FeN<sub>2+2</sub>/C or as a composite site N-FeN<sub>2+2</sub>...N<sub>prot</sub>/C, where N<sub>prot</sub> is a protonable pyridinic nitrogen atom appearing at the edge of the upper plane in the side view of Doublet 3. In all side views, graphene planes are drawn as lines [71].

Most recently, single-atom catalysts (SACs) with isolated metal atoms dispersed on solid supports have emerged as a new frontier in catalysis science and have attracted extensive research attention [72-78]. Despite tremendous progress in Me-N-C catalysts, their catalytic properties are still far from satisfactory. Downsizing the active species of Me-N<sub>x</sub>/C catalysts to single atoms can accomplish maximum atom-utilization efficiency and fully expose the active sites, which is an effective approach for enhancing the intrinsic activity of catalysts. Li and co-

workers prepared a highly reactive isolated single-atom Fe/N-doped porous carbon (ISA Fe/CN) catalyst with an Fe-N<sub>4</sub> active center [79]. The designed experiments were carried out to reveal that maintaining Fe as isolated atoms and incorporating N was essential for excellent alkaline ORR performance. When Fe NPs were removed and isolated Fe atoms were exposed by acid leaching, enhanced activity was observed in view of more positive E<sub>1/2</sub>, which was ascribed to the exposure of single-Fe atomic sites. When atomically dispersed Fe-N<sub>4</sub> sites were poisoned by SCN<sup>-</sup>, Fe ISAs/CN exhibited remarkably degraded ORR performance. The performance of Fe ISAs/CN can be restored to the original level by removing SCN<sup>-</sup>. These results revealed that the active centers for the ORR on Fe ISAs/CN were isolated Fe-N<sub>4</sub> sites. DFT calculations further demonstrated that the outstanding activity of Fe ISAs/CN originated from the high efficiency of single-atom Fe-N<sub>4</sub> sites in transporting electrons to the adsorbed OH species. Zelenay and co-workers reported an iron-nitrogen-carbon ((CM+PANI)-Fe-C) catalyst with atomically dispersed Fe-N<sub>4</sub> sites and hierarchical porosity [80]. This catalyst exhibited an outstanding performance in both a rotating ring-disk electrode (RDE) test in 0.5 M H<sub>2</sub>SO<sub>4</sub> and membrane electrode assembly (MEA) under realistic cathode operation in air conditions. They suggested that the catalytic active sites were carbon-embedded Fe-N<sub>4</sub> sites, which were directly visualized by aberration-corrected scanning transmission electron microscopy (AC-STEM) (Figure 1.8). Currently, SACs have been of great interest and importance for designing a new generation of low-cost ORR catalysts. SACs afford many fascinating characteristics, such as maximum atomic utilization, high activity, and selectivity. Moreover, the structural uniformity of single-atom Me-N<sub>x</sub>/C catalysts makes them a model system to precisely control their coordination environments and geometric configurations at the atomic scale, for optimization of catalytic properties and deeper understanding of the ORR mechanism. Therefore, the development of strategies for preparation of SACs appears to be particularly important.

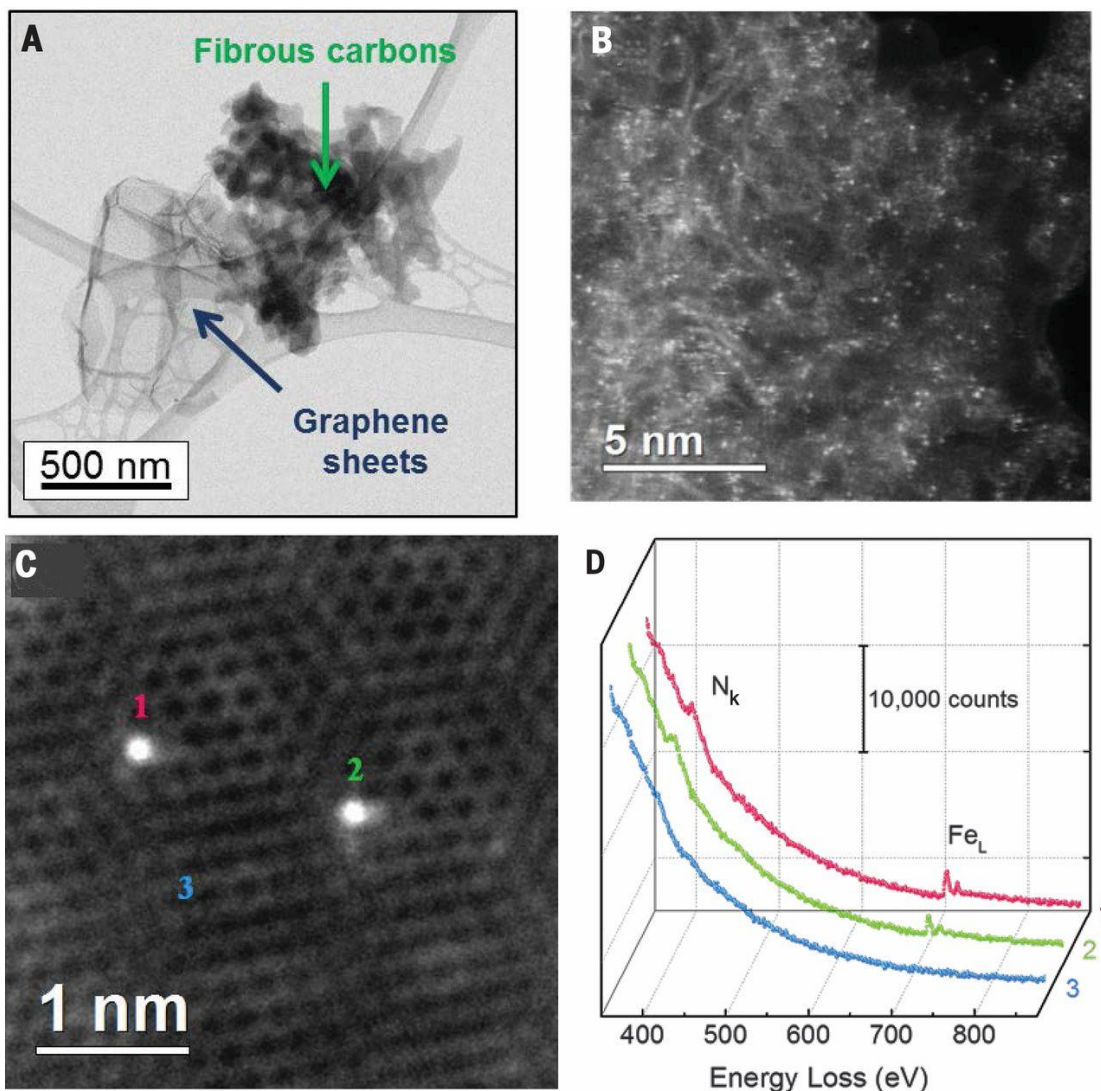


**Figure 1.8** (a) BF-STEM image of a typical (CM+PANI)-Fe-C catalyst showing primary fibrous carbons and secondary graphene sheets. (b) Atomic-resolution HAADF-STEM image of Fe atoms distributed across the surface of fibrous carbon phase showing randomly oriented, intertwined graphitic domains. (c) HAADF-STEM image of individual Fe atoms (labeled 1, 2, and 3) in a few-layer graphene sheet. (d) EEL spectra of the N k-edge ( $N_k$ ) and Fe L-edge ( $Fe_L$ ) acquired from single atoms (1 and 2) and few-layer graphene (3), demonstrating the presence of N around the Fe atoms [80].

### c) Metal-Free Catalysts

Metal-free catalysts typically consist of various carbon-based materials such as graphite, graphene, carbon nanotubes (CNTs) and ordered mesoporous carbon. With the progress in tuning intrinsic property of these carbon material with a series of heteroatoms, such as B [81, 82], N [32, 83-87], S [88, 89], Se [90], P [91, 92], Si [93], and F [94], plenty of doped carbon-based catalysts,

including dual-doped [95-98] and trinary-doped [99, 100] carbon materials, have been reported. However, the catalytic mechanism of different doped carbon catalysts is complicated and still remains unrevealed. Dai *et al.* [101] proposed that the high activity of N-doped carbon catalysts is attributed to the larger electronegativity of N (electronegativity of nitrogen: 3.04) with respect to C atoms (electronegativity of carbon: 2.55), and the creating of positive charge density on the adjacent C atoms. These factors result in the very favorable adsorption of O<sub>2</sub>. While this explanation is not suitable for other carbon materials doped with the low electronegative atoms such as P-doped (electronegativity of phosphorus: 2.19) and B-doped (electronegativity of boron: 2.04) carbon materials, which have also shown pronounced catalytic activity. Recently, theoretical studies using simulation calculations have confirmed that breaking the electroneutrality of graphitic materials to create charged sites favorable for O<sub>2</sub> adsorption is a key factor in enhancing ORR activity, regardless of whether the dopant is electron-rich (*e.g.*, N) or electron-deficient (*e.g.* P, B) [81].

Heteroatom doping is the replacement of some carbon atoms in the graphitic structure with other atoms. Figure 1.9a gives a simple illustration of the doping process with heteroatoms, such as B, N, P, S, and/or F, while Figure 1.9b shows possible graphitic structure changes induced by doping. More than 10 non-metal elements enclosed by the red line in the periodic table of elements shown in Figure 1.9c could be doped into carbon nanomaterials. As the size and electronegativity of the heteroatoms are different from those of carbon atom (Figure 1.9c), the introduction of heteroatoms into carbon nanomaterials could cause electron modulation to change the charge distribution and electronic properties [102-104]. This, together with the doping-induced defects (Figure 1.9b), could further change the chemical activity of carbon nanomaterials, thus leading to many novel applications, including electrocatalysis for ORR [105-107].



doped CNTs [81], graphene [109], and graphite [110], with a good methanol and CO tolerance and excellent durability for fuel cell and many other applications [111]. These new findings proved to be sufficiently important to trigger worldwide attention. More recently, carbon-based metal-free ORR catalysts have been demonstrated to show an excellent operational stability and high energy efficiency even in acidic PEMFCs—the mainstream fuel cell technology [112]. Despite the promising performance of electrodes based on CNT or graphene, their use on a large scale is presently limited by the high costs [113]. Therefore, sustainable and abundant biomass resources have captured attention as alternative options [114]. Every year more than 140 billion metric tons of biomass are generated globally as waste from agricultural products [114]; hence, their conversion into novel materials makes sense if one considers the benefits related to waste reduction. Biomass from plants and animal biomass from livestock farming or human activities are generated vastly every day, bringing ecological impact, greenhouse gas (GHG) emission, and burdens to waste management. Therefore, it is of strategic importance to develop new class of biomass-derived carbon-based catalysts for fuel cell and metal–air battery applications, which could enable significant cost reduction while maintaining high efficiency with economic viability.

## **1.5 Na-Ion Batteries**

Sodium (Na), the fourth most abundant element on earth, has a seemingly unlimited distribution [115]. Supplies of Na-containing precursors are vast, with 23 billion tons of soda ash located in the United States alone. The abundance of resources and the much lower cost of trona (about \$135–165 per ton), from which  $\text{Na}_2\text{CO}_3$  is produced, compared to  $\text{Li}_2\text{CO}_3$  (about \$5000 per ton in 2010), provide a compelling rationale for the development of SIBs to be used as alternatives to LIBs [116]. Because an alternative to Li is needed to realize large-scale applications, SIBs have attracted considerable research attention in recent years. SIBs were initially studied when the development of LIBs began in the 1970s and 1980s, but due to rapid advances in the development and success of commercial applications of LIBs, SIBs were largely abandoned [117-119]. Moreover, during those years, the overall quality of materials, electrolytes and glove boxes was insufficient for handling Na, making it difficult to observe electrode performance. In the 1980s, prior to the commercialization of LIBs, a few US and Japanese companies developed SIBs in full cell configurations with remarkable cyclability over 300 cycles, but the average discharge voltages were lower than 3.0 V, which did not attract much attention against

carbon//LiCoO<sub>2</sub> cells that exhibit an average discharge voltage of 3.7 V [120]. The battery components and the electrical storage mechanism of SIBs and LIBs are basically the same except for their ion carriers (Figure 1.10). In terms of cathode materials, the intercalation chemistry of Na is very similar to that of Li, making it possible to use similar compounds for both systems. However, there are some obvious differences between these systems. Na<sup>+</sup> ions (1.09 Å) are larger compared to Li<sup>+</sup> ions (0.76 Å), which affects the phase stability, transport properties, and interphase formation [121]. Na is also heavier than Li (23 g mol<sup>-1</sup> compared to 6.9 g mol<sup>-1</sup>) and has a higher standard electrode potential (-2.71 V vs. SHE as compared to -3.02 V vs. SHE for Li); thus, SIBs will always fall short in terms of energy density. However, the weight of cyclable Li or Na is a small fraction of the mass of the components, and the capacity is determined primarily by the characteristics of the host structures that serve as electrodes. Hence, in principle, there should be no energy density consequences of the transition from LIBs to SIBs [116]. In addition, aluminum (Al) undergoes alloy reaction with Li below 0.1 V vs. Li/Li<sup>+</sup>, which indicates that Al is available as a current collector for anodes in Na cells [122]. Therefore, Al is a cost-effective alternative to copper (Cu) as an anode current collector for SIBs.

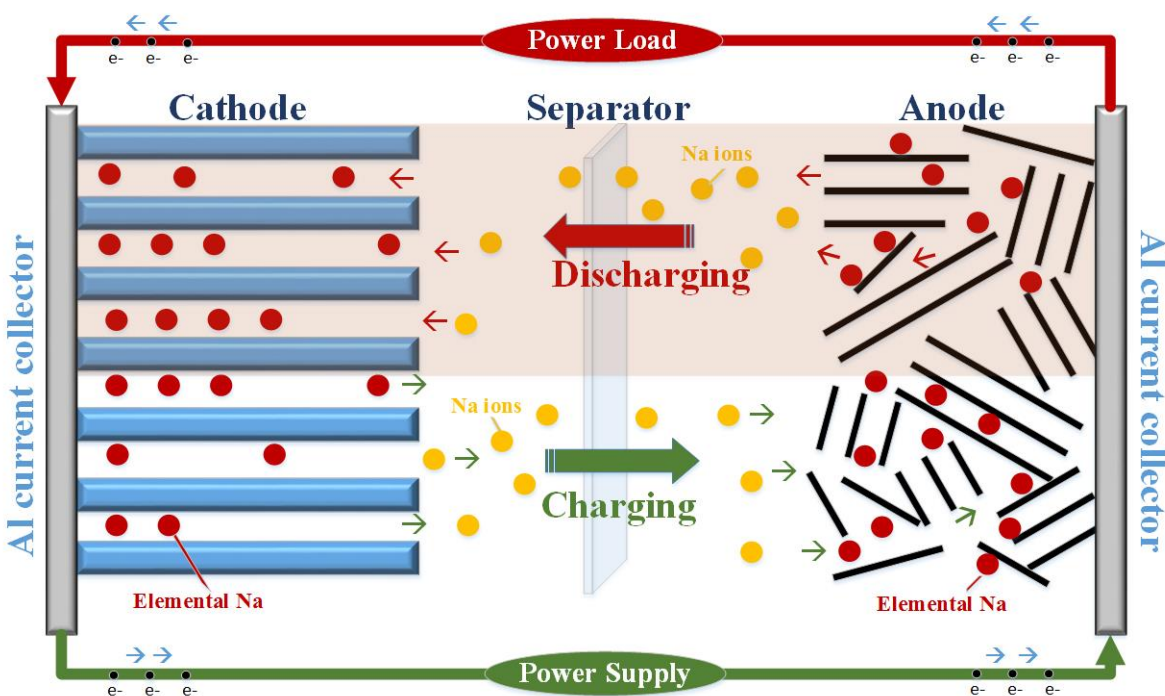


Figure 1.10 Scheme of a rechargeable SIB [123].

In the past three decades, exciting progress on cathode materials for SIBs has been achieved; an important reason of the shelved research about SIBs was the absence of suitable anode materials. In 1980s, carbonaceous materials were initially investigated and considered as promising candidates for the anode materials of LIBs. It was demonstrated that graphite can deliver a high theoretical capacity of anode  $372 \text{ mAh g}^{-1}$  and present a flat potential plateaus at a low potential region of  $0.1\text{--}0.2 \text{ V}$  (vs  $\text{Li/Li}^+$ ) [124]. Regrettably, it was found that the  $\text{Na}^+$  cannot be easily intercalated into the graphite interlayer due to its larger ionic radius. Before 2000, only several anode materials were proved to have Na storage properties, but their energy densities were much lower than that of graphite for LIBs. In 1988, Ge and Foulletier reported the electrochemical intercalation behavior of Na in graphite and deduced the formation of  $\text{NaC}_{64}$ , corresponding to the theoretical capacity of  $35 \text{ mAh g}^{-1}$  [125]. In 1993, Doeff et al. demonstrated that the intercalation of  $\text{Na}^+$  into graphite, petroleum coke and Shawinigan black could lead to the formation of  $\text{NaC}_{70}$  ( $31 \text{ mAh g}^{-1}$ ),  $\text{NaC}_{30}$  ( $70 \text{ mAh g}^{-1}$ ) and  $\text{NaC}_{15}$  ( $132 \text{ mAh g}^{-1}$ ), respectively, which was calculated from the time and amount of current passed [126]. At the beginning of the 21<sup>st</sup> century, the situation was somewhat changed. In 2000, Dahn and co-workers confirmed that the hard carbon can deliver a high reversible capacity of  $\approx 300 \text{ mAh g}^{-1}$ , close to the Li storage capacity of graphite, although the cycle ability was insufficient for practical applications, which still brought new hope to the development of SIBs. After that, the research of SIBs presented the trend of blowout development. A large number of materials have been explored to be utilized as anode for SIBs, which includes metal/alloys (Sn, Sb, Ge, P, and their alloys) [127-132], metal oxide/sulfide/phosphide [133-144], and carbonaceous materials [145]. The emerging anode materials with special structure or composition exhibit greatly enhanced electrochemical performances, which can even compare favorably with that of LIBs. The metal and alloy with alloying reaction usually delivered high specific capacities, but this type of anode materials are often burdened with volume expansion during the charge-discharge process, leading to the poor cycle stability. For large-scale commercialized batteries, some crucial characters should be equipped with, such as, high safety, excellent cycling stability and low cost. Thus, the choice of electrode material should be based on some standards, e.g., abundance, nontoxicity, stability and durability. Carbon materials have shown good properties that meet almost the above-mentioned requirements, but the achievements are still insufficient, further exploration is desired. Especially,

the design and easy fabrication of carbon materials with special micro/nanostructures containing rich reversible Na storage active sites and shortened Na<sup>+</sup> diffusion path is necessary.

## **1.6 Thesis Objectives and Organization**

### **1.6.1 Objectives**

The topic of this thesis is carbon-based non-precious materials for various energy storage and conversion devices, i.e., batteries and fuel cells. Metal-air batteries and fuel cells with improved specific energy, energy density, cost, safety and grid compatibility are necessary to electrify the long-range, low-cost and high-utilization transportation sectors. The major technological issue of these technologies lies in developing NPMCs to replace the expensive and scarce Pt-based catalyst for catalyzing the sluggish cathode oxygen electrochemical reactions. The central theme of this thesis is the development of NPMCs for ORR in the application of PEMFCs and ZABs; more specifically, is to develop novel porous carbon-based oxygen electrocatalysts and study the relationships between ORR activities, single-cell performance with the microporous structure of the NPMCs. Furthermore, developing novel strategies to fabricate highly-porous structures to improve the activity, power performance and stability of the NPMCs for PEMFCs and ZABs is also the important component in this thesis. For SIBs, reducing the processing cost and improving the Na storage capacity are crucial to the practical application, the high-performance carbon materials produced through an effective synthesizing method with cheap precursor and high yield are quite desired to exploit. In this thesis, the development of microporous carbon with adjustable interlayer spacing for SIBs is also included, as a sub-project.

Objective I: Study and design highly active and stable NPMCs towards ORR.

Objective II: Performance enhancement of fuel cell and metal-air batteries based on the designed oxygen electrocatalysts at the cathodes.

Objective III: Develop low-cost and high-performance anodes for Na-ion batteries.

### **1.6.2 Thesis Organization**

This thesis includes four chapters which are organized as follows:

**Chapter 1** Introduction: This chapter briefly introduces the background and development of most advanced electrochemical energy storage and conversion devices, highlighting the advantages of PEM fuel cells, Zn-air batteries and sodium-ion batteries. Then, the oxygen electrocatalysis and the progress of the state of art oxygen electrocatalysts are presented in detail.

**Chapter 2** Experimental: The experimental chapter describes the details of materials synthesis, the physical and electrochemical characterizations involved in this thesis.

**Chapter 3** Results: This chapter is divided into six parts. The first part investigates the optimal Fe content as well as the microstructures for the Fe/N/C catalysts. In the second part, based on the optimized Fe/N/C catalyst, a new simple route involving sulfur (S) as a “promoter” was developed to achieve a litchi-like porous Fe/N/C catalyst with abundant FeN<sub>x</sub> species, presenting a large surface area with a high pore volume and showing high activity for ORR/OER, as well as an power density enhancement of a Zn-air battery. The third part presents a bimetallic (Fe-Cu)/N/C as cathode catalyst with higher power density and better stability for PEM fuel cells. The fourth part reports a Si-contained Fe/N/C catalyst showing exhibits high activity and outstanding stability, based on the porous carbon deriving from the biomass reed stalk. In the fifth part, based on a more direct and simple way, a metal-free catalyst was synthesised by employing the bio-waste reed as the single precursor for both C and Si, the obtained Si, N-codoped carbon catalyst is active for ORR, and shows excellent performance as an air cathode for a Zn-air battery device. Moreover, the DFT calculation was used to explain the active sites in this highly performing metal-free catalyst. In the last part, the highly-ordered spherical MPCs were fabricated based on the SPRMs precursor, and the optimized MPCs showed promising electrochemical performance for Na-ion battery.

**Chapter 4** Conclusion and Perspective: Main conclusions are presented based on the results and analysis, and potential work in this research direction in the future is proposed.

In this thesis, most of the work was completed by Qiliang Wei; Dr. Gaixia Zhang gave important comments and crucial guidance for the work; Mr. Xiaohua Yang assisted on the pyrolysis experiments in some parts of work; the DFT part in the fifth part of work was conducted by Prof. Vidal François’s group; and the synchrotron measurement and analysis was accomplished with the help from the scientists of different beamlines at CLS: Dr. Dongniu Wang, Dr. Lucia Zuin,

Dr. Ning Chen and Dr. Yongfeng Hu, as well as Jiatang Chen in Prof. Tsun-Kong Sham's group. Qiliang Wei and Prof. Shuhui Sun conceived the project and designed the experiments. All authors discussed the results and commented on the manuscripts.

## CHAPTER 2 EXPERIMENTAL

This chapter introduces the detailed synthesis process of various catalysts: Fe/N/C, bimetallic (Fe-Me)/N/C and metal-free carbon materials. Various physical and electrochemical characterizations on these electrocatalysts or electrodes are also included.

### 2.1 Chemicals and Materials

Phenol (99%), formaldehyde solution (37%), iron(II) acetate (95%), 1,10 phenanthroline (99%), sodium hydroxide (NaOH, 95.0%), sulfuric acid (H<sub>2</sub>SO<sub>4</sub>, 95.0–98.0%), hydrochloric acid (HCl, 32% in H<sub>2</sub>O), sulfur (S), and potassium hydroxide (KOH, 87.1%), were bought from Fisher Scientific. PluronicF-127, Nafion solution (5 wt%) were purchased from Sigma-Aldrich. Pt/C (20%) was purchased from E-TEK. All chemicals were used as received and solutions were prepared using deionized water (Millipore Milli-Q, 18.2 MΩ cm).

### 2.2 Material Synthesis

#### 2.2.1 Fe/N/C Catalysts

In a typical synthesis of Fe/N/C catalyst, the precursors were prepared by first mixing the carbon host, 1,10-phenanthroline, and iron(II) acetate in a solution of ethanol and deionized water (ethanol: water = 1:2) under stirring at room temperature. The mixture was then heated to 60–80 °C for 2–3 h until about 50 mL of a thick slurry was obtained. The slurry was placed overnight in a drying oven at 95 °C. Afterward, the dry powder was ground sufficiently and placed in the quartz tube, followed by pyrolyzing in Ar and then in ammonia with different pyrolysis time in order to obtain expected weight losses.

#### 2.2.2 Bimetallic (Fe-M)/N/C Catalysts

The bimetallic (Fe-M)/N/C catalysts in this work was prepared by three precursors: ZIF-8 as carbon precursor (Labeled as MOF. Trade name: Basolite Z1200, Aldrich, produced by BASF); 1,10-Phen (Labeled as Phen. Trade name: 1,10-Phenanthroline, ≥ 99%, Aldrich); and metal salts (FeAc, CuAc, CoAc, NiAc, MnAc). For the (Fe-Cu)/N/C, the total metal mole (Fe + Cu) keeps the same. These precursors were first uniformly mixed together with a mixture of ethanol and

deionized (DI) water to form a slurry, then dried at 90 °C overnight. The dry sheet and powder was then undergoing 3 h of ball-milling at 400 rpm. The resulting dry powder was the catalyst precursor ready for pyrolysis. Then the catalyst precursor underwent two stages of pyrolysis in Ar at 1050 °C and in NH<sub>3</sub> at 950 °C, respectively. The weight loss of catalyst in the NH<sub>3</sub> pyrolysis step were kept on hold at 50%.

### **2.2.3 Metal-Free Catalyst**

The procedure of the preparation of metal-free Si-N-C catalyst is described as the following: before carbonization, the reed were carefully cut into small pieces, washed with DI-water, and dried in oven at 80 °C for 2 days. The dry samples were pre-carbonized in combustion boat at 800 °C for 1 h under Ar flow. Afterwards, the pre-carbonized materials were mixed with KOH sufficiently and heated in a homemade copper boat under Ar flow at 700 °C for 1 h (to obtain porous Si-C sample), followed by pyrolysis under ammonia atmosphere at 950 °C with different extent (in this work, we use 70 mg of each Si-C sample to undergo the NH<sub>3</sub> pyrolysis with 4 min, 6 min, and 8 min respectively, the samples are denoted as Si-N-C- $x$  min,  $x = 4, 6, 8$ ). To investigate the role of Si, the Si-N-C sample was washed by HF (to remove the Si atoms), denoted as N-C- $x$  min-HF.

## **2.3 Physical Characterizations**

### **2.3.1 Scanning Electron Microscopy (SEM)**

Electron microscopy is used to image materials at the nanoscale by measuring their interaction with an incident stream of electrons. SEM operates in several modes which either detects incident electrons bouncing back off the sample (backscattered electrons) or electrons that are given off by the sample in response to being excited by the incident beam (secondary electrons). Secondary electrons have very low interaction volume in the sample since they typically have much lower energy than backscattered electrons. Due to this, they give great topographical contrast and can be used to image surface morphology. The process of backscattering is highly dependent on atomic number, and can thus be used to determine the composition of a sample. Samples may also give off characteristic X-rays as core electrons are excited by the incident beam. These X-rays can be collected in the Energy Dispersive X-ray Spectroscopy (EDS) mode

and be used to measure the composition of the material. Since these X-rays have a high interaction volume, this mode gives a well-averaged count.

### **2.3.2 Transmission Electron Microscopy (TEM)**

Transmission electron microscopy (TEM) is a very powerful tool for material science. A high energy beam of electrons is shone through a very thin sample, and the interactions between the electrons and the atoms can be used to observe features such as the crystal structure and features in the structure like dislocations and grain boundaries. Chemical analysis can also be performed. The TEM operates on the same basic principles as the light microscope but uses electrons instead of light. Because the wavelength of electrons is much smaller than that of light, the optimal resolution attainable for TEM images is many orders of magnitude better than that from a light microscope. Thus, TEMs can reveal the finest details of internal structure - in some cases as small as individual atoms. Figure 2.1 below shows the basic setup of a TEM. The beam of electrons from the electron gun is focused into a small, thin, coherent beam by the use of the condenser lens. This beam is restricted by the condenser aperture, which excludes high angle electrons. The beam then strikes the specimen and parts of it are transmitted depending upon the thickness and electron transparency of the specimen. This transmitted portion is focused by the objective lens into an image on phosphor screen or charge coupled device (CCD) camera. Optional objective apertures can be used to enhance the contrast by blocking out high-angle diffracted electrons. The image then passed down the column through the intermediate and projector lenses, is enlarged all the way. The image strikes the phosphor screen and light is generated, allowing the user to see the image. The darker areas of the image represent those areas of the sample that fewer electrons are transmitted through while the lighter areas of the image represent those areas of the sample that more electrons were transmitted through.

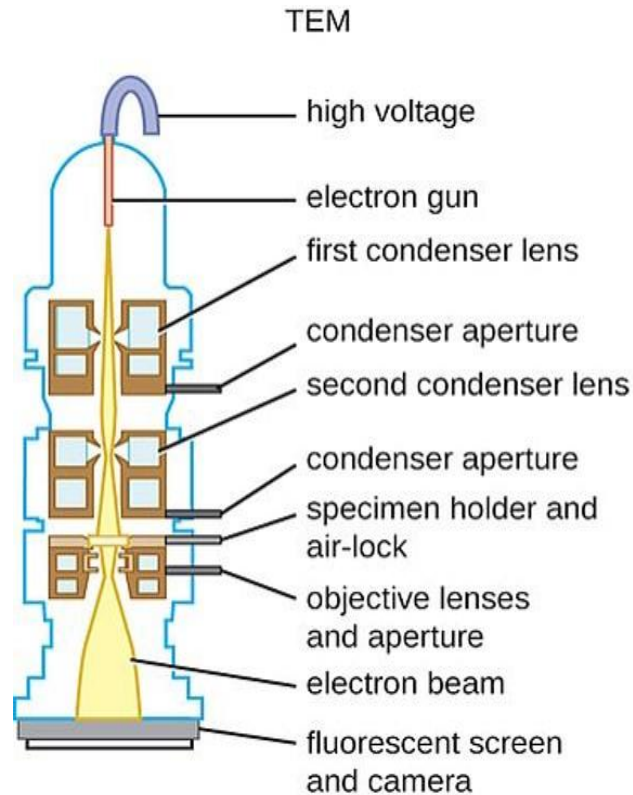


**Figure 2.1** Basic principle of a TEM [146].

### 2.3.3 X-Ray Diffraction (XRD)

X-ray diffraction is a crystal structural characterization tool and is predominantly used to determine atomic arrangement in crystalline materials. In principle, it features a source and a detector. In the source, a high voltage filament is used to accelerate electrons toward a target (e.g. copper). The incident electrons excite core electrons from atoms in the target, which during relaxation emit X-rays of characteristic wavelength (e.g. Cu-K $\alpha$  X-rays have a wavelength of approximately 1.54 Å). The X-rays are then fired at the sample of interest in which they are diffracted by the different crystalline planes and finally detected by the detector. Since different crystalline planes interact with X-rays in specific geometries, the scanning is carried out over a range incidence angles. Figure 2.2 below shows a schematic of the interaction between X-rays and a typical sample. The dots in the graph correspond to the building blocks of a crystalline material. Due to the crystalline nature, the atoms are arranged periodically. The incident X-ray beam is scattered at different planes of the material. The resulting diffracted X-rays therefore have a different optical path length to travel. The magnitude of this path length only depends on

the distance between the crystal planes and the incident angle of the X-ray beam. This is summarized in the famous Bragg-Equation:

$$n\lambda = 2d \sin\theta \quad (9)$$

This equation can be described as follows: constructive interference occurs only if the path difference (given by  $2d \sin\theta$ ) is a multiple ( $n=1,2,\dots$ ) of the used wavelength of the X-ray beam. As the wavelength in XRD experiments is known and the angles at which constructive interference occurs are measured, the use of the Bragg equation allows determining the distance between the lattice planes of the material. The XRD study was carried out with a Bruker D8 advanced diffractometer using a Cu  $K_\alpha$  radiation source in the thesis.

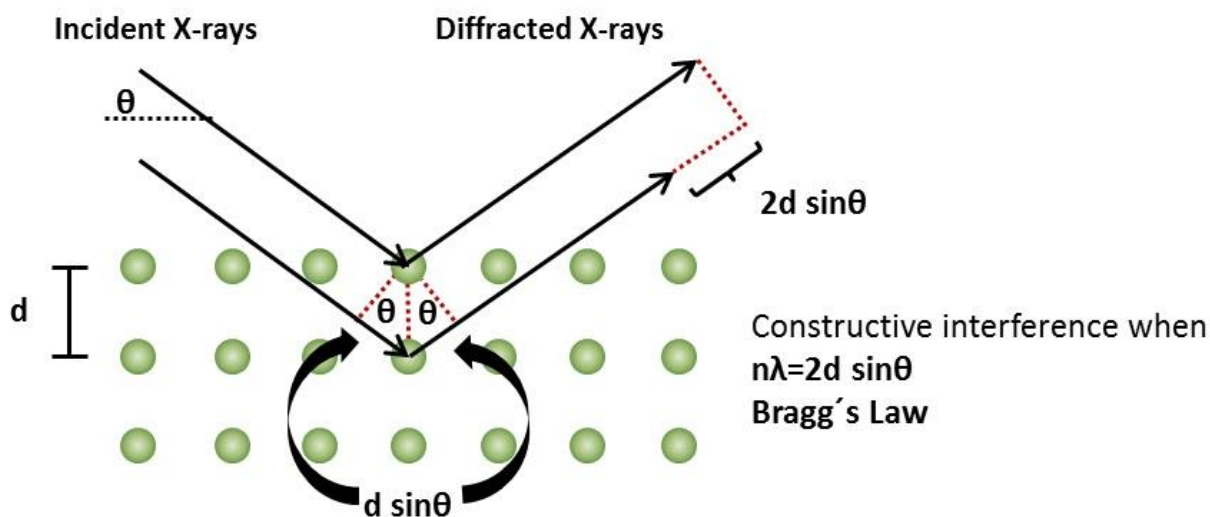


**Figure 2.2** Schematic showing the interaction between x-rays and a typical crystalline sample [147].

### 2.3.4 X-Ray Photoelectron Spectroscopy (XPS)

X-ray photoelectron spectroscopy (XPS) is a surface-sensitive quantitative spectroscopic technique that measures the elemental composition at the parts per thousand range, empirical formula, chemical state and electronic state of the elements that exist within a material. XPS spectra are obtained by irradiating a material with a beam of X-rays while simultaneously measuring the kinetic energy and number of electrons that escape from the top 0 to 10 nm of the material being analyzed. XPS requires high vacuum ( $P \sim 10^{-8}$  millibar) or ultra-high vacuum (UHV;  $P < 10^{-9}$  millibar) conditions, although a current area of development is ambient-pressure

XPS, in which samples are analyzed at pressures of a few tens of millibar. A typical XPS spectrum is a plot of the number of electrons detected (sometimes per unit time) (Y-axis, ordinate) versus the binding energy of the electrons detected (X-axis, abscissa). Each element produces a characteristic set of XPS peaks at characteristic binding energy values that directly identify each element that exists in or on the surface of the material being analyzed. These characteristic spectral peaks correspond to the electron configuration of the electrons within the atoms, e.g., 1s, 2s, 2p, 3s, etc. The number of detected electrons in each of the characteristic peaks is directly related to the amount of element within the XPS sampling volume. To generate atomic percentage values, each raw XPS signal must be corrected by dividing its signal intensity (number of electrons detected) by a "relative sensitivity factor" (RSF), and normalized over all of the elements detected. In this thesis, XPS was performed using a VG Escalab 220i-XL equipped with a hemispherical analyzer for a Twin Anode X-ray Source. The C 1s peak (BE = 284.6 eV) was used as the reference line to accurately determine the positions of other spectral lines. The fine structure of the photoelectron lines was treated using Casa XPS software (2.3.15 Version). XPS was used to measure the elements composition, the oxidation state and configuration of the elements.



**Figure 2.3** The XPS equipment at INRS-EMT.

### 2.3.5 X-Ray Absorption Spectroscopy (XAS)

X-ray absorption spectroscopy (XAS) is very powerful as a structural probe, since each element has a unique X-ray absorption spectrum, which enables information to be obtained about the local atomic environment and geometry, electron density, oxidation state, electronic configuration, site symmetry, coordination number and interatomic distances. The X-ray absorption near edge structure (XANES) measurements were performed on three beamlines at the Canadian Light Source (CLS) (Saskatoon, Canada).

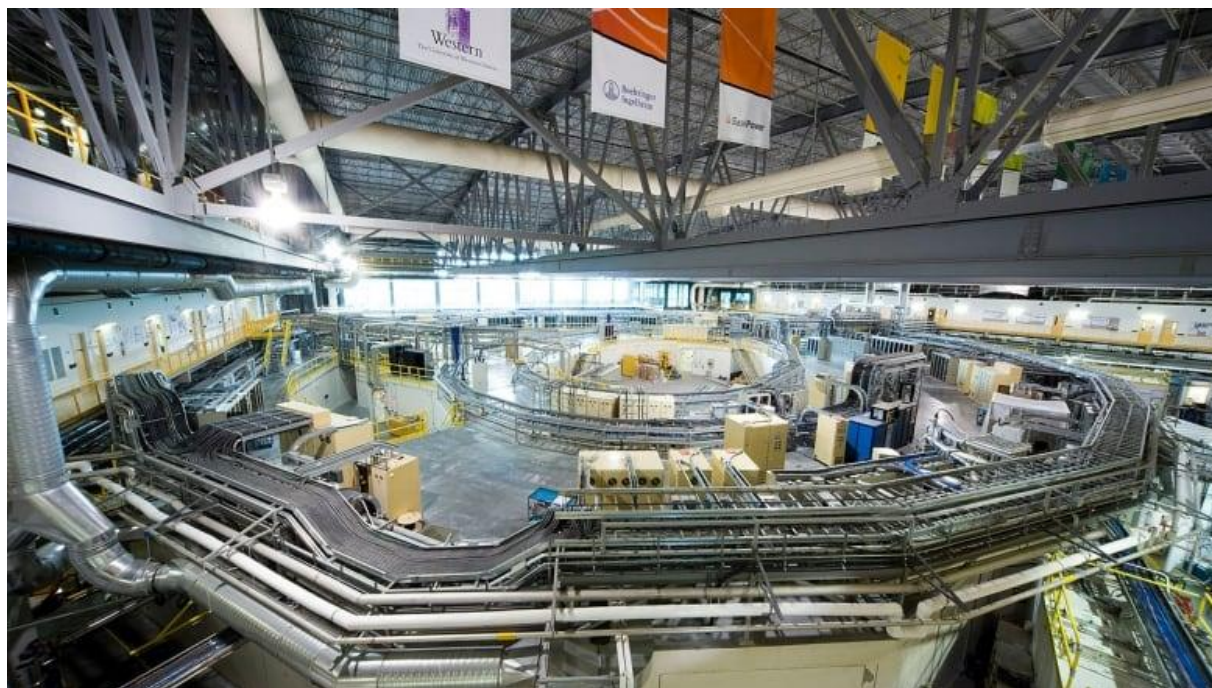


**Figure 2.4** The beamlines at Canadian Light Source.

(1) Variable Line Spacing Plane Grating Monochromator (VLS-PGM) beamline. All the powder samples were smeared on carbon tape as a thin layer and placed in the vacuum chamber of the beamline for the measurement. The XANES spectra were collected in both total electron yield (TEY) and fluorescent yield (FLY) mode with a chamber pressure better than  $1 \times 10^{-7}$  torr at room temperature. The beamline slits sizes were  $50 \mu\text{m} \times 50 \mu\text{m}$  with an instrumental resolution  $E/\Delta E > 10,000$ . The data are normalized by the  $I_0$  current, which is measured by a Nickel mesh placed in front of the sample.

(2) The Si K-edge XANES were obtained at the soft X-ray micro characterization beamline (SXRMB). It can provide  $10^{11}$  photons/s at 100 mA with a resolution higher than 10000 ( $E/\Delta E$ ). The spectra were normalized with respect to the edge height after subtracting the pre-edge and post-edge backgrounds, and then convert the data from energy space to  $k$  space using Athena software.

(3) The Fe K-edge XANES and Extended X-ray Absorption Fine Structure (EXAFS) data were collected on the 06ID-1 Hard X-ray MicroAnalysis (HXMA) beamline at the Canadian Light Source. During data collection, the CLS storage ring (2.9 GeV) was operated under 250 mA mode and the HXMA superconducting wiggler was run at 1.9 T. Measurements were made at room temperature in fluorescence mode using a 32-element Ge detector. Data collection configuration was using metal Fe foil as energy calibration by in step calibration for every data sets. To prepare the electrode for the XANES measurement, powder Fe/N/C catalysts were mixed with Nafion solution (5 wt%) and isopropanol to form homogeneous ink followed by dropping onto a gas diffusion layer (GDL). The spectra were normalized with respect to the edge height after subtracting the pre-edge and post-edge backgrounds, and then convert the data from energy space to  $k$  space using Athena software.

### **2.3.6 N<sub>2</sub> Adsorption and Desorption**

The specific surface area of a powder is determined by physical adsorption of a gas on the surface of the solid and by calculating the amount of adsorbate gas corresponding to a monomolecular layer on the surface. Physical adsorption results from relatively weak forces (van der Waals forces) between the adsorbate gas molecules and the adsorbent surface area of the test powder. The determination is usually carried out at the temperature of liquid nitrogen. The amount of gas adsorbed can be measured by a volumetric or continuous flow procedure. The surface areas were estimated from the Brunauer–Emmett–Teller (BET) equation and from the fitting of the N<sub>2</sub>-adsorption isotherms based on a slit-pore model, with the Quenched solid density functional theory (QSDFT) available in the AS1WIN software. QSDFT is an advanced DFT method for the pore size analysis of geometrically and chemically disordered micromesoporous carbons, which allows the calculation of pore size distributions from ca. 0.5 nm up to ca. 40 nm. It allows for a major improvement of the accuracy of DFT pore size distribution analyses of disordered carbon materials from low-temperature N<sub>2</sub> adsorption

isotherms because it takes into account the effects of surface roughness and heterogeneity explicitly.

### **2.3.7 Raman Spectroscopy**

The Raman effect was first experimentally discovered and described by the physicist Chandrasekhara Venkata Raman in 1928. The Raman effect is based on inelastic light scattering at the chemical bonds of a sample. Due to vibrations in the chemical bonds this interaction causes a specific energy shift in parts of the back scattered light which results in a unique Raman spectrum. Raman scattering can be further differentiated as Stokes and Anti-Stokes scattering. Both contain information about the material and its molecular composition. For Stokes scattering, the emitted photon has a lower energy than the absorbed photon; for Anti-Stokes scattering the emitted photon has a higher energy than the absorbed photon. In addition to inelastic scattering, elastic scattering can also appear. Elastic scattering at the same energy as the incident radiation is called Rayleigh scattering. It does not contain any information about the molecules and cannot be used for chemical sample analysis in a confocal Raman microscope.

A Raman spectrum is the unique fingerprint of a material. It can provide qualitative and quantitative information. The bands shifted to higher wavenumbers (blue shifted) are called anti-Stokes Raman bands and those shifted to lower wavenumbers (red shifted) are called Stokes Raman bands. Usually, the intensities of the Stokes-shifted Raman bands are more intense and therefore used for qualitative and quantitative analysis. In addition to the chemical compound distribution, there are further properties that can be derived from the Raman spectrum: (i) the peak intensity gives information about the quantity of a specific compound; (ii) a peak shift can identify stress and strain states; (iii) the peak width reveals the degree of crystallinity; (iv) the polarization state provides information regarding crystal symmetry and orientation.

### **2.3.8 Neutron Activation Analysis (NAA)**

Neutron activation analysis (NAA) is a physical technique that is based on nuclear reactions whereby the elemental content is determined by irradiating the subject sample with neutrons, creating radioactive forms of the desired element in the sample. As the sample becomes radioactive from the interaction of the neutron particle source and the nuclei of the element's atoms, radioisotopes are formed that subsequently decay, emitting gamma rays unique in half-

life and energy. These distinct energy signatures provide positive identification of the targeted element(s) present in the sample, while quantification is achieved by measuring the intensity of the emitted gamma rays that are directly proportionate to the concentration of the respective element(s) in the sample. It allows the precise identification and quantification of the elements, above all of the trace elements in the sample. When neutrons activate the nucleus of the atom, it allows the total elemental content to be observed regardless of the oxidation state, physical location, or chemical form of the desired element. Since neutrons possess the ability to pass through most materials with little difficulty, this allows the center of the sample to become as radioactive as the surface, thereby reducing or even eliminating the potential for matrix effects. Because neutron activation can be applied to any element with an appropriate isotope, nearly 70% of elements in the Periodic Table can be analyzed by NAA. Since the metal content in Me/N/C catalysts are very low, NAA is a useful technique to analyze the metal content.

## **2.4 Electrochemical Characterizations**

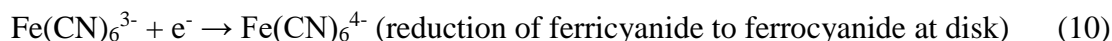
### **2.4.1 Rotating Ring-Disk Electrode (RRDE)**

In 1958, Russian electrochemist Alexander Frumkin suggested the idea of placing a concentric ring electrode around the rotating disk electrode [148]. His colleague, Lev Nekrasov, supervised construction of the world's first rotating ring-disk electrode (RRDE) apparatus [149, 150]. At the same time, Benjamin Levich and Yuri Ivanov began working on a theoretical description of solution flow at the RRDE. The four Russian researchers published their initial findings in 1959, and their work caught the attention of both Stanley Bruckenstein at the University of Minnesota and John Albery at Oxford University. Bruckenstein travelled to Moscow to learn more about the RRDE, and after he returned home in 1965, Albery joined Bruckenstein's research group (along with Dennis Johnson and Duane Napp). The experimental and mathematical work performed by these four researchers at Minnesota generated a significant series of papers about the RRDE [151-156] and placed the new technique on a firm theoretical foundation. Albery returned to Oxford and (working with his student Michael Hitchman) drew these theoretical papers together in a seminal volume titled Ring-Disk Electrodes [151].

The overall flow pattern at the RRDE initially brings molecules and ions to the disk electrode. After encountering the disk electrode, the subsequent outward radial flow carries a fraction of

these molecules or ions past the surface of the ring electrode. This flow pattern allows products generated (upstream) by the half reaction at the disk electrode to be detected as they are swept (downstream) past the ring electrode.

Two of the key parameters which characterize a given ring-disk geometry are the collection efficiency and the transit time. The collection efficiency is the fraction of the material from the disk which subsequently flows past the ring electrode. It can be expressed as a fraction between 0.0 and 1.0 or as a percentage. Typical ring-disk geometries have collection efficiencies between 20% and 30%. It is common practice to empirically measure the collection efficiency using a well-behaved redox system. The ferrocyanide/ferricyanide half reaction is a simple, single-electron, reversible half reaction that is often used as the basis for measuring collection efficiency [157]. The RRDE is placed in a solution containing a small concentration (10 mM) of potassium ferricyanide,  $\text{K}_3\text{Fe}(\text{CN})_6$ , in a suitable aqueous electrolyte solution (such as 1.0 M potassium nitrate,  $\text{KNO}_3$ ) and is operated at rotation rates between 500 and 2000 RPM. Initially, both the ring and the disk electrodes are held at a sufficiently positive potential that no reaction occurs. Then, the potential of the disk electrode is slowly swept towards more negative potentials, and a cathodic current is observed which corresponds to the reduction of ferricyanide to ferrocyanide at the disk.



As ferricyanide is reduced at the disk electrode, the ferrocyanide generated by this process is swept outward (radially) away from the disk electrode and toward the ring electrode. The ring electrode is held constant at a positive (oxidizing) potential throughout the experiment. Some (but not all) of the ferrocyanide generated at the disk travels close enough to the ring electrode that it is oxidized back to ferricyanide. Thus, an anodic current is observed at the ring electrode due to the oxidation of ferrocyanide to ferricyanide at the ring.



The measured ratio of the ring (anodic) limiting current to the disk (cathodic) limiting current is the empirical collection efficiency. As the rotation rate increases, both the disk and the ring currents increase (see Figure 2.5). Because both the anodic and cathodic limiting currents are

proportional to the square root of the rotation rate, the empirical collection efficiency is expected to be independent of the rotation rate.

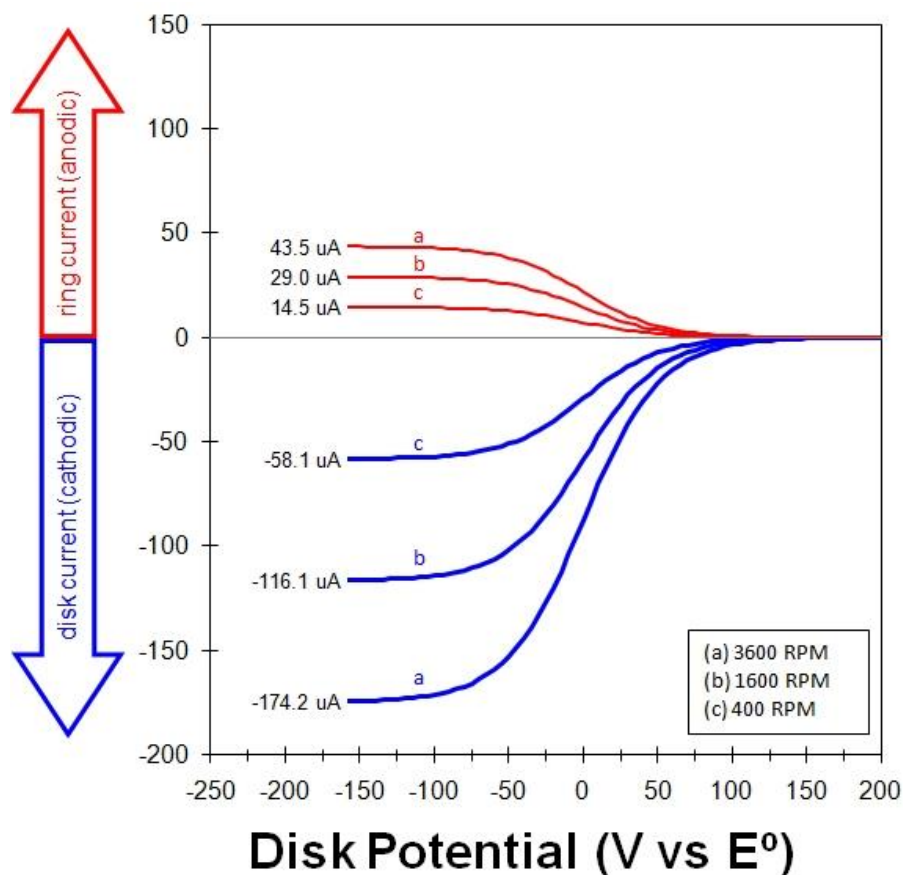


**Figure 2.5** Rotating ring-disk voltammograms at various rotation rates [158].

Once the collection efficiency value has been established empirically for a particular RRDE, it can be treated as a property of that particular RRDE, even if the RRDE is used to study a different half reaction in a different solution on a different day. Although the empirically measured collection efficiency ( $N_{\text{empirical}}$ ) is a ratio of two currents with opposite mathematical signs (anodic and cathodic), the collection efficiency is always expressed as a positive number.

$$N_{\text{empirical}} = -\dot{i}_{\text{Limiting, ring}} / \dot{i}_{\text{Limiting, disk}} \quad (12)$$

The ORR electrochemical measurements were carried out in a three-electrode cell using a RRDE (PINE Research Instrumentation) with a bipotentiostat (Pine, Model PGSTAT-72637) workstation at room temperature. A Pt wire and a saturated calomel electrode (SCE) were used

as the counter and reference electrodes, respectively. All potentials in this study refer to RHE. The RRDE with a Pt ring and a GC disk (5.61 mm diameter) were used as the substrate for the working electrodes. Before use, the GC electrodes in RRDE are polished using aqueous alumina suspension on felt polishing pads.

The catalyst suspension in this work was prepared as the following: 10 mg of catalyst was mixed in a glass vial with 95  $\mu\text{L}$  of 5 wt% Nafion solution and 350  $\mu\text{L}$  of ethanol, followed by sonication and agitation in a vortex mixer, alternatively, for a total of 1 h. Then 9  $\mu\text{L}$  of the catalyst suspension was dropped onto the GC electrode surface ( $\sim 0.8 \text{ mg cm}^{-2}$ ). For comparison, the 20 wt% Pt/C catalyst (E-TEK) was prepared through the same procedure with a loading amount of  $100 \mu\text{g cm}^{-2}$  (i.e.,  $20 \mu\text{g}_{\text{Pt}} \text{ cm}^{-2}$ ). Although the NPMC loading is much greater than that for Pt/C, the limiting factor for the Pt loading is the high-cost and limited-reserve, unlike the low-cost and high-abundant NPMCs. Before testing,  $\text{N}_2$  (or  $\text{O}_2$ ) was bubbled through the electrolyte for 30 min and the  $\text{N}_2$ - (or  $\text{O}_2$ ) was kept bubbling during the measurements, in order to keep the  $\text{N}_2$ - or  $\text{O}_2$ -saturated solution. In 0.1 M KOH (or 0.1 M  $\text{HClO}_4$ ), the cyclic voltammetry (CV) profiles were recorded at  $50 \text{ mV s}^{-1}$  and the linear sweep voltammograms (LSV) were recorded at  $10 \text{ mV s}^{-1}$ , between 0-1.2 V (vs. RHE). ORR activities were extracted from the negative-going scan for both NPMCs and Pt/C. All of the LSV curves were recorded after subtraction of the background current recorded in  $\text{N}_2$ -saturated solution. The current density was normalized based on the geometry area of the glassy carbon area ( $0.2475 \text{ cm}^2$ ). For detecting peroxide formed at the disc electrode, the potential for the Pt ring electrode was set at 1.3 V (vs. RHE) and the voltammograms were recorded at 1600 rpm. The collection efficiency of the RRDE was  $N = 0.37$ . The peroxide yield ( $\text{H}_2\text{O}_2\%$ ) and the electron transfer number ( $n$ ) were calculated as follows:

$$\text{H}_2\text{O}_2\% = 200 \times (\text{I}_r/\text{N})/(\text{I}_d + \text{I}_r/\text{N}) \quad (13)$$

$$n = 4 \times \text{I}_d / (\text{I}_d + \text{I}_r/\text{N}) \quad (14)$$

Where  $\text{I}_d$  is the disk current and  $\text{I}_r$  is the ring current.

To compare the electrocatalytic activity and to elucidate the reaction mechanism of electrocatalysts, a Tafel analysis is utilized. In this method, the sensitivity of the electric current response to the applied potential (Tafel slope) is analyzed, which provides information

associated with the rate determining steps. The Tafel slope tells how much it has to increase the overpotential to increase the reaction rate by a factor ten. This will be determined by the magnitude of the change in the activation energy for a given increase in overpotential.

#### **2.4.2 Single Cell MEA Tests in PEM Fuel Cells**

The ink formula for cathode is (i) 10 mg catalyst; (ii) 147  $\mu\text{L}$  of deionized (DI) water (Millipore Milli-Q, 18.2  $\text{M}\Omega\cdot\text{cm}$ ); (iii) 272  $\mu\text{L}$  of 5 wt% nafion solution; (iv) 206  $\mu\text{L}$  of ethanol. The ink was first sonicated for 15 minutes and then agitated on a vortex mixer for another 15 minutes; the sonication and agitation steps were then repeated. The homogeneous mixed catalyst inks were deposited using a micropipette onto carbon paper as gas diffusion layers (GDL, SGL Sigracet 25BC) by 284  $\mu\text{L}$  ink. The GDL which consists of teflonated carbon fiber paper is covered with a microporous layer made of carbon black and Teflon. The round GDL have an area of 1.14  $\text{cm}^2$ . The GDL with catalyst layer were named as gas diffusion electrodes (GDEs). The target catalyst loading of one GDE was 4  $\text{mg}/\text{cm}^2$ . The preparation of anode GDEs were similar to the cathode, but with 0.5  $\text{mg}_{\text{Pt}}/\text{cm}^2$  of a commercial Pt-based catalyst (Tanaka Kikinzo, 45.4 wt% Pt/C). The membrane electrode assembly (MEA) was prepared by hot pressing the anode, a Nafion<sup>®</sup> 211 membrane, and the cathode together at 130 °C for 2 min with a load of about 500 pounds.

Single cell MEA tests were carried out using a homemade fuel cell station and a BioLogic SP-150 Potentiostat with a VMP3B-20 Booster driven by EC-Lab V9.98 software. All of the operating parameters, such as hydrogen/oxygen stoichiometry, temperature and related humidity as well as backpressure are controlled automatically. The humidifier was automatically filled by the external DI water supply also. At the same time, information was gathered from thermal couples and gases' mass flow meters, etc. as feedback. The flow rates of H<sub>2</sub> and O<sub>2</sub> were both kept at 0.3 standard liter per minute (SLPM). The back pressures were set to 1.0 bar gauge for both anode and cathode sides, the cell temperature were set at 80 °C. After all fuel cell parameters were stabilized, electrochemical impedance spectra (EIS) were obtained at open circuit voltage (OCV) with frequencies ranging from 100 kHz to 10 Hz, to obtain the fuel cell resistance. Then, a polarization curve was recorded by scanning the cell voltage from OCV to 0 V (vs. anode) with a scan rate of 0.5  $\text{mV s}^{-1}$ . After recording the first polarization curve, the cell

voltage was set at 0.6 V to record the current density delivered by the cell, this current density was used to evaluate the stability of the cathode catalyst.

### **2.4.3 Zn-Air Batteries**

The Zn-air batteries were tested in home-built electrochemical cells, the electrolyte used was 6 M KOH and 0.2 M Zn(Ac)<sub>2</sub> solution. To prepare the air electrode, homogeneous catalyst ink consisting of catalysts, Nafion solution (5 wt%) and isopropanol was dropped onto a gas diffusion layer (GDL) with a catalyst loading of ~1.0 mg cm<sup>-2</sup>, a polished zinc plate was used as the anode. For comparing, 20 wt% Pt/C catalysts were prepared as the same procedure to achieve the same loading. Polarization data was collected using galvanodynamic method at a scan rate of 1.0 mA s<sup>-1</sup> with cut-off voltage of 0.6 V for the discharge and 2.2 V for the charge. Galvanostatic discharge and charge cycling was conducted at different current densities from 5 mA cm<sup>-2</sup> to 20 mA cm<sup>-2</sup> under 20 min for each stage.

### **2.4.4 Na-Ion Batteries**

The button-type cells were assembled in an argon-filled glove box, where water and oxygen concentration were kept less than 5 ppm. The working electrodes were fabricated by mixing 70 wt% of active materials, 20 wt% of acetylene black and 10 wt% of polymer binder (polyvinylidene fluoride, PVDF), which were then pasted on copper foil followed by drying under vacuum at 110 °C for 10 h. The mass loading of active material on each disk is about 1.3 mg cm<sup>-2</sup>. Metal sodium was used as negative electrode; the electrolyte was 1 M NaClO<sub>4</sub> in propylene carbonate (PC) solution; the separator was glass microfiber filters (Whatman, GF/D). The galvanostatic charge-discharge measurements were performed using a Battery Testing System (Neware BTS-4008) at different current densities with a cut-off voltage window of 0-3.0 V. Cyclic Voltammetry (CV) tests were carried out on Autolab electrochemical workstation at a scan rate of 0.1 mV s<sup>-1</sup> with the potential interval 0-3.0 V. Electrochemical impedance spectroscopy (EIS) was employed to measure the assembled coin cell on Autolab electrochemical workstation by applying an AC amplitude of 5 mV over the frequency range from 10<sup>5</sup> to 0.01 Hz at an open circuit voltage (OCV: about 2.0 V vs. Na<sup>+</sup>/Na). All the electrochemical measurements were performed at room temperature.

## CHAPTER 3 RESULTS

This chapter is divided into six parts, and each part corresponds to one article. All of the results are about the development of carbon-based materials (including Me-N-C and metal-free catalyst) in the applications of ORR, PEM fuel cells, ZABs and SIBs.

### 3.1 3D porous Fe/N/C spherical nanostructures as high-performance electrocatalysts for oxygen reduction in both alkaline and acidic media

Qiliang Wei, Gaixia Zhang, Xiaohua Yang, Régis Chenitz, Dustin Banham, Lijun Yang, Siyu Ye, Shanna Knight, Shuhui Sun

*ACS Appl. Mater. Interfaces*, 2017, **9**, 36944-36954.

Currently, the development of low-cost and high-performance non-precious metal catalysts (NPMCs) for ORR is critical for the wide-spread commercialization of low temperature fuel cells. Therefore, the design of highly efficient NPMCs, to replace Pt, is greatly desirable, while, very challenging. Among various NPMCs, Fe/N/C catalysts are the most promising ones. However, it is still very challenging to develop NPMC that is highly efficient and stable in both alkaline and acidic media. In this section, we adopted a spherical phenolic resol-F127 monomicelles (SPRMs) as the host for impregnating iron (II) acetate (FeAc) and 1,10-phenanthroline (1,10-Phen) to form a catalyst precursor that is subsequently annealed under Ar and then under NH<sub>3</sub>. By systematically investigating the relationships between the ORR performance and the nature of the catalysts (e.g., Fe content and porosity), we found that the micro-structure and the content of Fe of the catalysts largely affect the ORR performance. The optimized electrocatalyst shows very good ORR activity and stability in both alkaline and acidic conditions.

*Contributions:* I performed all the experimental synthesis, the electro-chemical measurements, and all characterizations except the TEM measurements that have been done by technicians. I conducted the data analysis and the interpretation of results, as well as the manuscript writing, with the help of co-authors.

# 3D porous Fe/N/C spherical nanostructures as high-performance electrocatalysts for oxygen reduction in both alkaline and acidic media

*Qiliang Wei<sup>1</sup>, Gaixia Zhang<sup>1,\*</sup>, Xiaohua Yang<sup>1</sup>, Régis Chenitz<sup>1</sup>, Dustin Banham<sup>2</sup>, Lijun Yang<sup>2</sup>, Siyu Ye<sup>2</sup>, Shanna Knights<sup>2</sup>, Shuhui Sun<sup>1,\*</sup>*

<sup>1</sup>Institut National de la Recherche Scientifique-Énergie Matériaux et Télécommunications, Varennes, QC J3X 1S2, Canada. E-mail: gaixia.zhang@emt.inrs.ca (G. Zhang); shuhui@emt.inrs.ca (S. Sun)

<sup>2</sup>Ballard Power Systems Inc., Burnaby, V5J 5J8, Canada

**Keywords:** Non-precious metal catalyst, 3D, Porous, Fe/N/C, Oxygen reduction reaction

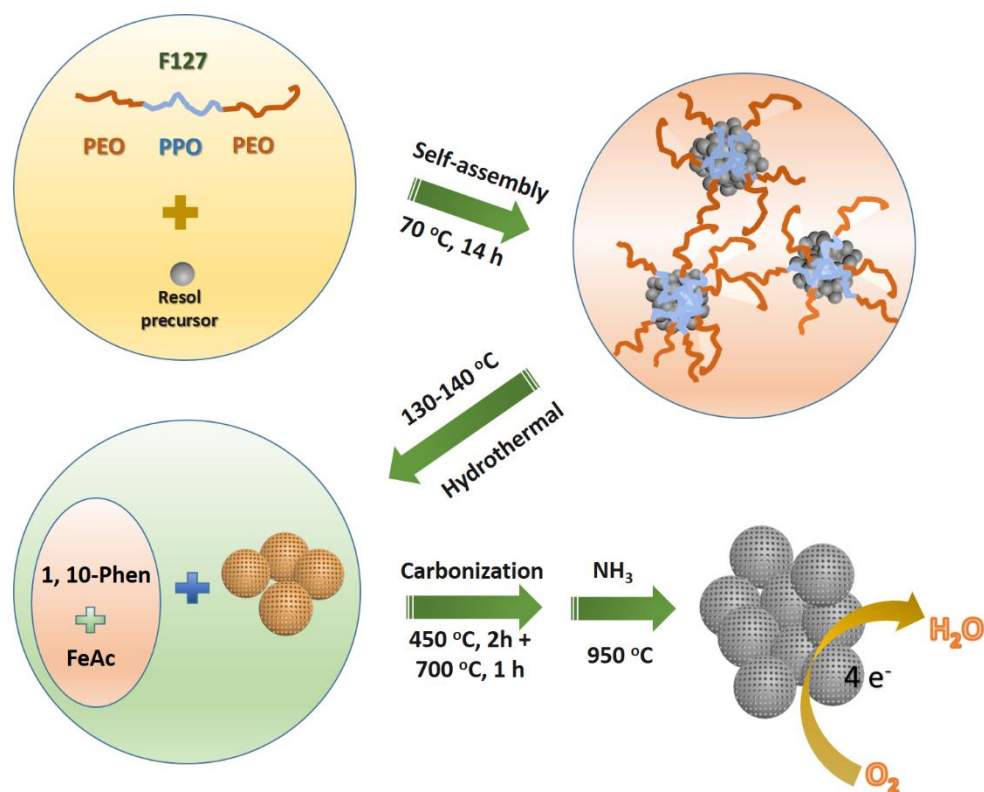
**Abstract:** Exploring inexpensive and high performance non-precious metal catalysts (NPMCs), to replace the rare and expensive Pt-based catalyst, for oxygen reduction reaction (ORR) is crucial for future low temperature fuel cell devices. Herein, we developed a new type of highly efficient 3D porous Fe/N/C electrocatalyst through a simple pyrolysis approach. Our systematic study revealed that the pyrolysis temperature, the surface area, and the Fe content in the catalysts largely affect the ORR performance of the Fe/N/C catalysts, and the optimized parameters have been identified. The optimized Fe/N/C catalyst, with an interconnected hollow and open structure, exhibits one of the highest ORR activity, stability and selectivity in both alkaline and acidic conditions. In 0.1 M KOH, compared to the commercial Pt/C catalyst, the 3D porous Fe/N/C catalyst exhibits ~6 times better activity (e.g., 1.91 mA cm<sup>-2</sup> for Fe/N/C vs. 0.32 mA cm<sup>-2</sup> for Pt/C, at 0.9 V) and excellent stability (e.g., no any decay for Fe/N/C vs. 35 mV negative half-wave potential shift for Pt/C, after 10000 cycles test). In 0.5 M H<sub>2</sub>SO<sub>4</sub>, this catalyst also exhibits comparable activity and better stability comparing to Pt/C catalyst. More importantly, in both alkaline and acidic media (RRDE environment), the as-synthesized Fe/N/C catalyst shows much better stability and methanol tolerance than those of the state-of-the-art commercial Pt/C catalyst. All these make the 3D porous Fe/N/C nanostructure an excellent candidate for non-precious-metal ORR catalyst in metal–air batteries and fuel cells.

## Introduction

Today, the design of inexpensive and highly efficient electrocatalysts for oxygen reduction reaction (ORR) is regarded as a key element for the large-scale application of polymer membrane fuel cells.<sup>1-4</sup> Platinum (Pt) and Pt-based materials are the most effective electrocatalysts for the ORR,<sup>5-7</sup> however, the limited natural reserves and the highly disproportionate geographical distribution of Pt hinder the fuel cell's wide commercialization in the future. Therefore, a wide range of non-Pt based materials have been actively explored, such as metal-free carbon materials doped with heteroatoms (N, S, B, P),<sup>8-13</sup> metal oxides (Co<sub>3</sub>O<sub>4</sub>,<sup>14</sup> Fe<sub>3</sub>O<sub>4</sub>,<sup>15</sup> MnO<sub>2</sub>,<sup>16</sup> etc.) and chalcogenides (Co<sub>3</sub>S<sub>4</sub>,<sup>17</sup> FeS<sub>2</sub>,<sup>18</sup> MnS,<sup>19</sup> etc.) supported on carbon, transition-metal-coordinating macrocyclic compounds,<sup>20-21</sup> and pyrolyzed metal/nitrogen/carbon (M/N/C, M = Fe, Co, Ni) compounds.<sup>22-26</sup> Among them, catalysts based on Fe/N/C are particularly promising, though the exact nature of the active sites (whether the transition metal acts as the activity center or just facilitates the formation of active N-C functional sites)<sup>23, 27-31</sup> is still under debate. Nevertheless, it is generally recognized that there are some key factors governing the ORR activity in the Fe/N/C catalysts: (i) the iron content, (ii) the nitrogen functionalities on the surface, and (iii) the microporous structure.<sup>32-33</sup> Therefore, the careful choice of N and Fe precursors, the carbon support or host for the catalytic sites, as well as the heat-treatment conditions, plays the crucial role in fabricating highly efficient Fe/N/C ORR catalysts. Since their emergence, various Fe and N precursors,<sup>26-27,34-37</sup> and different nanostructures (such as tubes,<sup>22</sup> nanorods,<sup>38</sup> sheets,<sup>39</sup> tetrapods,<sup>40</sup> core-shell structures,<sup>41</sup> porous structure,<sup>37,41</sup> and their hybrids,<sup>3,42</sup>) have been designed and reported extensively. Though promising, most of these well-established catalysts still can hardly compete with the overall performance of Pt/C catalyst, in addition, little information is known about the optimal Fe content as well as the micro-structures in the Fe/N/C catalysts.

In this work, we explore the use of spherical phenolic resol-F127 monomicelles (SPRMs)<sup>43-44</sup> as the host for impregnating FeAc and 1,10-Phen to form a catalyst precursor that is subsequently heat treated in Ar and NH<sub>3</sub>, respectively (Scheme 1). By adjusting the content of FeAc, the pyrolysis temperature in Ar, and pyrolysis time in NH<sub>3</sub>, a series of Fe/N/C samples (specifically named as Fe<sub>x</sub>NC-Ar $T$ -NH<sub>3</sub>-y%, in which,  $x$  means the content of FeAc added in the experiment,  $T$  means the pyrolysis temperature in Ar,  $y$  means the weight remaining after the

$\text{NH}_3$  pyrolysis, detailed experimental parameters are included in Table S1, Supporting Information) were prepared. The content of Fe and surface area of the catalysts can be controllably adjusted by the quantity of FeAc and the pyrolysis time in  $\text{NH}_3$  atmosphere. Accordingly, the optimized catalyst is obtained showing outstanding ORR activity, stability and methanol crossover tolerance both in alkaline and acidic conditions.



**Scheme 1.** Illustration of the formation of the Fe<sub>x</sub>NC-Ar700-NH<sub>3</sub>-y% catalysts.

## Experimental Section

**Materials.** Phenol (99 %), formaldehyde solution (37 %), iron (II) acetate (95 %), 1,10 phenanthroline (99 %), sodium hydroxide (NaOH, 95.0 %), sulfuric acid (H<sub>2</sub>SO<sub>4</sub>, 95.0-98.0 %) and potassium hydroxide (KOH, 87.1 %), were bought from Fisher Scientific; Pluronic®F-127, Nafion solution (5 wt%) were purchased from Sigma-Aldrich. All chemicals were used as received and solutions were prepared using deionized water (Millipore Milli-Q, 18.2 MΩ cm).

**Preparation of spherical phenolic resol-F127 monomicelles.** Firstly, F127 (0.96 g) was dissolved in 15 mL DI water at room temperature with stirring for 30 min. Then phenol (0.6 g), formaldehyde solution (2.1 mL), and NaOH aqueous solution (0.1 M, 15 mL) were mixed and stirred at 70 °C for 30 min to obtain a low-molecular-weight phenolic resols. After that, the F127 solution was dropped into the phenolic resols slowly with stirring. 2 h later, 50 mL of water was added and further stirred at 70 °C for 12-14 h. Afterwards, 12 mL of the as-prepared monomicelle solution and 25 mL of H<sub>2</sub>O was transferred into an autoclave (50 mL volume) for hydrothermal treatment at 130 °C for 20 h. In the end, the SPRMs were collected by centrifugation and washed with distilled water for several times, followed by drying in an oven at 60 °C, and then served as the carbon host for loading Fe and N in the next step.

**Preparation of Fe/N/C catalysts.** In a typical synthesis of Fe/N/C catalyst, taking Fe<sub>30</sub>NC-Ar<sub>700</sub>-NH<sub>3</sub>-45% as an example, the precursors were prepared by first mixing 700 mg SPRMs, 136 mg 1,10-phenanthroline, 30 mg iron(II) acetate in a solution of ethanol and deionized water (ethanol : water = 1 : 2) under stirring at room temperature. Then the mixture was heated to 60–80 °C for 2–3 h until about 50 ml of a thick slurry was obtained. The slurry was placed overnight in a drying oven at 95 °C. Afterwards, the dry powder was ground sufficiently and placed in the quartz tube, followed by heating at 450 °C in Ar for 2 h, and then pyrolyzed in Ar at 700 °C for 1h, followed by another pyrolysis in ammonia at 950 °C with different pyrolysis time in order to obtain expected weight losses. To clarify, all the as-synthesized samples were labelled as Fe<sub>x</sub>NC-Ar<sub>T</sub>-NH<sub>3</sub>-y%, where *x* is the amount of used FeAc, *T* is the pyrolysis temperature in Ar (600, 700, and 800 °C), and *y* is the weight remaining after the NH<sub>3</sub> pyrolysis. All information about the amount of precursors, temperatures, pyrolysis durations and weight remaining of the catalysts after a first pyrolysis in Ar eventually followed by a second pyrolysis in NH<sub>3</sub> are summarized in Table S1 (Supporting Information).

**Physical Characterizations.** The morphological structures of the catalysts were investigated by transmission electron microscopy (TEM) and high-resolution TEM (HRTEM) (JEOL JEM-2100F, operated at 200 kV). The surface properties were analyzed by X-Ray photoelectron spectroscopy (XPS, VG ESCALAB 220i-XL) equipped with a hemispherical analyser for a Twin Anode X-Ray Source. The C 1s peak (BE = 284.6 eV) was used as the reference line to accurately determine the positions of other spectral lines. The fine structure of the photoelectron lines was treated using Casa XPS software (2.3.15 Version). The surface areas of the catalysts

were measured through N<sub>2</sub> sorption isotherms that were collected using Quantachrome Instruments Autosorb-1 at liquid nitrogen temperature. The surface areas were estimated from the Brunauer-Emmett-Teller (BET) equation and from the fitting of the N<sub>2</sub>-adsorption isotherms based on a slit-pore model, with the Quenched solid density functional theory (QSDFT) available in the AS1WIN software. The P/P<sub>0</sub> range is 0.05-0.35. QSDFT is an advanced DFT method for the pore size analysis of geometrically and chemically disordered micro-mesoporous carbons, which allows the calculation of pore size distributions from ca. 0.5 nm up to ca. 40 nm. It allows for a major improvement of the accuracy of DFT pore size distribution analyses of disordered carbon materials from low-temperature nitrogen adsorption isotherms because it takes into account the effects of surface roughness and heterogeneity explicitly.

**Electrochemical Measurements.** All electrochemical measurements were carried out in a three-electrode cell using a rotating disk electrode (RDE, PINE Research Instrumentation) with a bipotentiostat (Pine, Model PGSTAT-72637) workstation at room temperature. A Pt wire and a saturated calomel electrode (SCE) were used as the counter and reference electrodes, respectively. All potentials in this study refer to RHE. A RDE with glassy carbon (GC) disk electrode (5 mm in diameter) and a rotating ring-disk electrode (RRDE) with a Pt ring and a GC disk (5.5 mm diameter) were used as the substrate for the working electrodes. Before use, the GC electrodes in RDE/RRDE are polished using aqueous alumina suspension on felt polishing pads. The catalyst suspension in this work was prepared as the following: 10 mg of catalyst was mixed in a glass vial with 95  $\mu\text{L}$  of 5 wt% Nafion solution and 350  $\mu\text{L}$  of ethanol, followed by sonication and agitation in a vortex mixer, alternatively, for a total of 1 h. Then 9  $\mu\text{L}$  of the catalyst suspension was dropped onto the GC electrode surface ( $\sim 0.8 \text{ mg cm}^{-2}$ ). For comparison, the 20 wt% Pt/C catalyst (ElectroChem, Inc) was prepared through the same procedure with a loading amount of 100  $\mu\text{g cm}^{-2}$  (i.e., 20  $\mu\text{g}_{\text{Pt}} \text{ cm}^{-2}$ ). Before testing, N<sub>2</sub> (or O<sub>2</sub>) was bubbled through the electrolyte for 30 min and the N<sub>2</sub>- (or O<sub>2</sub>) was kept bubbling during the measurements, in order to keep the N<sub>2</sub>- or O<sub>2</sub>-saturated solution. In 0.1 M KOH (or 0.5 M H<sub>2</sub>SO<sub>4</sub>), the cyclic voltammetry (CV) profiles were recorded at 50 mV s<sup>-1</sup> and the linear sweep voltammograms (LSV) were recorded at 10 mV s<sup>-1</sup>, between 0-1.2 V (vs. RHE). ORR activities were extracted from the negative-going scan for both NPMCs and Pt/C. All of the LSV curves were recorded after subtraction of the background current recorded in N<sub>2</sub>-saturated solution. For detecting peroxide formed at the disc electrode, the potential for the Pt ring electrode was set at

1.3 V (vs. RHE) and the voltammograms were recorded at 1600 rpm. The collection efficiency of the ring-disk electrode was  $N = 0.37$ . The peroxide yield ( $\text{H}_2\text{O}_2\%$ ) and the electron transfer number ( $n$ ) were calculated as follows:

$$\text{H}_2\text{O}_2\% = 200 \times (\text{I}_r/\text{N})/(\text{I}_d + \text{I}_r/\text{N})$$

$$n = 4 \times \text{I}_d / (\text{I}_d + \text{I}_r/\text{N})$$

Where  $\text{I}_d$  is the disk current and  $\text{I}_r$  is the ring current.

The catalyst tolerance to methanol crossover and the stability were tested in both  $\text{O}_2$  saturated 0.1 M KOH (or 0.5 M  $\text{H}_2\text{SO}_4$ ) aqueous electrolytes. The methanol crossover effects in CVs were recorded by adding 1.0 M methanol into the electrolytes. The stability test was performed by comparing the LSV curves in  $\text{O}_2$  saturated electrolytes before and after 2000 cycles with a rotation speed of 1600 rpm. During the cycling test,  $\text{O}_2$  flow was kept going through the electrolyte to keep the  $\text{O}_2$ -saturated solution.

## Results and Discussion

Previous studies showed that the heat-treatment temperature played a crucial role in the performance of pyrolyzed Fe/N/C catalysts.<sup>26</sup> To investigate the impact of pyrolysis temperature on our catalysts, we first examined the ORR activity of the Fe20NC-Ar*T*-NH<sub>3</sub>-30% catalysts, as a function of pyrolysis temperature ( $T$ ) (in the range of 600–800 °C) under Ar, with RRDE measurements performed in 0.1 M KOH electrolyte. As shown in Figure 1a, among these three catalysts, the sample annealed at 700 °C (Fe20NC-Ar700-NH<sub>3</sub>-30%) displays the highest ORR activity with more positive onset and half-wave potential. This is probably because an optimal balance of electrical conductivity, porosity, and density of active site was achieved at 700 °C.<sup>29,35,45</sup> Accordingly, a series of catalysts (FexNC-Ar700-NH<sub>3</sub>-y%) discussed below were prepared at 700 °C in the pyrolysis stage of Ar. Then, the content of FeAc ( $x$ ) and the pyrolysis time in NH<sub>3</sub> ( $y$ ) were adjusted and the ORR activities of the as-synthesized catalysts (FexNC-Ar700-NH<sub>3</sub>-y%) were investigated systematically by the RRDE measurement in 0.1 M KOH, in order to obtain the optimized  $x$  and  $y$  for the FexNC-Ar700-NH<sub>3</sub>-y% samples (Table S1, Supporting Information). Specifically, 20 mg, 30 mg and 50 mg FeAc were mixed with the same amount of 1,10-Phen and SPRMs, respectively, followed by the same pyrolysis parameter in Ar; then the samples with different quantities ( $x$ ) of FeAc (Fe20NC-Ar700, Fe30NC-Ar700, and

Fe50NC-Ar700) were further annealed under  $\text{NH}_3$  at 950 °C. For each Fe content group, three different lengths of pyrolysis time under  $\text{NH}_3$  were preformed, in order to obtain three representative samples with different values of weight remaining ( $y$ ). In the end, three groups of Fe/N/C samples, named as Fe20NC-Ar700- $\text{NH}_3$ - $y$ %, Fe30NC-Ar700- $\text{NH}_3$ - $y$ %, and Fe50NC-Ar700- $\text{NH}_3$ - $y$ %, were obtained. From the LSV curves for ORR in 0.1 M KOH (Figure 1b-d), samples Fe20NC-Ar700- $\text{NH}_3$ -30%, Fe30NC-Ar700- $\text{NH}_3$ -45%, and Fe50NC-Ar700- $\text{NH}_3$ -80% are proved to be the optimized ones among their corresponding  $\text{Fe}_x\text{NC-Ar700-NH}_3$ - $y$ % group samples. Impressively, in 0.1 M KOH, the half-wave potential of ORR on Fe30NC-Ar700- $\text{NH}_3$ -45% sample reaches 0.87 V (vs. RHE). In addition, the Tafel analysis was calculated to further evaluate the ORR kinetic characters of these catalysts. From Figure S1 (Supporting Information), we can see that the sample Fe30NC-Ar700- $\text{NH}_3$ -45% has higher current density (1.91  $\text{mA cm}^{-2}$ ) at 0.9 V with the same catalyst loading on the electrode, comparing to the other samples, which indicates its superior ORR activity. Based on these results, the representative samples, with a focus on the best sample Fe30NC-Ar700- $\text{NH}_3$ -45%, were selected for the physical characterizations.

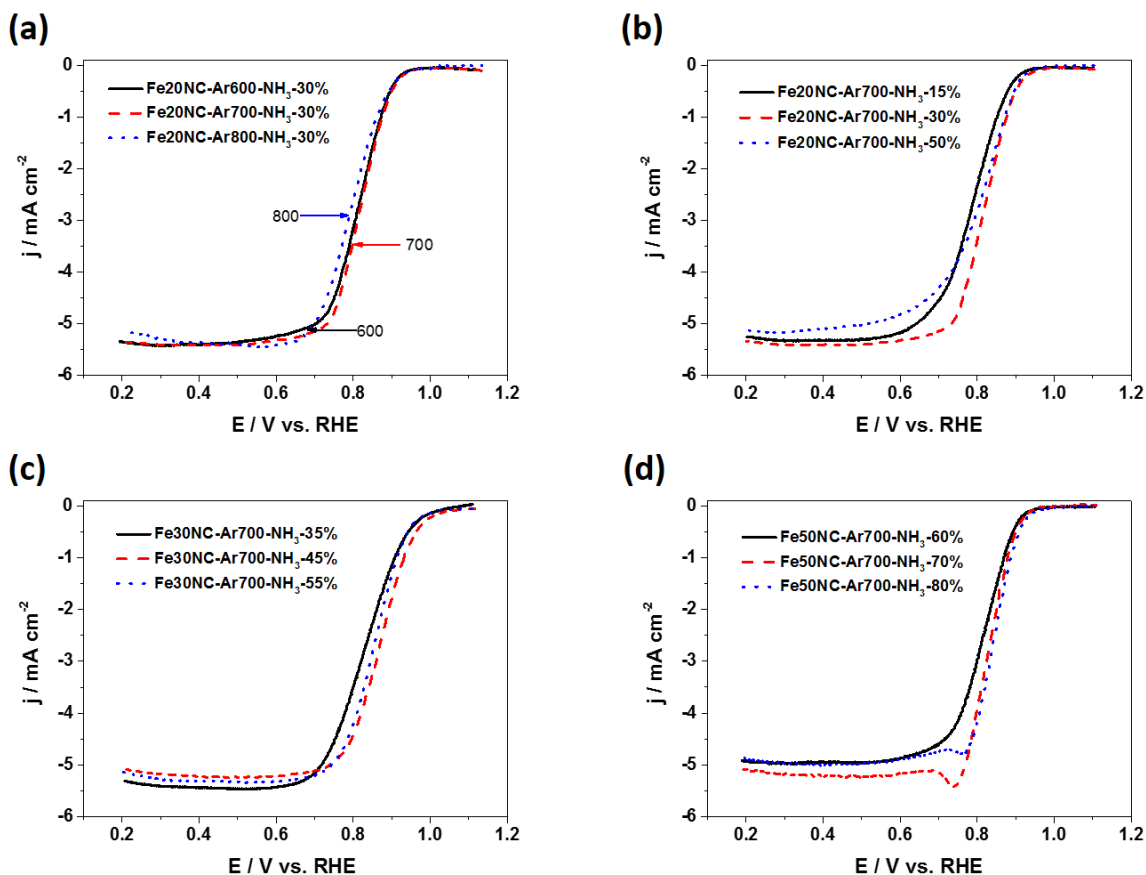


**Figure 1.** LSV curves of (a) Fe<sub>20</sub>NC-Ar<sub>T</sub>-NH<sub>3</sub>-30%, (b) Fe<sub>20</sub>NC-Ar<sub>700</sub>-NH<sub>3</sub>-y%, (c) Fe<sub>30</sub>NC-Ar<sub>700</sub>-NH<sub>3</sub>-y%, (d) Fe<sub>50</sub>NC-Ar<sub>700</sub>-NH<sub>3</sub>-y% in O<sub>2</sub>-saturated 0.1 M KOH at a scan rate of 10 mV s<sup>-1</sup>, rotation rate = 1600 rpm.

The chemical composition of the catalysts was analyzed by XPS. The typical XPS survey spectrum (Figure S2, Supporting Information) indicates the existence of Fe, N and C in all Fe<sub>x</sub>NC-Ar<sub>700</sub>-NH<sub>3</sub>-y% samples. In terms of the presence of oxygen, it probably originates from the SPRM precursors. The C 1s core level XPS spectrum (Figure 2a) of the Fe<sub>30</sub>NC-Ar<sub>700</sub>-NH<sub>3</sub>-45% could be fitted to several different types of C functionalities that correspond to Fe<sub>3</sub>C, C=C, C-O, C=O, C-N, and O-C=O, respectively, among of which, Fe<sub>3</sub>C has been demonstrated to have positive effects for ORR.<sup>46</sup> The high-resolution N 1s XPS spectrum (Figure 2b) of Fe<sub>30</sub>NC-Ar<sub>700</sub>-NH<sub>3</sub>-45% shows that the existence of pyridinic, pyrrolic, graphitic N and N-O species. It has been demonstrated that the electrocatalytic activity of N-containing catalysts is highly dependent on the pyridinic N content.<sup>42,47-49</sup> Hence, the high proportion of pyridinic N (44.7%) in sample Fe<sub>30</sub>NC-Ar<sub>700</sub>-NH<sub>3</sub>-45% is believed to contribute to the enhanced ORR activity. Two Fe 2p peaks at ~711 and 725 eV (Figure 2c) corresponding to lower (Fe 2p<sub>3/2</sub>) and

higher (Fe 2p<sub>1/2</sub>) energies due to spin-orbital splitting were also observed. These results further demonstrate that N and Fe heteroatoms have been doped into the samples, furthermore, the content of Fe measured by XPS (denoted as Fe<sub>xps</sub>) were concluded in Table S2 (Supporting Information). In addition, it has been reported that all the Fe in the precursor remains in the final catalysts after the pyrolysis,<sup>50</sup> so the Fe concentration can be calculated from the pyrolysis parameters (Table S2, Supporting Information), which is denoted as Fe<sub>cal</sub>. Since XPS is a surface-sensitive spectroscopic technique with only several nanometers effective testing depth, it is reasonable that the value of Fe<sub>xps</sub> is 3-5 times smaller than that of Fe<sub>cal</sub>. Combining the catalytic activities (half-wave potential), it can be concluded that the optimized Fe content (Fe<sub>cal</sub>) in our Fe/N/C catalyst is in the range of 5.5-8 wt% (vs. 1.2-2.0% detected by XPS, Fe<sub>xps</sub>). These values are expected to be the reference for similar catalysts in future research.

On the other hand, it has been reported that the large microporous surface area have critical positive influence on the formation of the active sites of Fe and N<sup>27</sup> and mesoporous structure for efficient mass transport, contributing to enhanced ORR activity.<sup>35, 40, 51</sup> The porous features and the BET specific surface areas of the catalysts were characterized by nitrogen isothermal adsorption/desorption measurements (Figure 2d and S6, Table S3, Supporting Information). They present a sharp uptake at low pressure and a smooth plateau at middle-to-high pressure, which is characteristic of microporous materials. As revealed by the QSDFT pore size distribution (Figure 2d), sample Fe30NC-Ar700-NH<sub>3</sub>-45% possesses plenty of micropores (around 0.6 nm) and high BET surface area of 536.3 m<sup>2</sup> g<sup>-1</sup> (with 435.7 m<sup>2</sup> g<sup>-1</sup> of micropores and 100.6 m<sup>2</sup> g<sup>-1</sup> of mesopores).

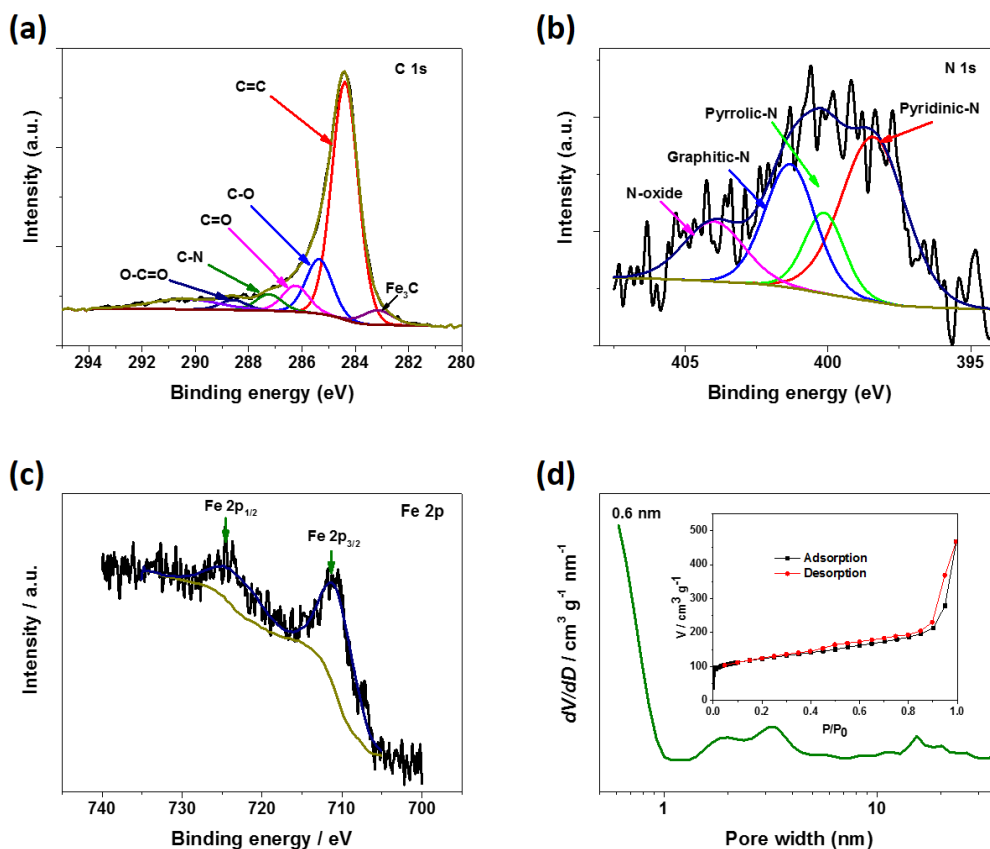


**Figure 2.** (a) Core level C 1s spectrum, (b) core level N 1s spectrum, (c) core level Fe 2p XPS spectrum of Fe30NC-Ar700-NH<sub>3</sub>-45%, and (d) pore size distribution of Fe30NC-Ar700-NH<sub>3</sub>-45%. Inset in Figure 2d is the corresponding N<sub>2</sub> isothermal adsorption/desorption curves.

We further investigated the factors which affect the activity of the Fe/N/C catalysts, such as BET surface area (micropores, mesopores, and their ratio), and the Fe content. As shown in Table S3 (Supporting Information), Figure 3 and Figure S7 (Supporting Information), it can be seen that (i) the BET surface area (from ~400, ~500, to ~700 m<sup>2</sup> g<sup>-1</sup>) of the samples increases with the increase of FeAc content (from 20, 30, to 50 mg) in raw materials; (ii) for the samples in the same FeAc content group, the BET surface area decrease with the increase of the Fe amount (Fe<sub>cal</sub>) in the final catalyst, i.e., during NH<sub>3</sub> pyrolysis process, the Fe content kept constant, while the carbon lost more weight with prolonged pyrolysis time, in the catalysts;<sup>52</sup> (iii) the optimized Fe% in the final catalysts is in the range of 5.5-8 wt% (Figure 3a); (iv) the optimized micropore surface area is around 450 m<sup>2</sup> g<sup>-1</sup> (Figure 3b); (v) the activity of our catalyst has increases as the ratio of mesopores increases (Figure 3c), so the optimal ratio of micro/meso-pore in these catalysts is around 4-5 (Figure 3d). In summary, the ORR activity can be optimized by the proper

balance of Fe content and surface area (microspore and mesopore, as illustrated in Figure 3e). For example, the most active Fe30NC-Ar700-NH<sub>3</sub>-45% possesses Fe content of 7.02 wt% and the micropore/mesopore ratio of 4.33.

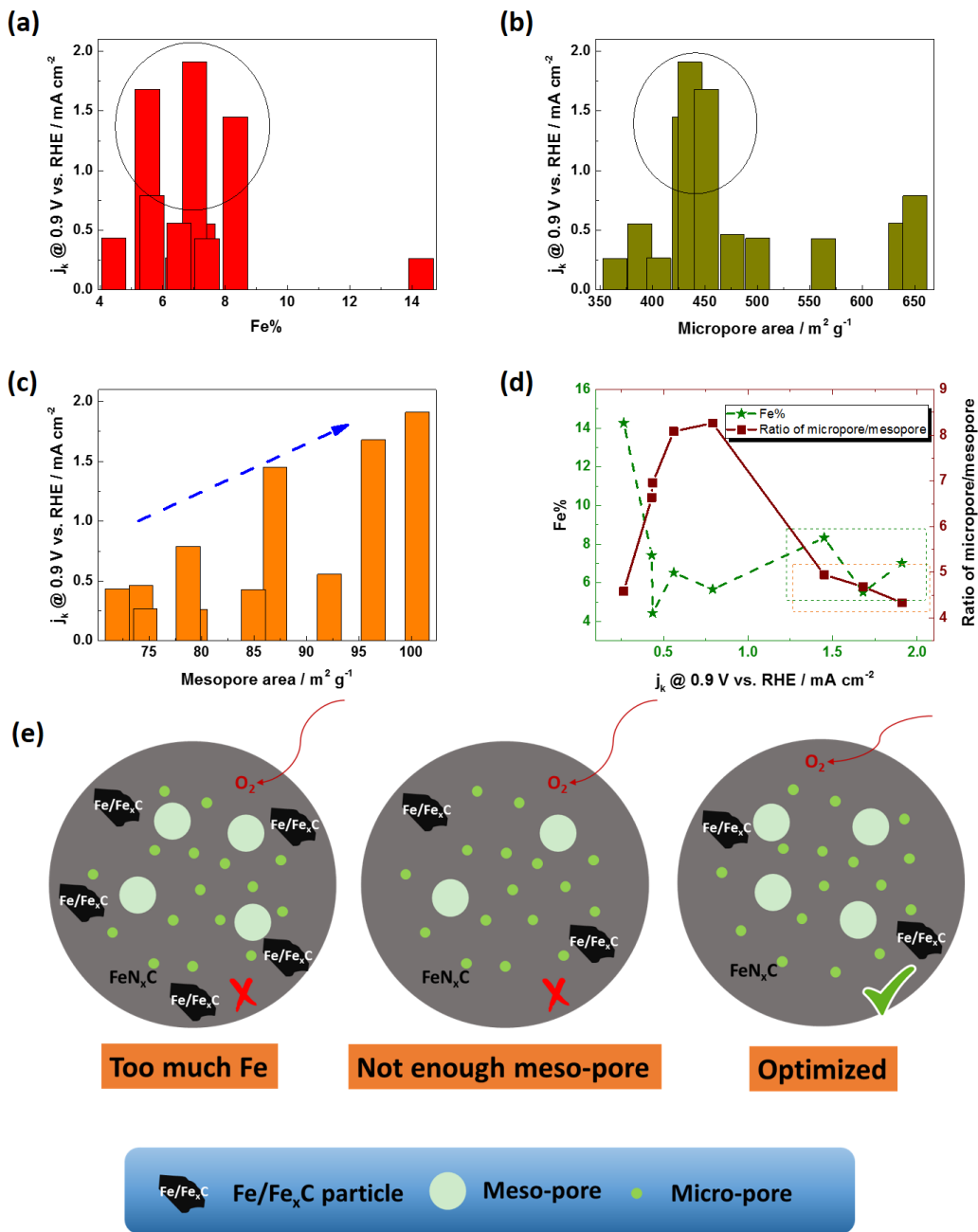


**Figure 3.** (a) The histogram of  $j_k$ @0.9 V with the Fe content in the catalysts, (b) and (c) histogram of  $j_k$ @0.9 V with the micropore surface area and mesopore surface area, and (d) The relationships of Fe content, ratio of micropore/mesopore and  $j_k$ @0.9 V. (e) Schematic images of the optimal microstructure of Fe/N/C catalysts.

The microstructures of the samples were further characterized by TEM. Figure S3 (Supporting Information) shows that the carbon host (SPRMs) are spherical with sphere diameter of 50-60 nm and many highly-ordered alveoli-like structures. Figure 4 is the TEM images of Fe<sub>30</sub>NC-Ar700-NH<sub>3</sub>-45% catalyst with different magnifications. The spherical morphology can be mostly preserved even after the high temperature pyrolysis of Ar and NH<sub>3</sub>, and most of them demonstrated an interconnected hollow and open structure, having typical wall thickness around 10 nm with 15-20 graphitic layers (Figure 4c), the graphitization nanoshells could enhance the corrosion resistance, thus improve the stability of the catalysts.<sup>25</sup> Besides, it has been reported that ORR can only occur at confined spatial sites, called “triple phase boundaries (TPB)” where electrolyte, gas, and electrically connected catalyst regions contact,<sup>53</sup> therefore, the open and interconnected spherical structure of Fe<sub>30</sub>NC-Ar700-NH<sub>3</sub>-45% is expected to offer more active sites for ORR by providing more TPB. While this is not strictly applicable when using RDE which is a two-phase ‘flooded electrolyte’ system, it could provide advantages at the membrane electrode assembly (MEA) level. In addition, the HRTEM image of the black spot in Fe<sub>30</sub>NC-Ar700-NH<sub>3</sub>-45% sample (Figure S4, Supporting Information) reveals the presence of Fe<sub>3</sub>C, this carbide may also have synergistic effects with the open and hollow structure in the catalysts to enhance the ORR performance.<sup>46</sup> From Figure S5 (Supporting Information), it can be seen that the structures for samples of Fe<sub>20</sub>NC-Ar700-NH<sub>3</sub>-30% and Fe<sub>50</sub>NC-Ar700-NH<sub>3</sub>-80% are similar to that of Fe<sub>30</sub>NC-Ar700-NH<sub>3</sub>-45%, while the difference lies in that Fe<sub>20</sub>NC-Ar700-NH<sub>3</sub>-30% with longer NH<sub>3</sub> pyrolysis time shows more irregular morphology, while less NH<sub>3</sub> pyrolysis time making Fe<sub>50</sub>NC-Ar700-NH<sub>3</sub>-80% keeping more regular spherical structure with less open structure.

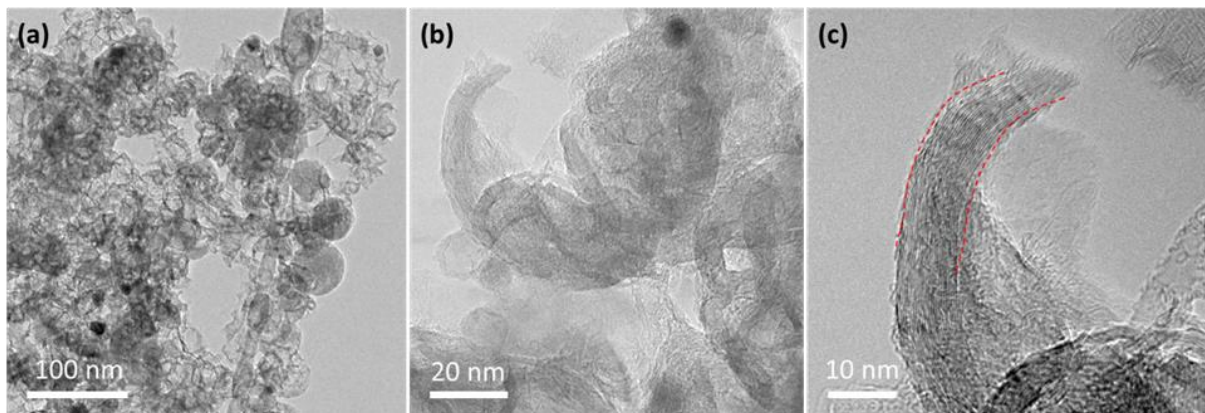


**Figure 4.** (a-c) TEM images of Fe<sub>30</sub>NC-Ar700-NH<sub>3</sub>-45% catalyst at different magnifications.

The electrocatalytic activity, stability, and methanol tolerance of the as-synthesized Fe<sub>x</sub>NC-Ar700-NH<sub>3</sub>-y% catalysts were studied by CV and RRDE techniques. RRDE testing is commonly used for determining the properties of ORR catalysts, in which, both the catalytic activity (from disk measurements) and selectivity to H<sub>2</sub>O<sub>2</sub> formation (from ring measurements) can be directly observed. As shown in Figure 1 and S1 (Supporting Information), by comparing the LSV curves and Tafel plot in 0.1 M KOH, relative to other Fe<sub>x</sub>NC-Ar700-NH<sub>3</sub>-y% catalysts, Fe<sub>30</sub>NC-Ar700-NH<sub>3</sub>-45% displays a superior ORR activity with more positive half-wave potential and onset potential ( $E_{\text{onset}}$ ), as well as higher activity at 0.9 V (vs. RHE). Figure 5a shows the typical RRDE voltammograms of Fe<sub>30</sub>NC-Ar700-NH<sub>3</sub>-45% and commercial Pt/C catalyst obtained at room temperature in O<sub>2</sub>-saturated 0.1 M KOH solution. It can be seen that the current density at 0.85 V can be achieved 3.43 mA cm<sup>-2</sup> for Fe<sub>30</sub>NC-Ar700-NH<sub>3</sub>-45% vs. 1.15 mA cm<sup>-2</sup> for Pt/C (with higher loading for NPMC). RRDE test results show that Fe<sub>30</sub>NC-Ar700-NH<sub>3</sub>-45% has a high electron-transfer number of 3.98, almost the same as that of the Pt/C catalyst. Moreover, the H<sub>2</sub>O<sub>2</sub> yield measured with the Fe<sub>30</sub>NC-Ar700-NH<sub>3</sub>-45% catalyst remained below 3% at all potentials in 0.1 M KOH. More impressively, in the range of 0.5-0.85 V (vs. RHE), the H<sub>2</sub>O<sub>2</sub> yielding of Fe<sub>30</sub>NC-Ar700-NH<sub>3</sub>-45% is below 1.5%, even lower than that of commercial Pt/C. This negligible H<sub>2</sub>O<sub>2</sub> yield clearly confirms that Fe<sub>30</sub>NC-Ar700-NH<sub>3</sub>-45% has extremely high ORR catalytic efficiency. Figure 5d shows the Tafel plots of Fe<sub>30</sub>NC-Ar700-NH<sub>3</sub>-45% and commercial Pt/C, derived from Figure 5a. In the low over-potential region, Fe<sub>30</sub>NC-Ar700-NH<sub>3</sub>-45% has a Tafel slope of 67 mV/decade in 0.1 M KOH, close to the 66 mV/decade of the Pt/C, indicating that the rate determining step for the ORR occurring at Fe<sub>30</sub>NC-Ar700-NH<sub>3</sub>-45% is similar to that of Pt.

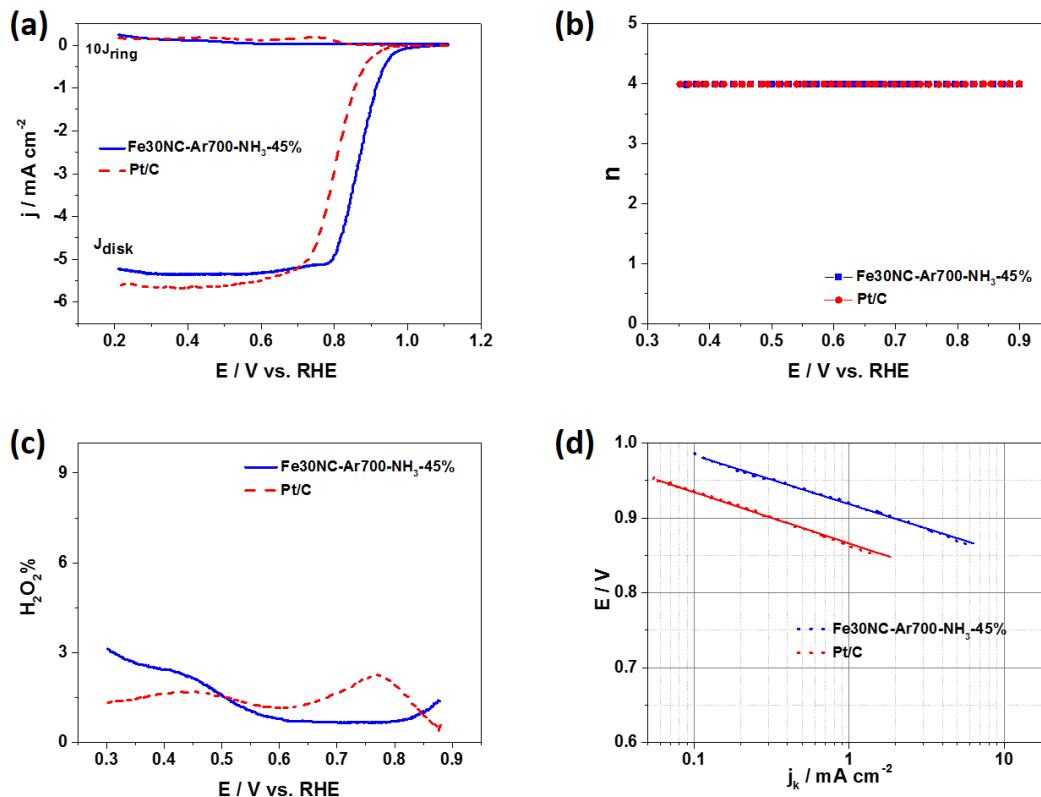


**Figure 5.** (a) RRDE voltammograms, (b) electron transfer number ( $n$ ), (c)  $\text{H}_2\text{O}_2$  yield, (d) Tafel plots of Fe30NC-Ar700-NH<sub>3</sub>-45% and Pt/C in O<sub>2</sub>-saturated 0.1 M KOH at a scan rate of 10 mV s<sup>-1</sup>, rotation rate = 1600 rpm.

Moreover, benefiting from the graphitized carbon phase (Figure 4c), Fe30NC-Ar700-NH<sub>3</sub>-45% shows outstanding stability for ORR in alkaline media, as confirmed by the absence of an ORR polarization curve shift after 10000 cycles between 0.6 to 1.2 V (Figure 6a), while there was a 35 mV negative shift of half-wave potential for the Pt/C catalyst under the same conditions (Figure 6b), suggesting that under RRDE experiment, Fe30NC-Ar700-NH<sub>3</sub>-45% is more stable than Pt/C. Furthermore, for the application of direct methanol fuel cells (DMFC), the methanol on the anode side could go through membrane to the cathode side, leading to a “mixed potential effect”, which would severely deteriorate the ORR performance, therefore, the methanol tolerance of the Fe30NC-Ar700-NH<sub>3</sub>-45% and Pt/C catalysts was evaluated by adding 1.0 M methanol into 0.1 M KOH electrolyte. After addition of methanol, there is almost no change in the ORR peak current for Fe30NC-Ar700-NH<sub>3</sub>-45% (Figure 6c); however, the typical inverse methanol oxidation peaks in CVs were observed (Figure 6d) for the Pt/C catalyst. These results

suggest that Fe<sub>3</sub>ONC-Ar700-NH<sub>3</sub>-45% has much better methanol tolerance (i.e., catalytic selectivity toward ORR) than the commercial Pt/C catalyst in alkaline media.

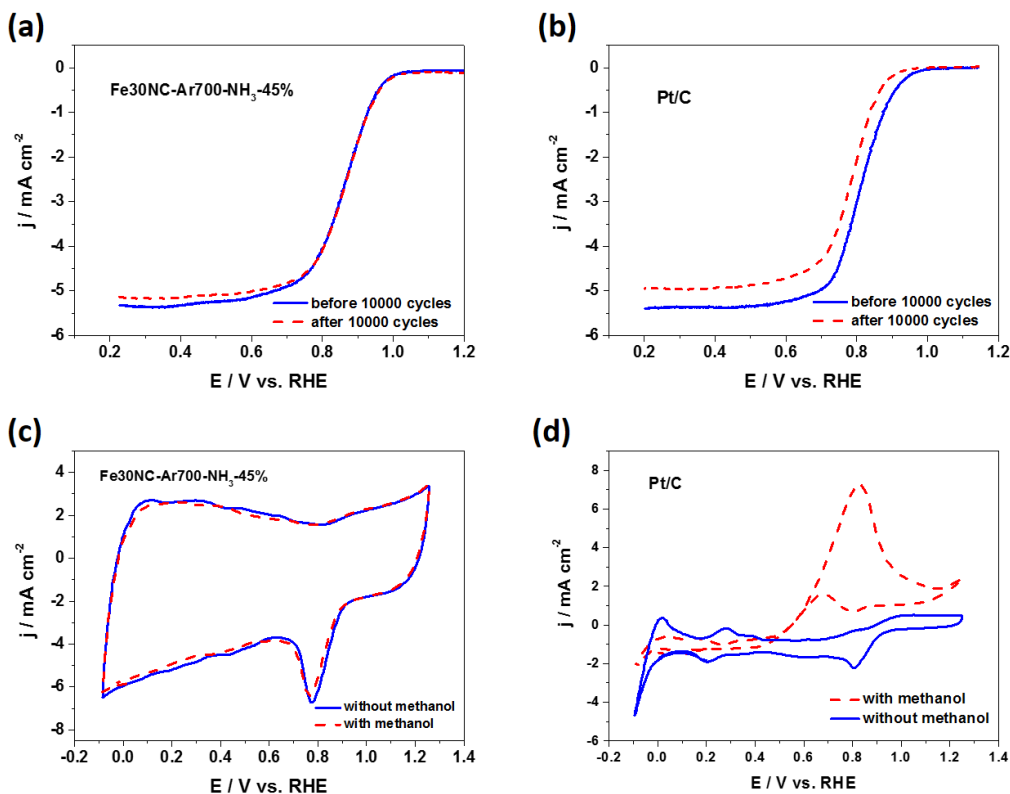


**Figure 6.** LSV curves of (a) Fe<sub>3</sub>ONC-Ar700-NH<sub>3</sub>-45% and (b) Pt/C for ORR in O<sub>2</sub>-saturated 0.1 M KOH before and after 10000 cycles at a scan rate of 200 mV s<sup>-1</sup> between 0.6-1.2 V vs. RHE. CV curves of (c) Fe<sub>3</sub>ONC-Ar700-NH<sub>3</sub>-45% and (d) Pt/C in O<sub>2</sub>-saturated 0.1 M KOH without and with 1.0 M methanol. Scan rate: 50 mV s<sup>-1</sup>.

Importantly, Fe<sub>3</sub>ONC-Ar700-NH<sub>3</sub>-45% catalyst is also active and stable for ORR in acidic media. As shown in Figure 7a, in 0.5 M H<sub>2</sub>SO<sub>4</sub> electrolyte, Fe<sub>3</sub>ONC-Ar700-NH<sub>3</sub>-45% shows slightly negative shift (~30 mV), in terms of the on-set potential and half-wave potential, compared with those of Pt/C. The transferred electron number per O<sub>2</sub> molecule for Fe<sub>3</sub>ONC-Ar700-NH<sub>3</sub>-45% and Pt/C electrodes in the acidic medium is 3.89 and 3.93 (Figure 7b), respectively, suggesting a nearly 4e<sup>-</sup> ORR pathway even in the acidic solution. The calculated yields of H<sub>2</sub>O<sub>2</sub> for the Fe<sub>3</sub>ONC-Ar700-NH<sub>3</sub>-45% and Pt/C electrodes are less than 6.5% and 4.1% respectively, under the potential range of 0.2–0.7 V (Figure 7c). Figure 7d shows the Tafel plots of Fe<sub>3</sub>ONC-Ar700-NH<sub>3</sub>-45% and commercial Pt/C, derived from Figure 7a. The Tafel slope of both Fe<sub>3</sub>ONC-Ar700-NH<sub>3</sub>-45% and the Pt/C are around 62 mV/decade, indicating that

Fe30NC-Ar700-NH<sub>3</sub>-45% also has the similar reaction mechanism of ORR as commercial Pt/C in the low over-potential area.

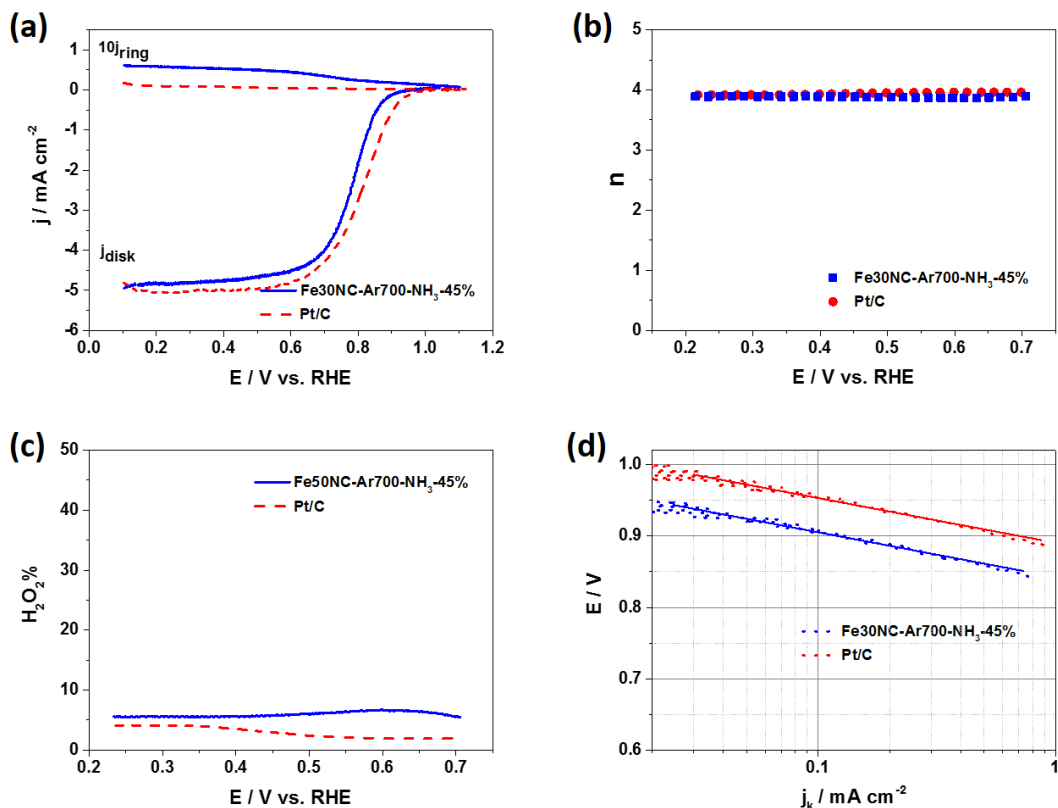


**Figure 7.** (a) RRDE voltammograms, (b) electron transfer number ( $n$ ), (c) H<sub>2</sub>O<sub>2</sub> yield, (d) Tafel plots of Fe30NC-Ar-NH<sub>3</sub>-45% and Pt/C in O<sub>2</sub>-saturated 0.5 M H<sub>2</sub>SO<sub>4</sub> at a scan rate of 10 mV s<sup>-1</sup>, rotation rate = 1600 rpm.

The stability test was also carried out under the identical conditions. From Figure 8a and 8d, it can be seen that Fe30NC-Ar700-NH<sub>3</sub>-45% sample shows better ORR stability than the Pt/C catalyst, as indicated by a much lower polarization curve shift (25 mV vs. 65 mV for Pt/C), after 2000 cycles' tests. From the methanol crossover test, we can see that in the presence of 1.0 M methanol, there is only a slight change of peak current for Fe30NC-Ar700-NH<sub>3</sub>-45% (Figure 8c), whereas significant methanol oxidation peaks in CVs for the Pt/C catalyst (Figure 8d) can be observed, suggesting that Fe30NC-Ar700-NH<sub>3</sub>-45% also has excellent selectivity for ORR with strong tolerance to methanol crossover effect in acidic media.

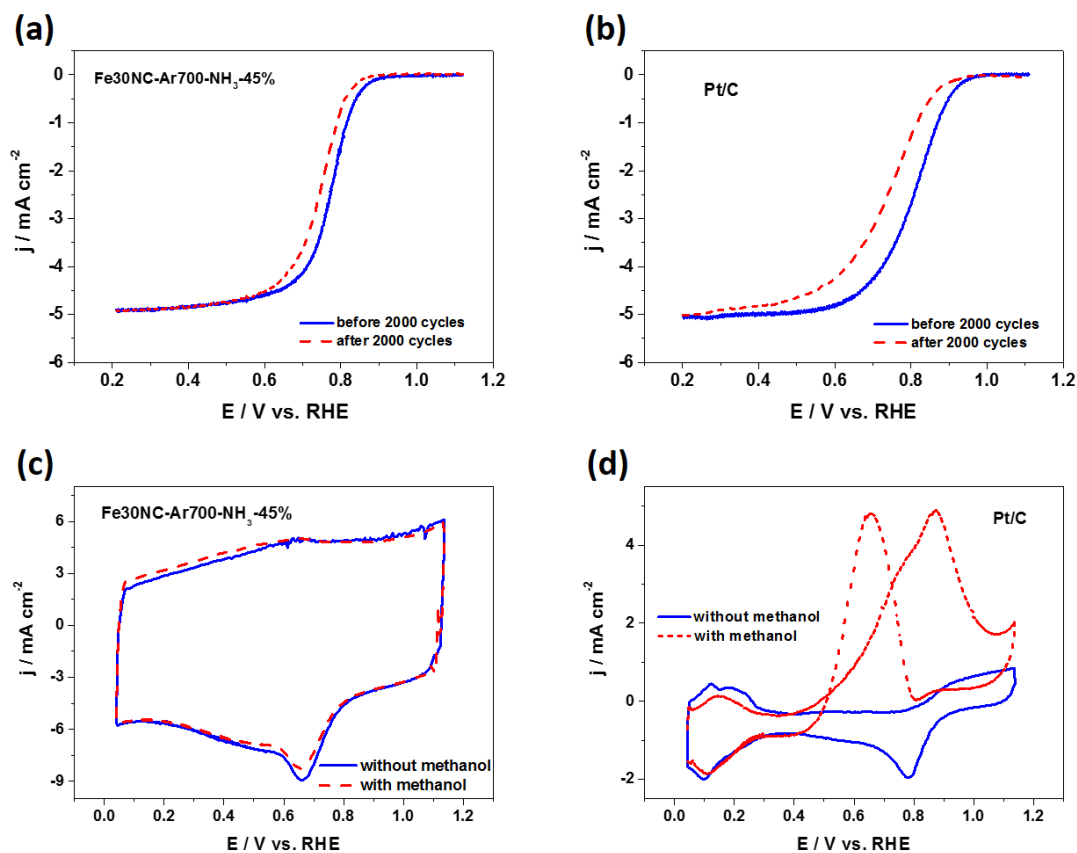


**Figure 8.** LSV curves of (a) Fe30NC-Ar700-NH<sub>3</sub>-45% and (b) Pt/C for ORR in O<sub>2</sub>-saturated 0.5 M H<sub>2</sub>SO<sub>4</sub> before and after 2000 cycles between 0.6-1.2 V vs. RHE. CV curves of (c) Fe30NC-Ar700-NH<sub>3</sub>-45% and (d) Pt/C in O<sub>2</sub>-saturated 0.5 M H<sub>2</sub>SO<sub>4</sub> without and with 1.0 M methanol. Scan rate: 50 mV s<sup>-1</sup>.

## Conclusions

To sum up, a series of 3D microporous Fe/N/C ORR catalysts were prepared by employing SPRMs as the carbon host for impregnating FeAc and 1,10-Phen, followed by high temperature pyrolysis in Ar in NH<sub>3</sub> atmosphere, consequently. Through the systematic studies, we found that (i) the content of Fe precursor and pyrolysis time under NH<sub>3</sub> have distinct influence on the morphology and structure of the final Fe/N/C catalysts; (ii) the pyrolysis temperature in Ar, the BET surface area, and the content of Fe in the catalysts largely affect the ORR activity; (iii) the optimized Fe content of the Fe/N/C catalysts is around 5.5-8 wt% and the optimized porosity is with 450 m<sup>2</sup> g<sup>-1</sup> micropore with preferably higher value of mesopores, only catalysts subjecting

within these two ranges exhibit high activity. The Fe<sub>30</sub>NC-Ar<sub>700</sub>-NH<sub>3</sub>-45% catalyst shows an interconnected hollow and open spherical structure with optimized Fe content (~7 wt%), BET surface area (536.3 m<sup>2</sup> g<sup>-1</sup>, with 435.7 m<sup>2</sup> g<sup>-1</sup> of micropores and 100.6 m<sup>2</sup> g<sup>-1</sup> of mesopores with a micro/meso of 4.33), and exhibits good ORR performances in both alkaline and acidic conditions. In alkaline solution, it shows a half-wave potential of 0.87 V, excellent stability even in O<sub>2</sub>-saturated solution, and strong methanol tolerance. Moreover, in acidic solution, Fe<sub>30</sub>NC-Ar<sub>700</sub>-NH<sub>3</sub>-45% also exhibits excellent stability and selectivity. Notably, the ORR process of Fe<sub>30</sub>NC-Ar<sub>700</sub>-NH<sub>3</sub>-45% catalyst in both alkaline and acidic media follows the direct 4e<sup>-</sup> transfer pathway, indicating a complete reduction of O<sub>2</sub> to water. All these characters make our Fe/N/C catalyst a very good non-noble-metal candidate for ORR. This work provides more insights to fabricate highly efficient Fe/N/C catalysts in both acidic and alkaline electrolytes, which may boost the development of various fuel cells.

**Supporting Information.** Tafel plots in O<sub>2</sub>-saturated 0.1 M KOH of Fe<sub>x</sub>NC-Ar<sub>T</sub>-NH<sub>3</sub>-y% (scan rate = 10 mV s<sup>-1</sup>, rotation rate = 1600 rpm), XPS spectrums of Fe<sub>x</sub>NC-Ar<sub>T</sub>-NH<sub>3</sub>-y% samples, TEM images of spherical phenolic resol-F127 monomicelles, HRTEM images of black spot part of Fe<sub>30</sub>NC-Ar<sub>700</sub>-NH<sub>3</sub>-45%, TEM images of Fe<sub>20</sub>NC-Ar<sub>700</sub>-NH<sub>3</sub>-30% and Fe<sub>50</sub>NC-Ar<sub>700</sub>-NH<sub>3</sub>-80%, N<sub>2</sub> isothermal adsorption/desorption curves of Fe<sub>x</sub>NC-Ar<sub>T</sub>-NH<sub>3</sub>-y%, the relationships of micro-pore, mesopore and Fe content with the current density j<sub>k</sub>@0.9 V, experimental parameters during the preparation of Fe<sub>x</sub>NC-Ar<sub>T</sub>-NH<sub>3</sub>-y% samples, the relationship of the catalytic activity and the Fe, N content (wt%), N<sub>2</sub> adsorption/desorption analysis of Fe<sub>x</sub>NC-Ar<sub>T</sub>-NH<sub>3</sub>-y% samples.

### Corresponding Author

\*Email: [gaixia.zhang@emt.inrs.ca](mailto:gaixia.zhang@emt.inrs.ca)

\*Email: [shuhui@emt.inrs.ca](mailto:shuhui@emt.inrs.ca)

### Author Contributions

The manuscript was written through contributions of all authors. All authors have given approval to the final version of the manuscript.

## Notes

The authors declare no competing financial interest.

## Acknowledgment

This work is supported financially by the Natural Sciences and Engineering Research Council of Canada (NSERC), Ballard Power Systems Inc., the Fonds de Recherche du Québec-Nature et Technologies (FRQNT), Canada Foundation for Innovation (CFI), Centre Québécois sur les Matériaux Fonctionnels (CQMF), and Institut National de la Recherche Scientifique (INRS). Q. Wei and X. Yang gratefully acknowledge the scholarship from FRQNT and China Scholarship Council (CSC).

## References

- [1] Peng, Z.; Freunberger, S. A.; Hardwick, L. J.; Chen, Y.; Giordani, V.; Bardé, F.; Novák, P.; Graham, D.; Tarascon, J. M.; Bruce, P. G. Oxygen Reactions in a Non-Aqueous Li<sup>+</sup> Electrolyte. *Angew. Chem., Int. Ed.* **2011**, *123* (28), 6475-6479.
- [2] Steele, B. C. H.; Heinzel, A. Materials for Fuel-Cell Technologies. *Nature* **2001**, *414* (6861), 345-352.
- [3] Liang, J.; Zhou, R. F.; Chen, X. M.; Tang, Y. H.; Qiao, S. Z. Fe-N Decorated Hybrids of CNTs Grown on Hierarchically Porous Carbon for High-Performance Oxygen Reduction. *Adv. Mater.* **2014**, *26* (35), 6074-6079.
- [4] Shao, M.; Chang, Q.; Dodelet, J.-P.; Chenitz, R. Recent Advances in Electrocatalysts for Oxygen Reduction Reaction. *Chem. Rev.* **2016**, *116* (6), 3594-3657.
- [5] Sun, S.; Zhang, G.; Geng, D.; Chen, Y.; Li, R.; Cai, M.; Sun, X. A Highly Durable Platinum Nanocatalyst for Proton Exchange Membrane Fuel Cells: Multiarmed Starlike Nanowire Single Crystal. *Angew. Chem., Int. Ed.* **2011**, *123* (2), 442-446.
- [6] Sun, S.; Jaouen, F.; Dodelet, J. P. Controlled Growth of Pt Nanowires on Carbon Nanospheres and Their Enhanced Performance as Electrocatalysts in PEM Fuel Cells. *Adv. Mater.* **2008**, *20* (20), 3900-3904.

- [7] Bing, Y.; Liu, H.; Zhang, L.; Ghosh, D.; Zhang, J. Nanostructured Pt-Alloy Electrocatalysts for PEM Fuel Cell Oxygen Reduction Reaction. *Chem. Soc. Rev.* **2010**, *39* (6), 2184-2202.
- [8] Chen, L.; Chen, Z.; Huang, Z.; Huang, Z.; Wang, Y.; Li, H.; Zhou, H.; Kuang, Y. Influence of Carbon Precursors on the Structure, Composition and Oxygen Reduction Reaction Performance of Nitrogen-Doped Carbon Materials. *J. Phys. Chem. C* **2015**, *119* (52), 28757-28765.
- [9] Jiang, W.-J.; Hu, J.-S.; Zhang, X.; Jiang, Y.; Yu, B.-B.; Wei, Z.-D.; Wan, L.-J. In Situ Nitrogen-Doped Nanoporous Carbon Nanocables as An Efficient Metal-Free Catalyst for Oxygen Reduction Reaction. *J. Mater. Chem. A* **2014**, *2* (26), 10154-10160.
- [10] Wei, Q.; Tong, X.; Zhang, G.; Qiao, J.; Gong, Q.; Sun, S. Nitrogen-Doped Carbon Nanotube and Graphene Materials for Oxygen Reduction Reactions. *Catalysts* **2015**, *5* (3), 1574-1602.
- [11] Ma, Z.; Dou, S.; Shen, A.; Tao, L.; Dai, L.; Wang, S. Sulfur-Doped Graphene Derived from Cycled Lithium-Sulfur Batteries as a Metal-Free Electrocatalyst for the Oxygen Reduction Reaction. *Angew. Chem., Int. Ed.* **2015**, *127* (6), 1908-1912.
- [12] Gong, Y.; Fei, H.; Zou, X.; Zhou, W.; Yang, S.; Ye, G.; Liu, Z.; Peng, Z.; Lou, J.; Vajtai, R. Boron-and Nitrogen-Substituted Graphene Nanoribbons as Efficient Catalysts for Oxygen Reduction Reaction. *Chem. Mater.* **2015**, *27* (4), 1181-1186.
- [13] Zhang, C.; Mahmood, N.; Yin, H.; Liu, F.; Hou, Y. Synthesis of Phosphorus-Doped Graphene and Its Multifunctional Applications for Oxygen Reduction Reaction and Lithium Ion Batteries. *Adv. Mater.* **2013**, *25* (35), 4932-4937.
- [14] Liang, Y.; Li, Y.; Wang, H.; Zhou, J.; Wang, J.; Regier, T.; Dai, H. Co<sub>3</sub>O<sub>4</sub> Nanocrystals On Graphene as A Synergistic Catalyst for Oxygen Reduction Reaction. *Nat. Mater.* **2011**, *10* (10), 780-786.
- [15] Wu, Z.-S.; Yang, S.; Sun, Y.; Parvez, K.; Feng, X.; Müllen, K. 3D Nitrogen-Doped Graphene Aerogel-Supported Fe<sub>3</sub>O<sub>4</sub> Nanoparticles as Efficient Electrocatalysts for The Oxygen Reduction Reaction. *J. Am. Chem. Soc.* **2012**, *134* (22), 9082-9085.
- [16] Cheng, F.; Su, Y.; Liang, J.; Tao, Z.; Chen, J. MnO<sub>2</sub>-Based Nanostructures as Catalysts for Electrochemical Oxygen Reduction in Alkaline Media†. *Chem. Mater.* **2009**, *22* (3), 898-905.

- [17] Mahmood, N.; Zhang, C.; Jiang, J.; Liu, F.; Hou, Y. Multifunctional Co<sub>3</sub>S<sub>4</sub>/Graphene Composites for Lithium Ion Batteries and Oxygen Reduction Reaction. *Chem. Eur. J.* **2013**, *19* (16), 5183-5190.
- [18] Susac, D.; Zhu, L.; Teo, M.; Sode, A.; Wong, K. C.; Wong, P. C.; Parsons, R. R.; Bizzotto, D.; Mitchell, K. A. R.; Campbell, S. A. Characterization of FeS<sub>2</sub>-Based Thin Films as Model Catalysts for the Oxygen Reduction Reaction. *J. Phys. Chem. C* **2007**, *111* (50), 18715-18723.
- [19] Liu, X.; Du, J.; Li, C.; Han, X.; Hu, X.; Cheng, F.; Chen, J. The Anion Effect on the Oxygen Reduction of MnX (X= O, S, and Se) Catalysts. *J. Mater. Chem. A* **2015**, *3* (7), 3425-3431.
- [20] Cao, R.; Thapa, R.; Kim, H.; Xu, X.; Kim, M. G.; Li, Q.; Park, N.; Liu, M.; Cho, J. Promotion of Oxygen Reduction by a Bio-Inspired Tethered Iron Phthalocyanine Carbon Nanotube-based Catalyst. *Nat. Commun.* **2013**, *4*, 2076.
- [21] Wei, P. J.; Yu, G. Q.; Naruta, Y.; Liu, J. G. Covalent Grafting of Carbon Nanotubes with a Biomimetic Heme Model Compound to Enhance Oxygen Reduction Reactions. *Angew. Chem., Int. Ed.* **2014**, *53* (26), 6659-6663.
- [22] Chung, H. T.; Won, J. H.; Zelenay, P. Active and Stable Carbon Nanotube/Nanoparticle Composite Electrocatalyst for Oxygen Reduction. *Nat. Commun.* **2013**, *4*, 1922.
- [23] Lin, L.; Zhu, Q.; Xu, A.-W. Noble-Metal-Free Fe-N/C Catalyst for Highly Efficient Oxygen Reduction Reaction under Both Alkaline and Acidic Conditions. *J. Amer. Chem. Soc.* **2014**, *136* (31), 11027-11033.
- [24] Liu, J.; Sun, X.; Song, P.; Zhang, Y.; Xing, W.; Xu, W. High-Performance Oxygen Reduction Electrocatalysts based on Cheap Carbon Black, Nitrogen, and Trace Iron. *Adv. Mater.* **2013**, *25* (47), 6879-6883.
- [25] Wu, G.; More, K. L.; Johnston, C. M.; Zelenay, P. High-Performance Electrocatalysts for Oxygen Reduction Derived from Polyaniline, Iron, and Cobalt. *Science* **2011**, *332* (6028), 443-447.
- [26] Wu, Z. Y.; Xu, X. X.; Hu, B. C.; Liang, H. W.; Lin, Y.; Chen, L. F.; Yu, S. H. Iron Carbide Nanoparticles Encapsulated in Mesoporous Fe-N-Doped Carbon Nanofibers for Efficient Electrocatalysis. *Angew. Chem., Int. Ed.* **2015**, *127* (28), 8297-8301.
- [27] Lefèvre, M.; Proietti, E.; Jaouen, F.; Dodelet, J.-P. Iron-based Catalysts with Improved Oxygen Reduction Activity in Polymer Electrolyte Fuel Cells. *Science* **2009**, *324* (5923), 71-74.

- [28] Wu, G.; Chen, Z.; Artyushkova, K.; Garzon, F. H.; Zelenay, P. Polyaniline-Derived Non-Precious Catalyst for the Polymer Electrolyte Fuel Cell Cathode. *ECS Trans.* **2008**, *16* (2), 159-170.
- [29] Ferrandon, M.; Kropf, A. J.; Myers, D. J.; Artyushkova, K.; Kramm, U.; Bogdanoff, P.; Wu, G.; Johnston, C. M.; Zelenay, P. Multitechnique Characterization of A Polyaniline–Iron–Carbon Oxygen Reduction Catalyst. *J. Phys. Chem. C* **2012**, *116* (30), 16001-16013.
- [30] Wu, G.; Johnston, C. M.; Mack, N. H.; Artyushkova, K.; Ferrandon, M.; Nelson, M.; Lezama-Pacheco, J. S.; Conradson, S. D.; More, K. L.; Myers, D. J. Synthesis–Structure–Performance Correlation for Polyaniline–Me–C Non-Precious Metal Cathode Catalysts for Oxygen Reduction in Fuel Cells. *J. Mater. Chem.* **2011**, *21* (30), 11392-11405.
- [31] Zhu, Y.; Zhang, B.; Liu, X.; Wang, D. W.; Su, D. S. Unravelling the Structure of Electrocatalytically Active Fe–N Complexes in Carbon for the Oxygen Reduction Reaction. *Angew. Chem., Int. Ed.* **2014**, *53* (40), 10673-10677.
- [32] Kramm, U. I.; Herranz, J.; Larouche, N.; Arruda, T. M.; Lefèvre, M.; Jaouen, F.; Bogdanoff, P.; Fiechter, S.; Abs-Wurmbach, I.; Mukerjee, S. Structure of the Catalytic Sites in Fe/N/C-Catalysts for O<sub>2</sub>-Reduction in PEM Fuel Cells. *Phys. Chem. Chem. Phys.* **2012**, *14* (33), 11673-11688.
- [33] Jaouen, F.; Lefèvre, M.; Dodelet, J.-P.; Cai, M. Heat-Treated Fe/N/C Catalysts for O<sub>2</sub> Electroreduction: Are Active Sites Hosted in Micropores? *J. Phys. Chem. B* **2006**, *110* (11), 5553-5558.
- [34] Wang, M.-Q.; Yang, W.-H.; Wang, H.-H.; Chen, C.; Zhou, Z.-Y.; Sun, S.-G. Pyrolyzed Fe–N–C Composite As an Efficient Non-Precious Metal Catalyst for Oxygen Reduction Reaction in Acidic Medium. *ACS Catal.* **2014**, *4* (11), 3928-3936.
- [35] Liang, H.-W.; Wei, W.; Wu, Z.-S.; Feng, X.; Müllen, K. Mesoporous Metal–Nitrogen-Doped Carbon Electrocatalysts for Highly Efficient Oxygen Reduction Reaction. *J. Amer. Chem. Soc.* **2013**, *135* (43), 16002-16005.
- [36] Kramm, U. I.; Herrmann-Geppert, I.; Fiechter, S.; Zehl, G.; Zizak, I.; Dorbandt, I.; Schmeißer, D.; Bogdanoff, P. Effect of Iron-Carbide Formation on the Number of Active Sites in Fe–N–C Catalysts for the Oxygen Reduction Reaction in Acidic Media. *J. Mater. Chem. A* **2014**, *2* (8), 2663-2670.

- [37] Su, Y.; Jiang, H.; Zhu, Y.; Zou, W.; Yang, X.; Chen, J.; Li, C. Hierarchical Porous Iron and Nitrogen Co-Doped Carbons as Efficient Oxygen Reduction Electrocatalysts in Neutral Media. *J. Power Sources* **2014**, *265*, 246-253.
- [38] Wen, Z.; Ci, S.; Zhang, F.; Feng, X.; Cui, S.; Mao, S.; Luo, S.; He, Z.; Chen, J. Nitrogen-Enriched Core-Shell Structured Fe/Fe<sub>3</sub>C-C Nanorods as Advanced Electrocatalysts for Oxygen Reduction Reaction. *Adv. Mater.* **2012**, *24* (11), 1399-1404.
- [39] Xiang, Z.; Xue, Y.; Cao, D.; Huang, L.; Chen, J. F.; Dai, L. Highly Efficient Electrocatalysts for Oxygen Reduction Based on 2D Covalent Organic Polymers Complexed with Non-precious Metals. *Angew. Chem., Int. Ed.* **2014**, *53* (9), 2433-2437.
- [40] Lee, J. S.; Park, G. S.; Kim, S. T.; Liu, M.; Cho, J. A Highly Efficient Electrocatalyst for the Oxygen Reduction Reaction: N-Doped Ketjenblack Incorporated into Fe/Fe<sub>3</sub>C-Functionalized Melamine Foam. *Angew. Chem., Int. Ed.* **2013**, *125* (3), 1060-1064.
- [41] Zhou, M.; Yang, C.; Chan, K. Y. Structuring Porous Iron-Nitrogen-Doped Carbon in a Core/Shell Geometry for the Oxygen Reduction Reaction. *Adv. Energy Mater.* **2014**, *4* (18).
- [42] Yang, W.; Liu, X.; Yue, X.; Jia, J.; Guo, S. Bamboo-like Carbon Nanotube/Fe<sub>3</sub>C Nanoparticle Hybrids and Their Highly Efficient Catalysis for Oxygen Reduction. *J. Amer. Chem. Soc.* **2015**, *137* (4), 1436-1439.
- [43] Fang, Y.; Gu, D.; Zou, Y.; Wu, Z.; Li, F.; Che, R.; Deng, Y.; Tu, B.; Zhao, D. A Low-Concentration Hydrothermal Synthesis of Biocompatible Ordered Mesoporous Carbon Nanospheres with Tunable and Uniform Size. *Angew. Chem., Int. Ed.* **2010**, *49* (43), 7987-7991.
- [44] Wei, Q.; Fu, Y.; Zhang, G.; Wang, Y.; Wang, X.; Mohamedi, M.; Sun, S. Highly-Ordered Microporous Carbon Nanospheres: A Promising Anode for High-Performance Sodium-Ion Batteries. *RSC Adv.* **2016**, *6* (87), 84149-84154.
- [45] Wei, J.; Liang, Y.; Zhang, X.; Simon, G. P.; Zhao, D.; Zhang, J.; Jiang, S.; Wang, H. Controllable Synthesis of Mesoporous Carbon Nanospheres and Fe-N/Carbon Nanospheres As Efficient Oxygen Reduction Electrocatalysts. *Nanoscale* **2015**, *7* (14), 6247-6254.
- [46] Hu, Y.; Jensen, J. O.; Zhang, W.; Cleemann, L. N.; Xing, W.; Bjerrum, N. J.; Li, Q. Hollow Spheres of Iron Carbide Nanoparticles Encased in Graphitic Layers As Oxygen Reduction Catalysts. *Angew. Chem., Int. Ed.* **2014**, *53* (14), 3675-3679.

- [47] Rao, C. V.; Cabrera, C. R.; Ishikawa, Y. In Search of the Active Site in Nitrogen-Doped Carbon Nanotube Electrodes for the Oxygen Reduction Reaction. *J. Phys. Chem. L.* **2010**, *1* (18), 2622-2627.
- [48] Xing, T.; Zheng, Y.; Li, L. H.; Cowie, B. C. C.; Gunzelmann, D.; Qiao, S. Z.; Huang, S.; Chen, Y. Observation of Active Sites for Oxygen Reduction Reaction on Nitrogen-Doped Multilayer Graphene. *ACS Nano* **2014**, *8* (7), 6856-6862.
- [49] Guo, D.; Shibuya, R.; Akiba, C.; Saji, S.; Kondo, T.; Nakamura, J. Active Sites of Nitrogen-Doped Carbon Materials for Oxygen Reduction Reaction Clarified Using Model Catalysts. *Science* **2016**, *351* (6271), 361-365.
- [50] Yang, L.; Larouche, N.; Chenitz, R.; Zhang, G.; Lefèvre, M.; Dodelet, J.-P. Activity, Performance, and Durability for the Reduction of Oxygen in PEM Fuel Cells, of Fe/N/C Electrocatalysts Obtained from the Pyrolysis of Metal-Organic-Framework and Iron Porphyrin Precursors. *Electrochim. Acta* **2015**, *159*, 184-197.
- [51] Wang, H.; Ishihara, S.; Ariga, K.; Yamauchi, Y. All-Metal Layer-By-Layer Films: Bimetallic Alternate Layers with Accessible Mesopores for Enhanced Electrocatalysis. *J. Amer. Chem. Soc.* **2012**, *134* (26), 10819-10821.
- [52] Zhang, G.; Chenitz, R.; Lefèvre, M.; Sun, S.; Dodelet, J.-P. Is Iron Involved in the Lack of Stability of Fe/N/C Electrocatalysts Used to Reduce Oxygen at the Cathode of PEM Fuel Cells? *Nano Energy* **2016**, *29*, 111-125.
- [53] O'Hayre, R.; Barnett, D. M.; Prinz, F. B. The Triple Phase Boundary A Mathematical Model and Experimental Investigations for Fuel Cells. *J. Electrochem. Soc.* **2005**, *152* (2), A439-A444.

# Supporting Information

## **3D porous Fe/N/C spherical nanostructures as high-performance electrocatalysts for oxygen reduction in both alkaline and acidic media**

*Qiliang Wei,<sup>1</sup> Gaixia Zhang,<sup>\*1</sup> Xiaohua Yang,<sup>1</sup> Régis Chenitz,<sup>1</sup> Dustin Banham,<sup>2</sup> Lijun Yang,<sup>2</sup>  
Siyu Ye,<sup>2</sup> Shanna Knights,<sup>2</sup> Shuhui Sun<sup>\*1</sup>*

<sup>1</sup>Institut National de la Recherche Scientifique-Énergie Matériaux et Télécommunications, Varennes, Quebec, J3X 1S2, Canada.

<sup>2</sup>Ballard Power Systems Inc., Burnaby, British Columbia, V5J 5J8, Canada

Figures:

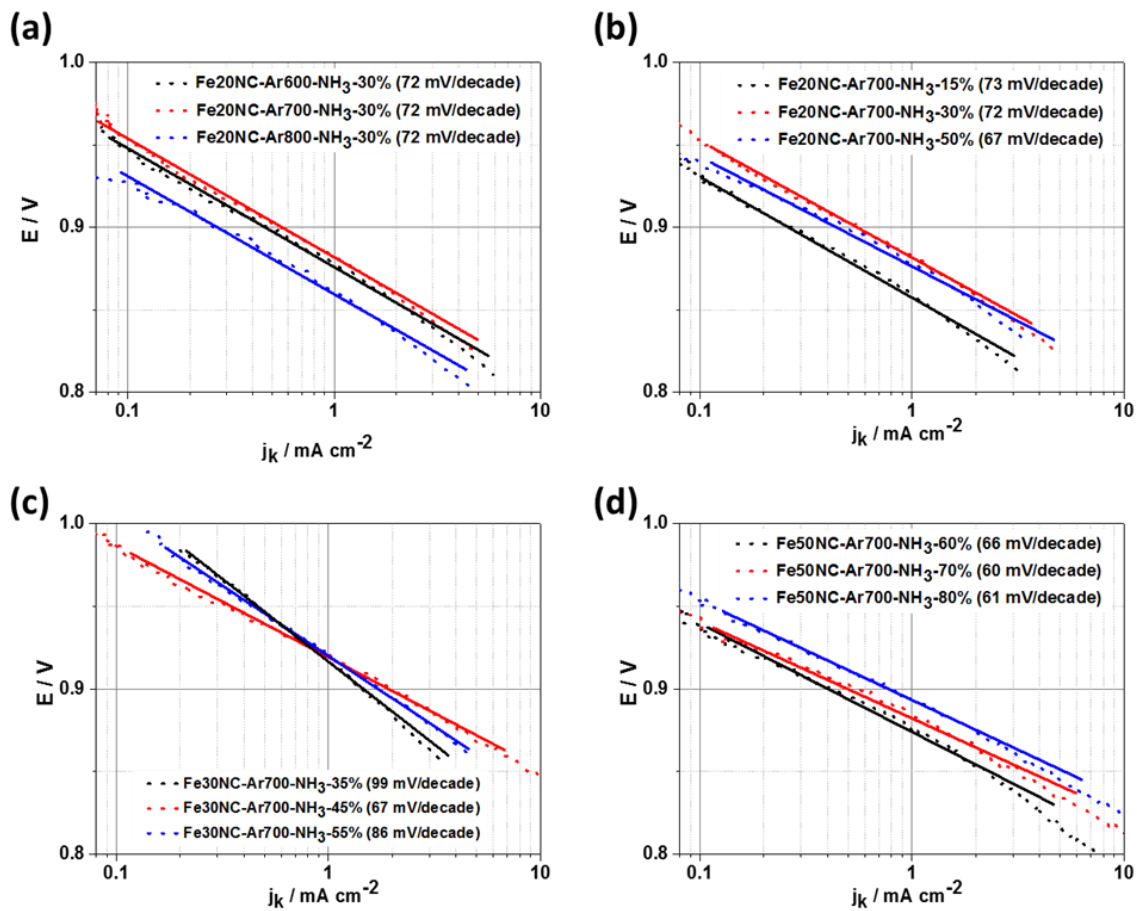


**Figure S1.** Tafel plots in O<sub>2</sub>-saturated 0.1 M KOH of (a) Fe20NC-ArT-NH<sub>3</sub>-30%, (b) Fe20NC-Ar700-NH<sub>3</sub>-y%, (c) Fe30NC-Ar700-NH<sub>3</sub>-y%, (d) Fe50NC-Ar700-NH<sub>3</sub>-y% (scan rate = 10 mV s<sup>-1</sup>, rotation rate = 1600 rpm).

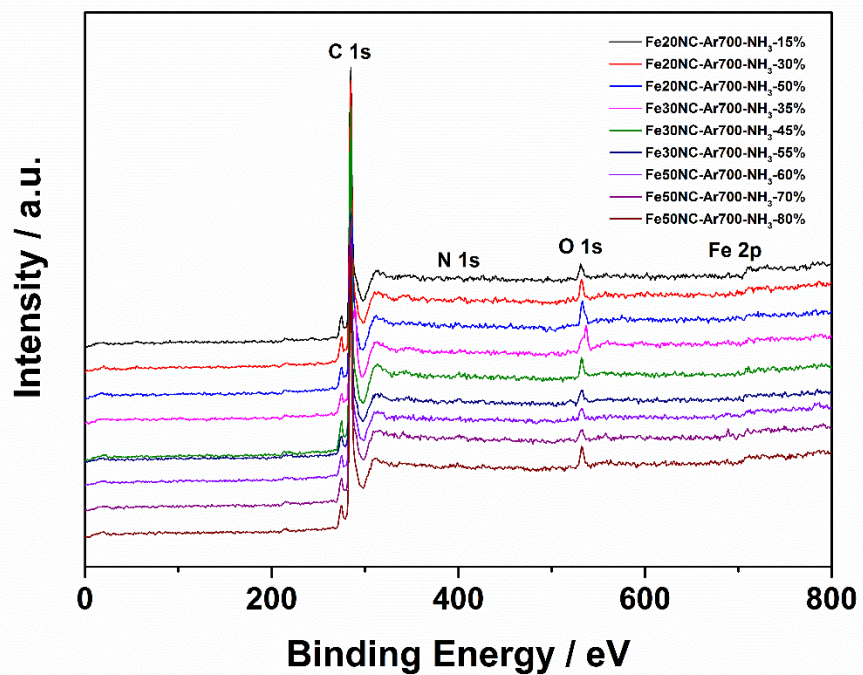


**Figure S2.** XPS spectrums of Fe<sub>x</sub>NC-Ar700-NH<sub>3</sub>-y% samples.

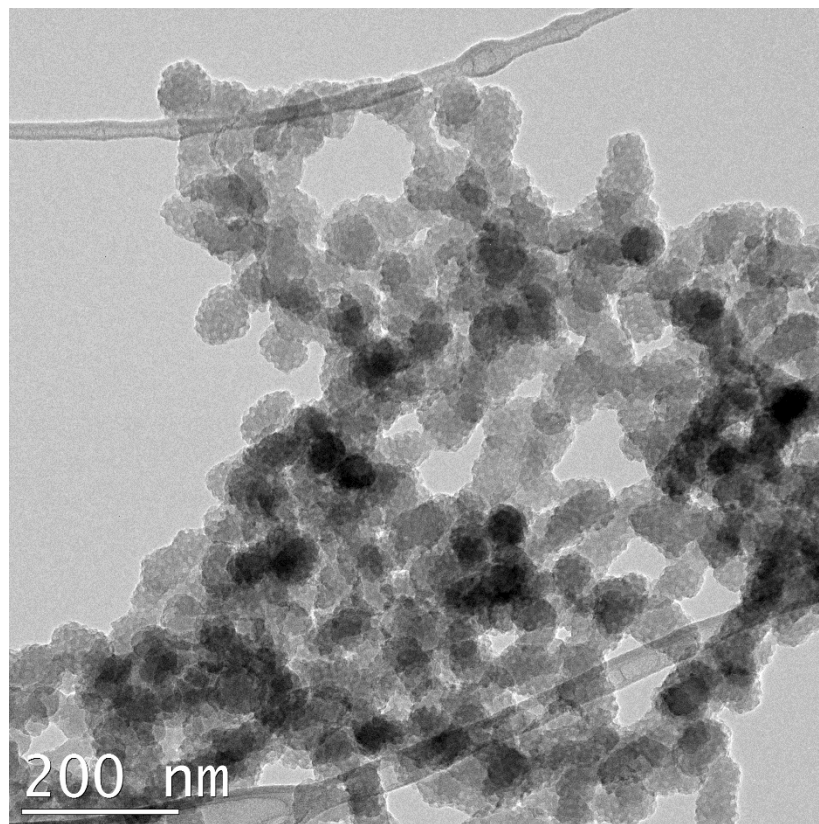


**Figure S3.** TEM images of spherical phenolic resol-F127 monomicelles.

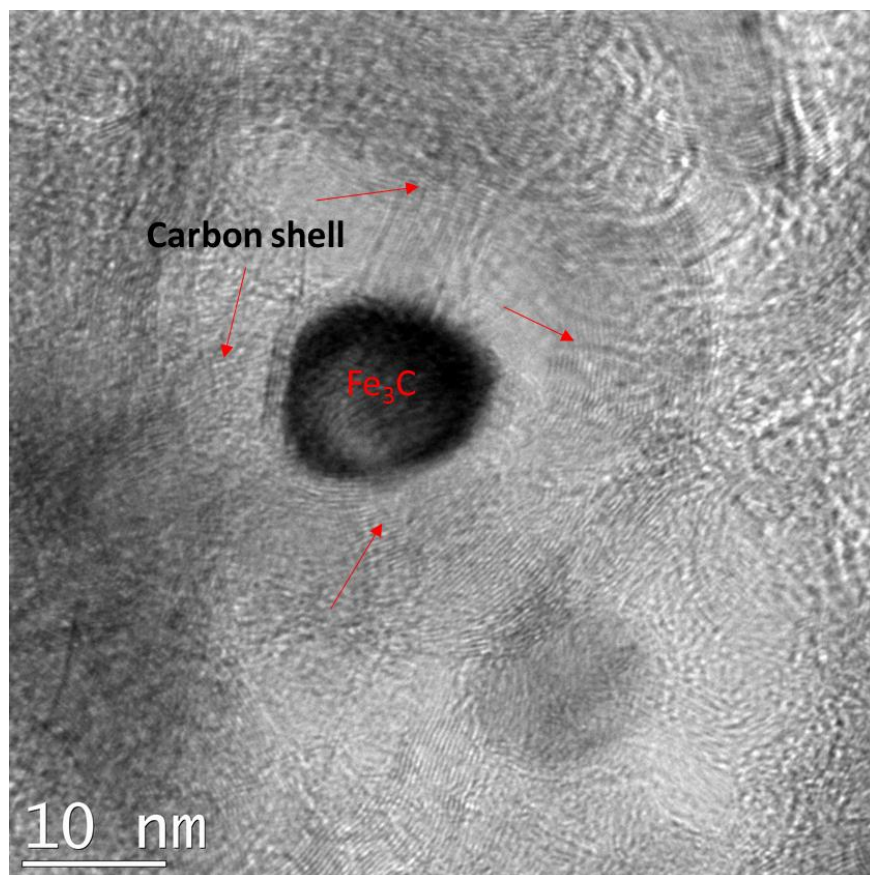


**Figure S4.** HRTEM images of black spot part of Fe<sub>30</sub>NC-Ar700-NH<sub>3</sub>-45%.

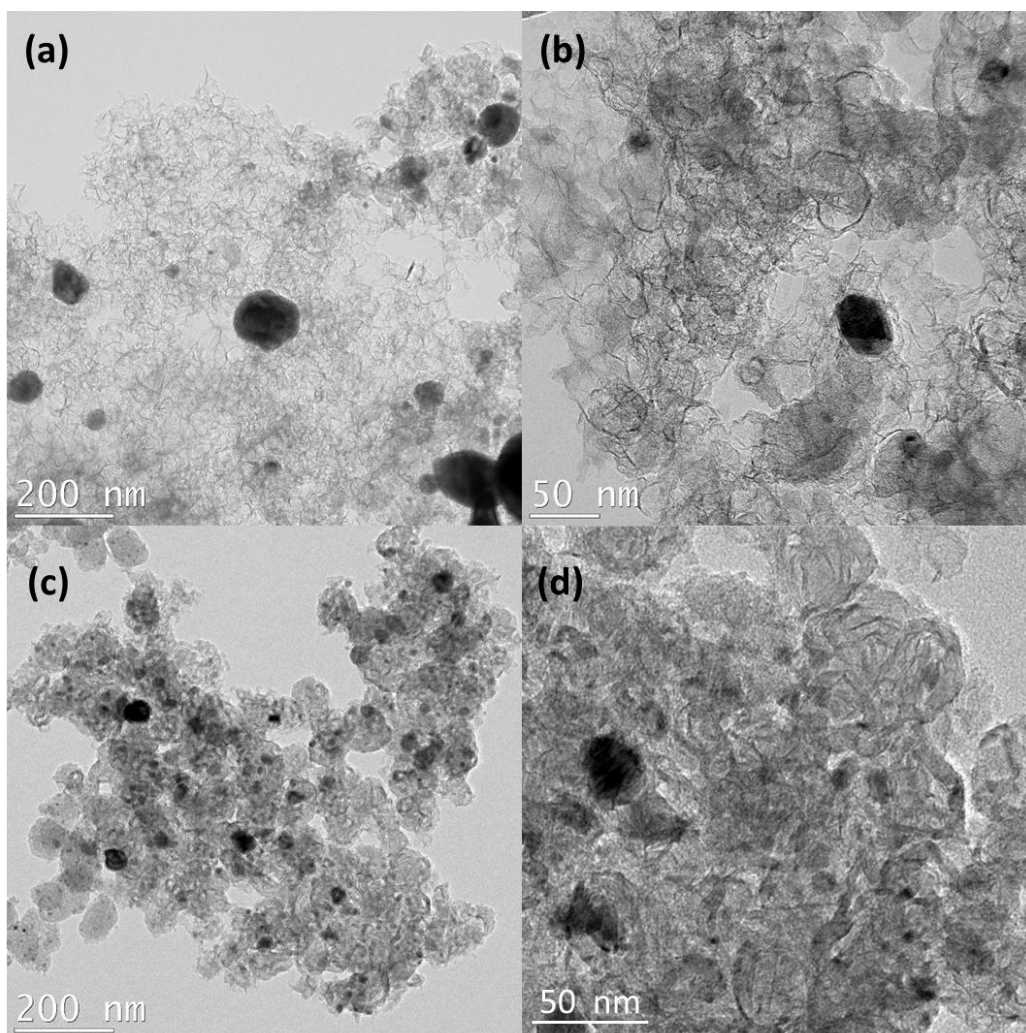


**Figure S5.** TEM images of (a-b) Fe<sub>20</sub>NC-Ar700-NH<sub>3</sub>-30% and (c-d) Fe<sub>50</sub>NC-Ar700-NH<sub>3</sub>-80%.

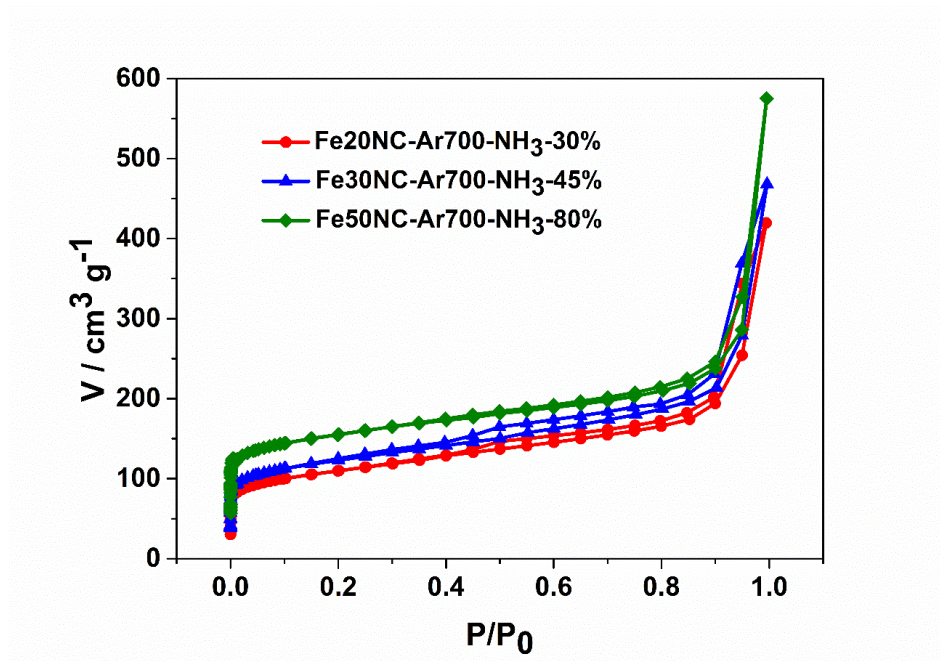


**Figure S6.** N<sub>2</sub> isothermal adsorption/desorption curves of Fe20NC-Ar700-NH<sub>3</sub>-30%, Fe30NC-Ar700-NH<sub>3</sub>-45%, Fe50NC-Ar700-NH<sub>3</sub>-80%.

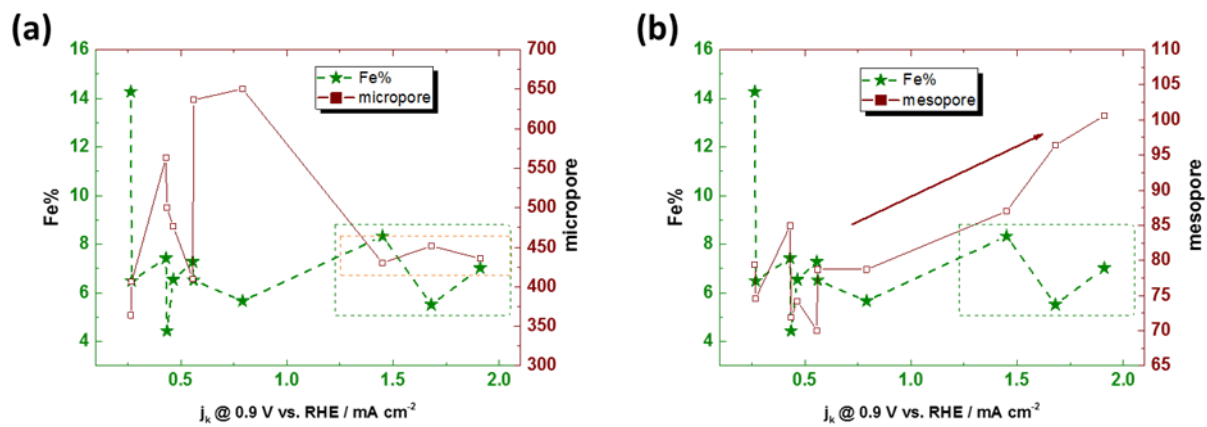


Figure S7. The relationship of micro-pore (a), mesopore (b) and Fe content with the current density  $j_k$ @0.9 V.

**Table S1** Experimental parameters.

Samples	Precursors			Ar pyrolysis			NH <sub>3</sub> pyrolysis	
	SPRMs (mg)	1,10-Phen (mg)	FeAc (mg)	T (°C)	Time (h)	Weight remaining	T (°C)	Weight remaining
<b>Fe20NC-Ar600-NH<sub>3</sub>- 30%</b>	700	136	20	450 + 600	2 + 1	32.7%	950	33.3%
<b>Fe20NC-Ar700-NH<sub>3</sub>- 30%</b>	700	136	20	450 + 700	2 + 1	31.8%	950	30.8%
<b>Fe20NC-Ar800-NH<sub>3</sub>- 30%</b>	700	136	20	450 + 800	2 + 1	30.5%	950	36%
<b>Fe20NC-Ar700-NH<sub>3</sub>- 15%</b>	700	136	20	450 + 700	2 + 1	31.8%	950	15.7%
<b>Fe20NC-Ar700-NH<sub>3</sub>- 50%</b>	700	136	20	450 + 700	2 + 1		950	50.6%
<b>Fe30NC-Ar700-NH<sub>3</sub>- 35%</b>	700	136	30	450 + 700	2 + 1	33.3%	950	38.1%
<b>Fe30NC-Ar700-NH<sub>3</sub>- 45%</b>	700	136	30	450 + 700	2 + 1		950	45.2%
<b>Fe30NC-Ar700-NH<sub>3</sub>- 55%</b>	700	136	30	450 + 700	2 + 1		950	57.6%
<b>Fe50NC-Ar700-NH<sub>3</sub>- 60%</b>	700	136	50	450 + 700	2 + 1	36.5%	950	63.6%
<b>Fe50NC-Ar700-NH<sub>3</sub>- 70%</b>	700	136	50	450 + 700	2 + 1		950	72.3%
<b>Fe50NC-Ar700-NH<sub>3</sub>- 80%</b>	700	136	50	450 + 700	2 + 1		950	83.3%

**Table S2.** The relationship of the catalytic activity and the Fe, N content (wt%):

	<b>Samples</b>	<b>Half-wave potential</b>	<b>J<sub>k</sub> @0.9 V vs. RHE (mA cm<sup>-2</sup>)</b>	<b>Fe content (Fe<sub>cal</sub>, calculated from the weight loss during pyrolysis)</b>	<b>Fe content (Fe<sub>xps</sub>, calculated from XPS)</b>
<b>Group 1 (Fe20)</b>	Fe20NC-Ar600-NH <sub>3</sub> -30%	0.81 V	0.465	6.54%	1.32%
	Fe20NC-Ar700-NH <sub>3</sub> -30%	0.82 V	0.556	7.28%	2.13%
	Fe20NC-Ar800-NH <sub>3</sub> -30%	0.80 V	0.268	6.49%	1.05%
	Fe20NC-Ar700-NH <sub>3</sub> -15%	0.79 V	0.264	14.27%	2.57%
	Fe20NC-Ar700-NH <sub>3</sub> -50%	0.81 V	0.435	4.43%	1.22%
<b>Group 2 (Fe30)</b>	Fe30NC-Ar700-NH <sub>3</sub> -35%	0.835 V	1.45	8.33%	1.41%
	Fe30NC-Ar700-NH <sub>3</sub> -45%	0.87 V	1.91	7.02%	1.35%
	Fe30NC-Ar700-NH <sub>3</sub> -55%	0.855 V	1.68	5.51%	1.23%
<b>Group 3 (Fe50)</b>	Fe50NC-Ar700-NH <sub>3</sub> -60%	0.82 V	0.431	7.42%	2.13%
	Fe50NC-Ar700-NH <sub>3</sub> -70%	0.84 V	0.560	6.52%	1.94%
	Fe50NC-Ar700-NH <sub>3</sub> -80%	0.85 V	0.789	5.66%	1.78%

**Table S3.** N<sub>2</sub> adsorption/desorption analysis of selected samples

	Samples	N <sub>2</sub> adsorption/desorption			Fe content (Fe <sub>cal</sub> ) (%)	Half-wave potential (V)
		Surface area (m <sup>2</sup> /g)	surface area of micropores (m <sup>2</sup> /g)	surface area of mesopores (m <sup>2</sup> /g)		
	Fe20NC-Ar600- NH <sub>3</sub> -30%	550.3	476.1	74.2	6.54	0.81
	Fe20NC-Ar700- NH <sub>3</sub> -15%	443.4	364.0	79.4	14.27	0.79
<b>Group 1 (Fe20)</b>	Fe20NC-Ar700- NH <sub>3</sub> -30%	480.0	410.0	70.0	7.28	0.82
	Fe20NC-Ar700- NH <sub>3</sub> -50%	572.2	500.3	71.9	4.43	0.81
	Fe20NC-Ar800- NH <sub>3</sub> -30%	480.6	406.0	74.6	14.27	0.80
	Fe30NC-Ar700- NH <sub>3</sub> -35%	517.2	430.2	87	8.33	0.835
<b>Group 2 (Fe30)</b>	Fe30NC-Ar700- NH <sub>3</sub> -45%	536.3	435.7	100.6	7.02	0.87
	Fe30NC-Ar700- NH <sub>3</sub> -55%	547.9	451.5	96.4	5.51	0.855
	Fe50NC-Ar-700- NH <sub>3</sub> -60%	648.1	563.2	84.9	7.42	0.82
<b>Group 3 (Fe50)</b>	Fe50NC-Ar-700- NH <sub>3</sub> -70%	715.1	636.4	78.7	6.52	0.84
	Fe50NC-Ar-700- NH <sub>3</sub> -80%	729.1	650.4	78.7	5.66	0.85

### **3.2 Litchi-like porous Fe/N/C spheres with atomically dispersed FeN<sub>x</sub> promoted by sulfur as highly efficient oxygen electrocatalysts for Zn–air batteries**

Qiliang Wei, Gaixia Zhang, Xiaohua Yang, Yanqing Fu, Guanhua Yang, Ning Chen, Weifeng Chen, Shuhui Sun

*J. Mater. Chem. A*, 2018, **6**, 4605–4610.

The fabrication of highly active, stable and porous carbon-based electrocatalysts is essential for high-performance metal-air batteries. In this section, we introduce a new and simple route involving sulfur (S) as a “promoter” to achieve a litchi-like porous Fe/N/C catalyst with abundant FeN<sub>x</sub> species. The obtained electrocatalyst exhibits large surface area with a high pore volume, and shows high activity for both ORR and OER. Moreover, a Zn–air battery device adopting this S-promoted litchi-like Fe/N/C catalyst shows excellent power density (double of the untreated counterpart) and good stability.

*Contributions:* I performed all the experimental synthesis, the electro-chemical measurements, and all characterizations except the TEM measurements that have been done by technicians. I conducted the data analysis and the interpretation of results, as well as the manuscript writing, with the help of co-authors.

# Litchi-like porous Fe/N/C spheres with atomically dispersed FeN<sub>x</sub> promoted by sulfur as high-efficient oxygen electrocatalysts for Zn–air batteries

*Qiliang Wei,<sup>1</sup> Gaixia Zhang,<sup>1,\*</sup> Xiaohua Yang,<sup>1</sup> Yanqing Fu,<sup>1</sup> Guanhua Yang,<sup>1</sup> Ning Chen,<sup>2</sup>  
Weifeng Chen,<sup>2</sup> Shuhui Sun<sup>1,\*</sup>*

<sup>1</sup>Énergie, Matériaux et Télécommunications, Institut National de la Recherche Scientifique (INRS), 1650 Boul. Lionel-Boulet, Varennes, Quebec J3X 1S2, Canada

<sup>2</sup>Canadian Light Source (CLS), 44 Innovation Boulevard, Saskatoon, SK, S7N 2V3, Canada.

**Abstract:** The fabrication of carbon-based electrocatalysts that is highly active and stable as well with plenty of pores for the mass transport is essential for high-performance metal-air batteries. Herein, a new simple route involving sulfur (S) as a “promoter” was developed to achieve a litchi-like porous Fe/N/C catalyst with abundant FeN<sub>x</sub> species. The obtained electrocatalyst exhibits a large surface area with a high pore volume, and shows high activity for oxygen reduction. Moreover, a Zn–air battery device adopting this S-promoted litchi-like Fe/N/C catalyst shows superior power density (double of the untreated counterpart).

## 1. Introduction

Ever-increasing energy demands and depleting fossil fuel resources require the exploration of sustainable and renewable energy conversion and storage systems (ECSS) that are reliable, low-cost and environmentally friendly.<sup>[1]</sup> Among various ECSS, metal-air batteries with intrinsic high energy density, have been widely considered as excellent candidates for energy storage systems.<sup>[2-6]</sup> In metal-air batteries, zinc-air battery with the merits of low-cost and abundance is regarded as one of the most economically feasible battery technologies for smart-grid energy storage.<sup>[7-9]</sup> However, the feasibility of large-scale commercialization has so far been plagued by the sluggish and inefficient reactions involved in a Zn-air battery during working process. Oxygen reduction reaction (ORR) is particularly more difficult to carry out and more responsible

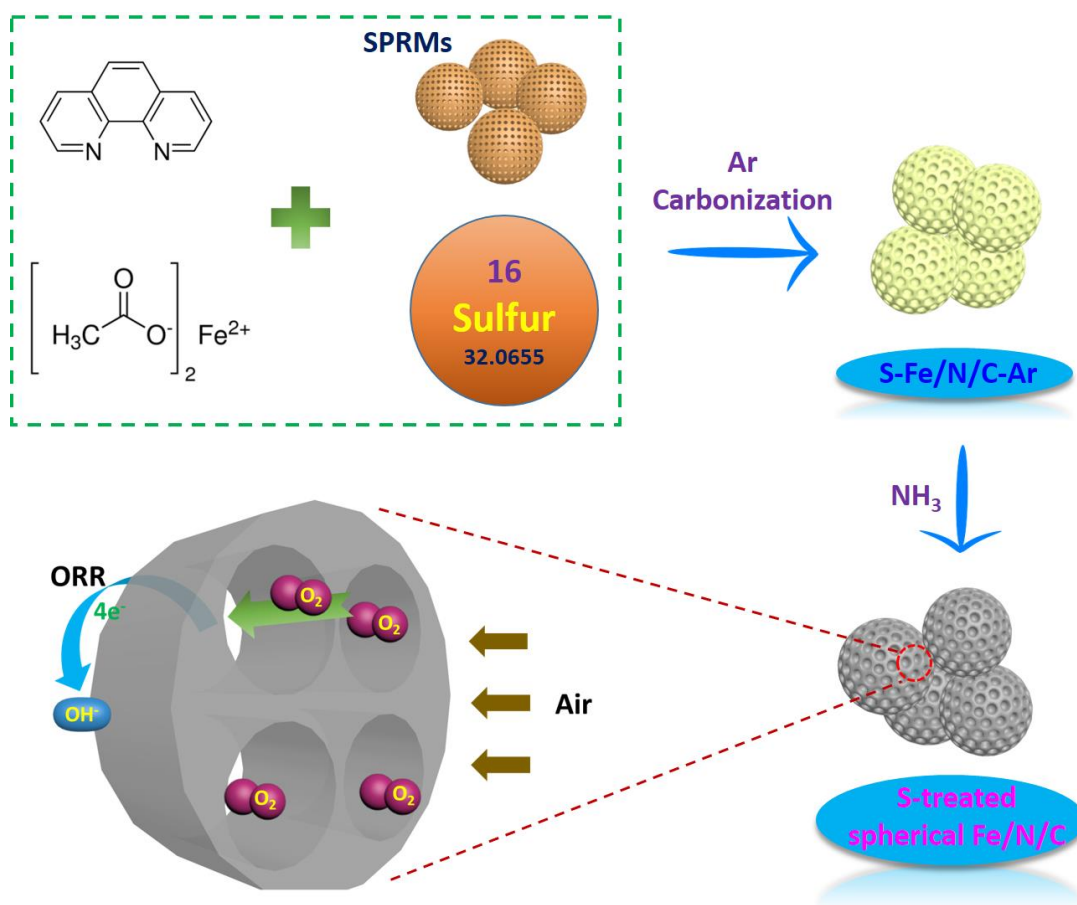
for the performance of metal-air batteries.<sup>[10-12]</sup> Currently, platinum (Pt) and Pt-based alloys have proven to be the most efficient catalysts for ORR, while suffering the limited supply of Pt in nature, prohibitive cost and low stability at the same time. Therefore, it is highly critical to develop non-precious metal catalyst (NPMC) alternatives to Pt-based catalysts. Among which, the materials containing transition metal–nitrogen coordination sites (M-N<sub>x</sub>, M = Fe, Co, etc.) have been considered to be the most promising substitutes.<sup>[13-18]</sup> Generally, two decisive elements need to be considered when designing an electrocatalysts for ORR in ECSS devices: one is the intrinsic activity of the catalyst towards ORR, and the second crucial factor is the porous structure.<sup>[19]</sup> It is widely considered that active sites exist in the micro-pores, and efficient mass transportation lies largely on the meso/macro-pores.<sup>20,21</sup> In this regard, so far Fe/N/C based catalysts, exhibiting superior ORR performance than the other NPMCs, have received intensive exploration.<sup>[13,14,16,22-25]</sup> Especially, a breakthrough for ORR NPMCs has been made by the Dodelet group, with catalyst activity approaching that of Pt for a PEMFC.<sup>[14]</sup> In parallel with efforts to enhance the ORR activity, it is also of great interest to improve the porous structure to further increase the mass/electron transport, especially in “triple phase boundaries (TPB)” where electrolyte, gas, and electrically connected catalyst regions contact, when applied in a single full-cell. To obtain a well-defined high surface area porous structure, great achievements have been made mostly by a hard-template method in the literature reports.<sup>[15,19,25-32]</sup> However, template removal would cause time-consuming and cost-efficiency problems in the post-treatment. Therefore, new strategies that enable turning carbon architectures and featuring well-defined porosity with fully exposed active sites are still urgently needed.

Herein, we developed a simple and straightforward method of preparing spherical litchi-like porous Fe/N/C structure by employing sulfur as a “promoter”, because S reacts with ammonia during the pyrolysis ( $3S + 2NH_3 = 3H_2S + N_2$ ), as a result, only Fe/N/C was obtained after the pyrolysis. Remarkably, sulfur not only significantly promotes the increase of the surface area, but also much better protects the integrity of the Fe/N/C spheres and suppresses the formation of large Fe-based particles. Consequently, these S-treated litchi-like porous Fe/N/C spheres possess large surface area of 982.1 m<sup>2</sup> g<sup>-1</sup>, and a high pore volume of 1.01 cc g<sup>-1</sup>. In this case, active sites are able to ‘breathe’ well inside the catalyst during charge–discharge without deterioration of the electrochemical properties. These unique structural features lead to a high activity with a half wave potential of 0.88 V (vs RHE) for ORR. Furthermore, when used to construct the air

cathode for zinc–air batteries, the S-treated Fe/N/C sample displays double of the untreated Fe/N/C in terms of peak power densities, and even outperforms the state-of-the-art Pt/C catalyst (with the same loading).

## 2. Results and discussion

The fabrication of the litchi-like S-treated Fe/N/C spheres can be illustrated in Scheme 1. After the Ar carbonization process, S was doped into the Fe/N/C spheres. During the stage of ammonia pyrolysis, S would react with ammonia as:  $3\text{S} + 2\text{NH}_3 = 3\text{H}_2\text{S} + \text{N}_2$ , as a result, only Fe, N, and C elements were obtained after the pyrolysis. However, during the first Ar pyrolysis stage, the addition of S is expected to (i) be doped into the carbon framework to increase the surface area,<sup>[33]</sup> (ii) help dispersing the Fe-N<sub>x</sub> active sites more evenly, (iii) buffer the carbon-based spheres from collapsing.



**Scheme 1.** Illustration of the formation of the litchi-like highly porous S-treated Fe/N/C catalyst.

The morphology of the Fe/N/C samples was characterized by TEM. Figure 1a-c show representative TEM images of the Fe/N/C without the S treatment, which possess irregular spherical morphology with certain amount of unavoidable large Fe particles, indicating its heterogeneity. While the S-treated Fe/N/C sample appears as a well-developed 3D litchi-like architecture with an average size of 100 nm (Figure 1d-f), this litchi-like 3D structure not only has many interpenetrative holes leading into large spaces inside the architectures, but also helps the whole carbon framework keeping a perfect 3D spherical shape and uniformly dispersed Fe-N<sub>x</sub> active sites to a large extent (Figure S3 and Figure 1d-f). From the high-angle annular dark field (HAADF) mode TEM image (Figure S6), a few nanoparticles unambiguously appear, which should correspond to the Fe. The elements were further identified and mapped out by electron energy loss spectroscopy (EELS) analysis. Due to the small amount of material and the low contents of the Fe and N, weak signals of Fe and N were observed. However, these EELS mapping images can still demonstrate the uniform distribution of C, N and Fe elements. This unique and well-defined architecture can be ascribed to a multifactor functioning formed by (i) the doping of S during the Ar carbonization increases the surface area, (ii) the volatilization of excess S during the whole pyrolysis process, (iii) introducing N dopants while simultaneously graphitizing the carbon frameworks under the activation of NH<sub>3</sub>, and (iv) the reaction between S and NH<sub>3</sub> during the ammonia pyrolysis. Such a hierarchical porous structure are expected to provide more active sites and a number of interpenetrating channels that are able to “breathe” well inside the catalyst during the electrochemical reactions.

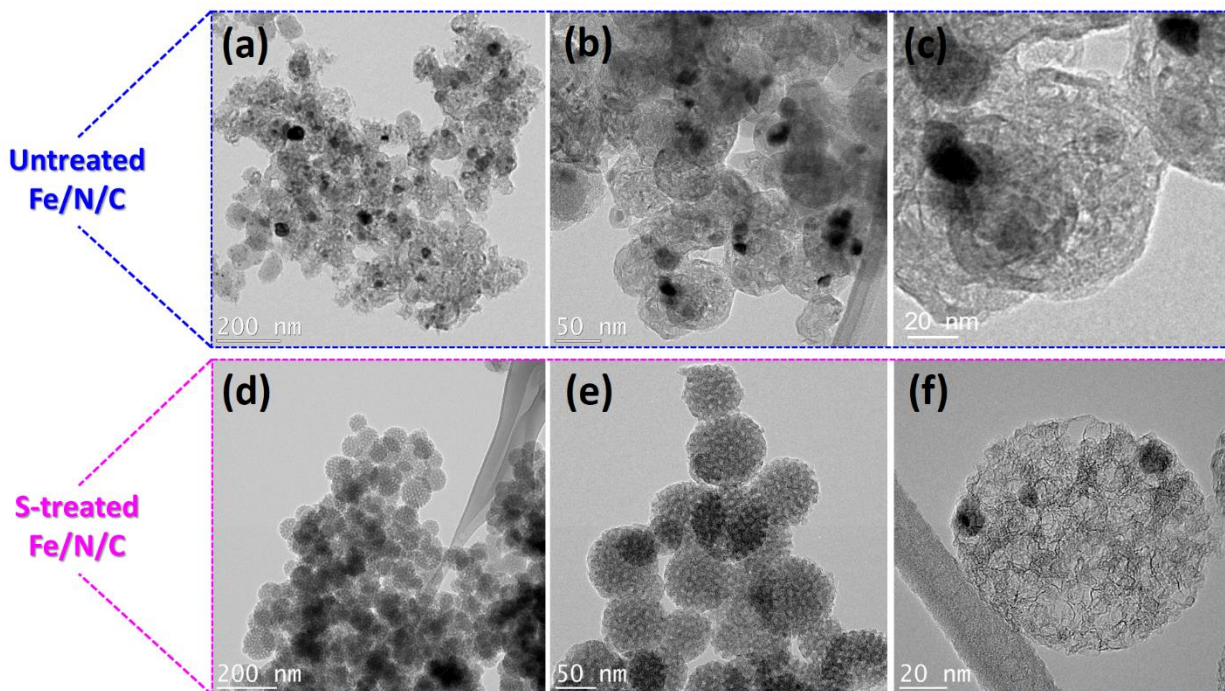


**Figure 1.** TEM images of untreated Fe/N/C (a–c) and S-treated Fe/N/C (d–f) catalysts at different magnifications.

$N_2$  adsorption-desorption tests were performed to evaluate the textural properties of the Fe/N/C samples (Figure 2 and Figure S2). Both of them present a sharp uptake at low pressure and a smooth plateau at middle-to-high pressure, which is characteristic of micropore-dominated materials. All of the S-treated Fe/N/C samples show a much higher surface area than the untreated one, which is benefited by the addition of S, and consistent with the TEM observations. By comparison, we can find an optimal ratio of SPRMs/S = 1 to obtain the sample with the largest surface area ( $982.1 \text{ m}^2 \text{ g}^{-1}$ ) and pore volume ( $1.01 \text{ cc g}^{-1}$ ) (Figure S2 and Table S1). Notably, the increased surface area of the S-treated Fe/N/C originates from both micropore (from  $436 \text{ m}^2 \text{ g}^{-1}$  to  $810 \text{ m}^2 \text{ g}^{-1}$ ) and mesopore (from  $101 \text{ m}^2 \text{ g}^{-1}$  to  $172 \text{ m}^2 \text{ g}^{-1}$ ). The pore size distribution curves indicate that the optimized litchi-like S-treated Fe/N/C spheres possess quite a wide range of pore sizes centred at 0.6, 1.5, 3.0, 8.1, 11.5, 15.4 and 20 nm, respectively (Figure 2b-c), further confirming the hierarchical porous structure in which micropores were incorporated into the walls of well-defined mesopores.

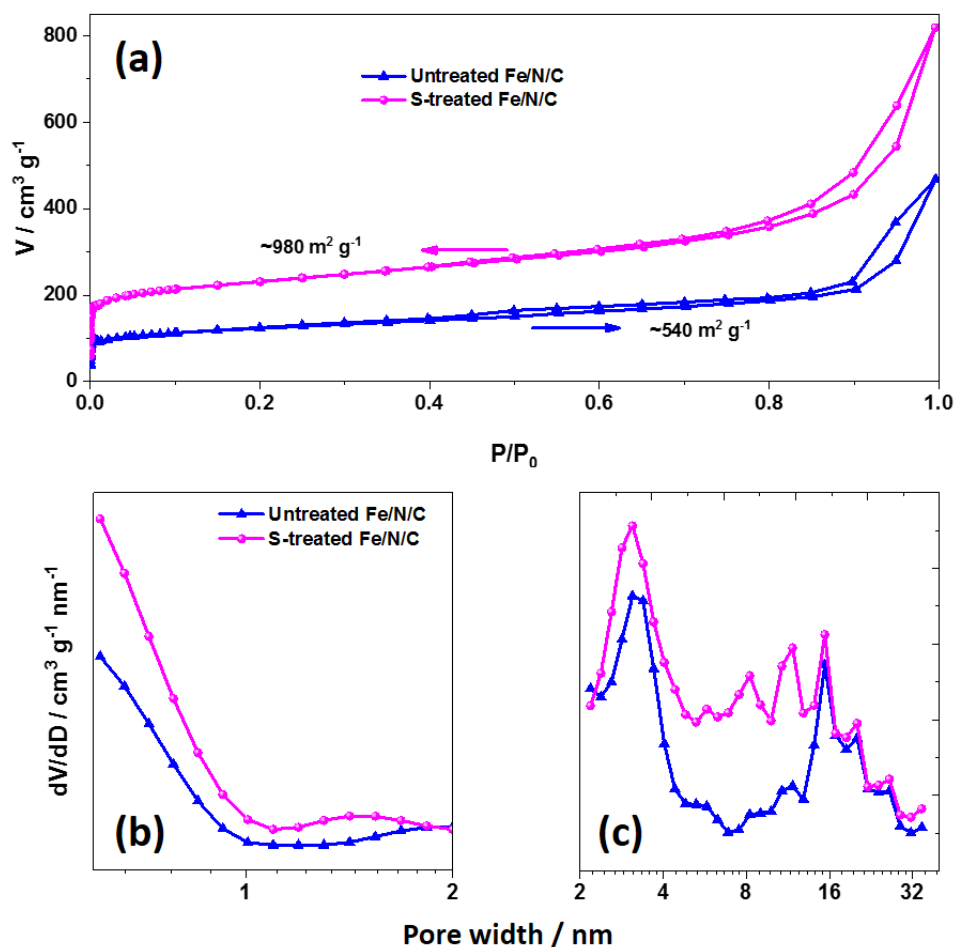


**Figure 2.** (a)  $N_2$  isothermal adsorption/desorption curves of untreated Fe/N/C and S-treated Fe/N/C catalysts. (b and c) The corresponding pore size distribution curves obtained from the adsorption branches.

XPS measurements were performed to elucidate the changes of the states of elements and chemical speciation for untreated Fe/N/C and S-treated Fe/N/C catalysts. For both samples, it shows only the presence of C, N, O and Fe elements. However, if we analyse peaks for these two samples before and after the ammonia pyrolysis (Figure 3a, b), we can find that (i) the oxygen peaks decrease a lot for both samples after the ammonia pyrolysis, due to the reactions between the oxygen-containing groups and  $NH_3$ , (ii) there is S existing for the S-treated Fe/N/C sample after the carbonization under Ar, indicating that part of the S was doped inside the carbon framework, from Figure S12a, the doping level of S is calculated as around 2% from the XPS spectrum, it consists of  $2p_{3/2}$  and  $2p_{1/2}$  components with a ratio of 2:1, corresponding to the thiophenic sulfur (-C-S-C-) incorporated in the graphitic framework, minor contributions of

oxidized sulfur species were indicated as component peaks around 168 eV,<sup>[34]</sup> (iii) after the ammonia pyrolysis, the S peaks disappear (not detectable by XPS as shown Figure 3b and S12b), indicating that NH<sub>3</sub> is playing multifunctional roles, i.e., further activation of Fe/N/C, expanding the surface area, etching off carbon, and removal of S species. As a result, these obtained S-treated Fe/N/C spheres show greatly improved pore volumes and surface area, consisting with the BET analysis.

To unravel the local and electronic structure of Fe/N/C samples, X-ray absorption near edge structure (XANES) and extended X-ray absorption fine structure (EXAFS) were analysed. As shown in Figure S7, a semicircle electrode was put on the sample holder for XAS measurement, the 2D fluorescence mapping image of untreated Fe/N/C sample has a hot spot, indicated in “red” area (Figure S7b), indicating much stronger Fe signal there due to the Fe agglomerates, on the contrary, more homogeneous Fe signals were demonstrated for the S-treated Fe/N/C sample (Figure S7c). As indicated by the Fe K-edge XANES in Figure 3c, the pre-edge peak (peak P) is caused by the forbidden 1s → 3d transition, its intensity in the XANES spectra could reflect the distortion degree from the perfect octahedral symmetry,<sup>[35]</sup> a stronger peak indicates a higher degree of Fe local structure distortion; in addition, the intensity ratio of the peak A to peak B (Figure 3c) is also attributed to the enhanced distortion of the Fe-N<sub>4</sub> local structure.<sup>[36]</sup> From the result shown in Figure 3c, a stronger peak P and higher intensity ratio of peak A/peak B are observed in S-treated Fe/N/C, so it can be deduced that due to the function of S, the Fe-N<sub>x</sub> active sites in S-treated Fe/N/C has a higher degree of distortion. The experimental Fourier transforms (FT) at the Fe K-edge of the EXAFS data of the samples were further analyzed and displayed in Figure 3d. The signal at ~1.6 Å in S-treated Fe/N/C should be attributed to the Fe–N scattering due to a nitrogen shell surrounding Fe, corroborating the existence of the Fe-N<sub>x</sub> configurations in the graphitic carbon framework,<sup>[37-39]</sup> interestingly, without S treatment, the dominant signal in untreated Fe/N/C is characterized instead by a peak at around 2.0-2.2 Å, which could be assigned to metallic Fe and Fe<sub>3</sub>C,<sup>[40]</sup> this indicates that with the existence of S, the elements of Fe, N, C tend to form Fe-N<sub>x</sub>-coordinated active sites, while, without S, they are mainly inclined to form Fe/Fe<sub>x</sub>C nanoparticles, consisting well with the TEM observation.

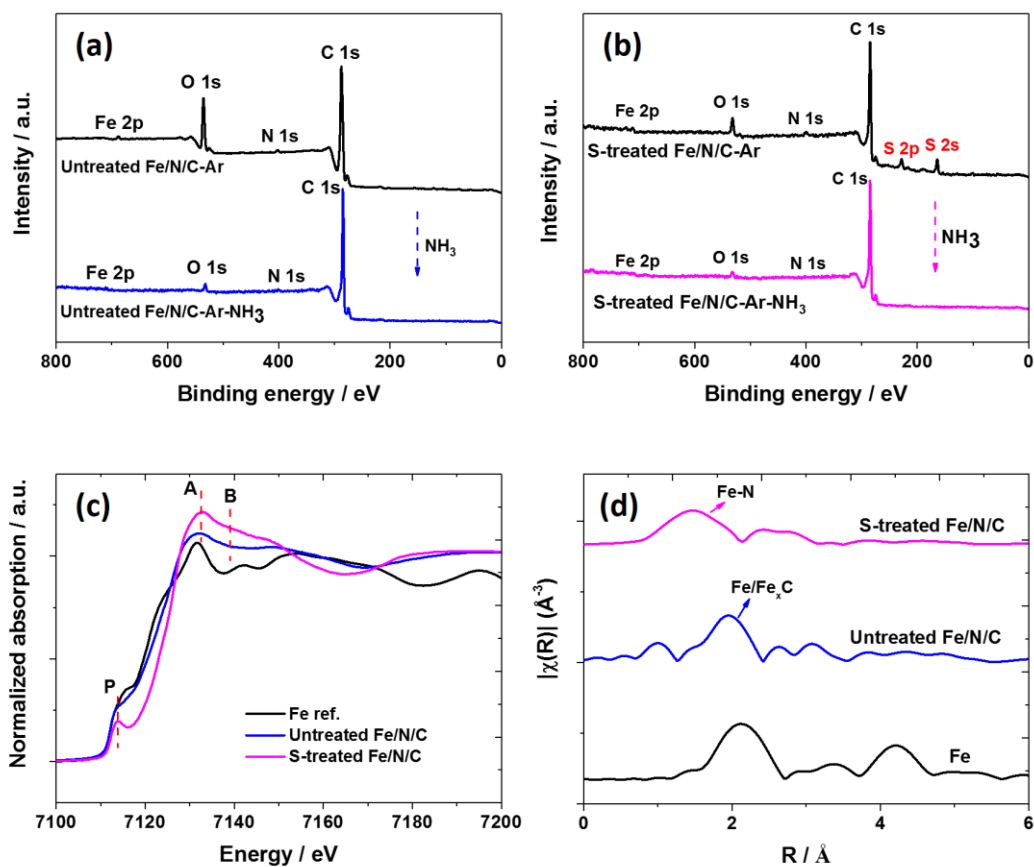


**Figure 3.** (a) XPS spectrum of untreated Fe/N/C (before and after ammonia pyrolysis) and (b) S-treated Fe/N/C catalysts (before and after ammonia pyrolysis). (c) Normalized Fe K-edge XANES spectra and (d) the magnitude of Fourier-transformed EXAFS oscillation  $k^2\chi(k)$  spectra of untreated Fe/N/C, S-treated Fe/N/C, and reference Fe foil.

The ORR activity of S-treated Fe/N/C and untreated Fe/N/C was first accessed by cyclic voltammetry (CV). In N<sub>2</sub>-saturated 0.1 M KOH, both Fe/N/C samples exhibited a featureless CV curve, while S-treated Fe/N/C shows a much larger capacitance due to the much higher surface area (Figure 4a). Figure 4b and Figure S1 show the typical RRDE voltammograms of untreated Fe/N/C, S-treated Fe/N/C and commercial Pt/C catalysts in O<sub>2</sub>-saturated 0.1 M KOH solution. Interestingly, both untreated Fe/N/C and S-treated Fe/N/C have higher activity than commercial Pt/C, and S-treatment could further improve the activity of Fe/N/C catalyst due to the increased surface area and active sites. For the S-treated Fe/N/C samples with different SPRMs/S ratio, there is very little difference for the half-wave potential, while the optimal one (SPRMs/S = 1) has larger limiting current (Figure S1). The current density at 0.8 V of untreated Fe/N/C, optimal S-treated Fe/N/C and commercial Pt/C are 4.4 mA cm<sup>-2</sup>, 4.7 mA cm<sup>-2</sup>, and 3.2 mA cm<sup>-2</sup>,

respectively (the detailed values of on-set potential and half-wave potential is shown in Table S3). The calculated  $\text{H}_2\text{O}_2$  yield according to the RRDE test results of the S-treated Fe/N/C catalyst remained below untreated Fe/N/C samples at all potentials in 0.1 M KOH (Figure 4c). This negligible  $\text{H}_2\text{O}_2$  yield clearly confirms that the S-treated Fe/N/C has extremely high ORR catalytic efficiency. Moreover, the electron transfer number during ORR is close to 4 in the entire potential region, indicating direct  $4e^-$  selectivity (Figure S8). The durability of the S-treated Fe/N/C and commercial Pt/C catalysts in a half-cell condition was evaluated by chronoamperometric measurements at 0.7 V (vs. RHE) in  $\text{O}_2$ -saturated 0.1 M KOH solution with a rotation speed of 1600 rpm. Figure 4d shows that the current density of the litchi-like S-treated Fe/N/C catalyst remains  $\sim 96\%$  after 500 min, which is apparently higher than that of the untreated Fe/N/C ( $\sim 90\%$ ) and commercial Pt/C catalyst ( $\sim 88\%$ ) in the same condition, suggesting its excellent durability of the litchi-like porous S-treated Fe/N/C spheres.

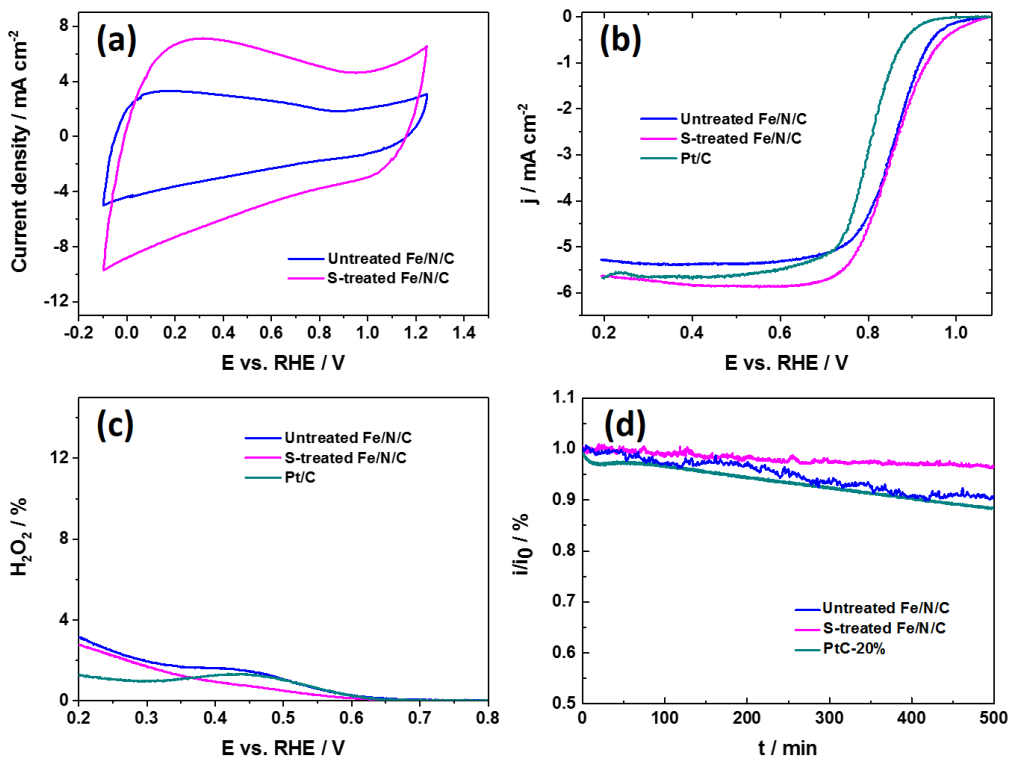


**Figure 4.** (a) CV curves in  $\text{N}_2$ -saturated 0.1 M KOH at a scan rate of  $50 \text{ mV s}^{-1}$ . (b) RRDE voltammograms of untreated Fe/N/C, S-treated Fe/N/C and Pt/C in  $\text{O}_2$ -saturated 0.1 M KOH at a scan rate of  $10 \text{ mV s}^{-1}$ , rotation rate = 1600 rpm. (c)  $\text{H}_2\text{O}_2$  yield calculated from the RRDE voltammograms in (b). (d) Chronoamperometric responses (at 0.7 V vs. the RHE) of untreated Fe/N/C, S-treated Fe/N/C, and commercial Pt/C catalysts in  $\text{O}_2$ -saturated 0.1 M KOH.

To explore the potential use of these litchi-like porous S-treated Fe/N/C spheres for real energy devices, a home-made Zn-air battery was assembled using untreated Fe/N/C, S-treated Fe/N/C and Pt/C as the air cathode and a polished zinc plate as the anode filled with the (6 M KOH + 0.2 M Zn(Ac)<sub>2</sub>) electrolyte (Figure 5a). Interestingly, a lower charge-discharge voltage gap was observed for the S-treated Fe/N/C (0.66 V) than that of the untreated Fe/N/C (0.76 V) and Pt/C (0.97 V) (Figure 5b), this suggests that the S-treated Fe/N/C sample also has decent oxygen evolution reaction (OER) activity (Figure S9), thus the improved efficiency and rechargeability of the Zn-air battery constructed by S-treated Fe/N/C, are most probably benefiting from its excellent ORR/OER activity and perfectly 3D litchi-like spherical structure with hierarchical micro/mesopores. Figure 5c depicted the polarization curves and corresponding power density plots of a single Zn-air battery constructed by untreated Fe/N/C, S-treated Fe/N/C and Pt/C, at the same condition (the power density of S-treated Fe/N/C with different SPRMs/S ratio was shown in Figure S10). Impressively, the litchi-like S-treated Fe/N/C sample displays >1.5 times of the untreated Fe/N/C in terms of current density at 1.0 V and almost double of the peak power densities (~250 mW cm<sup>-2</sup> vs. ~125 mW cm<sup>-2</sup>), and even outperforms the commercial Pt/C catalyst (~220 mW cm<sup>-2</sup>) with the same loading (Figure 5c). Considering the similar ORR activity of the untreated Fe/N/C ( $E_{1/2}=0.87$  V) and S-treated Fe/N/C ( $E_{1/2}=0.88$  V), the critical role of hierarchical porous structure to the single-cell devices is highlighted. With respect to the previously reported NPMCs, the Zn-air battery made of the litchi-like S-treated Fe/N/C represents one of the best (see comparison in Table S2). At different discharge current densities, the S-treated Fe/N/C sample could also keep very stable close voltages (Figure S11), indicating its excellent rate performance. Moreover, long-term cycling tests show that there is only a slight shift of the discharge plateau (from ~1.2 V to 1.1 V) over 120 cycles (Figure 5d), indicating the excellent stability of the S-treated Fe/N/C catalyst in Zn-air batteries. On the contrary, an obvious voltage fading was observed after around 65 cycles for commercial Pt/C catalyst. These results reveal that the as-obtained S-treated Fe/N/C catalyst has potential applications in the field of rechargeable metal-air batteries.

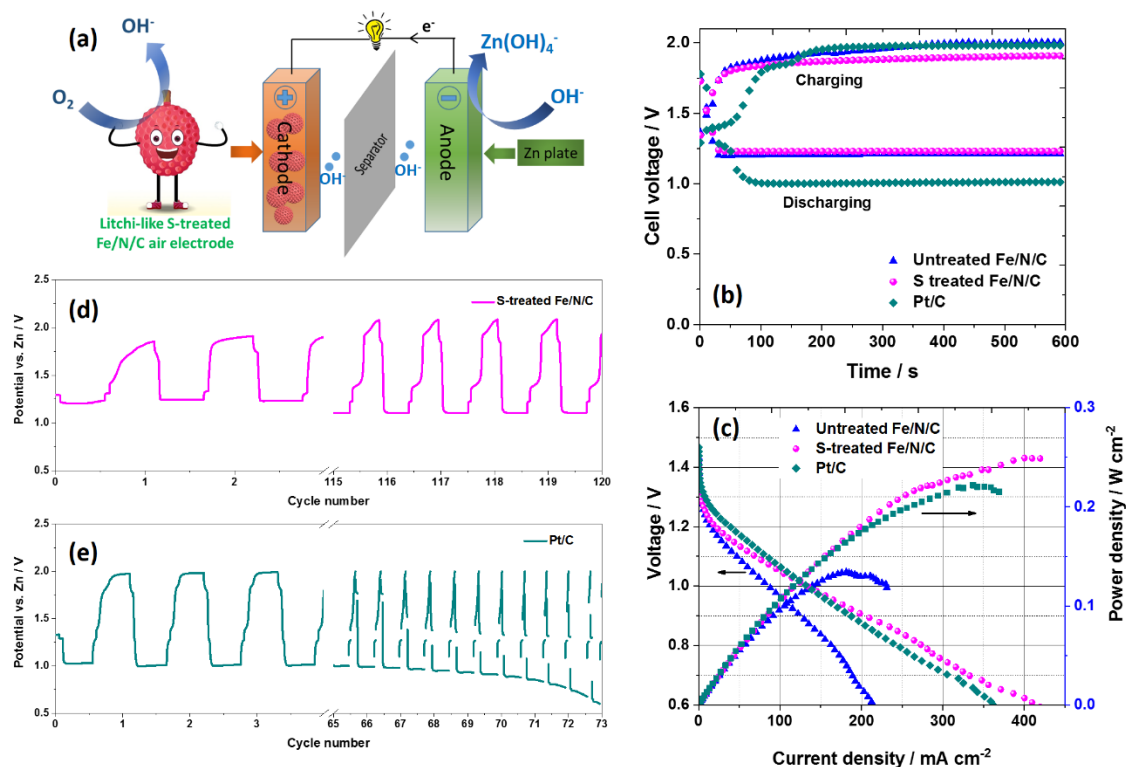


**Figure 5.** Electrochemical performance of S-treated Fe/N/C, untreated Fe/N/C and Pt/C in a homemade Zn-air battery. (a) Schematic of the discharge process for the rechargeable Zn-air battery. (b) Charge and discharge polarization curves of a two-electrode rechargeable Zn-air battery. (c) Discharge polarization curves and corresponding power density plots. (d and e) Charge-discharge cycling performance of a rechargeable Zn-air battery based on S-treated Fe/N/C and commercial Pt/C electrocatalysts at a constant charge-discharge current density of  $5 \text{ mA cm}^{-2}$ .

### 3. Conclusions

In conclusion, we have developed a straightforward yet highly efficient approach, based on using S as a promoter, to fabricate a litchi-like hierarchical porous Fe/N/C catalyst. The addition of S not only affords interpenetrating holes leading to a large surface area and pore volume inside the architecture, but also helps the whole carbon framework keep a perfect 3D spherical shape and uniformly dispersed Fe-N<sub>x</sub> active sites by reducing the bulk Fe particles to a large extent; moreover, a higher degree of distortion of the local Fe-N<sub>4</sub> structure was observed for the S-treated Fe/N/C sample. Consequently, the optimal S-treated Fe/N/C catalyst shows a litchi-like spherical structure, large surface area ( $982.1 \text{ m}^2 \text{ g}^{-1}$ ) with a huge pore volume ( $1.01 \text{ cm}^3 \text{ g}^{-1}$ ), and excellent ORR activity. Importantly, it achieves a superior performance ( $\sim 250 \text{ mW cm}^{-2}$ , double

the power density compared with the untreated one) as an air cathode for a Zn–air battery device. This work may provide a new strategy to develop high performance carbon-based electrocatalysts for low cost metal–air batteries and other electrochemical energy conversion/storage applications.

### **Conflicts of interest**

There are no conflicts to declare.

### **Corresponding Author**

\*E-mail: [gaixia.zhang@emt.inrs.ca](mailto:gaixia.zhang@emt.inrs.ca) (G. Zhang); [shuhui@emt.inrs.ca](mailto:shuhui@emt.inrs.ca) (S. Sun).

### **Acknowledgement**

This work is supported financially by the Natural Sciences and Engineering Research Council of Canada (NSERC), Ballard Power Systems Inc., the Fonds de Recherche du Québec-Nature et Technologies (FRQNT), Canada Foundation for Innovation (CFI), Centre Québécois sur les Matériaux Fonctionnels (CQMF), Institut National de la Recherche Scientifique (INRS) and China Scholarship Council (CSC). Synchrotron research described in this paper was performed at the Canadian Light Source, which is supported by CFI, NSERC, the University of Saskatchewan, the Government of Saskatchewan, Western Economic Diversification Canada, the National Research Council Canada, and the Canadian Institutes of Health Research. The authors also thank Dr. Siyu Ye, Dr. Dustin Banham, Dr. Lijun Yang, and Dr. Shanna Knights from Ballard Power Systems Inc. for their valuable discussions..

### **References**

- [1] S. Chu and Y. Cui and N. Liu, *Nat. Mater.*, 2017, **16**, 16.
- [2] Y. Li and J. Lu, *ACS Energy Lett.*, 2017, **2**, 1370.
- [3] J. Li, J. Chen, H. Wang, Y. Ren, K. Liu, Y. Tang and M. Shao, *Energy Storage Mater.*, 2017, **8**, 49.
- [4] J. Li, Z. Zhou, K. Liu, F. Li, Z. Peng, Y. Tang and H. Wang, *J. Power Sources*, 2017, **343**, 30.

- [5] K. Liu, Z. Peng, H. Wang, Y. Ren, D. Liu, J. Li, Y. Tang and N. Zhang, *J. Electrochem. Soc.*, 2017, **164**, F475.
- [6] K. Liu, X. Huang, H. Wang, F. Li, Y. Tang, J. Li and M. Shao, *ACS Appl. Mater. Interfaces*, 2016, **8**, 34422.
- [7] J. Fu, Z. P. Cano, M. G. Park, A. Yu, M. Fowler and Z. Chen, *Adv. Mater.*, 2017, **29**, 1604685.
- [8] X. Cai, L. Lai, J. Lin and Z. Shen, *Mater. Horiz.*, 2017, **4**, 945.
- [9] Q. Wei, Y. Fu, G. Zhang and S. Sun, *Curr. Opin. Electrochem.*, 2017, **4**, 45.
- [10] M. Yu, Z. Wang, C. Hou, Z. Wang, C. Liang, C. Zhao, Y. Tong, X. Lu and S. Yang, *Adv. Mater.*, 2017, **29**, 1602868.
- [11] J. S. Lee, G. Nam, J. Sun, S. Higashi, H. W. Lee, S. Lee, W. Chen, Y. Cui and J. Cho, *Adv. Energy Mater.*, 2016, **6**, 1601052.
- [12] Y. Liu, F. Chen, W. Ye, M. Zeng, N. Han, F. Zhao, X. Wang and Y. Li, *Adv. Funct. Mater.*, 2017, **27**, 1606034.
- [13] M. Lefèvre, E. Proietti, F. Jaouen and J.-P. Dodelet, *Science*, 2009, **324**, 71.
- [14] E. Proietti, F. Jaouen, M. Lefèvre, N. Larouche, J. Tian, J. Herranz and J.-P. Dodelet, *Nat. Commun.*, 2011, **2**, 416.
- [15] L. Shang, H. Yu, X. Huang, T. Bian, R. Shi, Y. Zhao, G. I. N. Waterhouse, L. Z. Wu, C. H. Tung and T. Zhang, *Adv. Mater.*, 2016, **28**, 1668.
- [16] G. Zhang, R. Chenitz, M. Lefèvre, S. Sun and J.-P. Dodelet, *Nano Energy*, 2016, **29**, 111.
- [17] S. H. Ahn, X. Yu and A. Manthiram, *Adv. Mater.*, 2017, **29**, 1606534.
- [18] G. Fu, Z. Cui, Y. Chen, Y. Li, Y. Tang and J. B. Goodenough, *Adv. Energy Mater.*, 2017, **7**, 1601172.
- [19] H.-W. Liang, X. Zhuang, S. Brüller, X. Feng and K. Müllen, *Nat. Commun.*, 2014, **5**, 4973.
- [20] X. Fu, F. M. Hassan, P. Zamani, G. Jiang, D. C. Higgins, J.-Y. Choi, X. Wang, P. Xu, Y. Liu and Z. Chen, *Nano Energy*, 2017, **42**, 249.
- [21] Y.-P. Deng, Y. Jiang, D. Luo, J. Fu, R. Liang, S. Cheng, Z. Bai, Y. Liu, W. Lei, L. Yang, J. Zhu and Z. Chen, *ACS Energy Lett.*, 2017, **2**, 2706.
- [22] D. Y. Chung, M. J. Kim, N. Kang, J. M. Yoo, H. Shin, O.-H. Kim and Y.-E. Sung, *Chem. Mater.*, 2017, **29**, 2890.
- [23] G. Wu, K. L. More, C. M. Johnston and P. Zelenay, *Science*, 2011, **332**, 443.

- [24] Y. Chen, S. Ji, Y. Wang, J. Dong, W. Chen, Z. Li, R. Shen, L. Zheng, Z. Zhuang and D. Wang, *Angew. Chem. Int. Ed.*, 2017, **129**, 7041.
- [25] Y. J. Sa, D.-J. Seo, J. Woo, J. T. Lim, J. Y. Cheon, S. Y. Yang, J. M. Lee, D. Kang, T. J. Shin and H. S. Shin, *J. Am. Chem. Soc.*, 2016, **138**, 15046.
- [26] X. Wen, D. Zhang, T. Yan, J. Zhang and L. Shi, *J. Mater. Chem. A*, 2013, **1**, 12334.
- [27] D. Lee, J.-Y. Jung, M.-J. Jung and Y.-S. Lee, *Chem. Eng. J.*, 2015, **263**, 62.
- [28] J. Liang, X. Du, C. Gibson, X. W. Du and S. Z. Qiao, *Adv. Mater.*, 2013, **25**, 6226.
- [29] Z. Li, G. Li, L. Jiang, J. Li, G. Sun, C. Xia and F. Li, *Angew. Chem. Int. Ed.*, 2015, **54**, 1494.
- [30] J. Anibal, H. G. Romero, N. D. Leonard, C. Gumeci, B. Halevi and S. C. Barton, *Appl. Catal., B*, 2016, **198**, 32.
- [31] H.-W. Liang, W. Wei, Z.-S. Wu, X. Feng and K. Müllen, *J. Am. Chem. Soc.*, 2013, **135**, 16002.
- [32] Z. Chen, X. Gao, X. Wei, X. Wang, Y. Li, T. Wu, J. Guo, Q. Gu, W. D. Wu and X. D. Chen, *Carbon*, 2017, **121**, 143.
- [33] I. Herrmann, U. I. Kramm, J. Radnik, S. Fiechter and P. Bogdanoff, *J. Electrochem. Soc.*, 2009, **156**, B1283.
- [34] W. Kiciński and A. Dziura, *Carbon*, 2014, **75**, 56.
- [35] M. Khalil, M. A. Marcus, A. L. Smeigh, J. K. McCusker, H. H. W. Chong and R. W. Schoenlein, *J. Phys. Chem. A*, 2006, **110**, 38.
- [36] Q. Jia, N. Ramaswamy, H. Hafiz, U. Tylus, K. Strickland, G. Wu, B. Barbiellini, A. Bansil, E. F. Holby and P. Zelenay, *ACS Nano*, 2015, **9**, 12496.
- [37] W.-J. Jiang, L. Gu, L. Li, Y. Zhang, X. Zhang, L.-J. Zhang, J.-Q. Wang, J.-S. Hu, Z. Wei and L.-J. Wan *J. Am. Chem. Soc.*, 2016, **138**, 3570.
- [38] A. Zitolo, V. Goellner, V. Armel, M.-T. Sougrati, T. Mineva, L. Stievano, E. Fonda and F. Jaouen, *Nat. Mater.*, 2015, **14**, 937.
- [39] Q.-L. Zhu, W. Xia, L.-R. Zheng, R. Zou, Z. Liu and Q. Xu, *ACS Energy Lett.*, 2017, **2**, 504.
- [40] K. Strickland, E. Miner, Q. Jia, U. Tylus, N. Ramaswamy, W. Liang, M.-T. Sougrati, F. Jaouen and S. Mukerjee, *Nat. Commun.*, 2015, **6**, 7343.

## Supporting Information

### **Litchi-like porous Fe/N/C spheres with atomically dispersed FeN<sub>x</sub> promoted by sulfur as high-efficient oxygen electrocatalysts for Zn–air batteries**

*Qiliang Wei,<sup>1</sup> Gaixia Zhang,<sup>\*1</sup> Xiaohua Yang,<sup>1</sup> Yanqing Fu,<sup>1</sup> Guanhua Yang,<sup>1</sup> Ning Chen,<sup>2</sup> Weifeng Chen,<sup>2</sup> Shuhui Sun<sup>\*1</sup>*

<sup>1</sup>Institut National de la Recherche Scientifique-Énergie Matériaux et Télécommunications, Varennes, QC J3X 1S2, Canada.

<sup>2</sup>Canadian Light Source (CLS), 44 Innovation Boulevard, Saskatoon, SK, S7N 2V3, Canada

## Experimental Section

### Materials

Phenol (99 %), formaldehyde solution (37 %), iron (II) acetate (95 %), 1,10 phenanthroline (99 %), sodium hydroxide (NaOH, 95.0 %), sulfur (S), and potassium hydroxide (KOH, 87.1 %), were bought from Fisher Scientific; Pluronic®F-127, Nafion solution (5 wt%) were purchased from Sigma-Aldrich. Pt/C (20%) was purchased from E-TEK. All chemicals were used as received and solutions were prepared using deionized water (Millipore Milli-Q, 18.2 MΩ cm).

### Preparation of spherical phenolic resol-F127 monomicelles (SPRMs)<sup>[1]</sup>

Firstly, F127 (0.96 g) was dissolved in 15 mL DI water at room temperature with stirring for 30 min. Then phenol (0.6 g), formaldehyde solution (2.1 mL), and NaOH aqueous solution (0.1 M, 15 mL) were mixed and stirred at 70 °C for 30 min to obtain a low-molecular-weight phenolic resols. After that, the F127 solution was dropped into the phenolic resols slowly with stirring. After 2 hrs, 50 mL of water was added and further stirred at 70 °C for 12-14 hrs. Afterwards, 12 mL of the as-prepared monomicelle solution and 25 mL of H<sub>2</sub>O was transferred into an autoclave (50 mL volume) for hydrothermal treatment at 130 °C for 20 hrs. In the end, the SPRMs were collected by centrifugation and washed with distilled water for several times, followed by a drying process in an oven at 60 °C, and then served as the carbon host for loading Fe and N in the next step.

### Preparation of Fe/N/C catalysts

In a typical synthesis of S treated Fe/N/C catalyst, the precursors were prepared by first mixing 0.7 g SPRMs, 0.7 g S, 136 mg 1,10-Phen, 30 mg FeAc in a solution of ethanol and deionized water (ethanol:water = 1:2) under stirring at room temperature. Then the mixture was heated to 60–80 °C for 2–3 hrs until about 30 ml of a thick slurry was obtained. The slurry was placed overnight in a drying oven at 95 °C. Afterwards, the dry powder was ground sufficiently and placed in the quartz tube, followed by heating at 450 °C in Ar for 2 hrs, and then pyrolyzed in Ar at 700 °C for 1 hr, followed by another pyrolysis in ammonia at 950 °C with different pyrolysis time in order to obtain expected ~50% weight remaining.<sup>[2-5]</sup> In the experiment, different amount of S were used (the mass

ratio of SPRMs/S = 0.5, 1.0, 1.5) to find the optimal S content of the S treated-Fe/N/C catalysts. For comparing, the porous Fe/N/C without the addition of S (denoted as untreated Fe/N/C) was prepared as the same process.

### **Physical characterizations**

The morphological structures of the catalysts were investigated by transmission electron microscopy (TEM) and high-resolution TEM (HRTEM) (JEOL JEM-2100F, operated at 200 kV). The surface properties were analysed by X-Ray photoelectron spectroscopy (XPS, VG ESCALAB 220i-XL) equipped with a hemispherical analyser for a Twin Anode X-Ray Source (Al K $\alpha$  was used in this work). The C 1s peak (BE = 284.6 eV) was used as the reference line to accurately determine the positions of other spectral lines. The fine structure of the photoelectron lines was treated using Casa XPS software (2.3.15 Version). The surface areas of the catalysts were measured through N<sub>2</sub> sorption isotherms that were collected using Quantachrome Instruments Autosorb-1 at liquid nitrogen temperature (77.3 K). The surface areas were estimated from the Brunauer-Emmett-Teller (BET) equation and from the fitting of the N<sub>2</sub>-adsorption isotherms based on a slit-pore model, with the Quenched solid density functional theory (QSDFT) available in the AS1WIN software. The P/P<sub>0</sub> range is 0.05-0.35. QSDFT is the most advanced DFT method developed from 2006 for the pore size analysis of geometrically and chemically disordered micro-mesoporous carbons, which allows the calculation of pore size distributions from ca. 0.6 nm up to ca. 40 nm. It allows for a major improvement of the accuracy of DFT pore size distribution analyses of disordered carbon materials from low-temperature nitrogen adsorption isotherms because it takes into account the effects of surface roughness, anisotropy and heterogeneity explicitly.

The Fe K-edge X-ray absorption near-edge structure (XANES) and Extended X-ray Absorption Fine Structure (EXAFS) data were collected on the 06ID-1 Hard X-ray MicroAnalysis (HXMA) beamline at the Canadian Light Source. During data collection, the CLS storage ring (2.9 GeV) was operated under 250 mA mode and the HXMA superconducting wiggler was run at 1.9 T. Measurements were made at room temperature in fluorescence mode using a 32-element Ge detector. Data collection configuration was using metal Fe foil as energy calibration by in step calibration for every data sets. To prepare the electrode for the XANES measurement, powder Fe/N/C catalysts were mixed with Nafion solution (5 wt%) and isopropanol to form

homogeneous ink followed by dropping onto a gas diffusion layer (GDL). The spectra were normalized with respect to the edge height after subtracting the pre-edge and post-edge backgrounds, then convert the data from energy space to k space using Athena software.

### **Electrochemical measurements**

All electrochemical measurements were carried out in a three-electrode cell using a rotating ring disk electrode (RRDE, PINE Research Instrumentation) with a bipotentiostat (Pine, Model PGSTAT-72637) workstation at room temperature. A Pt wire and a Hg/HgO were used as the counter and reference electrodes, respectively. All potentials in this study refer to reversible hydrogen electrode (RHE). A RDE with glassy carbon (GC) disk electrode (5 mm in diameter) and a rotating ring-disk electrode (RRDE) with a Pt ring and a GC disk (5.61 mm diameter) were used as the substrate for the working electrodes. Before use, the GC electrodes in RDE/RRDE were polished using aqueous alumina suspension on felt polishing pads.

The catalyst suspension in this work was prepared as the following: 10 mg of catalyst was mixed in a glass vial with 95  $\mu\text{L}$  of 5 wt% Nafion solution and 350  $\mu\text{L}$  of ethanol, followed by sonication and agitation in a vortex mixer, alternatively, for a total of 1 h. Then 9  $\mu\text{L}$  of the catalyst suspension was dropped onto the GC electrode surface ( $\sim 0.8 \text{ mg cm}^{-2}$ ). For comparison, the 20 wt% Pt/C catalyst (E-ETK) was prepared with a loading amount of  $100 \mu\text{g cm}^{-2}$  (i.e.,  $20 \mu\text{g}_{\text{Pt}} \text{ cm}^{-2}$ ). Before testing,  $\text{N}_2$  (or  $\text{O}_2$ ) was bubbled through the electrolyte for 30 min and the  $\text{N}_2$ - (or  $\text{O}_2$ ) was kept bubbling during the measurements, in order to keep the  $\text{N}_2$ - or  $\text{O}_2$ -saturated in the solution. In 0.1 M KOH, the cyclic voltammetry (CV) profiles were recorded at  $50 \text{ mV s}^{-1}$  and the linear sweep voltammograms (LSV) were recorded at  $10 \text{ mV s}^{-1}$ , between 0-1.2 V (vs. RHE). All of the LSV curves were recorded after subtraction of the background current recorded in  $\text{N}_2$ -saturated solution. For detecting peroxide formed at the disc electrode, the potential for the Pt ring electrode was set at 1.3 V (vs. RHE) and the voltammograms were recorded at 1600 rpm. The collection efficiency of the ring-disk electrode was  $N = 0.37$ . The peroxide yield ( $\text{H}_2\text{O}_2$ , %) and the electron transfer number ( $n$ ) were calculated as follows:

$$\text{H}_2\text{O}_2\% = 200 \times (\text{I}_r/\text{N})/(\text{I}_d + \text{I}_r/\text{N})$$

$$n = 4 \times \text{I}_d / (\text{I}_d + \text{I}_r/\text{N})$$

Where  $\text{I}_d$  is the disk current and  $\text{I}_r$  is the ring current.

The stability of the catalysts was tested on fresh electrodes by chronoamperometry at 0.7 V (vs. RHE) for 500 min in O<sub>2</sub>-saturated 0.1 M KOH with a rotation speed of 1600 rpm.

Linear sweep voltammograms for the OER are obtained using a RDE (1600 rpm) in 1 M KOH solution at a scan rate of 10 mV s<sup>-1</sup> in O<sub>2</sub>-saturated solution.

#### **Zn-air battery assembly and measurement:**

The Zn-air batteries were tested in home-built electrochemical cells, the electrolyte used was 6 M KOH and 0.2 M Zn(Ac)<sub>2</sub> solution. To prepare the air electrode, homogeneous catalyst ink consisting of Fe/N/C catalysts, Nafion solution (5 wt%) and isopropanol was dropped onto a gas diffusion layer (GDL) with a catalyst loading of ~1.0 mg cm<sup>-2</sup>, a polished zinc plate was used as the anode. For comparing, 20 wt% Pt/C catalysts were prepared as the same procedure to achieve the same loading. Polarization data was collected using galvanodynamic method at a scan rate of 1.0 mA s<sup>-1</sup> with cut-off voltage of 0.6 V for the discharge and 2.2 V for the charge. Galvanostatic discharge and charge cycling was conducted at a constant current density of 5 mA cm<sup>-2</sup> with each cycle for 20 min.

Figures:

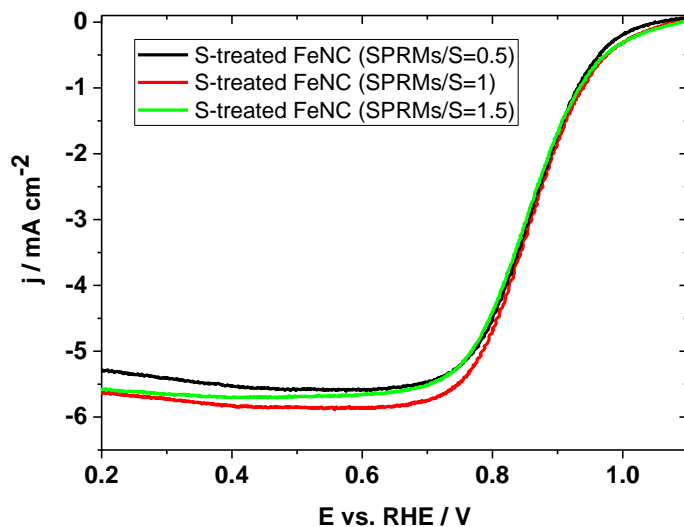


**Figure S1.** LSV results of (a) the S-treated Fe/N/C with different SPRMs/S ratio (scan rate = 10 mV s<sup>-1</sup>, rotation rate = 1600 rpm).

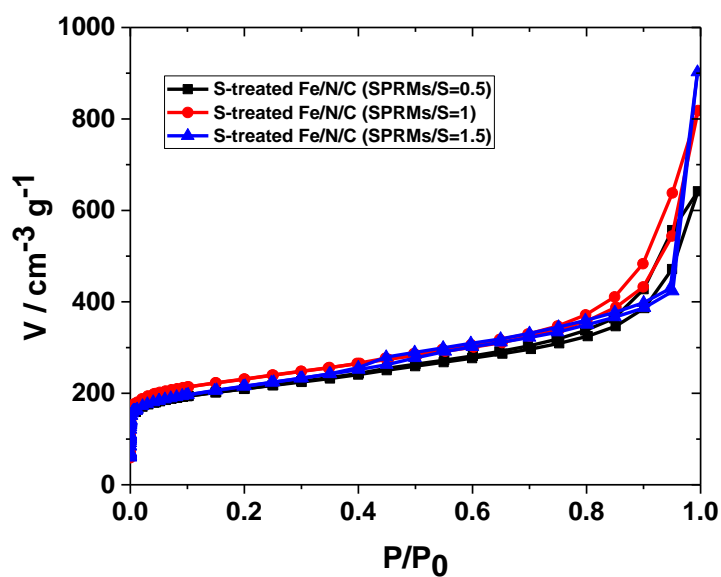


**Figure S2.** (a) N<sub>2</sub> adsorption/desorption of S-treated Fe/N/C samples.

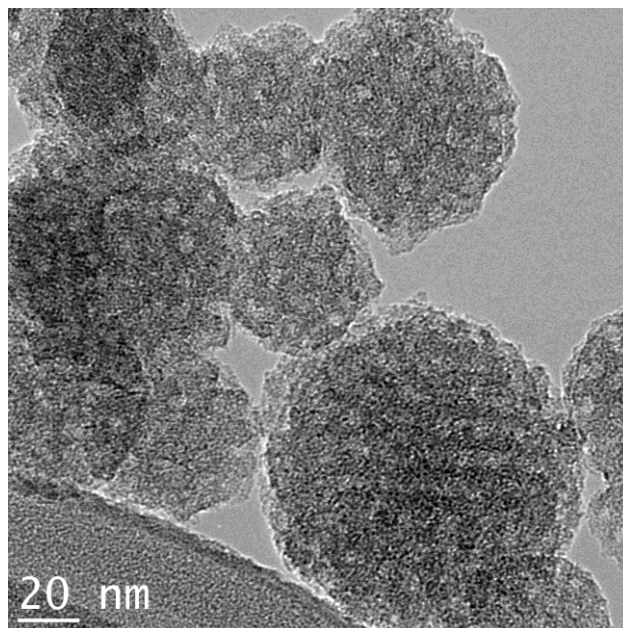


**Figure S3.** TEM image of S-treated Fe/N/C after Ar pyrolysis (before NH<sub>3</sub> pyrolysis).

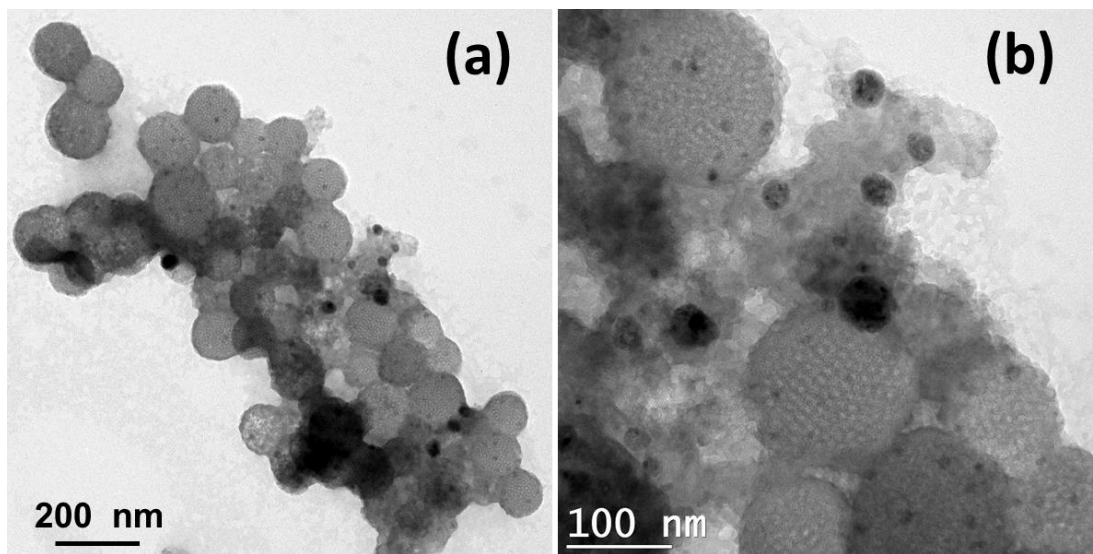


**Figure S4.** TEM images of S-treated Fe/N/C after NH<sub>3</sub> pyrolysis (S : SPRMs = 0.5)

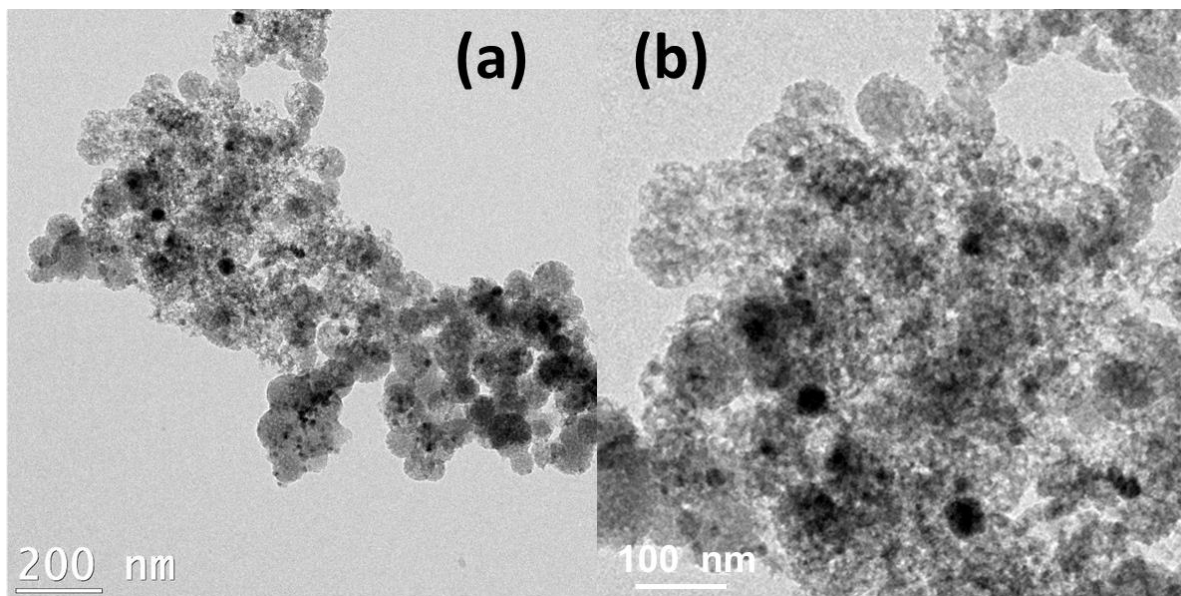


**Figure S5.** TEM images of S-treated Fe/N/C after  $\text{NH}_3$  pyrolysis (S : SPRMs = 1.5)

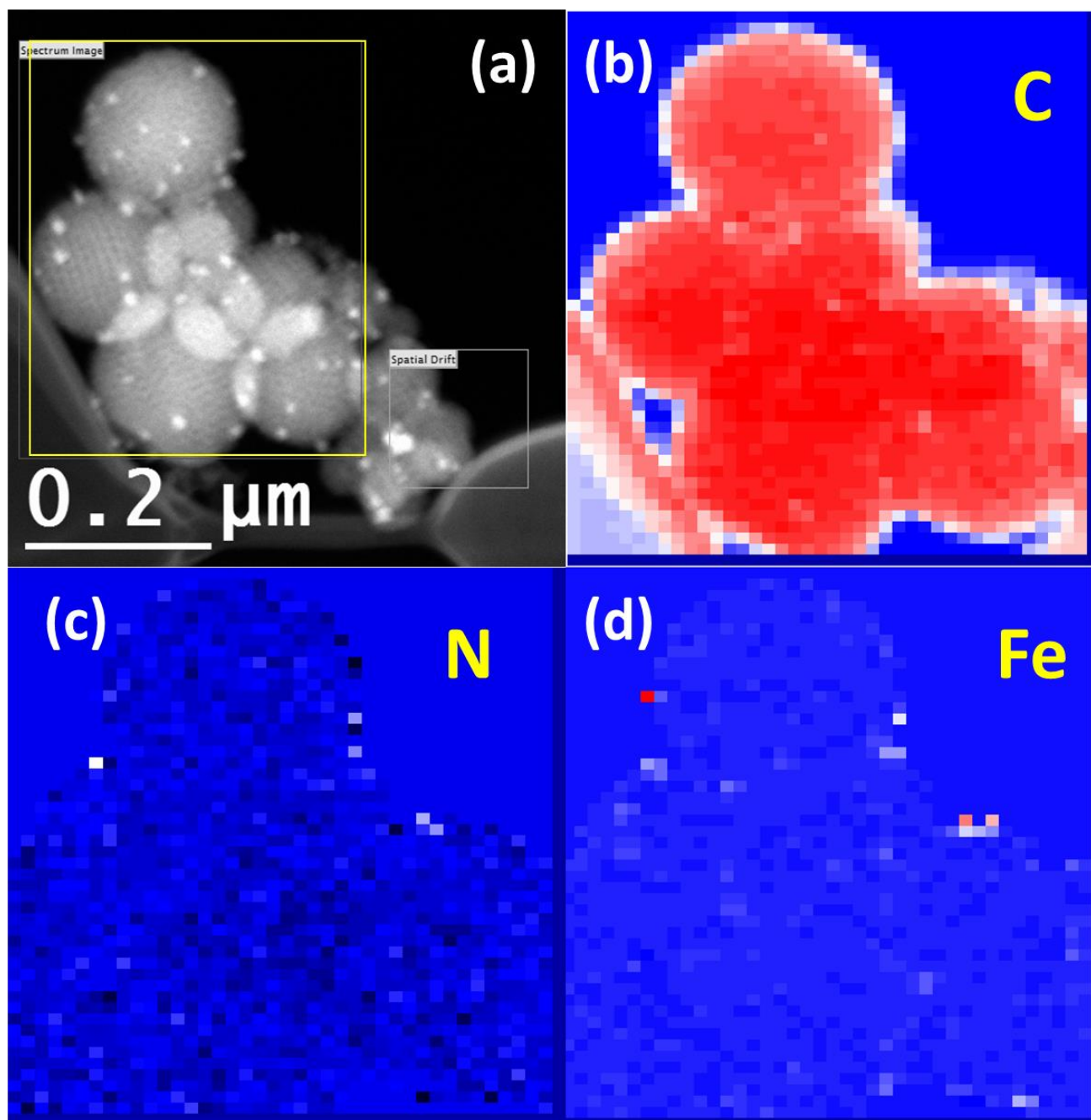


**Figure S6.** (a) HAADF TEM image, and (b-d) EELS mapping of C, N, and Fe of the area marked by yellow square in (a).

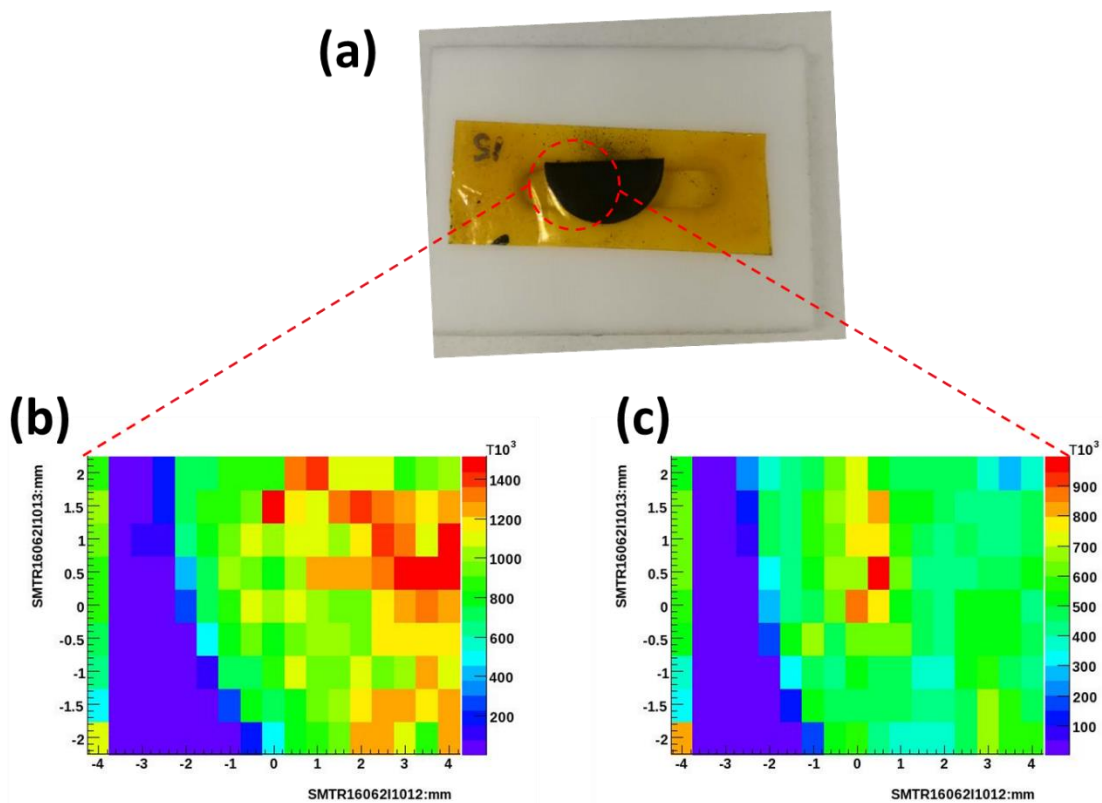


**Figure S7.** The 2D fluorescence mapping collected at 50 eV above the Fe K edge: (a) is the picture of the sample loaded on the holder, (b) Untreated Fe/N/C electrode, (c) S-treated Fe/N/C electrode.

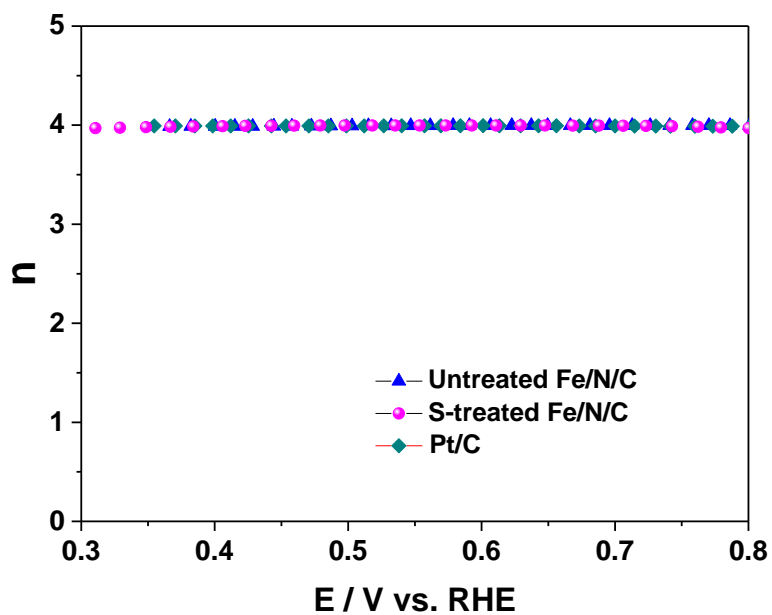


**Figure S8.** Electron-transfer numbers ( $n$ ) of untreated Fe/N/C, S-treated Fe/N/C and Pt/C in O<sub>2</sub>-saturated 0.1 M KOH at a scan rate of 10 mV s<sup>-1</sup>, rotation rate = 1600 rpm.

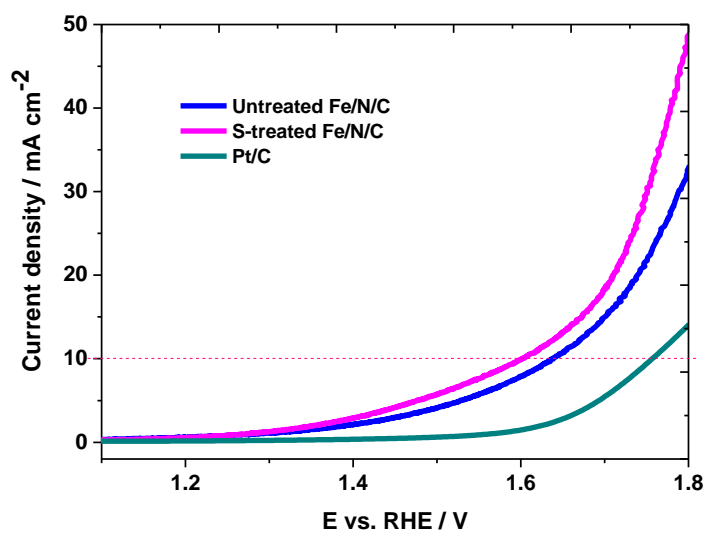


**Figure S9.** OER LSVs of untreated Fe/N/C, S-treated Fe/N/C, and Pt/C samples in 1 M KOH (scan rate =  $10 \text{ mV s}^{-1}$ , rotation rate = 1600 rpm).

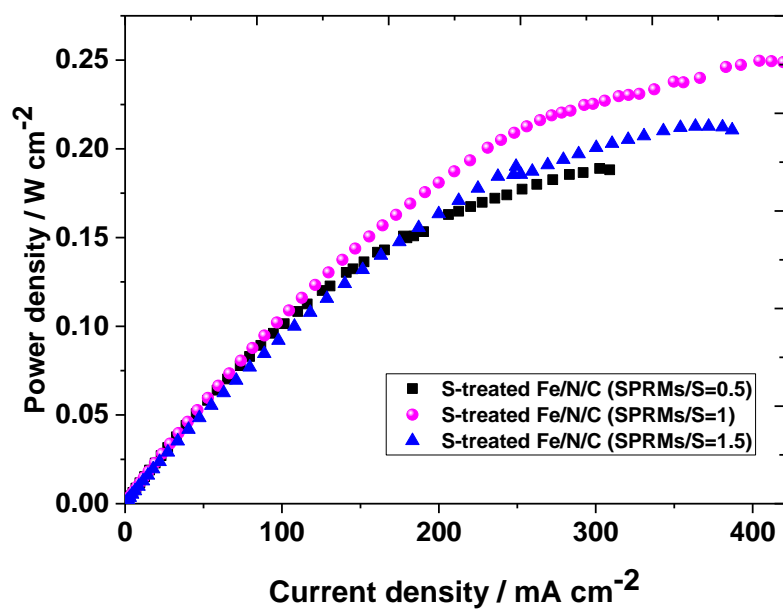


**Figure S10.** Power density of S-treated Fe/N/C samples, loading is  $\sim 1.0 \text{ mg cm}^{-2}$ .

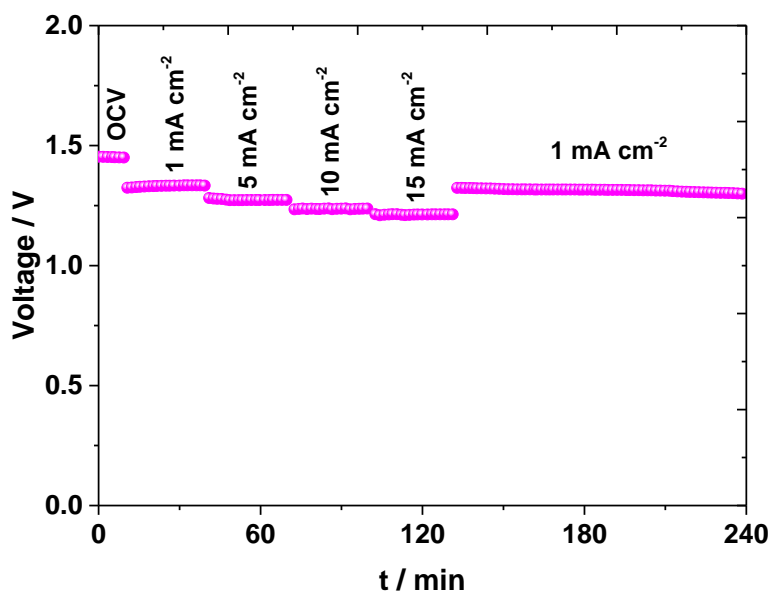


**Figure S11.** Discharge voltage of S-treated Fe/N/C sample at various current densities.

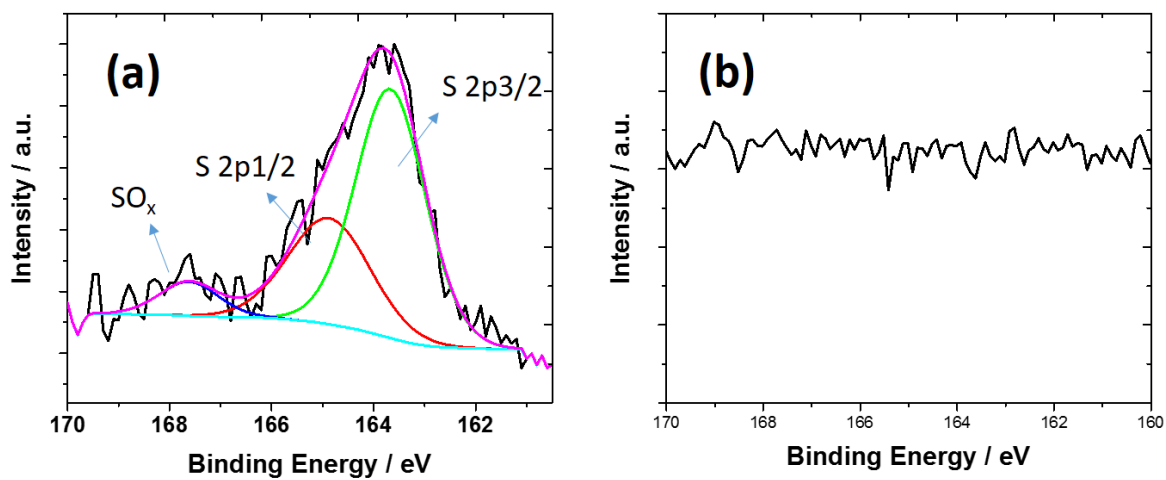


**Figure S12.** High-resolution of S 2p spectrum of S-treated Fe/N/C sample before (a) and after (b)  $\text{NH}_3$  pyrolysis.

**Table S1.** N<sub>2</sub> adsorption/desorption parameters.

<b>Samples</b>	<b>N<sub>2</sub> adsorption/desorption</b>			
	<b>Surface area (m<sup>2</sup>/g)</b>	<b>Surface area of micropore (m<sup>2</sup>/g)</b>	<b>Surface area of mesopore (m<sup>2</sup>/g)</b>	<b>Pore volume (cc/g)</b>
<b>Untreated Fe/N/C</b>	536.3	435.7	100.6	0.586
<b>S-treated Fe/N/C (SPRMs/S=0.5)</b>	911.6	755.9	155.7	0.821
<b>S-treated Fe/N/C (SPRMs/S=1)</b>	982.1	810.1	172.0	1.01
<b>S-treated Fe/N/C (SPRMs/S=1.5)</b>	921.9	752.1	169.8	0.858

**Table S2.** Electrochemical performance comparison of zinc-air batteries employing various ORR catalysts as the cathode.

ORR Catalyst	Zn electrode	Electrolyte	Catalyst loading (mg cm <sup>-2</sup> )	Cathode active material	Peak power density (mW cm <sup>-2</sup> )	Ref.
<b>Fe@N-C-700</b>	Zn plate	6 M KOH + 0.2 M Zn(Ac) <sub>2</sub>	2.2	Air	220	S1 <sup>[6]</sup>
<b>NiFe@NCX</b>	Zn plate	6 M KOH	1.0	Air	~85	S2 <sup>[7]</sup>
<b>Nitrogen-doped hierarchically porous carbon</b>	Zn foil	6 M KOH	1.0	Air	80	S3 <sup>[8]</sup>
<b>Co<sub>4</sub>N/CNW/CC</b>	Zn plate	6 M KOH + 0.2 M Zn(Ac) <sub>2</sub>	1.0	Air	174	S4 <sup>[9]</sup>
<b>Co-doped TiO<sub>2</sub> nanoparticle</b>	Zn plate	6 M KOH + 0.2 M Zn(Ac) <sub>2</sub>	-	Air	136	S5 <sup>[10]</sup>
<b>Fe-N-SCCFs</b>	Zn foil	6 M KOH	1.0	O <sub>2</sub>	~300	S6 <sup>[11]</sup>
<b>S,N-Fe/N/C-CNT</b>	Zn plate	6 M KOH + 0.2 M Zn(Ac) <sub>2</sub>	1.25	Air	102.7	S7 <sup>[12]</sup>
<b>NiCo<sub>2</sub>S<sub>4</sub>/N-CNT</b>	Zn foil	6 M KOH + 0.2 M ZnCl <sub>2</sub>	1.0	O <sub>2</sub>	147	S8 <sup>[13]</sup>
<b>Carbon-Coated Core-Shell Fe-Cu Nanoparticles</b>	Zn plate	6 M KOH	---	Air	212	S9 <sup>[14]</sup>
<b>Co/CoO nanoparticles immobilized on</b>	Zn foil	6 M KOH + 0.2 M	2.0	Air	157	S10 <sup>[15]</sup>

<b>Co–N-doped carbon</b>		ZnCl <sub>2</sub>				
<b>Cu(I)-N-graphene</b>	Zn plate	6 M KOH	0.4	Air	~210	S11 <sup>[16]</sup>
<b>NiFeO@MnO<sub>x</sub> Core–Shell Structures</b>	Zn plate	6 M KOH	0.25	Air	81	S12 <sup>[17]</sup>
<b>ZnCo<sub>2</sub>O<sub>4</sub>/N-CNT</b>	Zn plate	6 M KOH	2.0	Air	82.3	S13 <sup>[18]</sup>
<b>Co<sub>3</sub>O<sub>4</sub> nanoparticle supported NGr</b>	Zn foil	6 M KOH	1.0	Air	190	S14 <sup>[19]</sup>
<b>Co(OH)<sub>2</sub>/N-doped reduced graphene oxide</b>	Zn plate	6 M KOH	1.0	Air	44	S15 <sup>[20]</sup>
<b>3D N-doped CNT arrays</b>	Zn foil	6 M KOH + 0.2 M Zn(Ac) <sub>2</sub>	---	Air	190	S16 <sup>[21]</sup>
<b>Fe-NSCNT</b>	Zn foil	6 M KOH	1.0	Air	100	S17 <sup>[22]</sup>
<b>Litchi-like S-treated Fe/N/C</b>	<b>Zn plate</b>	<b>6 M KOH + 0.2 M Zn(Ac)<sub>2</sub></b>	<b>1.0</b>	<b>Air</b>	<b>~250</b>	<b>This work</b>

**Table S3.** On-set potential and half-wave potential parameters.

Samples	Potential values	
	On-set potential <sup>a</sup>	Half-wave potential
Untreated Fe/N/C	0.98 V	0.87 V
S-treated Fe/N/C (SPRMs/S=0.5)	0.99 V	0.875 V
S-treated Fe/N/C (SPRMs/S=1)	1.02 V	0.88 V
S-treated Fe/N/C (SPRMs/S=1.5)	1.02 V	0.875 V
Pt/C (20%, E-TEK)	0.92 V	0.81 V

<sup>a</sup>(here we define the potential at 0.2 mA cm<sup>-2</sup> as on-set potential)

## References

- [1] Q. Wei, Y. Fu, G. Zhang, Y. Wang, X. Wang, M. Mohamedi, S. Sun, *RSC Advances* **2016**, *6*, 84149.
- [2] M. Lefèvre, E. Proietti, F. Jaouen, J.-P. Dodelet, *science* **2009**, *324*, 71.
- [3] E. Proietti, F. Jaouen, M. Lefèvre, N. Larouche, J. Tian, J. Herranz, J.-P. Dodelet, *Nature communications* **2011**, *2*, 416.
- [4] G. Zhang, R. Chenitz, M. Lefèvre, S. Sun, J.-P. Dodelet, *Nano Energy* **2016**, *29*, 111.
- [5] L. Yang, N. Larouche, R. Chenitz, G. Zhang, M. Lefèvre, J.-P. Dodelet, *Electrochimica Acta* **2015**, *159*, 184.
- [6] J. Wang, H. Wu, D. Gao, S. Miao, G. Wang, X. Bao, *Nano Energy* **2015**, *13*, 387.

- [7] J. Zhu, M. Xiao, Y. Zhang, Z. Jin, Z. Peng, C. Liu, S. Chen, J. Ge, W. Xing, *ACS Catalysis* **2016**, *6*, 6335.
- [8] L. Wang, C. Yang, S. Dou, S. Wang, J. Zhang, X. Gao, J. Ma, Y. Yu, *Electrochimica Acta* **2016**, *219*, 592.
- [9] F. Meng, H. Zhong, D. Bao, J. Yan, X. Zhang, *Journal of the American Chemical Society* **2016**, *138*, 10226.
- [10] L.-N. Han, L.-B. Lv, Q.-C. Zhu, X. Wei, X.-H. Li, J.-S. Chen, *Journal of Materials Chemistry A* **2016**, *4*, 7841.
- [11] B. Wang, X. Wang, J. Zou, Y. Yan, S. Xie, G. Hu, Y. Li, A. Dong, *Nano Letters* **2017**, *17*, 2003.
- [12] P. Chen, T. Zhou, L. Xing, K. Xu, Y. Tong, H. Xie, L. Zhang, W. Yan, W. Chu, C. Wu, *Angewandte Chemie International Edition* **2017**, *56*, 610.
- [13] X. Han, X. Wu, C. Zhong, Y. Deng, N. Zhao, W. Hu, *Nano Energy* **2017**, *31*, 541.
- [14] G. Nam, J. Park, M. Choi, P. Oh, S. Park, M. G. Kim, N. Park, J. Cho, J.-S. Lee, *ACS nano* **2015**, *9*, 6493.
- [15] X. Zhang, R. Liu, Y. Zang, G. Liu, G. Wang, Y. Zhang, H. Zhang, H. Zhao, *Chemical Communications* **2016**, *52*, 5946.
- [16] H. Wu, H. Li, X. Zhao, Q. Liu, J. Wang, J. Xiao, S. Xie, R. Si, F. Yang, S. Miao, *Energy & Environmental Science* **2016**, *9*, 3736.
- [17] Y. Cheng, S. Dou, J.-P. Veder, S. Wang, M. Saunders, S. P. Jiang, *ACS Applied Materials & Interfaces* **2017**, *9*, 8121.
- [18] Z. Q. Liu, H. Cheng, N. Li, T. Y. Ma, Y. Z. Su, *Advanced Materials* **2016**, *28*, 3777.
- [19] S. K. Singh, V. M. Dhavale, S. Kurungot, *ACS applied materials & interfaces* **2015**, *7*, 21138.
- [20] Y. Zhan, G. Du, S. Yang, C. Xu, M. Lu, Z. Liu, J. Y. Lee, **2015**.
- [21] Z. Li, M. Shao, Q. Yang, Y. Tang, M. Wei, D. G. Evans, X. Duan, *Nano Energy* **2017**.
- [22] S. Zeng, F. Lyu, H. Nie, Y. Zhan, H. Bian, Y. Tian, Z. H. E. Li, A. Wang, J. Lu, Y. Y. Li, *Journal of Materials Chemistry A* **2017**.

### **3.3 Bio-inspired nonprecious bimetallic (Fe-Cu)/N/C catalyst for oxygen reduction in proton exchange membrane fuel cells**

Qiliang Wei, Xiaohua Yang, Gaixia Zhang, Ning Chen, Shuhui Sun

To be submitted.

Inspired by the metal-centered structure of the ORR-functioned enzyme in life and the synergistic effects between transition metals, in this section, we prepared highly porous (Fe-Cu)/N/C catalyst based on MOF. We found that compared with the Fe/N/C, the as-synthesized (Fe-Cu)/N/C possesses higher surface area, and lower H<sub>2</sub>O<sub>2</sub> yield in the range of 0.3-0.8 V in a half-cell test. Importantly, when applied in a MEA in the H<sub>2</sub>-Air PEMFC, the (Fe-Cu)/N/C catalyst demonstrates higher power density (0.4 W cm<sup>-2</sup>) than that of the Fe/N/C (0.36 W cm<sup>-2</sup>), and an enhanced stability, i.e., improvement of 3.7% of the current density under a potentiostatic testing at 0.6 V after 40 h.

*Contributions:* I performed most of the experimental synthesis, the electro-chemical measurements, and all characterizations except the TEM measurements that have been done by technicians. Xiaohua Yang assisted me on the pyrolysis of the catalysts. I conducted the data analysis and the interpretation of results, as well as the manuscript writing, with the help of co-authors.

# Bio-inspired nonprecious bimetallic (Fe-Cu)/N/C catalyst for oxygen reduction in proton exchange membrane fuel cells

*Qiliang Wei,<sup>1</sup> Xiaohua Yang,<sup>1</sup> Gaixia Zhang,<sup>1,\*</sup> Ning Chen,<sup>2</sup> Shuhui Sun<sup>1,\*</sup>*

<sup>1</sup>Énergie, Matériaux et Télécommunications, Institut National de la Recherche Scientifique (INRS), 1650 Boul. Lionel-Boulet, Varennes, Quebec J3X 1S2, Canada

<sup>2</sup>Canadian Light Source (CLS), 44 Innovation Boulevard, Saskatoon, SK, S7N 2V3, Canada.

## Abstract

Fuel cells powered by hydrogen are poised to be the solution for long-range electromobility applications, but the expensive platinum (Pt) currently required for catalyzing the oxygen reduction reaction (ORR) on the cathode still hinders their widespread commercialization. Fe/N/C, showing superior ORR activity, has been proposed as promising Pt-free electrocatalysts. It is interesting and well-known that the structure of the active sites FeN<sub>4</sub> motif in Fe/N/C is analogous to the porphyrin-chelated iron (heme) in natural systems. Heme-copper centre in many enzymes are also very active for ORR in aerobic respiration processes. Inspired by Nature's choice, a highly porous bimetallic (Fe-Cu)/N/C catalyst was prepared based on ZIF-8 in this work. The electrochemical results show that the (Fe-Cu)/N/C catalyst possesses very close ORR activity with the Fe/N/C counterpart, but with lower H<sub>2</sub>O<sub>2</sub> yield in the range of 0.3-0.8 V in a half-cell environment. When applied in a practical H<sub>2</sub>/Air fuel cell, the (Fe-Cu)/N/C catalyst demonstrates a higher power density of 0.4 W cm<sup>-2</sup> than Fe/N/C (0.36 W cm<sup>-2</sup>), and an improvement of 3.7% of the current density under a potentiostatic testing at 0.6 V after 40 h. In addition, the active sites in both catalysts are also discussed.

## 1. Introduction

Developing clean-energy technologies has become significantly more intensive with increased demands arising from global warming and environmental pollution issues.<sup>1-2</sup> Proton exchange membrane fuel cells (PEMFCs) are ideal clean-energy systems due to the merits of low/zero emissions, high conversion efficiency, high energy density, low-operation temperature, and low-noise.<sup>3-7</sup> They can be widely used for many applications ranging from portable electronics, electric vehicles (EVs), and house back-up power, to large-scale stationary power systems. The wide-spread employment of PEMFCs are expected to effectively reduce the burden of energy crisis, environmental issue and electric power construction. Unfortunately, the high cost of PEMFCs largely impeded their wide commercialization. Sufficiently powerful PEMFCs rely on high platinum (Pt) loadings on both sides of the membrane electrode assembly (MEA), especially on the cathode side (up to 90%). It is estimated that the price of Pt accounts for almost half of the total price in a H<sub>2</sub>-powered PEMFC. Therefore, developing low-cost and high-efficient non-precious-metal catalysts (NPMCs) for oxygen reduction reaction (ORR) in PEMFCs brooks no delay.<sup>8-12</sup> With this regard, a rational design of Me-N-C (Me stands for transition metal, such as Fe, Co, Ni, Mn, Cu, etc.) has attracted great attention, because of their good electrocatalytic activity and potential low-cost scalable synthesis.<sup>13-17</sup> Among which, Fe/N/C has shown excellent ORR activity in alkaline medium.<sup>18-19</sup> Comparatively, Fe/N/C is exhibiting inferior activity to Pt/C under acid medium. Despite of much progress,<sup>13, 20-25</sup> Fe/N/C catalysts are still facing the insufficient activity and inferior stability compared to Pt/C. In addition, most of these Fe/N/C catalysts were evaluated in a half cell (RDE) environment, rather than in a real MEA fuel cell system. When applied in a single cell, the porous structure of the Fe/N/C catalyst plays an important role to promote the mass-transport and to achieve a high power density. One typical example is the metal-organic framework (MOF)-derived Fe-N-C catalyst developed by Dodelet's group, based on which, the peak power density of a single H<sub>2</sub>/O<sub>2</sub> fuel cell could reach to 0.91 W cm<sup>-2</sup> at 1 bar back-pressure.<sup>6</sup> Till now, it is still one of best NPMCs for PEMFCs. In another work in Zelenay group, the stability of the catalysts was improved by a simultaneous utilization of Fe and Co in the precursors.<sup>26</sup> The optimized (Fe-Co)/N/C catalysts showed the H<sub>2</sub>O<sub>2</sub> production below 1%, and displayed high stability in a H<sub>2</sub>-air fuel cell under 0.4 V. Other similar reports from different research groups also demonstrated that bimetallic (Fe-*M*)/N/C (where *M* = Co, Cu, Ni, Mn) catalysts show better ORR performance

than their single-metal Fe/N/C counterpart, benefiting from the synergistic effects between different metals.<sup>16-17, 27-34</sup> However, almost all these reports only compared the ORR activity either in alkaline or acid media in half-cell ORR tests. The evaluation of these NPMCs in MEA single-cell test has become more and more crucial from a practical view.

As for the active sites of Fe/N/C catalysts, evidence from both theory and experimental is mounting that carbon hosted FeN<sub>4</sub> structure is the key structural motif, which has anatomic homology with heme, containing in hemoglobin.<sup>35-36</sup> Copper is another vital element in bio-tissue for oxygen reduction, which are existing in haem-copper oxidases (HCOs).<sup>37</sup> HCOs perform a 4-electron ORR process to water, which are involved in aerobic respiration in many forms of life from bacteria, eukaryotes, to human. Inspired by nature's choice, as well as the synergistic effects from bimetallic (Fe-*M*)/N/C, in the present work, we prepared (Fe-Cu)/N/C with different Fe/Cu ratio and investigated their performance both in ORR half-cell and H<sub>2</sub>-air PEMFC single-cell. The results show that the optimized (Fe-Cu)/N/C has a lower H<sub>2</sub>O<sub>2</sub> yield, and achieves a higher power density and a better stability than Fe/N/C catalyst, under the same testing condition. Furthermore, the active sites in Fe/N/C and (Fe-Cu)/N/C are also investigated and discussed.

## 2. Experimental

### 2.1 Catalyst synthesis

The catalyst synthesis method can be found in previous report.<sup>6</sup> It was prepared by three precursors: ZIF-8 as carbon precursor (Labeled as MOF. Trade name: Basolite Z1200, Aldrich, produced by BASF); 1,10-Phen (Labeled as Phen. Trade name: 1,10-Phenanthroline, ≥ 99%, Aldrich); and metal acetate salts (FeAc, CuAc, CoAc, NiAc, MnAc). For the (Fe-Cu)/N/C, the total metal mole (Fe + Cu) keeps the same. These precursors were first uniformly mixed together with a mixture of ethanol and deionized (DI) water to form a slurry, then dried at 90 °C overnight. The dry sheet and powder was then undergoing 3 h of ball-milling at 400 rpm. The resulting dry powder was the catalyst precursor ready for pyrolysis. Then the catalyst precursor underwent two stages of pyrolysis in Ar at 1050 °C and in pure ammonia (NH<sub>3</sub>) at 950 °C, respectively. The weight loss of catalyst in the NH<sub>3</sub> pyrolysis step were kept on hold at 50%.

## 2.2 ORR test

All ORR electrochemical measurements were carried out in a three-electrode cell using a rotating disk electrode (RDE, PINE Research Instrumentation) with a bipotentiostat (Pine, Model PGSTAT-72637) workstation at room temperature. A Pt wire and a saturated calomel electrode (SCE) were used as the counter and reference electrodes, respectively. All potentials in this study refer to reversible hydrogen electrode (RHE). A rotating ring-disk electrode (RRDE) with a Pt ring and a GC disk (5.61 mm diameter) was used as the substrate for the working electrodes. Before use, the GC electrode in RRDE was polished using aqueous alumina suspension on felt polishing pads.

The catalyst suspension in this work was prepared as the following: 10 mg of catalyst was mixed in a glass vial with 95  $\mu\text{L}$  of 5 wt% Nafion solution and 350  $\mu\text{L}$  of ethanol, followed by sonication and agitation in a vortex mixer, alternatively, for a total of 1 h. Then 9  $\mu\text{L}$  of the catalyst suspension was dropped onto the GC electrode surface ( $\sim 0.8 \text{ mg cm}^{-2}$ ). For comparison, the 20 wt% Pt/C catalyst (E-TEK) was prepared through the same procedure with a loading amount of 100  $\mu\text{g cm}^{-2}$  (i.e., 20  $\mu\text{g}_{\text{Pt}} \text{ cm}^{-2}$ ). Before testing,  $\text{N}_2$  (or  $\text{O}_2$ ) was bubbled through the electrolyte for 30 min and the  $\text{N}_2$ - (or  $\text{O}_2$ ) was kept bubbling during the measurements, in order to keep the  $\text{N}_2$ - or  $\text{O}_2$ -saturated solution. In 0.1 M KOH (or 0.1 M  $\text{HClO}_4$ ), the cyclic voltammetry (CV) profiles were recorded at 50  $\text{mV s}^{-1}$  and the linear sweep voltammograms (LSV) were recorded at 10  $\text{mV s}^{-1}$ , between 0-1.2 V (vs. RHE). ORR activities were extracted from the negative-going scan for both NPMCs and Pt/C. All of the LSV curves were recorded after subtraction of the background current recorded in  $\text{N}_2$ -saturated solution. For detecting peroxide formed at the disc electrode, the potential for the Pt ring electrode was set at 1.3 V (vs. RHE) and the voltammograms were recorded at 1600 rpm. The collection efficiency of the ring-disk electrode was  $N = 0.37$ . The peroxide yield ( $\text{H}_2\text{O}_2\%$ ) and the electron transfer number ( $n$ ) were calculated as follows:

$$\text{H}_2\text{O}_2\% = 200 \times (\text{I}_r/\text{N})/(\text{I}_d + \text{I}_r/\text{N})$$

$$n = 4 \times \text{I}_d / (\text{I}_d + \text{I}_r/\text{N})$$

Where  $\text{I}_d$  is the disk current and  $\text{I}_r$  is the ring current.

### 2.3 Membrane electrode assembly (MEA)

The ink formula for cathode is (i) 10 mg catalyst; (ii) 147  $\mu\text{L}$  of deionized (DI) water (Millipore Milli-Q, 18.2  $\text{M}\Omega\cdot\text{cm}$ ); (iii) 272  $\mu\text{L}$  of 5 wt% nafion solution; (iv) 206  $\mu\text{L}$  of ethanol. The ink was first sonicated for 15 minutes and then agitated on a vortex mixer for another 15 minutes; the sonication and agitation steps were then repeated. The homogeneous mixed catalyst inks were deposited using a micropipette onto carbon paper as gas diffusion layers (GDL, SGL Sigracet 25BC) by 284  $\mu\text{L}$  ink. The GDL which consists of teflonated carbon fiber paper is covered with a microporous layer made of carbon black and Teflon. The round GDL have an area of 1.14  $\text{cm}^2$ . The GDL with catalyst layer were named as gas diffusion electrodes (GDEs). The target catalyst loading of one GDE was 4  $\text{mg}/\text{cm}^2$ . The preparation of anode GDEs were similar to the cathode, but with 0.5  $\text{mg}_{\text{Pt}}/\text{cm}^2$  of a commercial Pt-based catalyst (Tanaka Kikinzoku, 45.4 wt% Pt/C). The membrane electrode assembly (MEA) was prepared by hot pressing the anode, a Nafion<sup>®</sup> 211 membrane, and the cathode together at 130 °C for 2 min with a load of about 1000 pounds.

### 2.4 PEMFC test

Single cell PEMFC tests were carried out using a homemade fuel cell station and a BioLogic SP-150 Potentiostat with a VMP3B-20 Booster driven by EC-Lab V9.98 software. All of the operating parameters, such as hydrogen/Oxygen stoichiometry, temperature and related humidity as well as backpressure are controlled automatically. The humidifier was automatically filled by the external DI water supply also. At the same time, information was gathered from thermal couples and gases' mass flow meters, etc. as feedback. The flow rates of  $\text{H}_2$  and  $\text{O}_2$  were both kept at 0.3 standard liter per minute (SLPM). The back pressures were set to 1.0 bar gauge for both anode and cathode sides, the cell temperature were set at 80 °C. After all fuel cell parameters were stabilized, electrochemical impedance spectra (EIS) were obtained at open circuit voltage (OCV) with frequencies ranging from 100 kHz to 10 Hz, to obtain the fuel cell resistance. Then, a polarization curve was recorded by scanning the cell voltage from OCV to 0 V (vs. anode) with a scan rate of 0.5  $\text{mV s}^{-1}$ . After recording the first polarization curve, the cell voltage was set at 0.6 V to record the current density delivered by the cell, this current density was used to evaluate the stability of the cathode catalyst.

## 2.5 Physical characterization

The surface properties were analyzed by X-Ray photoelectron spectroscopy (XPS, VG ESCALAB 220i-XL) equipped with a hemispherical analyzer for a Twin Anode X-Ray Source. The C 1s peak (BE = 284.6 eV) was used as the reference line to accurately determine the positions of other spectral lines. The fine structure of the photoelectron lines was treated using Casa XPS software (2.3.15 Version). The surface areas of the catalysts were measured through N<sub>2</sub> sorption isotherms that were collected using Quantachrome Instruments Autosorb-1 at liquid nitrogen temperature. The surface areas were estimated from the Brunauer-Emmett-Teller (BET) equation and from the fitting of the N<sub>2</sub>-adsorption isotherms, with the Quenched solid density functional theory (QSDFT) available in the AS1WIN software. Bulk Fe and Cu contents were determined by neutron activation analysis (NAA) measured at École Polytechnique de Montréal.

The Fe K-edge X-ray absorption near-edge structure (XANES) and Extended X-ray Absorption Fine Structure (EXAFS) data were collected on the 06ID-1 Hard X-ray MicroAnalysis (HXMA) beamline at the Canadian Light Source. During data collection, the CLS storage ring (2.9 GeV) was operated under 250 mA mode and the HXMA superconducting wiggler was run at 1.9 T. Measurements were made at room temperature in fluorescence mode using a 32-element Ge detector. Data collection configuration was using metal Fe foil as energy calibration by in step calibration for every data sets. The spectra were normalized with respect to the edge height after subtracting the pre-edge and post-edge backgrounds, then convert the data from energy space to k space using Athena software.

## 3. Results and Discussion

According to the MOF-derived Fe/N/C developed previously,<sup>6</sup> we firstly prepared Me/N/C (Me=Fe, Co, Cu, Mn, Ni) by physical mixing ZIF-8, metal acetates (the same ratio of other metal as the optimized Fe) and 1,10-phenanthroline, followed by two annealing treatments under Ar and NH<sub>3</sub> respectively. Figure S1 displays the catalytic ORR performance of different Me/N/C in acid electrolyte. The potential at 3 mA cm<sup>-2</sup> of these catalysts are shown in Figure S1c. From our results, the ORR activity of the different Me/N/C catalysts decreased in the order Fe > Cu > Co > Ni > Mn. The H<sub>2</sub>O<sub>2</sub>% yield at 0.6 V decreased as the order Fe ≈ Cu < Co < Ni < Mn. These trends confirm Nature's choice of metal-center in ORR-functioned enzymes of many forms of

lives (Figure S2). It has also been reported that the synergistic effect of bimetallic (Fe-Me)/N/C can further improve the ORR performance. Based on these points, we prepared the bimetallic (Fe-Cu)/N/C catalysts by keeping the total (Fe+Cu) equals the optimized Fe content. The ORR activity of Fe/N/C and (Fe-Cu)/N/C was first assessed by cyclic voltammetry (CV). In N<sub>2</sub>-saturated 0.1 M HClO<sub>4</sub>, both samples exhibited a featureless CV curve, while (Fe-Cu)/N/C shows a much larger capacitance, indicating a higher surface area. Figure 1b and Figure S3 compares the ORR polarization curves of Fe/N/C and (Fe-Cu)/N/C in O<sub>2</sub>-saturated 0.1 M HClO<sub>4</sub>, the current density in the low-overpotential area of these two samples are very close, while (Fe-Cu)/N/C displays a higher limiting current, might be caused by the higher percentage of mesopore. Different content of Cu has little effects on the ORR activity in the half cell testing condition (Figure S3), but from the polarization curves of different *x*%-(Fe-Cu)/N/C in the H<sub>2</sub>-air fuel cell test, we can obtain the optimized content of 5% of Cu in (Fe-Cu)/N/C (Figure S4), the neutron activation analysis (NAA) results confirmed the ratio of Cu/Fe around 5%. Figure 1c is the calculated H<sub>2</sub>O<sub>2</sub> yield according to the RRDE test results, the (Fe-Cu)/N/C catalyst remained below that of Fe/N/C samples at all potentials in 0.1 M HClO<sub>4</sub>. Under 0.6 V, an acceptable balance voltage between energy efficiency and power density for well-performing catalysts, the H<sub>2</sub>O<sub>2</sub> yield of (Fe-Cu)/N/C is 1.3% lower than that of Fe/N/C. To compare the kinetic current, Tafel slope was plotted in Figure 1d, showing a 65 mV/decade for (Fe-Cu)/N/C, a little lower than Fe/N/C (70 mV/decade), indicating a better kinetic process by using the Fe-Cu bimetallic strategy. These results in the acidic half-cell test indicate that a possible synergistic effect brought by co-doping with Fe and Cu could improve the ORR kinetic process, mass transportation property, and decrease the H<sub>2</sub>O<sub>2</sub> yield.

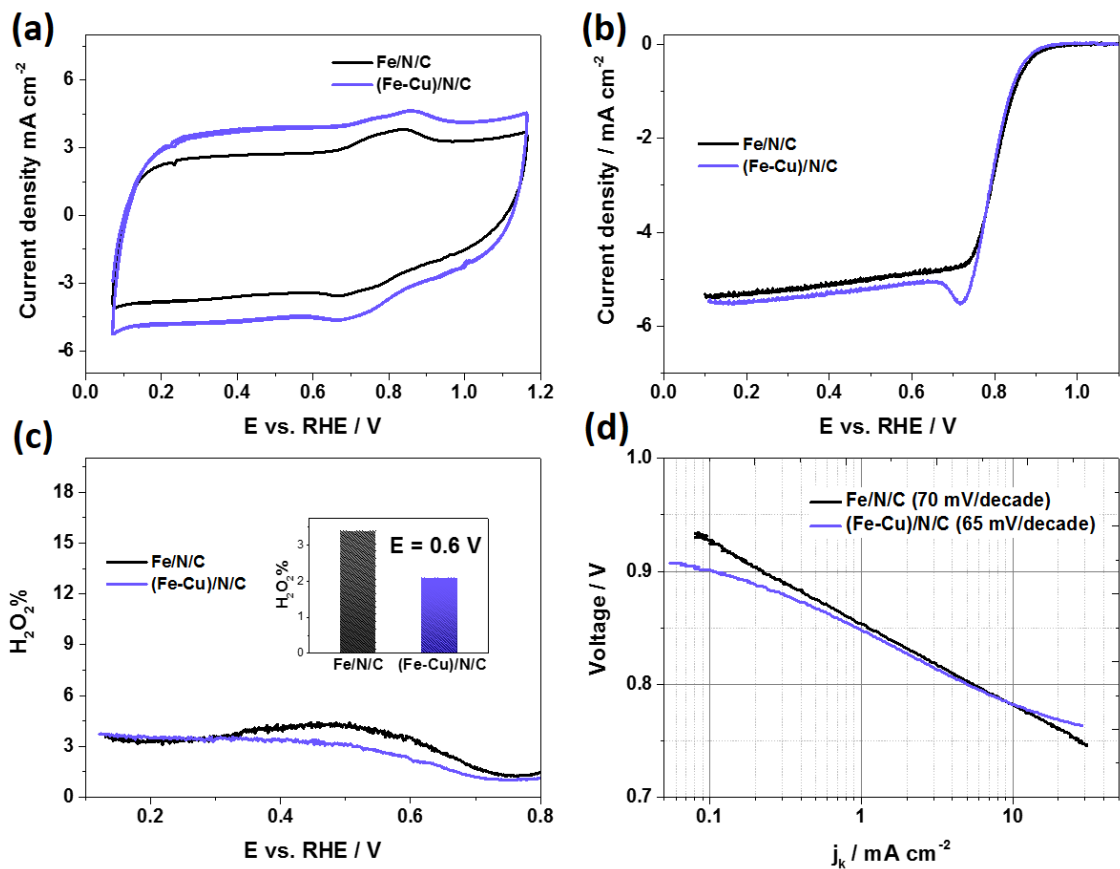


**Figure 1.** (a) CV curves in  $N_2$ -saturated  $0.1\text{ M HClO}_4$  at a scan rate of  $50\text{ mV s}^{-1}$ . (b) ORR polarization curves of (Fe-Cu)/N/C and Fe/N/C in  $O_2$ -saturated  $0.1\text{ M HClO}_4$  at a scan rate of  $10\text{ mV s}^{-1}$ , rotation rate = 1600 rpm. (c)  $H_2O_2$  yield calculated from the RRDE voltammograms in (b). (d) Tafel plot derived from (b).

Previously, most of NPMC cathodes for PEMFC were performed under  $O_2$ , which may disguise the effects of concentration polarization. Herein,  $H_2$ -air fuel cell tests were conducted to evaluate both Fe/N/C and (Fe-Cu)/N/C, in terms of its feasibility to be a practical Pt-free cathode in PEMFCs. Membrane assembly electrodes (MEAs) consisted a NPMC loading of  $4.0\text{ mg cm}^{-2}$  on the cathode, and  $0.5\text{ mg}_{Pt}\text{ cm}^{-2}$  on the anode. A back-pressure of 1 bar was applied to enhance the mass transfer. In order to investigate the impedance of MEA, EIS testing was conducted at the OCV. The typical Nyquist plot were displayed in Figure S5, the intersection of curves with X-axis at the high frequency represents the Ohm resistance ( $R_0$ ) of MEA. The  $R_0$  values are decreasing with the increasing stability test time for both samples. This is caused by the membrane wetting process during the reaction to moisten the membrane and provide better proton conduction. Figure 2a illustrates the polarization curves and power density plots of the

PEMFC with Fe/N/C and (Fe-Cu)/N/C as cathode catalysts. Apparently, the current density of (Fe-Cu)/N/C is higher than Fe/N/C, especially in the mass transport area (low potential area). To eliminate the potential loss caused by ohmic resistance due to proton conduction through the electronic contact resistances, the  $iR$ -corrected current density and power density were exhibited in Figure 2b. After  $iR$  correction, the peak power density of (Fe-Cu)/N/C reaches  $0.4 \text{ W cm}^{-2}$ , higher than  $0.36 \text{ W cm}^{-2}$  for Fe/N/C. Except the activity and power density, the durability is also required to ultimately replace Pt for a NPMC. To evaluate the durability, the PEMFC with Fe/N/C and (Fe-Cu)/N/C was operated under 0.6 V at  $80 \text{ }^\circ\text{C}$  for 40 h. Like the most NPMC in the single PEMFC stability test, a fast decay can be observed for both samples in the initial 15 h,<sup>38</sup> but the current density of (Fe-Cu)/N/C is higher in the whole process, after 40 h, the current density can keep as  $267 \text{ mA cm}^{-2}$ ; while the current density for Fe/N/C is  $213 \text{ mA cm}^{-2}$ , around 80% of (Fe-Cu)/N/C. Figure 2d presents the normalized to its initial current density at 0.6 V in Figure 2c. From the normalization, we can see that after 12 h, the (Fe-Cu)/N/C emerges better stability than Fe/N/C, after 40 h stability test at 0.6 V, the current density of (Fe-Cu)/N/C-based fuel cell keeps 47.8% of the initial value, versus 44.1% of Fe/N/C-based one. We attribute the slightly improvement of the stability to the lower  $\text{H}_2\text{O}_2$  yield at around 0.6 V shown in Figure 1c. The results here indicate that carbon oxidation attack by  $\text{H}_2\text{O}_2$  playing more roles in the slow decay part after 15 h during the potentiostatic stability test.

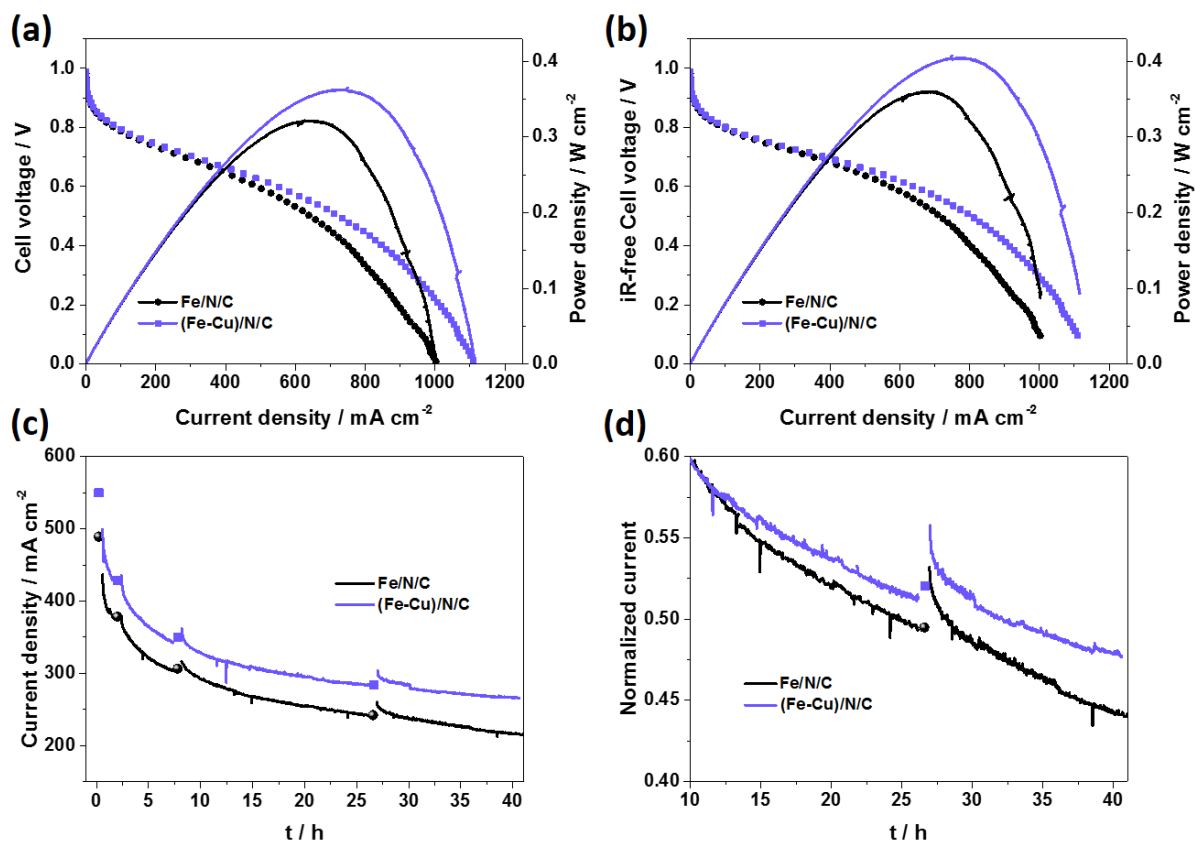


**Figure 2.** (a) Polarization and power density plots for H<sub>2</sub>-air PEMFC with (Fe-Cu)/N/C and Fe/N/C as cathode catalyst at 80 °C. (b) i-R corrected of (a). (c) Chronoamperometry curves showing the current density decay at 0.6 V for H<sub>2</sub>-air PEMFC. (d) The normalized stability, each curve is normalized to its initial current density at 0.6 V in (c). The back pressure is 1 bar; flow rate: 0.3 slpm; MEA active area: 1.14 cm<sup>2</sup>; NRE 211 membrane; cathode loading: 4.0 mg cm<sup>-2</sup>; anode catalyst: Pt/C (45.4%, TKK) with 0.5 mg<sub>Pt</sub> cm<sup>-2</sup>.

To explain why (Fe-Cu)/N/C has similar ORR activity, but higher power density and better stability than the Fe/N/C counterpart, some physical characterizations were conducted. Figure 3 shows the result of N<sub>2</sub> isothermal adsorption/desorption measurements. A high BET surface area was calculated for (Fe-Cu)/N/C sample (722.4 m<sup>2</sup> g<sup>-1</sup>) compared with Fe/N/C (657 m<sup>2</sup> g<sup>-1</sup>). From the sorption isotherm in Figure 3a, the N<sub>2</sub> adsorption tracks very similar trend under low pressure and middle pressure area, however, there is an abrupt increase at around P/P<sub>0</sub> = 0.9, this indicates that the (Fe-Cu)/N/C sample has a much larger external surface area. As revealed by the QSDFT pore size distribution shown in the inset of Figure 3a and the histogram of the micropore surface area and mesopore surface area in Figure 3b, the mesopore area of the (Fe-Cu)/N/C sample (292 m<sup>2</sup> g<sup>-1</sup>) is 5.6 times higher than Fe/N/C (52 m<sup>2</sup> g<sup>-1</sup>), but micropore area of the former is smaller

( $430 \text{ m}^2 \text{ g}^{-1}$  vs.  $605 \text{ m}^2 \text{ g}^{-1}$ ). In the fuel-cell test, the high external surface area and large pore size of the (Fe-Cu)/N/C can facilitate the accessibility of reactant for ORR, corresponding well with the CV results in Figure 1 and power density plots in Figure 2.

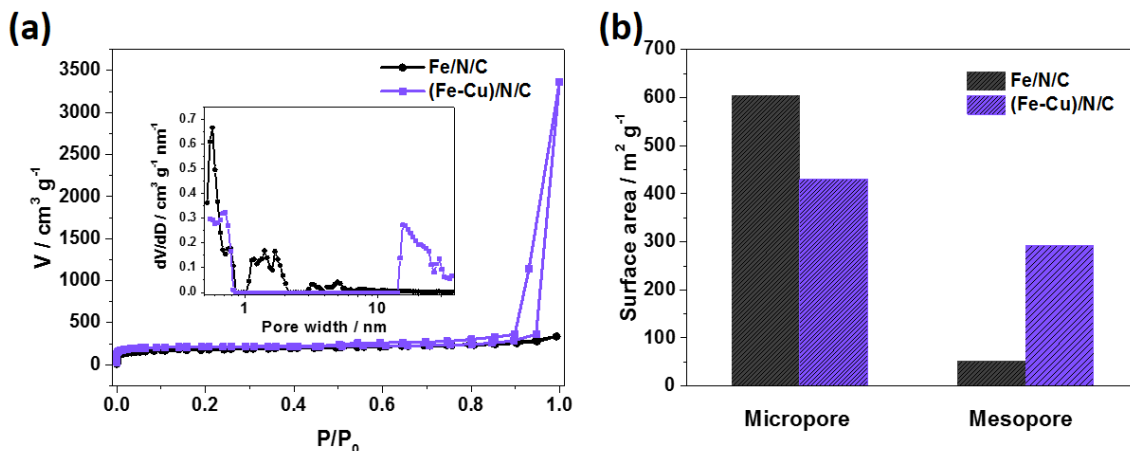


**Figure 3.** (a)  $\text{N}_2$  adsorption/desorption isotherm of Fe/N/C and (Fe-Cu)/N/C. Inset: the corresponding pore size distribution curves obtained from the adsorption branches. (b) The histogram of micropore and mesopore of the Fe/N/C and (Fe-Cu)/N/C samples.

The presence of C, N, O, was clearly observed in the XPS survey spectra of both the (Fe-Cu)/N/C and Fe/N/C samples (Figure S6), while the Fe or Cu peak is almost invisible due to the low content. Moreover, the content of pyridinic-N, pyrrolic-N, graphitic-N and N-oxides, obtained from deconvolution of the refined N1s spectra were displayed in Figure 4a. As can be seen, with the addition of Cu, the pyrrolic-N decreased obviously, while the variation of other types of N is not very distinct. Moreover, X-ray absorption near-edge structure (XANES) analysis is a powerful tool to analyze transition metal elements. The Fe K-edge XANES of (Fe-Cu)/N/C and Fe/N/C, with Fe foil, FePc, FeAc,  $\text{Fe}_2\text{O}_3$  as references, was showed in Figure 4b. The valence of Fe species in (Fe-Cu)/N/C and Fe/N/C followed the similar feature. Both of them situated between  $\text{Fe}^{2+}$  and  $\text{Fe}^{3+}$ , because their absorption edges located between that of FeAc and  $\text{Fe}_2\text{O}_3$ . The Fourier transform (FT)  $k^3$ -weighted extended X-ray absorption fine structure (EXAFS) curve of (Fe-Cu)/N/C, Fe/N/C and references were shown in Figure 4c. Both (Fe-Cu)/N/C and Fe/N/C possess a main peak at  $\sim 1.5 \text{ \AA}$  assigning to Fe-N<sub>4</sub> structure, and very weak signals at  $2.2 \text{ \AA}$  attributing to the metallic Fe-Fe bond. Interestingly, by carefully comparing (Figure 4d), we can find that the average Fe-N bond distance in (Fe-Cu)/N/C is longer than that

in Fe/N/C. The longer Fe-N bond distance caused by the addition of Cu resembles those of the noncoplanar  $N_{\text{axi}}\text{-Fe}^{2+}(\text{HS})\text{-N}_4$  site in myoglobin and biomimetic catalysts.<sup>39</sup> As for the active sites, it has been reported two kinds of active sites (Figure S7) being well accepted,<sup>40-41</sup> (i) FeN<sub>4</sub>/C modeled as a porphyrin-like  $\text{Fe}^{\text{II}}\text{N}_4\text{C}_{12}$ , either hosted in a micropore bridging the “zig-zag” sides of two graphene layers or integrated into a graphene layer. In this case, the N configuration should be penta-heterocycles, corresponding the “pyrrolic-N” in XPS spectrum of N; (ii) FeN<sub>2+2</sub>/C modeled as  $[\text{Fe}^{\text{II}}(\text{N}_2\text{R})_2]^{2+}$ , either hosted in a micropore bridging the “armchair” side of two graphene layers or integrated into a graphene layer. In this case, the N configuration should be hexatomic ring, corresponding the “pyridinic-N” in XPS spectrum of N. According to our XPS results (Figure 4a), more pyrrolic-N is observed for the Fe/N/C, indicating more porphyrin-like  $\text{Fe}^{\text{II}}\text{N}_4\text{C}_{12}$  active sites existing in Fe/N/C. Moreover, the shorter average Fe-N bond distance of Fe/N/C also corresponds well with the higher porphyrin-like  $\text{Fe}^{\text{II}}\text{N}_4\text{C}_{12}$  existing among the “pyrrolic-N”; while for longer average Fe-N bond distance of (Fe-Cu)/N/C, the active sites formation of FeN<sub>2+2</sub>/C model are promoted.

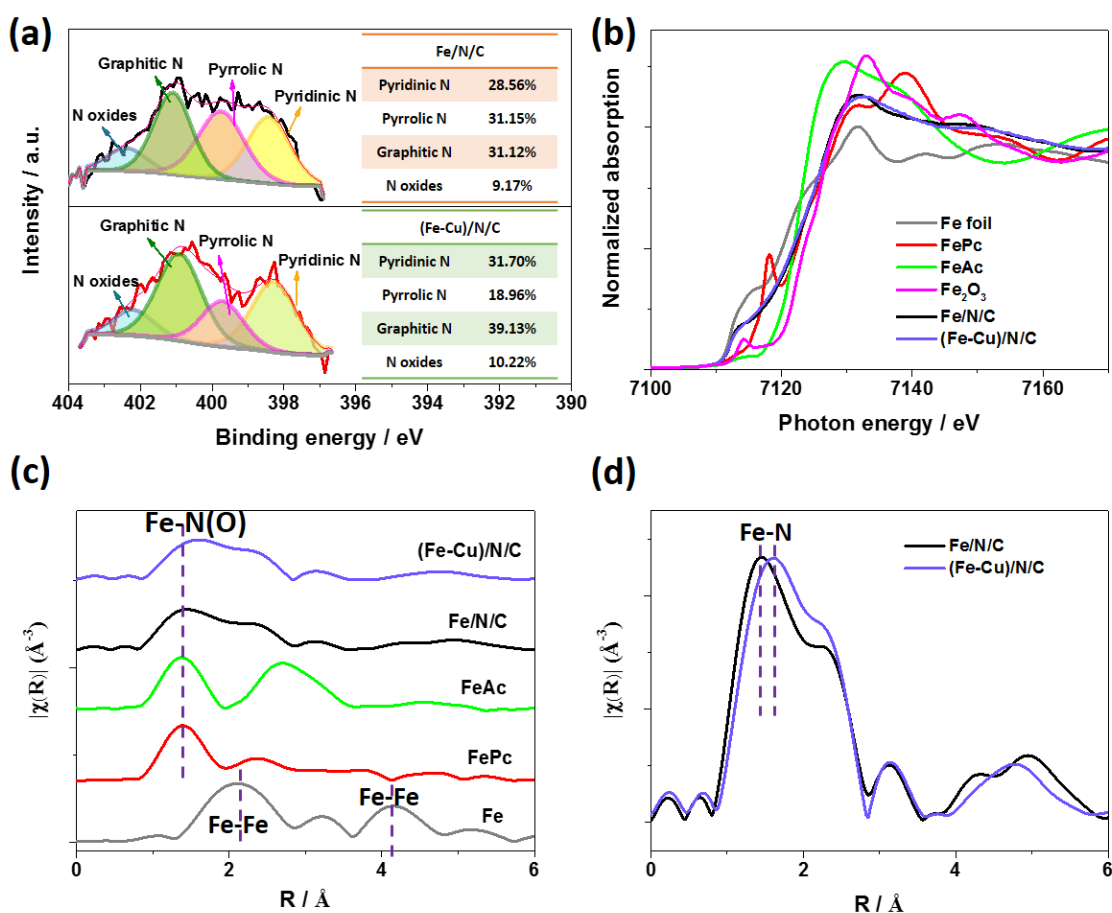


**Figure 4.** (a) Core level N 1s XPS spectrum of (Fe-Cu)/N/C and Fe/N/C. (b) Normalized Fe K-edge XANES spectra of Fe/N/C, (Fe-Cu)/N/C, and reference samples. (c) The magnitude of Fourier-transformed EXAFS oscillation  $k^3\chi(k)$  spectra of Fe/N/C, (Fe-Cu)/N/C, and reference samples. (d) A close comparison of the EXAFS oscillation  $k^3\chi(k)$  spectra of Fe/N/C, (Fe-Cu)/N/C.

#### 4. Conclusion

In summary, inspired by the metal-centered structure of the ORR-functioned enzyme in life and the synergistic effects between transition metals, we prepared highly porous (Fe-Cu)/N/C based on MOF. We found that compared with the Fe/N/C, the as-synthesized (Fe-Cu)/N/C possesses higher surface area, longer Fe-N bond, shows high ORR activity with lower H<sub>2</sub>O<sub>2</sub> yield in the range of 0.3-0.8 V in a half-cell test in acid medium. Importantly, when applied in a MEA in the H<sub>2</sub>-air PEMFC, the (Fe-Cu)/N/C catalyst demonstrate a higher power density of 0.4 W cm<sup>-2</sup>, and an enhanced stability, i.e., improvement of 3.7% of the current density under a potentiostatic testing after 40 h. Moreover, from the XPS and XAS analysis, it can be obtained that more

porphyrin-like Fe<sup>II</sup>N<sub>4</sub>C<sub>12</sub> active sites existing in Fe/N/C, while FeN<sub>2+2</sub>/C modeled active sites are more prominent in (Fe-Cu)/N/C catalyst.

## References

- [1] Jacobson, M. Z. Roadmaps to transition countries to 100% clean, renewable energy for all purposes to curtail global warming, Air Pollution, and Energy Risk. *Earth's Future* **2017**, 5 (10), 948-952.
- [2] Li, C.; Meckler, S. M.; Smith, Z. P.; Bachman, J. E.; Maserati, L.; Long, J. R.; Helms, B. A. Engineered Transport in Microporous Materials and Membranes for Clean Energy Technologies. *Advanced Materials* **2018**, 30 (8), 1704953.
- [3] Banham, D.; Ye, S.; Pei, K.; Ozaki, J.-i.; Kishimoto, T.; Imashiro, Y. A review of the stability and durability of non-precious metal catalysts for the oxygen reduction reaction in proton exchange membrane fuel cells. *Journal of Power Sources* **2015**, 285, 334-348.
- [4] Bashyam, R.; Zelenay, P. A class of non-precious metal composite catalysts for fuel cells. *Nature* **2006**, 443 (7107), 63.
- [5] Lefevre, M.; Proietti, E.; Jaouen, F.; Dodelet, J. P. Iron-based catalysts with improved oxygen reduction activity in polymer electrolyte fuel cells. *Science* **2009**, 324 (5923), 71.
- [6] Proietti, E.; Jaouen, F.; Lefevre, M.; Larouche, N.; Tian, J.; Herranz, J.; Dodelet, J. P. Iron-based cathode catalyst with enhanced power density in polymer electrolyte membrane fuel cells. *Nat Commun* **2011**, 2, 416.
- [7] Fu, X.; Zamani, P.; Choi, J. Y.; Hassan, F. M.; Jiang, G.; Higgins, D. C.; Zhang, Y.; Hoque, M. A.; Chen, Z. In Situ Polymer Graphenization Ingrained with Nanoporosity in a Nitrogenous Electrocatalyst Boosting the Performance of Polymer-Electrolyte-Membrane Fuel Cells. *Adv Mater* **2017**, 29 (7).
- [8] Wang, X. X.; Cullen, D. A.; Pan, Y. T.; Hwang, S.; Wang, M.; Feng, Z.; Wang, J.; Engelhard, M. H.; Zhang, H.; He, Y.; Shao, Y.; Su, D.; More, K. L.; Spendelow, J. S.; Wu, G. Nitrogen-Coordinated Single Cobalt Atom Catalysts for Oxygen Reduction in Proton Exchange Membrane Fuel Cells. *Adv Mater* **2018**, 30.

- [9] Liu, Q.; Liu, X.; Zheng, L.; Shui, J. The Solid-Phase Synthesis of an Fe-N-C Electrocatalyst for High-Power Proton-Exchange Membrane Fuel Cells. *Angew Chem Int Ed Engl* **2018**, *57* (5), 1204-1208.
- [10] Fei, H.; Dong, J.; Feng, Y.; Allen, C. S.; Wan, C.; Voloskiy, B.; Li, M.; Zhao, Z.; Wang, Y.; Sun, H.; An, P.; Chen, W.; Guo, Z.; Lee, C.; Chen, D.; Shakir, I.; Liu, M.; Hu, T.; Li, Y.; Kirkland, A. I.; Duan, X.; Huang, Y. General synthesis and definitive structural identification of MN<sub>4</sub>C<sub>4</sub> single-atom catalysts with tunable electrocatalytic activities. *Nature Catalysis* **2018**, *1* (1), 63-72.
- [11] Yuan, K.; Sfaelou, S.; Qiu, M.; Lützenkirchen-Hecht, D.; Zhuang, X.; Chen, Y.; Yuan, C.; Feng, X.; Scherf, U. Synergetic Contribution of Boron and Fe–N<sub>x</sub> Species in Porous Carbons toward Efficient Electrocatalysts for Oxygen Reduction Reaction. *ACS Energy Letters* **2018**, *3* (1), 252-260.
- [12] Zitolo, A.; Ranjbar-Sahraie, N.; Mineva, T.; Li, J.; Jia, Q.; Stamatina, S.; Harrington, G. F.; Lyth, S. M.; Krttil, P.; Mukerjee, S.; Fonda, E.; Jaouen, F. Identification of catalytic sites in cobalt-nitrogen-carbon materials for the oxygen reduction reaction. *Nat Commun* **2017**, *8* (1), 957.
- [13] Zhang, H.; Hwang, S.; Wang, M.; Feng, Z.; Karakalos, S.; Luo, L.; Qiao, Z.; Xie, X.; Wang, C.; Su, D.; Shao, Y.; Wu, G. Single Atomic Iron Catalysts for Oxygen Reduction in Acidic Media: Particle Size Control and Thermal Activation. *J Am Chem Soc* **2017**, *139* (40), 14143-14149.
- [14] Kuang, M.; Wang, Q.; Han, P.; Zheng, G. Cu, Co-Embedded N-Enriched Mesoporous Carbon for Efficient Oxygen Reduction and Hydrogen Evolution Reactions. *Advanced Energy Materials* **2017**, *7* (17), 1700193.
- [15] Zhang, L.; Wilkinson, D. P.; Liu, Y.; Zhang, J. Progress in nanostructured (Fe or Co)/N/C non-noble metal electrocatalysts for fuel cell oxygen reduction reaction. *Electrochimica Acta* **2018**, *262*, 326-336.
- [16] Sahraie, N. R.; Kramm, U. I.; Steinberg, J.; Zhang, Y.; Thomas, A.; Reier, T.; Paraknowitsch, J. P.; Strasser, P. Quantifying the density and utilization of active sites in non-precious metal oxygen electroreduction catalysts. *Nat Commun* **2015**, *6*, 8618.

- [17] Fan, W.; Li, Z.; You, C.; Zong, X.; Tian, X.; Miao, S.; Shu, T.; Li, C.; Liao, S. Binary Fe, Cu-doped bamboo-like carbon nanotubes as efficient catalyst for the oxygen reduction reaction. *Nano Energy* **2017**, *37*, 187-194.
- [18] Yang, W.; Liu, X.; Yue, X.; Jia, J.; Guo, S. Bamboo-like carbon nanotube/Fe<sub>3</sub>C nanoparticle hybrids and their highly efficient catalysis for oxygen reduction. *J Am Chem Soc* **2015**, *137* (4), 1436.
- [19] Wei, Q.; Zhang, G.; Yang, X.; Chenitz, R.; Banham, D.; Yang, L.; Ye, S.; Knights, S.; Sun, S. 3D Porous Fe/N/C Spherical Nanostructures As High-Performance Electrocatalysts for Oxygen Reduction in Both Alkaline and Acidic Media. *ACS Appl Mater Interfaces* **2017**, *9* (42), 36944-36954.
- [20] Wang, J.; Huang, Z.; Liu, W.; Chang, C.; Tang, H.; Li, Z.; Chen, W.; Jia, C.; Yao, T.; Wei, S.; Wu, Y.; Li, Y. Design of N-Coordinated Dual-Metal Sites: A Stable and Active Pt-Free Catalyst for Acidic Oxygen Reduction Reaction. *J Am Chem Soc* **2017**, *139* (48), 17281-17284.
- [21] Lai, Q.; Zheng, L.; Liang, Y.; He, J.; Zhao, J.; Chen, J. Metal–Organic-Framework-Derived Fe-N/C Electrocatalyst with Five-Coordinated Fe-N<sub>x</sub> Sites for Advanced Oxygen Reduction in Acid Media. *ACS Catalysis* **2017**, *7* (3), 1655-1663.
- [22] Yi, J.-D.; Xu, R.; Wu, Q.; Zhang, T.; Zang, K.-T.; Luo, J.; Liang, Y.-L.; Huang, Y.-B.; Cao, R. Atomically Dispersed Iron–Nitrogen Active Sites within Porphyrinic Triazine-Based Frameworks for Oxygen Reduction Reaction in Both Alkaline and Acidic Media. *ACS Energy Letters* **2018**, *3* (4), 883-889.
- [23] Osmieri, L.; Escudero-Cid, R.; Armandi, M.; Videla, A. H. A. M.; Fierro, J. L. G.; Ocón, P.; Specchia, S. Fe-N/C catalysts for oxygen reduction reaction supported on different carbonaceous materials. Performance in acidic and alkaline direct alcohol fuel cells. *Applied catalysis b: environmental* **2017**, *205*, 637-653.
- [24] Goellner, V.; Armel, V.; Zitolo, A.; Fonda, E.; Jaouen, F. Degradation by hydrogen peroxide of metal-nitrogen-carbon catalysts for oxygen reduction. *Journal of The Electrochemical Society* **2015**, *162* (6), H403-H414.
- [25] Lefèvre, M.; Dodelet, J.-P. Fe-based catalysts for the reduction of oxygen in polymer electrolyte membrane fuel cell conditions: determination of the amount of peroxide released during electroreduction and its influence on the stability of the catalysts. *Electrochimica Acta* **2003**, *48* (19), 2749-2760.

- [26] Wu, G.; More, K. L.; Johnston, C. M.; Zelenay, P. High-performance electrocatalysts for oxygen reduction derived from polyaniline, iron, and cobalt. *Science* **2011**, *332* (6028), 443-447.
- [27] Lin, L.; Yang, Z. K.; Jiang, Y.-F.; Xu, A.-W. Nonprecious Bimetallic (Fe,Mo)-N/C Catalyst for Efficient Oxygen Reduction Reaction. *ACS Catalysis* **2016**, *6* (7), 4449-4454.
- [28] Deng, L.; Zhou, M.; Liu, C.; Liu, L.; Liu, C.; Dong, S. Development of high performance of Co/Fe/N/CNT nanocatalyst for oxygen reduction in microbial fuel cells. *Talanta* **2010**, *81* (1-2), 444-8.
- [29] Wu, M.; Hu, X.; Li, C.; Li, J.; Zhou, H.; Zhang, X.; Liu, R. Encapsulation of metal precursor within ZIFs for bimetallic N-doped carbon electrocatalyst with enhanced oxygen reduction. *International Journal of Hydrogen Energy* **2018**.
- [30] He, Q.; Yang, X.; He, R.; Bueno-López, A.; Miller, H.; Ren, X.; Yang, W.; Koel, B. E. Electrochemical and spectroscopic study of novel Cu and Fe-based catalysts for oxygen reduction in alkaline media. *Journal of Power Sources* **2012**, *213*, 169-179.
- [31] Palaniselvam, T.; Kashyap, V.; Bhange, S. N.; Baek, J. B.; Kurungot, S. Nanoporous Graphene Enriched with Fe/Co-N Active Sites as a Promising Oxygen Reduction Electrocatalyst for Anion Exchange Membrane Fuel Cells. *Advanced Functional Materials* **2016**, *26* (13), 2150-2162.
- [32] Noh, S. H.; Seo, M. H.; Kang, J.; Okajima, T.; Han, B.; Ohsaka, T. Towards a comprehensive understanding of FeCo coated with N-doped carbon as a stable bi-functional catalyst in acidic media. *NPG Asia Materials* **2016**, *8* (9), e312.
- [33] An, L.; Jiang, N.; Li, B.; Hua, S.; Fu, Y.; Liu, J.; Hao, W.; Xia, D.; Sun, Z. A highly active and durable iron/cobalt alloy catalyst encapsulated in N-doped graphitic carbon nanotubes for oxygen reduction reaction by a nanofibrous dicyandiamide template. *Journal of Materials Chemistry A* **2018**, *6* (14), 5962-5970.
- [34] Zhu, C.; Shi, Q.; Xu, B. Z.; Fu, S.; Wan, G.; Yang, C.; Yao, S.; Song, J.; Zhou, H.; Du, D. Hierarchically Porous M-N-C (M= Co and Fe) Single-Atom Electrocatalysts with Robust MN<sub>x</sub> Active Moieties Enable Enhanced ORR Performance. *Advanced Energy Materials* **2018**, 1801956.
- [35] Momenteau, M.; Reed, C. A. Synthetic heme-dioxygen complexes. *Chemical Reviews* **1994**, *94* (3), 659-698.

- [36] Kramm, U. I.; Lefèvre, M.; Larouche, N.; Schmeisser, D.; Dodelet, J.-P. Correlations between mass activity and physicochemical properties of Fe/N/C catalysts for the ORR in PEM fuel cell via  $^{57}\text{Fe}$  Mossbauer spectroscopy and other techniques. *Journal of the American Chemical Society* **2014**, *136* (3), 978-985.
- [37] Bhagi-Damodaran, A.; Michael, M. A.; Zhu, Q.; Reed, J.; Sandoval, B. A.; Mirts, E. N.; Chakraborty, S.; Moënné-Loccoz, P.; Zhang, Y.; Lu, Y. Why copper is preferred over iron for oxygen activation and reduction in haem-copper oxidases. *Nature Chemistry* **2017**, *9* (3), 257.
- [38] Zhang, G.; Chenitz, R.; Lefèvre, M.; Sun, S.; Dodelet, J.-P. Is iron involved in the lack of stability of Fe/N/C electrocatalysts used to reduce oxygen at the cathode of PEM fuel cells? *Nano Energy* **2016**, *29*, 111-125.
- [39] Jia, Q.; Ramaswamy, N.; Hafiz, H.; Tylus, U.; Strickland, K.; Wu, G.; Barbiellini, B.; Bansil, A.; Holby, E. F.; Zelenay, P. Experimental observation of redox-induced Fe–N switching behavior as a determinant role for oxygen reduction activity. *ACS Nano* **2015**, *9* (12), 12496-12505.
- [40] Chenitz, R.; Kramm, U. I.; Lefèvre, M.; Glibin, V.; Zhang, G.; Sun, S.; Dodelet, J.-P. A specific demetalation of Fe–N<sub>4</sub> catalytic sites in the micropores of NC\_Ar+ NH<sub>3</sub> is at the origin of the initial activity loss of the highly active Fe/N/C catalyst used for the reduction of oxygen in PEM fuel cells. *Energy & Environmental Science* **2018**, *11* (2), 365-382.
- [41] Glibin, V. P.; Dodelet, J.-P. Thermodynamic Stability in Acid Media of FeN<sub>4</sub>-Based Catalytic Sites Used for the Reaction of Oxygen Reduction in PEM Fuel Cells. *Journal of The Electrochemical Society* **2017**, *164* (9), F948-F957.

## Supporting Information

### **Bio-inspired nonprecious bimetallic (Fe-Cu)/N/C catalyst for oxygen reduction in proton exchange membrane fuel cells**

*Qiliang Wei<sup>1</sup>, Xiaohua Yang<sup>1</sup>, Gaixia Zhang<sup>1,\*</sup>, Ning Chen<sup>2</sup>, Shuhui Sun<sup>1,\*</sup>*

<sup>1</sup>Énergie, Matériaux et Télécommunications, Institut National de la Recherche Scientifique (INRS), 1650 Boul. Lionel-Boulet, Varennes, Quebec J3X 1S2, Canada

<sup>2</sup>Canadian Light Source (CLS), 44 Innovation Boulevard, Saskatoon, SK, S7N 2V3, Canada.

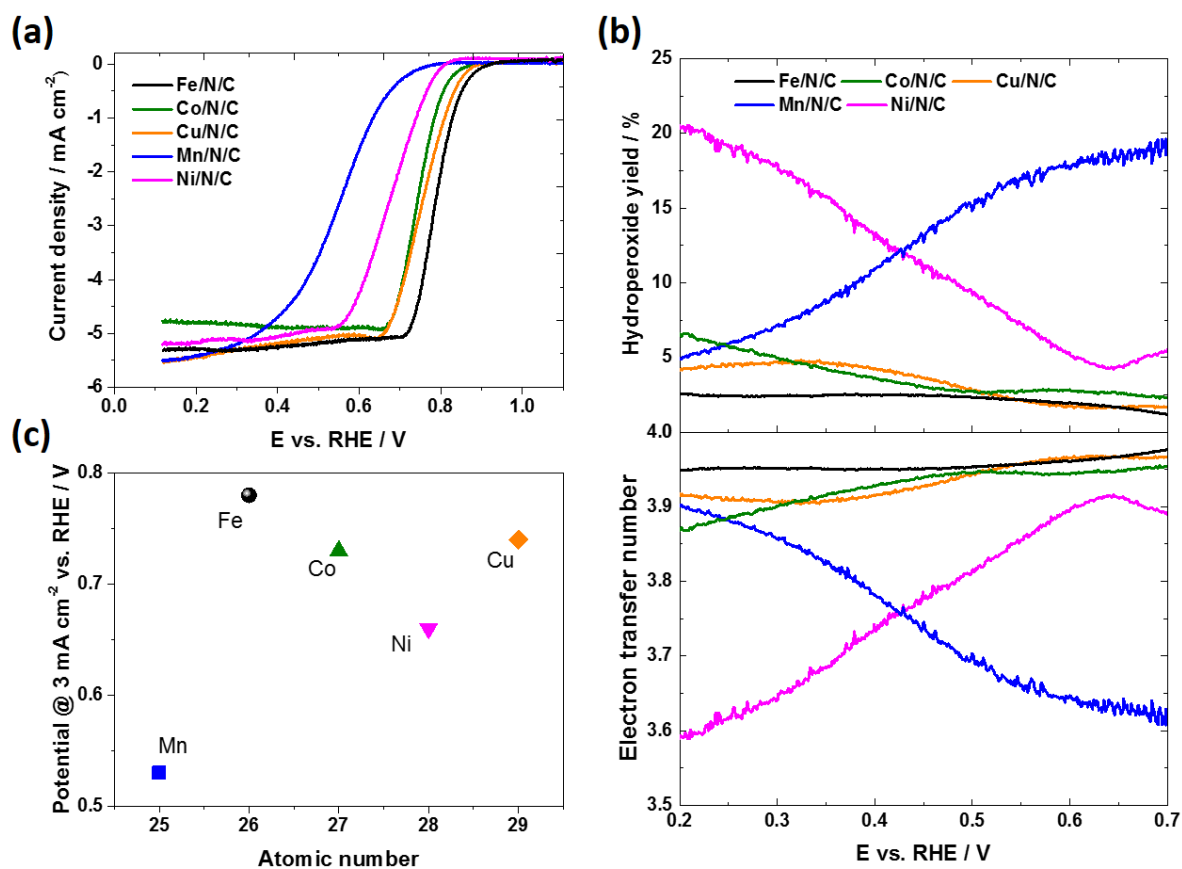


**Figure S1.** (a) ORR polarization curves of Me/N/C (Me = Fe, Co, Cu, Ni, Mn) in O<sub>2</sub>-saturated 0.1 M HClO<sub>4</sub> at a scan rate of 10 mV s<sup>-1</sup>, rotation rate = 1600 rpm. (b) Percentage of produced peroxide and number of exchanged electrons as a function of the applied potential. (c) A comparison of potential at 3 mA cm<sup>-2</sup> for different Me/N/C, measured condition: O<sub>2</sub>-saturated 0.1 M HClO<sub>4</sub> at a scan rate of 10 mV s<sup>-1</sup>, rotation rate = 1600 rpm.

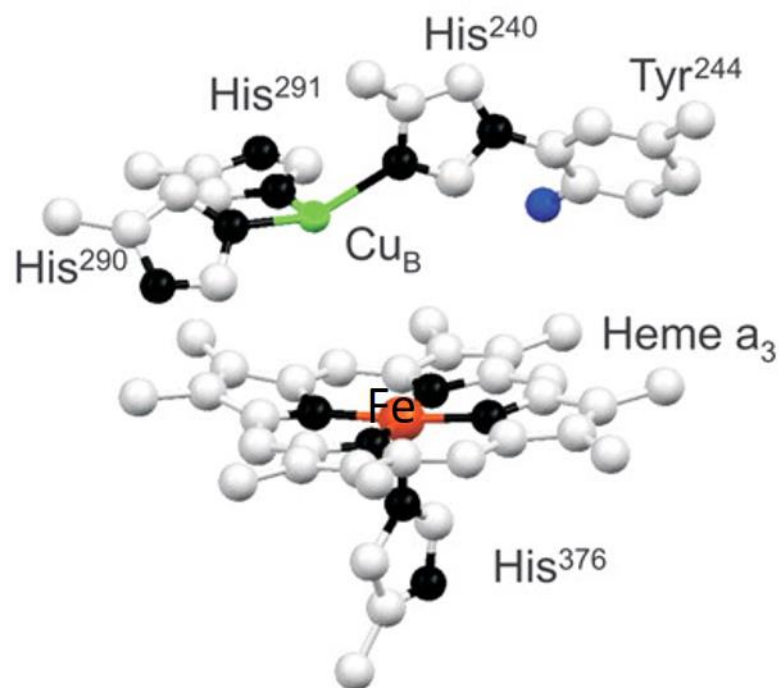


**Figure S2.** Crystal structure of the active site of CcO from the bovine heart. [Ref: Science, 2007, 315, 1565-1568]

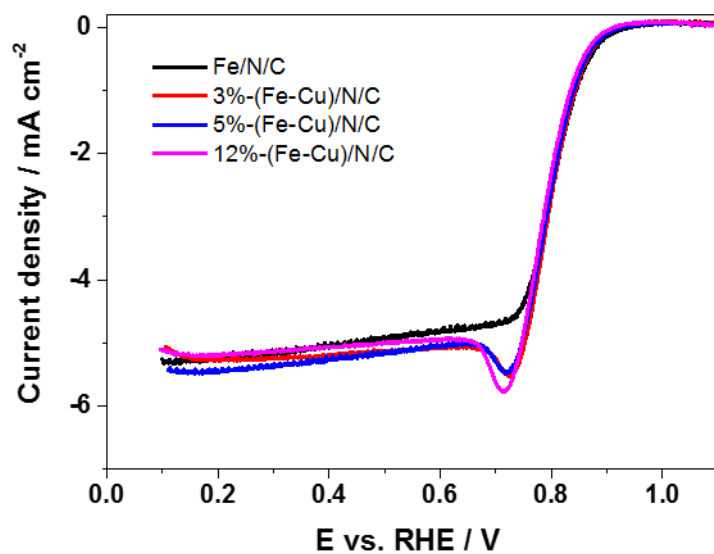


**Figure S3.** ORR polarization curves of (Fe-Cu)/N/C with different percentage of Cu in O<sub>2</sub>-saturated 0.1 M HClO<sub>4</sub> at a scan rate of 10 mV s<sup>-1</sup>, rotation rate = 1600 rpm.

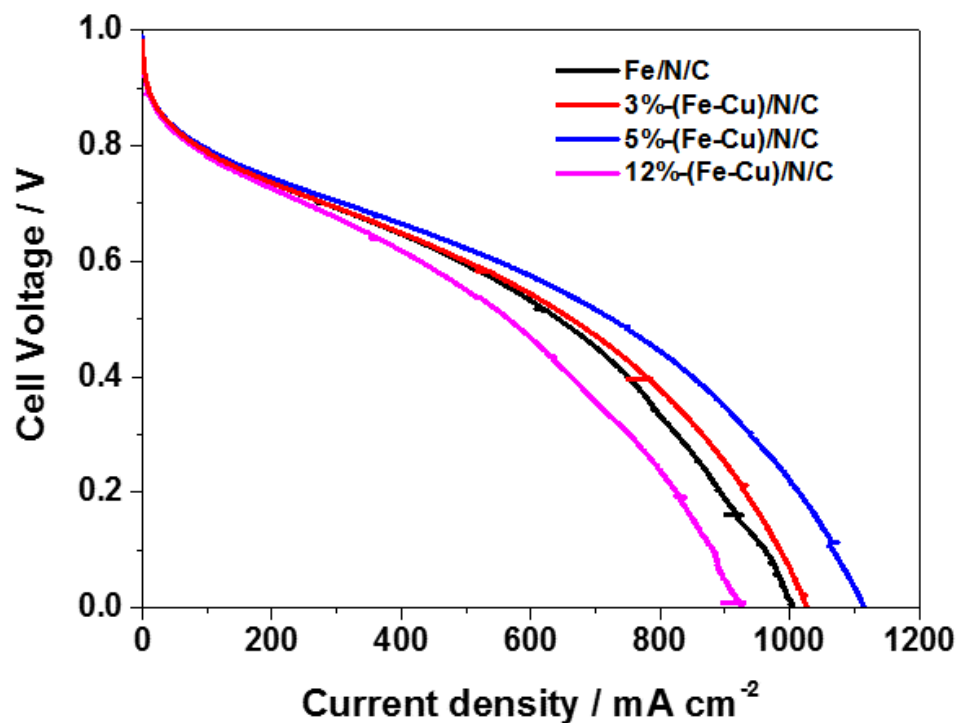


**Figure S4.** . Initial Polarization curves of single cells between OCP and 0 V using Fe/N/C and (Fe-Cu)/N/C with different ratio of Cu as cathode and commercial 46.4% Pt/C as anode with a Pt loading of 0.5 mg cm<sup>-2</sup>. Cathode catalyst loadings are displayed. Nafion to catalyst ratio is 1.25. Membrane is N211. The H<sub>2</sub> and Air flows are set to 0.3 nlpm. The temperatures of H<sub>2</sub> humidifier, air humidifier and cell are 85 °C, 70 °C and 80 °C, respectively.

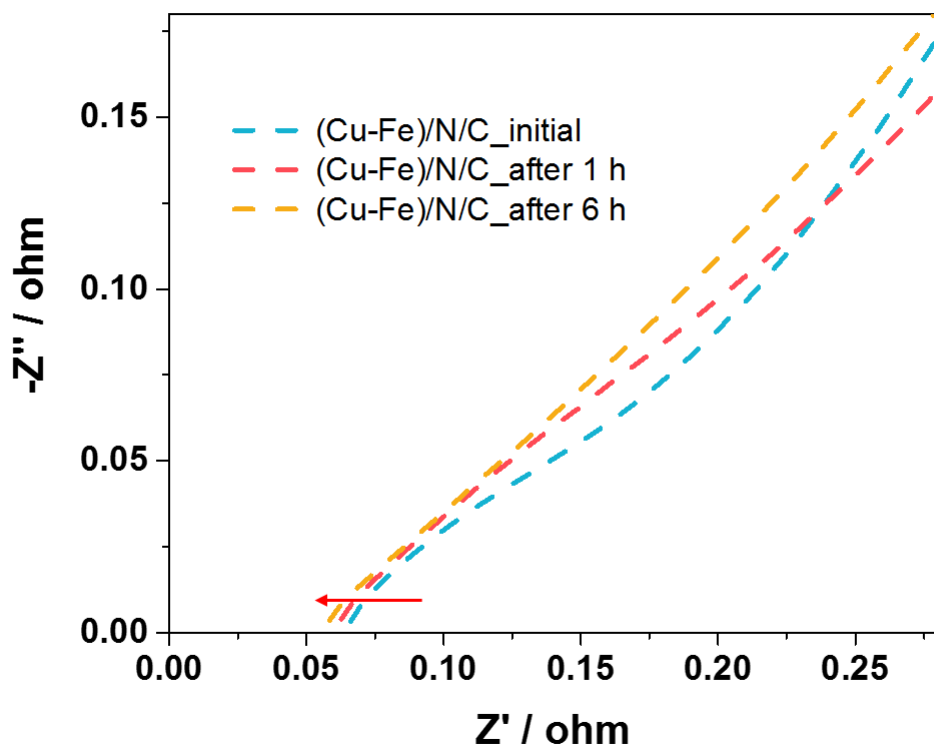


Figure S5. Nyquist plot of a PEMFC operated at OCV under 1 bar backpressure at 80 °C.

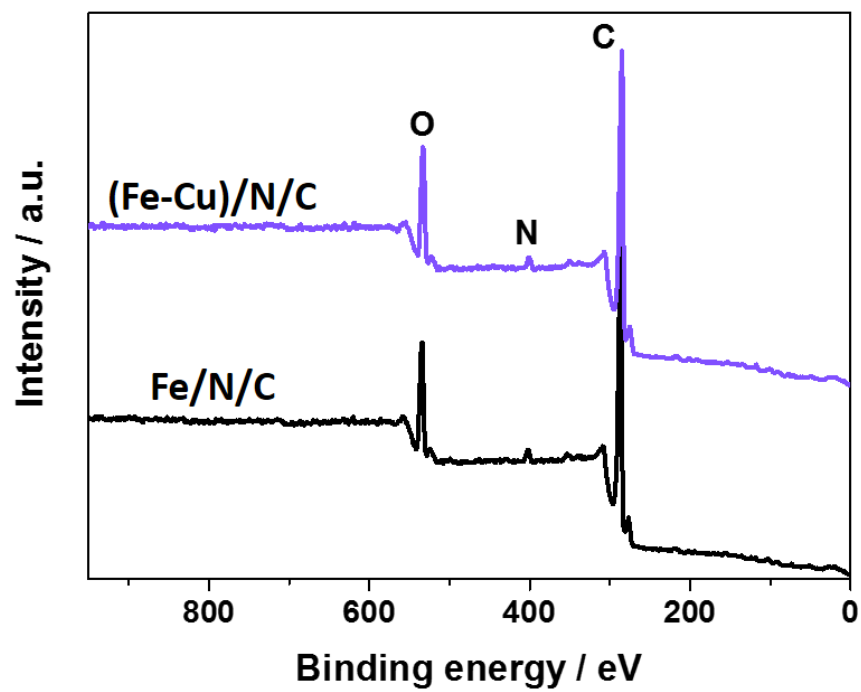
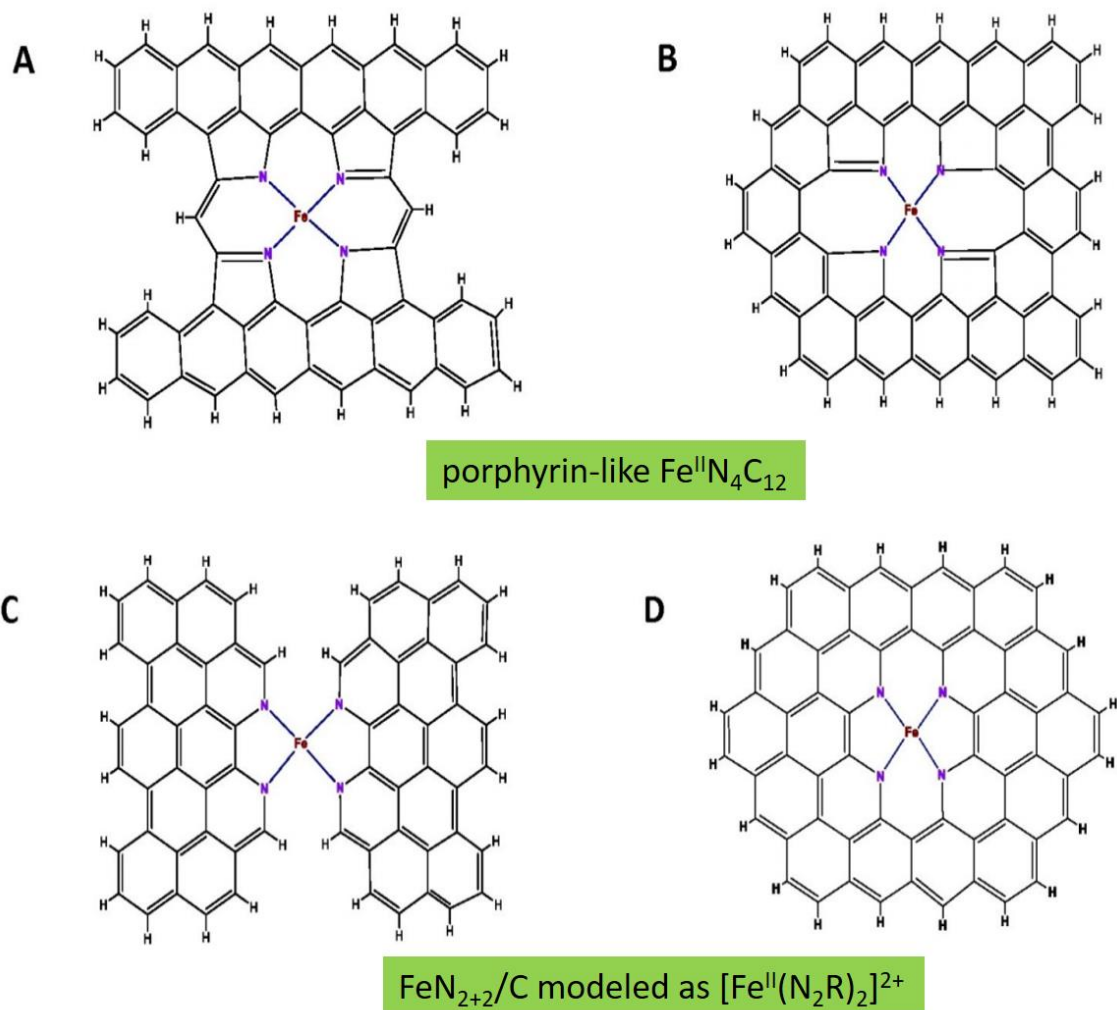


Figure S6. XPS spectra of Fe/N/C and (Fe-Cu)/N/C catalyst.



**Figure S7.** Two models of active sites for Fe/N/C catalyst (Ref: Energy Environ. Sci., 2018, 11, 365-382).

**Table S1.** NAA results of the optimized (Fe-Cu)/N/C.

Weight (g)	Cu (ppm)	Fe (ppm)
0.0192	2310	50027

### **3.4 An active and robust Si-Fe/N/C catalyst derived from waste reed for oxygen reduction**

Qiliang Wei, Xiaohua Yang, Gaixia Zhang, Dongniu Wang, Lucia Zuin, Dustin Banham, Lijun Yang, Siyu Ye, Youling Wang, Mohamed Mohamedi, Shuhui Sun

*Appl. Catal., B.*, 2018, **237**, 85-93.

The conversion of biomass waste into valuable carbon composites as efficient non-precious metal oxygen-reduction electrocatalysts is attractive for the development of commercially viable fuel-cell and metal-air battery technologies. In this section, an efficient Si-contained Fe/N/C ORR catalyst was developed by using the waste reed stalk as the Si and C source. Due to the participating of Si in the Fe/N doping process, the Si-Fe/N/C catalyst possesses enhanced graphitic carbon structure with more nitrogen moieties coordinating with Fe. The optimized Si-Fe/N/C exhibits better stability (with 94.8% retention of the current after 20,000 s under a high voltage of 0.8 V) than the Fe/N/C counterpart (83.3%) and Pt/C (65.5%).

*Contributions:* I performed most of the experimental synthesis, the electro-chemical measurements, and all characterizations. TEM measurements have been done by technicians. I also got the help from Xiaohua Yang, who did the pyrolysis work. Youling Wang helped on the Raman measurement. I conducted the data analysis and the interpretation of results, as well as the manuscript writing, with the help of co-authors.

# An active and robust Si-Fe/N/C catalyst derived from waste reed for oxygen reduction

*Qiliang Wei<sup>†,1</sup>, Xiaohua Yang<sup>†,1</sup>, Gaixia Zhang<sup>1,\*</sup>, Dongniu Wang<sup>2</sup>, Lucia Zuin<sup>2</sup>, Dustin Banham<sup>3</sup>, Lijun Yang<sup>3</sup>, Siyu Ye<sup>3</sup>, Youling Wang<sup>1</sup>, Mohamed Mohamedi<sup>1</sup>, Shuhui Sun<sup>1,\*</sup>*

<sup>1</sup>Institut National de la Recherche Scientifique-Énergie Matériaux et Télécommunications, Varennes, QC J3X 1S2, Canada.

<sup>2</sup>Canadian Light Source Inc., 44 Innovation Boulevard, Saskatoon, SK, S7N 2V3, Canada.

<sup>3</sup>Ballard Power Systems Inc., Burnaby, V5J 5J8, Canada

\*E-mail: [gaixia.zhang@emt.inrs.ca](mailto:gaixia.zhang@emt.inrs.ca) (G. Zhang); [shuhui@emt.inrs.ca](mailto:shuhui@emt.inrs.ca) (S. Sun)

## Highlights:

- Novel Si-containing Fe/N/C are prepared from biomass reed.
- Si places an important role in enhancing the performance of Fe/N/C catalysts.
- Si facilitates the incorporation of more pyridinic- and pyrrolic-N into the porous carbon.
- Si can induce a higher degree of graphitization in the Fe/N/C catalyst.
- Si-containing Fe/N/C exhibits high activity and outstanding stability.

**Abstract:** The conversion of biomass waste into valuable carbon composites as efficient non-precious metal oxygen-reduction electrocatalysts is attractive for the development of commercially viable fuel-cell and metal-air battery technologies. Herein, a highly active and robust Si-contained Fe/N/C catalyst is prepared based on the porous carbon deriving from waste reed stalk after carbonization and KOH corrosion. Reed waste is a natural, abundantly available, and yearly renewable source, acting as the single precursor for Si containing-carbon substrate. The typical product (Si-Fe<sub>20</sub>/N/C<sub>1\_6</sub> in this work) possesses a high BET specific surface area, porous structure with high pyridinic-N and pyrrolic-N content. The X-ray absorption near edge structure (XANES), Raman, X-ray photoelectron spectroscopy (XPS) measurements and

electrochemical measurements show that Si facilitates incorporation of more N to coordinate with Fe in the porous carbon and induces more graphitic carbon in the catalyst. The sample Si-Fe<sub>20</sub>/N/C<sub>1\_6</sub> exhibits better activity and superior stability than the Fe<sub>20</sub>/N/C counterpart and commercial Pt/C catalyst for the oxygen reduction reaction (ORR) in 0.1 M KOH electrolyte. The results suggest a promising route based on economical and sustainable biomass towards the development and engineering of value-added carbon materials as robust catalysts for oxygen reduction.

## 1. Introduction

Oxygen reduction reaction (ORR) is a pivotal process in clean renewable energy conversion systems such as fuel cells and metal-air batteries. Currently, the most efficient and widely used ORR catalysts are platinum group metal (PGM) materials, wherein Pt is the most efficient. However, the high cost and scarcity of PGMs seriously restrict their large-scale commercialization. Therefore, the development of low-cost and high-performance non-precious metal catalysts (NPMCs) for ORR is extremely imperative. Among various NPMCs, Fe- and N-doped carbon (Fe/N/C) materials have emerged as the most promising catalysts, in which, the ORR properties are mainly attributed to metal-containing active sites (usually labeled as FeN<sub>x</sub> or even FeN<sub>4</sub>) [1-3]. Another promising NPMCs is the so-called “metal free” catalysts (MFCs), in which no metal atoms are introduced. For MFCs, heteroatom doping is considered as an effective strategy to enhance the ORR activity by changing the electronic structure of adjacent carbon and/or producing additional active sites, extensive work has been committed to developing metal-free ORR electrocatalysts, such as doping N- [4-11], S- [12,13], P- [14,15], B- [16,17], F- [18-20], Si- [21,22], and/or their co-doping, tri-doping carbon materials [23-27]. However, fewer research has been investigated on heteroatom doped Fe/N/C catalyst, except some work on S-doped Fe/N/C [28-30] and B-doped Fe/N/C [31] recently, in which the synergistic effects between the heteroatom and Fe/N structure further promote the ORR performance. On the other hand, great efforts have been achieved in high performance NPMC catalysts by using expensive or toxic materials as starting precursors. From a more sustainable perspective, lots of research on the doping carbon materials has moved from expensive, often hazardous inorganic and/or organic chemicals to renewable biomass waste as precursors, mainly for sustainable consideration [32-37].

For the carbon-based electrocatalysts, it is widely accepted that graphitization of the carbon is beneficial in enhancing the conductivity and avoiding the chemical attack, thus improving the stability of the catalysts. It is also interesting to note that Si was proposed to promote the graphitization processes in the catalysts [38,39]. It has been known that Si exists in reed, a sustainable plant that are widely distributed worldwide [40]. In a very favorable nanoscale arrangement, this sustainable Si source has been exploited as anodes for lithium ion batteries [41]. In this work, inspired by the Si-promoting graphitization findings, based on the reed waste, Si contained Fe/N/C (Si-Fe/N/C) catalyst was synthesized by a simple route (Figure 1). The strategy was to use a cost-effective and easily available natural reed as a single precursor with both Si and C, to fabricate Si-Fe/N/C catalysts. To the best of our knowledge, there is no report on Si-containing Fe/N/C synthesized from natural reed and its use for the ORR yet.

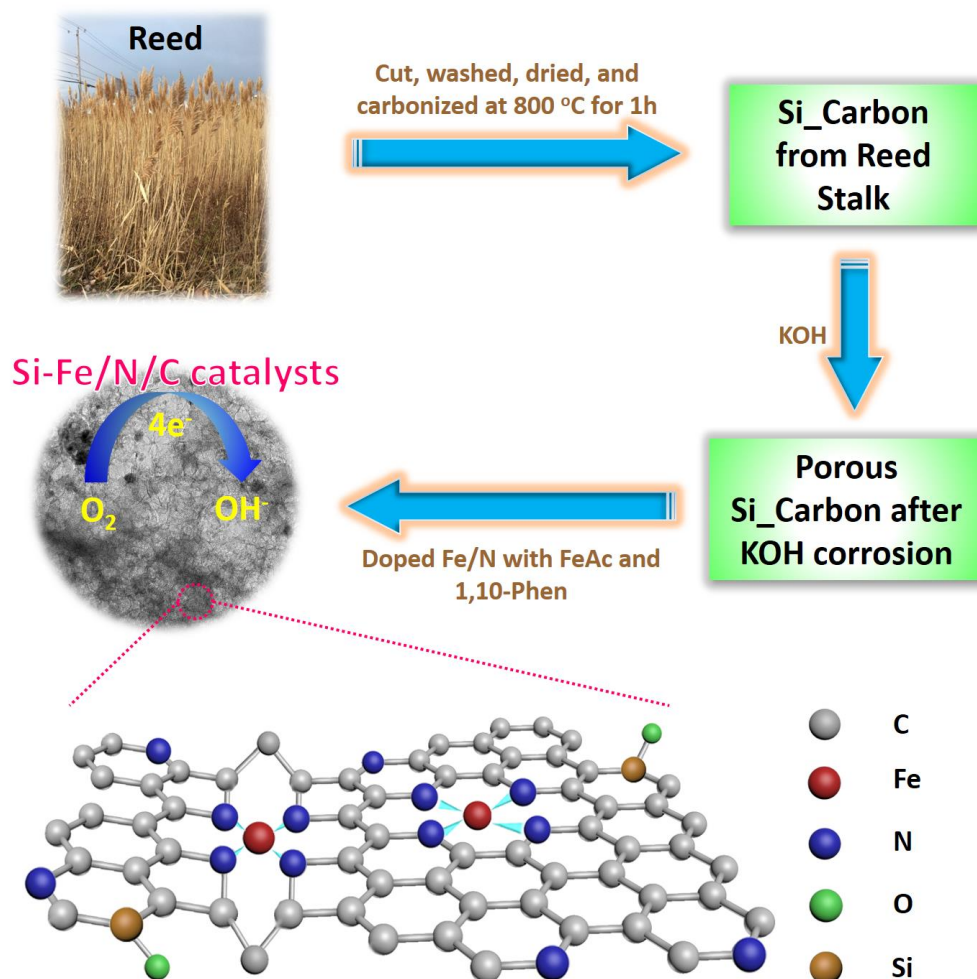


**Figure 1.** Schematic procedure for the fabrication of porous Si-Fe/N/C from reed waste.

## 2. Experimental

### 2.1. Materials

Iron (II) acetate (95 %), 1,10 phenanthroline (99 %), hydrochloric acid (HCl, 32% in H<sub>2</sub>O) and potassium hydroxide (KOH, 87.1 %), were purchased from Fisher Scientific; Reed stalk was obtained from a local farmland in Varennes (Quebec). All chemicals were used as received and solutions were prepared with deionized water (Millipore Milli-Q, 18.2 MΩ cm).

### 2.2. Preparation of porous Si-contained carbon precursor

The procedure of the preparation of porous carbons from reed was summarized in Fig 1. Before carbonization, the reed were carefully cut into small pieces, washed with deionized (DI)-water, and dried in oven at 80 °C for 2 days. The dried samples were pre-carbonized in combustion boat at 800 °C for 1 h under Ar flow. Afterwards, the pre-carbonized materials were mixed with KOH at different amount and grind together (weight ratio of materials/KOH is 1:2, 1:6 and 1:10, named as RC1<sub>x</sub>KOH, where *x* is the ratio of KOH/carbon). After that, the mixture was heated in a homemade copper boat under Ar flow at 700 °C for 1 h. Then the porous carbon after KOH corrosion was served as the carbon host for loading Fe and N in the next step. To investigate the effects of Si on the catalyst, some of the carbonized materials before KOH corrosion were leached by HF to remove the Si atoms, followed by mixing with KOH and doping Fe/N in the same way.

### 2.3. Preparation of Si-Fe/N/C catalysts

In a typical synthesis of Fe/N/C catalyst, taking Si-Fe<sub>20</sub>/N/C<sub>1\_6</sub> (simplified as Si-Fe/N/C) as an example, the precursors were prepared by first mixing 100 mg RC1<sub>6</sub>KOH, 55 mg 1,10-phenanthroline, 20 mg iron(II) acetate in a solution of ethanol and DI-water under stirring at room temperature. Then the mixture was heated to 60–80 °C for 2–3 h until about 20-25 ml of thick slurry was obtained. The slurry was placed overnight in a drying oven at 95 °C. Afterwards, the dry powder was ground sufficiently and placed in the quartz tube, followed by heating at 1050 °C in Ar for 1 h, and another pyrolysis in ammonia at 950 °C with weight losses around an optimum value of 50% [1,42-45]. In the experiment, different amount of FeAc were used (10, 20, and 30 mg) to find the optimal Fe content of the Si-Fe/N/C catalysts.

## 2.4. Physical characterizations

The crystal structure of the as-prepared samples was characterized by X-ray diffraction (XRD, Bruker D8 Advanced Diffractometer, Cu K $\alpha$  radiation). The morphological structures of the catalysts were imaged by using a JEOL 2100F TEM. XPS data was obtained by using a VG ESCALAB 220i-XL equipped with a Twin Anode X-Ray Source, and analysed by Casa XPS software (2.3.15 Version). The C 1s peak (BE = 284.6 eV) was used as the reference line to accurately determine the positions of other spectral lines. The specific surface areas of the catalysts were measured through N<sub>2</sub> sorption isotherms that were collected using Quantachrome Instruments Autosorb-1 at liquid nitrogen temperature (77.3 K), with the Quenched solid density functional theory (QSDFT) available in the AS1WIN software. Raman spectroscopy (Renishaw Imaging Microscope Wire™) was performed using the 785 nm laser radiation with a circular polarization. The laser beam was focused onto the sample to a spot size of 1  $\mu$ m. X-ray absorption near edge structure (XANES) measurement was performed at the Canadian Light Source (CLS) (Saskatoon, Canada) on the Variable Line Spacing Plane Grating Monochromator (VLS-PGM) beamline [46]. All the powder samples were smeared on carbon tape as a thin layer and placed in the vacuum chamber of the beamline for the measurement. The XANES spectra were collected in both total electron yield (TEY) and fluorescent yield (FLY) mode [47] (only TEY is presented in this work) with a chamber pressure better than  $1 \times 10^{-7}$  torr at room temperature [48]. The beamline slits sizes were 50  $\mu$ m x 50  $\mu$ m with an instrumental resolution  $E/\Delta E > 10000$ . The data are normalized by the  $I_0$  current, which is measured by a Nickel mesh placed in front of the sample.

## 2.5. Electrochemical measurements

All electrochemical measurements were performed in a three-electrode cell using a rotating ring disk electrode (RRDE, PINE Research Instrumentation), a saturated calomel electrode (SCE) and Pt wire were used as the reference and counter electrodes, respectively, as described in our previous study [44,45]. The catalyst suspension in this work was prepared as the following: 10 mg of catalyst was mixed with 95  $\mu$ L of 5 wt% Nafion solution and 350  $\mu$ L of ethanol in a glass vial (the Nafion-to-catalyst ratio is ~40%), followed by sonication and agitation for 1 h. Then 9  $\mu$ L of the catalyst suspension was dropped onto the GC electrode surface (~0.8 mg cm<sup>-2</sup>). For

comparison, the 20 wt% Pt/C catalyst (E-ETK) with a loading of 100  $\mu\text{g cm}^{-2}$  was prepared. In order to keep the gas-saturated in the solution,  $\text{N}_2$  (or  $\text{O}_2$ ) was bubbled through the electrolyte for 30 min before testing and kept bubbling during the measurements. The linear sweep voltammograms (LSV) were recorded between 0-1.2 V (vs. RHE) with 10  $\text{mV s}^{-1}$  at rotation speed of 1600 rpm, and plotted after subtraction of the background non-Faradic current recorded in  $\text{N}_2$ -saturated solution. For detecting peroxide formed at the disc electrode, the ring potential was set at 1.3 V. The collection efficiency was  $N = 0.37$ . The electron transfer number ( $n$ ) and peroxide yield ( $\text{H}_2\text{O}_2\%$ ) were calculated as follows:

$$\text{H}_2\text{O}_2\% = 200 \times (\text{I}_r/\text{N})/(\text{I}_d + \text{I}_r/\text{N})$$

$$n = 4 \times \text{I}_d / (\text{I}_d + \text{I}_r/\text{N})$$

Where  $\text{I}_d$  is the disk current and  $\text{I}_r$  is the ring current.

The stability of the catalysts was tested on fresh electrodes by chronoamperometry at 0.8 V (vs. RHE) for 20000 s in  $\text{O}_2$ -saturated 0.1 M KOH at a rotation speed of 1600 rpm (and 1 day without rotation). In addition, the catalysts were assessed by cycling over 10,000 cycles between 0.6 and 1.0 V at 100  $\text{mV s}^{-1}$  under  $\text{O}_2$ -saturated electrolyte, which is a more common and standard protocol to evaluate the stability [49-51]. The methanol crossover effects were recorded by adding 4 mL methanol into the 100 mL  $\text{O}_2$ -saturated 0.1 M KOH solution in the chronoamperometric measurement.

### 3. Results and discussion

To investigate the impact of the ratio of carbon/KOH and Fe content on our catalysts, we first examined the ORR activity of the Si- $\text{Fe}_x\text{NC-1}_y$  catalysts ( $x$  is the amount of Fe added,  $y$  is the ratio of KOH to carbon), with RDE measurements performed in 0.1 M KOH electrolyte. As shown in Figure S1, by comparing the half-wave potential and Tafel slope in lower over-potential area (Table 1), it can be obtained: (i) Si-Fe20/N/C1\_6 shows the best activity as 1) it has the most positive half-wave potential (0.88 V vs. RHE) than Si-Fe20/N/C1\_2 (0.79 V) and Si-Fe20/N/C1\_10 (0.85 V), though these three samples have very similar Tafel slope, and 2) the kinetic current density at 0.9 V has the order of Si-Fe20/N/C1\_6 ( $4.1 \text{ mA cm}^{-2}$ ) > Si-Fe20/N/C1\_10 ( $0.92 \text{ mA cm}^{-2}$ ) > Si-Fe20/N/C1\_2 ( $0.20 \text{ mA cm}^{-2}$ ). These results indicate that Si-

C1\_6 is the optimized carbon host. This benefit from the KOH activation plays an important role in the development of the micro-pore structure. As shown in Figure S2 and Table S1, Si-C1\_6 has the largest micro-pore surface area, which provides the possibility to host for the FeN<sub>x</sub> active sites [52]. (ii) Fe content has certain effects on the catalytic performance in the catalysts, as shown in Fig S1b and 1d, where it is seen that the Si-Fe20/N/C1\_6 has more positive half-wave potential and higher kinetic current density at 0.9 V than other catalysts. This demonstrates that optimal activity can be achieved by tuning the Fe content (too low of Fe content results in too few active sites, and too much Fe results in agglomeration).

The morphology of the as-prepared porous Si-C and Si-Fe/N/C samples from waste reed stalks was investigated by TEM and HR-TEM. Activated carbons are normally composed of randomly stacked graphite-like planes with a high level of disorder (Figure 2b), associated with a high porosity and specific surface area. The Si-C1\_6 in this work displayed a spongy and porous structure, suggesting a large specific surface area. From Figure 2d and 2e, after doping with Fe and N, the obtained Si-Fe/N/C has a typical 3D network with open-hollow and inter-connected pores (as indicated in the red circles in Figure 2e), which is expected to offer more active sites for ORR [52]. From Figure 2e, the graphitic carbon could be clearly observed, possibly due to metal-promoted dissolution-recrystallization [53] and Si-promoted graphitization effects [38]. In addition, NH<sub>3</sub> pyrolysis removed part of amorphous carbon, resulting in the open and hollow structure (Figure 2d-e). The graphitization carbon could enhance the corrosion resistance, thus improving the stability of the catalysts [54]. By investigating the BET specific surface area of activated porous carbon with different ratios of KOH, it can be obtained that the specific surface area of Si-C-1\_6 (1873 m<sup>2</sup> g<sup>-1</sup>) is higher than both Si-C-1\_2 (826.9 m<sup>2</sup> g<sup>-1</sup>) and Si-C-1\_10 (1537 m<sup>2</sup> g<sup>-1</sup>). Figure 2c and 2f presents the N<sub>2</sub> adsorption/desorption isotherms and pore-size distribution (PSD) of the Si-C1\_6 and its derived Si-Fe20/N/C. Figure 2c showed a typical type-I isotherm, which has relative large microporous structures and small external surfaces. The absorption takes place at a very low relative pressure as monolayer absorption. Once the micropores are full filled, the absorption on the external surface are very small [55]. While, after doping Fe and N, Figure 2f (Si-Fe20/N/C1\_6) and Figure S3 (the Fe20/N/C1\_6 counterpart) showed an obvious microporous adsorption and a small hysteresis loop. This indicates the coexistence of micropores and mesopores with solids consisting of agglomerates of particles forming slit shaped pores (plate structure) [56]. Table S2 lists the porous structure characteristics

as two ranges: micropores ( $<2.0$  nm), and mesopores ( $2 \leq d \leq 35$  nm). From it, we can see that the Si-Fe/N/C samples possess larger portion of micropores (where is believed the main host for the active sites) than the corresponding Fe/N/C catalyst. It should be noted that Si-Fe<sub>20</sub>/N/C has relative small area but shows the best activity. This is caused by the Fe content effect (another factor on the ORR performance) as discussed in this work and our previous work [44]. The specific surface area of the counterpart Fe<sub>20</sub>/N/C<sub>1\_6</sub> sample is  $479.1 \text{ m}^2 \text{ g}^{-1}$  (vs.  $534.9 \text{ m}^2 \text{ g}^{-1}$  of Si-Fe<sub>20</sub>/N/C<sub>1\_6</sub>) with less micropores and more mesopores between 3.3-5.9 nm (Figure S3), which is due to the corrosion of HF treatment of the porous carbon.

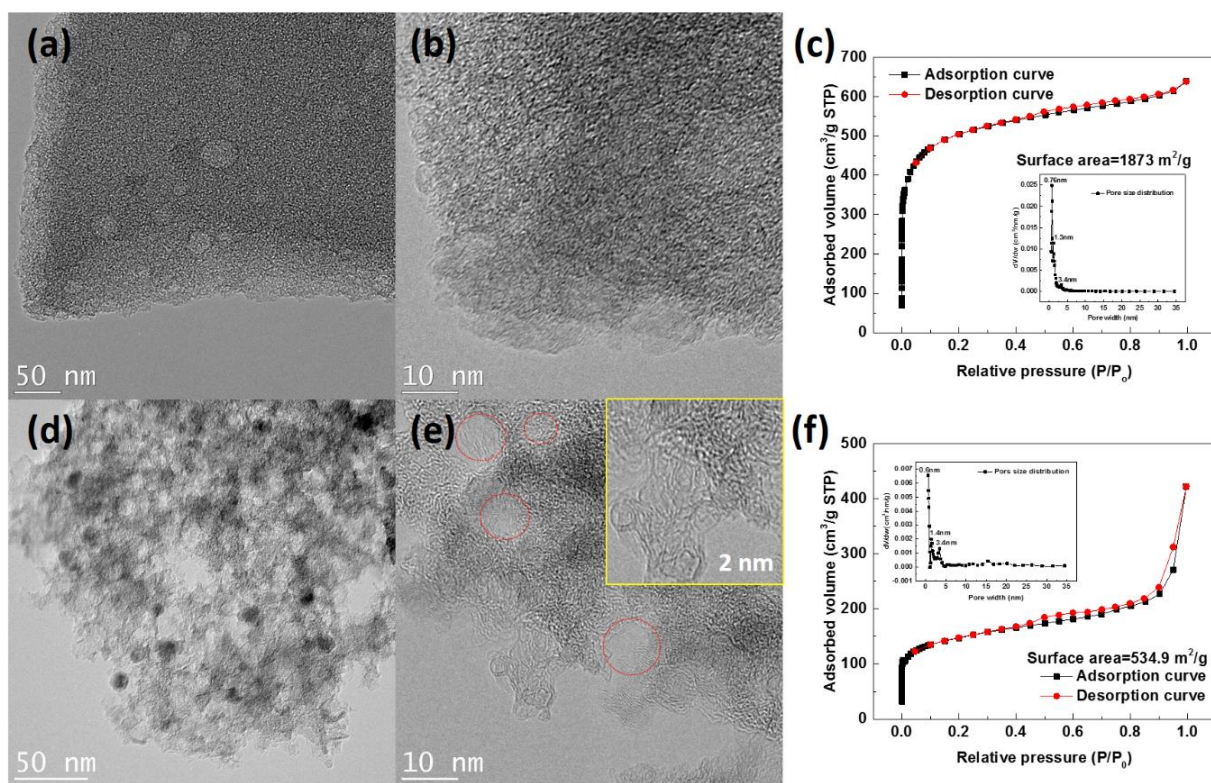


**Figure 2.** (a-b) TEM images of porous Si-RC1<sub>6</sub> at different magnifications; (c) N<sub>2</sub>-adsorption/desorption isotherms of Si-RC-1<sub>6</sub>; (d-e) TEM images of porous Si-Fe/N/C from Si-RC1<sub>6</sub> at different magnifications; (f) N<sub>2</sub>-adsorption/desorption isotherms of porous Si-Fe<sub>20</sub>/N/C<sub>1\_6</sub>.

XPS, Raman and XANES analysis were carried out to investigate the elemental composition and chemical status. The typical XPS survey spectrum (Figure S5) indicates the existence of C, O and Si in porous Si-RC1<sub>6</sub> derived from the natural reed stalks, after the HF treatment, the Si element was removed successfully. After doping with Fe and N, it can be found the existence of Fe, N, C, O and Si in porous Si-Fe<sub>20</sub>NC\_RC1<sub>6</sub> from the XPS survey spectrum (Figure 3a). For

comparison, based on the porous carbon without Si, the corresponding Fe/N/C sample was prepared with the same preparation method and the XPS survey spectrum further confirmed the absence of Si (Figure 3a). The Si 2p peaks at ~102 eV and ~105 eV show the presence of the chemical bonds of -C-Si-O- and SiO<sub>2</sub> in the Si-Fe20/N/C1\_6 sample (Figure S6). The high-resolution N 1s XPS spectrum (Figure 3b) of Si-Fe20/N/C and Fe20/N/C can be deconvoluted into four main peaks: namely pyridinic N, pyrrolic N, graphitic N and N oxides, their contents are also listed in Figure 3b. From it, it can be found that more pyridinic N and pyrrolic N are existed in Si-Fe20/N/C than Fe20/N/C. As known, the peaks of N coordinated with Fe, either as a porphyrin-like Fe<sup>II</sup>N<sub>4</sub>C<sub>12</sub> structure or FeN<sub>2+2</sub>/C model [57, 58], should be subjected to pyridinic N and pyrrolic N, thus, it can be deduced that the existence of Si may promote more N to coordinate with Fe. The graphitic structure of the Si-Fe20/N/C1\_6 and Fe20/N/C1\_6 was further studied by Raman analysis (Figure 3c). As it is well known, G band around 1640 cm<sup>-1</sup> corresponds to the E<sub>2g</sub> symmetry of graphitic sp<sup>2</sup> bonded carbon, and the D band peak located around 1340 cm<sup>-1</sup> is caused by the defects and disorders in the hexagonal graphitic layers. By comparison of the intensity ratios of the I<sub>D</sub>/I<sub>G</sub>, it can be found that the proportion of graphitic carbon is enhanced in the Si-containing Fe/N/C sample (1.78 vs. 1.34 of the Si-absent Fe/N/C sample), indicating the graphitization effects of Si [38,39].

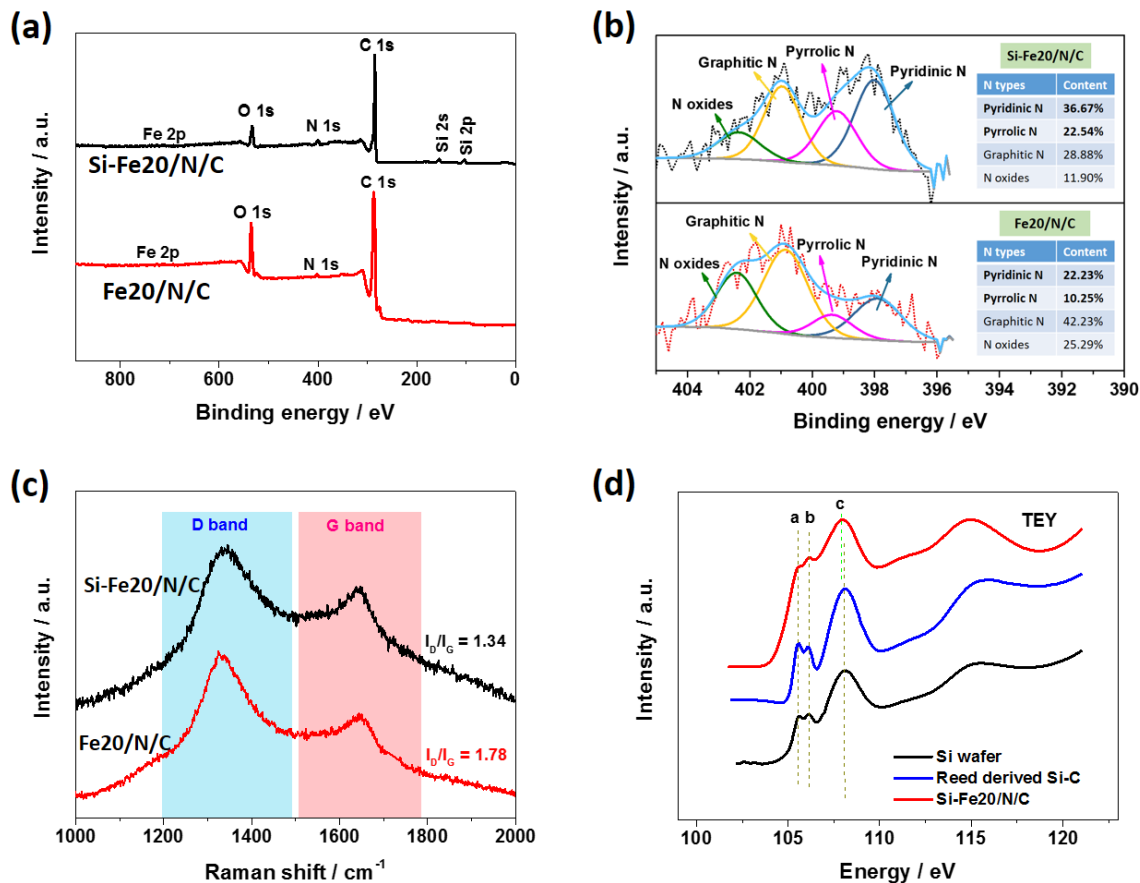


**Figure 3.** (a) XPS survey spectra of Si-Fe20/N/C1\_6, and Fe20/N/C1\_6 (prepared based on the HF treated reed derived porous carbon), (b) core level N 1s XPS spectrum of Si-Fe20/N/C1\_6 and Fe20/N/C, (c) Raman spectra of Si-Fe20/N/C1\_6 and Fe20/N/C1\_6, (d) Si L<sub>2,3</sub>-edge XANES spectra of model Si wafer, reed derived porous Si-containing carbon and the prepared Si-Fe20/N/C.

Figure 3d and Figure S7 are the Si L<sub>2,3</sub>-edge XANES spectra for the standard model Si wafer and the Si-containing samples in this work. For all the samples, three well resolved main peaks (**a**, **b** and **c**) can be observed. The intense peak **c** is caused by the transition of Si 2p electrons to 3s or 3d-like orbitals [59]. Closer observation revealed an energy shift for the Si-Fe20/N/C sample compared with the Si wafer and its precursor Si-containing porous carbon, indicating that the different local chemistry environment of Si and the participation of Si during the Fe and N doping process. The two peaks **a** (~105.5 eV) and **b** (~106.1 eV) are the fingerprints of SiO<sub>2</sub> due to the formation of tetrahedron bonds of Si with O, which can be attributed to transitions of 2p electrons to unoccupied 3d orbitals which were split by the 2p spin-orbit splitting [59,60]. It has been reported that the intensity ratio **a/b** can be used as a reference to differentiate the samples

[61]. In the samples of this work, the surface sensitive TEY spectra clearly track Si-O bond in Si wafer due to surface oxidation. Precursor Si-containing porous carbon exhibits similar and sharper features with slight higher resonance than that of Si wafer, illustrating better crystallization upon carbonization. After doping with Fe and N, the **a/b** ratio is greatly reduced, where peak **a** is greatly suppressed to a broad shoulder due to the incorporation of Fe and N. From Figure S8 and Table S3, it can be found that the lower of the **a/b** ratio, the higher activity of the catalyst performs at 0.9 V is, indicating that the Fe content in the precursor for Si-Fe20/N/C is the optimized amount for suppressing the **a** peak. Although the mechanism behind the **a/b** ratio and ORR activity is not clear yet, these distinct features reveal the participation of Si during the doping process, which is directly related with the formation of more graphitic carbon and the specific nitrogen configuration, as demonstrated from Raman and XPS results. Furthermore, Figure 4a and d show the C1s spectrum of Si-Fe20/N/C and Fe20/N/C, the peak located at 284.6 eV is related to the  $sp^2$  C=C band of graphitic carbon. Obviously, the component of  $sp^2$  C=C in the Si-Fe20/N/C (62.2%) is higher than that of Fe20/N/C (38.6%). To further confirm the enhanced graphitic structure character of Si-Fe20/N/C, more HRTEM images were taken randomly for both samples, as shown in Figure 4b and c for Si-Fe20/N/C, turbostratic structure of graphitic is clearly present; comparatively, for Fe20/N/C, only weak layered graphitization structure can be observed (Figure 4e and f). These results confirmed the graphitization effects of Si in a more direct way, consisting with the previous analysis.

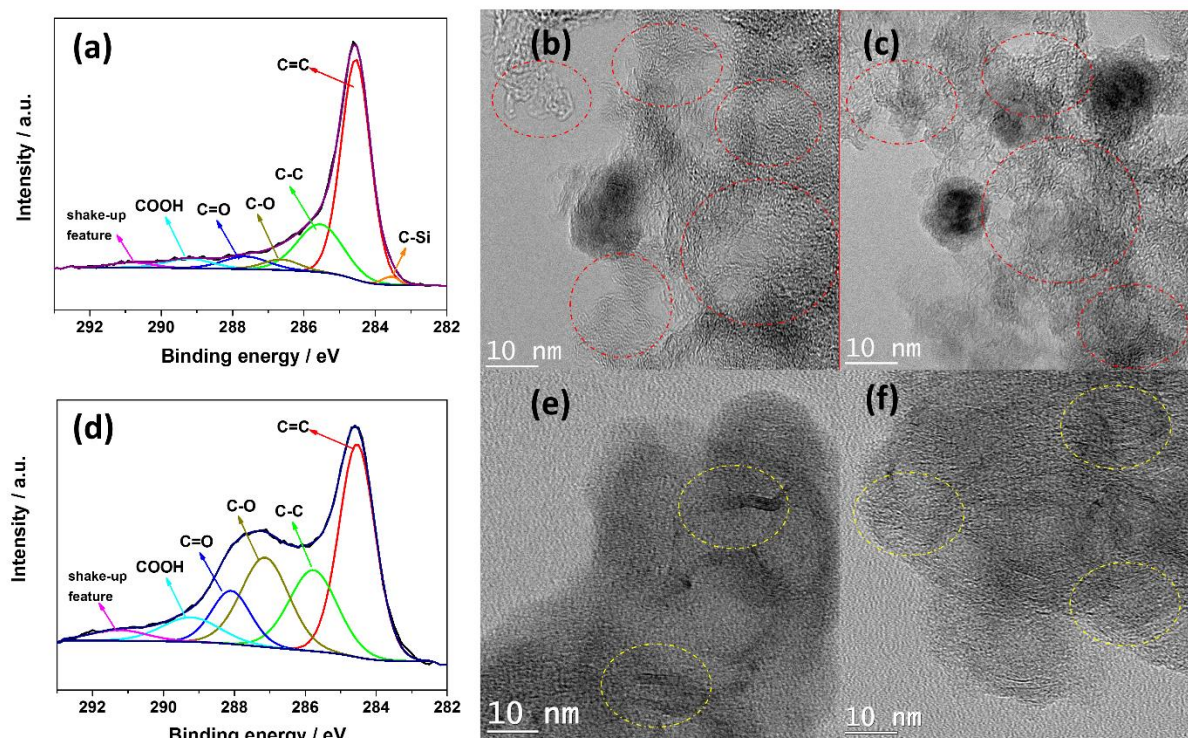


**Figure 4.** (a, d) Core level C 1s XPS spectrum of Si-Fe<sub>20</sub>/N/C and Fe<sub>20</sub>/N/C, (b, c) HRTEM images of Si-Fe<sub>20</sub>/N/C, (e, f) HRTEM images of Fe<sub>20</sub>/N/C.

To gain insight into the ORR activity, we examined the electrocatalytic properties of Si-Fe<sub>20</sub>/N/C1\_6 by employing a rotating ring–disk electrode (RRDE) technique in a N<sub>2</sub>- and O<sub>2</sub>-saturated 0.1 M aqueous KOH electrolyte solution at a scan rate of 10 mV s<sup>-1</sup> at a rotation speed of 1600 rpm. The amount of H<sub>2</sub>O<sub>2</sub> generated at the disk electrode and the electron transfer number (*n*) could be accurately calculated from RRDE. For comparison, the Fe<sub>20</sub>/N/C1\_6 prepared based on the HF treated porous carbon and the commercial Pt/C were also measured with the same condition as Si-Fe<sub>20</sub>/N/C1\_6. The onset potential for the ORR is an important criterion to evaluate the activity of an electrocatalyst. Figure 5a is the LSV curves of these three samples, it can be seen that both Si-Fe<sub>20</sub>/N/C1\_6 and Fe<sub>20</sub>/N/C1\_6 have more positive onset potential (0.99 V) than Pt/C (0.91 V). This demonstrates the excellent catalytic activity for ORR of the reed-derived NPMCs. Interestingly, though the onset potential suggests very similar kinetics between Fe<sub>20</sub>/N/C and Si-Fe<sub>20</sub>/N/C1\_6, the existence of Si in Si-Fe<sub>20</sub>/N/C1\_6 has positive effects to the mixed kinetic-diffusion controlled region. Figure S9 shows the Tafel plots of catalysts. A low value of Tafel slope is highly advantageous, and indicates a more efficient

electrochemical process. To see more differences of the two samples with and without Si doping, we divided 2 zones in Figure S9. The Tafel slope at higher potentials (zone 1) usually suggests that ORR rate is determined by oxygen intermediates absorption (corresponding to the on-set potential). The two catalysts have very similar values in zone 1, but with different Tafel slopes ( $82 \text{ mV dec}^{-1}$  for Si-Fe20/N/C1\_6 vs  $93 \text{ mV dec}^{-1}$  for Fe20/N/C1\_6) showing the better kinetics of the former catalyst. In zone 2, at lower potentials, we can regard it as the mixed region of the kinetics and diffusion. Obviously, Si-Fe20/N/C1\_6 has a much smaller slope than Fe20/N/C1\_6 ( $95 \text{ mV dec}^{-1}$  vs  $120 \text{ mV dec}^{-1}$ ), showing its high efficient electrochemical process. Notably, the electron transferred number ( $n$ ) of Si-Fe20/N/C1\_6 displays very close value with the commercial Pt/C over a potential range of 0.2-0.8 V (Figure 5b), implying a high selectivity toward one-step oxygen reduction to water. By calculating, the measured  $\text{H}_2\text{O}_2$  yield of Si-Fe20/N/C1\_6 is below 6% in the measured potential range, even lower than the corresponding Fe20/N/C1\_6 sample (Figure 5b), demonstrating its higher ORR catalytic efficiency.

The durability is an important factor for evaluating the performance of ORR catalysts. Figure 5c shows that the current density of the Si-Fe20/N/C1\_6 catalyst remains 94.8% after 20000 s at a rotation speed of 1600 rpm under 0.8 V (vs. RHE), which is apparently higher than that of the Fe20/N/C1\_6 catalyst (83.3%) and commercial Pt/C catalyst (65.5%) in the same condition. A long-term chronoamperometric stability evaluation (at 0.8 V vs. RHE) showed no significant loss in ORR activity after  $\approx 24$  hours of continuous measurement (Figure S10), indicating that Si-Fe20/N/C1\_6 is able to sustain a stable ORR performance over a long period of time. Moreover, we further evaluated the stability by assessing the LSV curves after cycling the electrode potential between 0.6-1.0 V under  $\text{O}_2$ -saturated electrolyte. The results are shown in Figure S11 and Figure 5e, only  $\sim 12$  mV of change can be observed for Si-Fe20/N/C at  $3 \text{ mA cm}^{-2}$ , lower than that of Fe20/N/C ( $\sim 19$  mV) and Pt/C ( $\sim 40$  mV). The higher stability of Si-Fe20/N/C1\_6 might be attributed to the higher graphitization of the carbon structure (probably promoted by Si) [38,39] in it. Methanol crossover effect should be considered in fuel cells that use methanol as the fuel, because the methanol crossover could severely deteriorate the ORR performance on the cathode. So the methanol tolerant ability of the Si-Fe20/N/C1\_6 catalyst and the commercial Pt/C catalyst in 0.1 M KOH electrolyte are compared. As illustrated in Figure 5d, the Pt/C catalyst suffers from remarkable loss in current density upon the introduction of methanol into the electrolyte, indicating methanol oxidation on the electrode. On the contrast, the Si-

Fe20/N/C1\_6 catalyst displays very little change on current density after the introduction of methanol, demonstrating much better resistance to methanol crossover than the Pt/C catalyst.

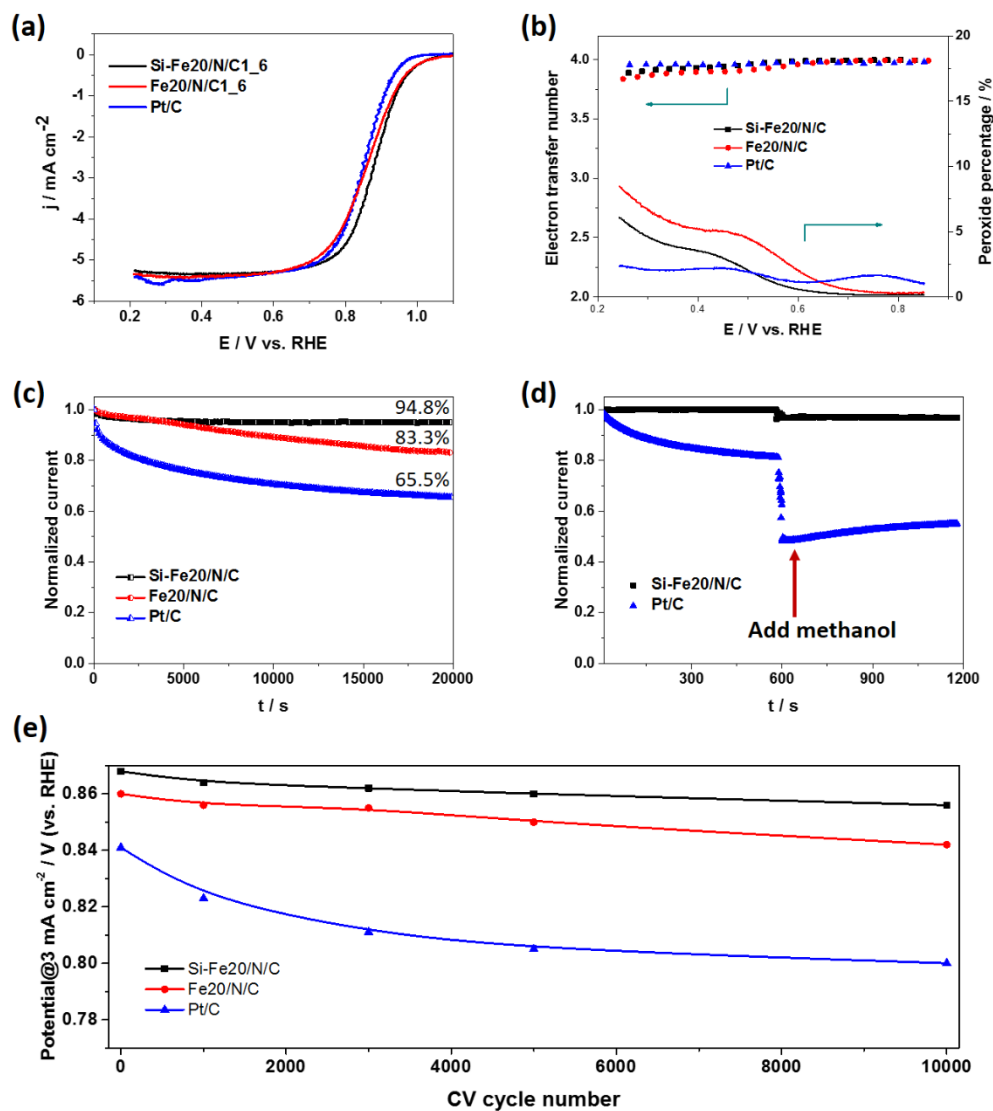


**Figure 5.** (a) LSV curves, (b) electron transfer number ( $n$ ), and H<sub>2</sub>O<sub>2</sub> selectivity of Si-Fe20/N/C1\_6, Fe20/N/C1\_6 and commercial Pt/C in O<sub>2</sub>-saturated 0.1 M KOH at a scan rate of 10 mV s<sup>-1</sup>, rotation rate = 1600 rpm. (c) Chronoamperometric responses (at 0.8 V vs. RHE) of Si-Fe20/N/C1\_6, Fe20/N/C1\_6 and commercial Pt/C catalysts in O<sub>2</sub>-saturated 0.1 M KOH with rotation speed of 1600 rpm, (d) chronoamperometric responses of Si-Fe20/N/C1\_6 and Pt/C catalysts show the effect of adding 4 mL methanol into the 100 mL O<sub>2</sub>-saturated 0.1 m KOH solution. (e) Potential at 3 mA cm<sup>-2</sup> of Si-Fe20/N/C1\_6, Fe20/N/C1\_6 and commercial Pt/C as a function of the number of potential cycles in O<sub>2</sub>-saturated electrolyte.

#### **4. Conclusions**

In summary, we have developed an efficient Si-contained Fe/N/C ORR catalyst by using the waste reed stalk as the Si and C source. XANES, Raman and XPS measurements indicate that due to the participating of Si in the Fe/N doping process, the Si-Fe/N/C catalyst possesses enhanced graphitic carbon structure with more nitrogen moieties coordinating with Fe. These features make Si-Fe/N/C catalyst showing good ORR activity, and importantly, Si-Fe/N/C exhibits better stability (with 94.8% retention of the current after 20000 s under a high voltage of 0.8 V) than the Fe/N/C counterpart (83.3%) and Pt/C (65.5%); and only ~12 mV of change at 3 mA cm<sup>-2</sup> for Si-Fe/N/C after 10,000 potential cycles under O<sub>2</sub>-saturated electrolyte (vs. ~19 mV for Fe/N/C and ~40 mV for Pt/C). as well as higher tolerance toward methanol compared with Pt/C. Moreover, ORR on the Si-Fe/N/C follows the efficient 4e<sup>-</sup> pathway. Taking together, our developed Si-Fe/N/C catalyst as a substitute for commercial Pt/C could provide possibility in alkaline fuel cells and other applications with good ORR performance and high stability. We believe that this work will give more insights to design highly stable catalysts for the clean energy related devices and have significant economic and environment effects by making full use of biomass wastes.

#### **Author Contributions**

The manuscript was written through contributions of all authors. All authors have given approval to the final version of the manuscript. †These authors contributed equally.

#### **Notes**

The authors declare no competing financial interest.

#### **Acknowledgements**

This work is supported financially by the Natural Sciences and Engineering Research Council of Canada (NSERC), Ballard Power Systems Inc., the Fonds de Recherche du Québec-Nature et Technologies (FRQNT), Canada Foundation for Innovation (CFI), Centre Québécois sur les Matériaux Fonctionnels (CQMF), Institut National de la Recherche Scientifique (INRS) and China Scholarship Council (CSC). Synchrotron research described in this paper was performed at the Canadian Light Source, which is supported by the Canada Foundation for Innovation, the

Natural Sciences and Engineering Research Council of Canada (NSERC), the University of Saskatchewan, the Government of Saskatchewan, Western Economic Diversification Canada, the National Research Council Canada, and the Canadian Institutes of Health Research.

## References

- [1] M. Lefèvre, E. Proietti, F. Jaouen, J.-P. Dodelet, Iron-based catalysts with improved oxygen reduction activity in polymer electrolyte fuel cells. *Science* 324 (2009) 71-74.
- [2] H. Tang, Y. Zeng, Y. Zeng, R. Wang, S. Cai, C. Liao, H. Cai, X. Lu, P. Tsiakaras, Iron-embedded nitrogen doped carbon frameworks as robust catalyst for oxygen reduction reaction in microbial fuel cells. *Applied Catalysis B: Environmental*, 202 (2017) 550-556.
- [3] M. Shao, Q. Chang, J.-P. Dodelet, R. Chenitz, Recent advances in electrocatalysts for oxygen reduction reaction. *Chem. Rev.* 116 (2016) 3594-3657.
- [4] K. Gong, F. Du, Z. Xia, M. Durstock, L. Dai, Nitrogen-doped carbon nanotube arrays with high electrocatalytic activity for oxygen reduction. *Science* 323 (2009) 760-764.
- [5] L. Lai, J. R. Potts, D. Zhan, L. Wang, C. K. Poh, C. Tang, H. Gong, Z. Shen, J. Lin, R. S. Ruoff, Exploration of the active center structure of nitrogen-doped graphene-based catalysts for oxygen reduction reaction. *Energy Environ. Sci.* 5 (2012) 7936-7942.
- [6] W. Wei, H. Liang, K. Parvez, X. Zhuang, X. Feng, K. Müllen, Nitrogen-doped carbon nanosheets with size-defined mesopores as highly efficient metal-free catalyst for the oxygen reduction reaction. *Angew. Chem.* 126 (2014) 1596-1600.
- [7] S. Chen, J. Bi, Y. Zhao, L. Yang, C. Zhang, Y. Ma, Q. Wu, X. Wang, Z. Hu, Nitrogen-doped carbon nanocages as efficient metal-free electrocatalysts for oxygen reduction reaction. *Adv. Mater.* 24 (2012) 5593-5597.
- [8] P. Zhang, F. Sun, Z. Xiang, Z. Shen, J. Yun, D. Cao, ZIF-derived in situ nitrogen-doped porous carbons as efficient metal-free electrocatalysts for oxygen reduction reaction. *Energy Environ. Sci.* 7 (2014) 442-450.
- [9] D. Guo, R. Shibuya, C. Akiba, S. Saji, T. Kondo, J. Nakamura, Active sites of nitrogen-doped carbon materials for oxygen reduction reaction clarified using model catalysts. *Science* 351 (2016) 361-365.

- [10] K. Wan, G.-F. Long, M.-Y. Liu, L. Du, Z.-X. Liang, P. Tsiakaras, Nitrogen-doped ordered mesoporous carbon: synthesis and active sites for electrocatalysis of oxygen reduction reaction. *Appl. Catal., B* 165 (2015) 566-571.
- [11] Q. Wei, X. Tong, G. Zhang, J. Qiao, Q. Gong, S. Sun, Nitrogen-doped carbon nanotube and graphene materials for oxygen reduction reactions. *Catalysts* 5 (2015) 1574-1602.
- [12] Z. Ma, S. Dou, A. Shen, L. Tao, L. Dai, S. Wang, Sulfur-doped graphene derived from cycled lithium-sulfur batteries as a metal-free electrocatalyst for the oxygen reduction reaction. *Angew. Chem.* 54 (2015) 1888-1892.
- [13] L. Zhang, J. Niu, M. Li, Z. Xia, Catalytic mechanisms of sulfur-doped graphene as efficient oxygen reduction reaction catalysts for fuel cells. *J. Phys. Chem. C* 118 (2014) 3545-3553.
- [14] C. Zhang, N. Mahmood, H. Yin, F. Liu, Y. Hou, Synthesis of phosphorus-doped graphene and its multifunctional applications for oxygen reduction reaction and lithium ion batteries. *Adv. Mater.* 25 (2013) 4932-4937.
- [15] D.-S. Yang, D. Bhattacharjya, S. Inamdar, J. Park, J.-S. Yu, Phosphorus-doped ordered mesoporous carbons with different lengths as efficient metal-free electrocatalysts for oxygen reduction reaction in alkaline media. *J. Am. Chem. Soc.* 134 (2012) 16127-16130.
- [16] Z.-H. Sheng, H.-L. Gao, W.-J. Bao, F.-B. Wang, X.-H. Xia, Synthesis of boron doped graphene for oxygen reduction reaction in fuel cells. *J. Mater. Chem.* 22 (2012) 390-395.
- [17] X. Bo, L. Guo, Ordered mesoporous boron-doped carbons as metal-free electrocatalysts for the oxygen reduction reaction in alkaline solution. *Phys. Chem. Chem. Phys.* 15 (2013) 2459-2465.
- [18] X. Sun, Y. Zhang, P. Song, J. Pan, L. Zhuang, W. Xu, W. Xing, Fluorine-doped carbon blacks: highly efficient metal-free electrocatalysts for oxygen reduction reaction. *ACS Catal.* 3 (2013) 1726-1729.
- [19] G. Panomsuwan, N. Saito, T. Ishizaki, Simple one-step synthesis of fluorine-doped carbon nanoparticles as potential alternative metal-free electrocatalysts for oxygen reduction reaction. *J. Mater. Chem. A* 3 (2015) 9972-9981.
- [20] X. Sun, P. Song, T. Chen, J. Liu, W. Xu, Fluorine-doped BP 2000: highly efficient metal-free electrocatalysts for acidic oxygen reduction reaction with superlow H<sub>2</sub>O<sub>2</sub> yield. *Chem. Commun.* 49 (2013) 10296-10298.

- [21] Z. Liu, X. Fu, M. Li, F. Wang, Q. Wang, G. Kang, F. Peng, Novel silicon-doped, silicon and nitrogen-codoped carbon nanomaterials with high activity for the oxygen reduction reaction in alkaline medium. *J. Mater. Chem. A* 3 (2015) 3289-3293.
- [22] X. Fu, Q.-D. Wang, Z. Liu, F. Peng, Si-doped carbon nanotubes as efficient metal-free electrocatalysts for O<sub>2</sub> reduction in alkaline medium. *Mater. Lett.* 158 (2015) 32-35.
- [23] Y. Zhao, L. Yang, S. Chen, X. Wang, Y. Ma, Q. Wu, Y. Jiang, W. Qian, Z. Hu, Can boron and nitrogen co-doping improve oxygen reduction reaction activity of carbon nanotubes? *J. Am. Chem. Soc.* 135 (2013) 1201-1204.
- [24] W. Ai, Z. Luo, J. Jiang, J. Zhu, Z. Du, Z. Fan, L. Xie, H. Zhang, W. Huang, T. Yu, Nitrogen and sulfur codoped graphene: multifunctional electrode materials for high-performance Li-ion batteries and oxygen reduction reaction. *Adv. Mater.* 26 (2014) 6186-6192.
- [25] S. Wang, L. Zhang, Z. Xia, A. Roy, D. W. Chang, J. B. Baek, L. Dai, BCN graphene as efficient metal-free electrocatalyst for the oxygen reduction reaction. *Angew. Chem. Int. Ed.* 51 (2012) 4209-4212.
- [26] J. Zhang, Z. Zhao, Z. Xia, L. Dai, A metal-free bifunctional electrocatalyst for oxygen reduction and oxygen evolution reactions. *Nat. Nanotech.* 10 (2015) 444-452.
- [27] Y. Su, Z. Yao, F. Zhang, H. Wang, Z. Mics, E. Cánovas, M. Bonn, X. Zhuang, X. Feng, Sulfur-enriched conjugated polymer nanosheet derived sulfur and nitrogen co-doped porous carbon nanosheets as electrocatalysts for oxygen reduction reaction and zinc-air battery. *Adv. Funct. Mater.* 26 (2016) 5893-5902.
- [28] Y. C. Wang, Y. J. Lai, L. Song, Z. Y. Zhou, J. G. Liu, Q. Wang, X. D. Yang, C. Chen, W. Shi, Y. P. Zheng, S-doping of an Fe/N/C ORR catalyst for polymer electrolyte membrane fuel cells with high power density. *Angew. Chem.* 127 (2015) 10045-10048.
- [29] K. Hu, L. Tao, D. Liu, J. Huo, S. Wang, Sulfur-doped Fe/N/C nanosheets as highly efficient electrocatalysts for oxygen reduction reaction. *ACS Appl. Mater. Interfaces* 8 (2016) 19379-19385.
- [30] P. Chen, T. Zhou, L. Xing, K. Xu, Y. Tong, H. Xie, L. Zhang, W. Yan, W. Chu, C. Wu, Atomically dispersed iron-nitrogen species as electrocatalysts for bifunctional oxygen evolution and reduction reactions. *Angew. Chem.* 56 (2017) 610-614.
- [31] K. Yuan, S. Sfaelou, M. Qiu, D. F. Lützenkirchen-Hecht, X. Zhuang, Y. Chen, C. Yuan, X. Feng, U. Scherf, The synergetic contribution of boron and Fe-N<sub>x</sub> species in porous carbons

towards efficient electrocatalysts for oxygen reduction reaction. *ACS Energy Lett.* 3 (2018) 252–260.

[32] S. Gao, K. Geng, H. Liu, X. Wei, M. Zhang, P. Wang, J. Wang, Transforming organic-rich amaranthus waste into nitrogen-doped carbon with superior performance of the oxygen reduction reaction. *Energy Environ. Sci.* 8 (2015) 221-229.

[33] M. Y. Song, H. Y. Park, D. S. Yang, D. Bhattacharjya, J. S. Yu, Seaweed-derived heteroatom-doped highly porous carbon as an electrocatalyst for the oxygen reduction reaction. *ChemSusChem* 7 (2014) 1755-1763.

[34] J. Wei, Y. Liang, Y. Hu, B. Kong, G. P. Simon, J. Zhang, S. P. Jiang, H. Wang, A versatile iron-tannin-framework ink coating strategy to fabricate biomass-derived iron carbide/Fe-N-carbon catalysts for efficient oxygen reduction. *Angew. Chem.* 128 (2016) 1377-1381.

[35] P. Chen, L.-K. Wang, G. Wang, M.-R. Gao, J. Ge, W.-J. Yuan, Y.-H. Shen, A.-J. Xie, S.-H. Yu, Nitrogen-doped nanoporous carbon nanosheets derived from plant biomass: an efficient catalyst for oxygen reduction reaction. *Energy Environ. Sci.* 7 (2014) 4095-4103.

[36] S. Gao, Y. Chen, H. Fan, X. Wei, C. Hu, H. Luo, L. Qu, Large scale production of biomass-derived N-doped porous carbon spheres for oxygen reduction and supercapacitors. *J. Mater. Chem. A* 2 (2014) 3317-3324.

[37] C. Zhu, J. Zhai, S. Dong, Bifunctional fluorescent carbon nanodots: green synthesis via soy milk and application as metal-free electrocatalysts for oxygen reduction. *Chem. Commun.* 48 (2012) 9367-9369.

[38] Q. Lin, Z. Feng, Z. Liu, Q. Guo, Z. Hu, L. He, H. Ye, Atomic scale investigations of catalyst and catalytic graphitization in a silicon and titanium doped graphite. *Carbon* 88 (2015) 252-261.

[39] A. B. García, I. Cameán, I. Suelves, J. L. Pinilla, M. J. Lázaro, J. M. Palacios, R. Moliner, The graphitization of carbon nanofibers produced by the catalytic decomposition of natural gas. *Carbon* 47 (2009) 2563-2570.

[40] Epstein, E. Silicon: Its manifold roles in plants. *Ann. Appl. Biol.* 155 (2009) 155-160.

[41] J. Liu, P. Kopold, P. A. van Aken, J. Maier, Y. Yu, Energy storage materials from nature through nanotechnology: a sustainable route from reed plants to a silicon anode for lithium-ion batteries. *Angew. Chem.* 127 (2015) 9768-9772.

- [42] E. Proietti, F. Jaouen, M. Lefèvre, N. Larouche, J. Tian, J. Herranz, J.-P. Dodelet, Iron-based cathode catalyst with enhanced power density in polymer electrolyte membrane fuel cells. *Nat. Commun.* 2 (2011) 416.
- [43] G. Zhang, R. Chenitz, M. Lefèvre, S. Sun, J.-P. Dodelet, Is iron involved in the lack of stability of Fe/N/C electrocatalysts used to reduce oxygen at the cathode of PEM fuel cells? *Nano Energy* 29 (2016) 111-125.
- [44] Q. Wei, G. Zhang, X. Yang, R. Chenitz, D. Banham, L. Yang, S. Ye, S. Knights, S. Sun, 3D porous Fe/N/C spherical nanostructures as high-performance electrocatalysts for oxygen reduction in both alkaline and acidic media. *ACS Appl. Mater. Interfaces* 9 (2017) 36944-36954.
- [45] Q. Wei, G. Zhang, X. Yang, Y. Fu, G. Yang, N. Chen, W. Chen, S. Sun, Litchi-like porous Fe/N/C spheres with atomically dispersed FeN<sub>x</sub> promoted by sulfur as highly efficient oxygen electrocatalysts for Zn–air batteries. *J. Mater. Chem. A* (2018).
- [46] Y. F. Hu, L. Zuin, G. Wright, R. Igarashi, M. McKibben, T. Wilson, S. Y. Chen, T. Johnson, D. Maxwell, B. W. Yates, Commissioning and performance of the variable line spacing plane grating monochromator beamline at the Canadian Light Source. *Rev. Sci. Instrum.* 78 (2007) 083109.
- [47] M. Kasrai, Z. Yin, G. M. Bancroft, K. H. Tan, X–ray fluorescence measurements of X–ray absorption near edge structure at the Si, P, and S L edges. *J. Vac. Sci. Technol., A* 11 (1993) 2694-2699.
- [48] D. Wang, L. Zuin, Li K-edge X-ray absorption near edge structure spectra for a library of lithium compounds applied in lithium batteries. *J. Power Sources* 337 (2017) 100-109.
- [49] L. Osmieri, E.-C. Ricardo, A. Marco, O. Pilar, H.A.M.V. Alessandro, S. Stefania. Effects of using two transition metals in the synthesis of non-noble electrocatalysts for oxygen reduction reaction in direct methanol fuel cell. *Electrochim. Acta* 266 (2018) 220-232.
- [50] A. Ohma, S. Kazuhiko, I. Akihiro, Y. Toshihiko, D. Akimasa. Membrane and catalyst performance targets for automotive fuel cells by FCCJ membrane, catalyst, MEA WG. *ECS Trans.* 41, 1 (2011) 775-784.
- [51] L. Osmieri, Z. Claudio, L. Wang, H.A.M.V. Alessandro, L. Alessandro, S. Stefania. Polypyrrole-derived Fe-Co-N-C catalyst for oxygen reduction reaction: performance in alkaline hydrogen and ethanol fuel cells. *ChemElectroChem.* 5 (2018) 1-13.

- [52] F. Jaouen, M. Lefèvre, J.-P. Dodelet, M. Cai, Heat-treated Fe/N/C catalysts for O<sub>2</sub> electroreduction: are active sites hosted in micropores? *J. Phys. Chem. B* 110 (2006) 5553-5558.
- [53] K. Elumeeva, J. Ren, M. Antonietti, T. P. Fellingner, High surface iron/cobalt-containing nitrogen-doped carbon aerogels as non-precious advanced electrocatalysts for oxygen reduction. *ChemElectroChem* 2 (2015) 584-591.
- [54] G. Wu, K. L. More, C. M. Johnston, P. Zelenay, High-performance electrocatalysts for oxygen reduction derived from polyaniline, iron, and cobalt. *Science* 332 (2011) 443-447.
- [55] K. S. Sing, Reporting physisorption data for gas/solid systems with special reference to the determination of surface area and porosity (Recommendations 1984). *Pure Appl. Chem.* 57 (1985) 603-619.
- [56] G. Leofanti, M. Padovan, G. Tozzola, B. Venturelli, Surface area and pore texture of catalysts. *Catal. Today* 41 (1998) 207-219.
- [57] V. Glibin, J.-P. Dodelet. Thermodynamic stability in acid media of FeN<sub>4</sub>-based catalytic sites used for the reaction of oxygen reduction in PEM fuel cells. *J. Electrochem. Soc.* 164 (2017) F948-F957.
- [58] R. Chenitz, I. K. Ulrike, M. Lefèvre, V. Glibin, G. Zhang, S. Sun, J.-P. Dodelet. A specific demetalation of Fe-N<sub>4</sub> catalytic sites in the micropores of NC-Ar+ NH<sub>3</sub> is at the origin of the initial activity loss of the highly active Fe/N/C catalyst used for the reduction of oxygen in PEM fuel cells." *Energy Environ. Sci.* 11 (2018) 365-382.
- [59] D. Li, G. M. Bancroft, M. Kasrai, M. E. Fleet, X. H. Feng, K. H. Tan, B. X. Yang, High-resolution Si K- and L<sub>2, 3</sub>-edge XANES of  $\alpha$ -quartz and stishovite. *Solid State Commun.* 87 (1993) 613-617.
- [60] D. Li, G. M. Bancroft, M. Kasrai, M. E. Fleet, X. H. Feng, K. H. Tan, High-resolution Si and P K- and L-edge XANES spectra of crystalline SiP<sub>2</sub>O<sub>7</sub> and amorphous SiO<sub>2</sub>-P<sub>2</sub>O<sub>5</sub>. *Am. Mineral.* 79 (1994) 785-788.
- [61] H. Demirkiran, Y. Hu, L. Zuin, N. Appathurai, P. B. Aswath, XANES analysis of calcium and sodium phosphates and silicates and hydroxyapatite-bioglass®45S5 co-sintered bioceramics. *Mater. Sci. Eng., C* 31 (2011) 134-143.

# Supporting Information

## **An active and robust Si-Fe/N/C catalyst derived from waste reed for oxygen reduction**

*Qiliang Wei<sup>†,1</sup>, Xiaohua Yang<sup>†,1</sup>, Gaixia Zhang<sup>1,\*</sup>, Dongniu Wang<sup>2</sup>, Lucia Zuin<sup>2</sup>, Dustin Banham<sup>3</sup>  
Lijun Yang<sup>3</sup>, Siyu Ye<sup>3</sup>, Youling Wang<sup>1</sup>, Mohamed Mohamedi<sup>1</sup>, Shuhui Sun<sup>1,\*</sup>*

<sup>1</sup>Institut National de la Recherche Scientifique-Énergie Matériaux et Télécommunications, Varennes, QC J3X 1S2, Canada. E-mail: [gaixia.zhang@emt.inrs.ca](mailto:gaixia.zhang@emt.inrs.ca) (G. Zhang); [shuhui@emt.inrs.ca](mailto:shuhui@emt.inrs.ca) (S. Sun)

<sup>2</sup>Canadian Light Source Inc., 44 Innovation Boulevard, Saskatoon, SK, S7N 2V3, Canada.

<sup>3</sup>Ballard Power Systems Inc., Burnaby, V5J 5J8, Canada

Figures:

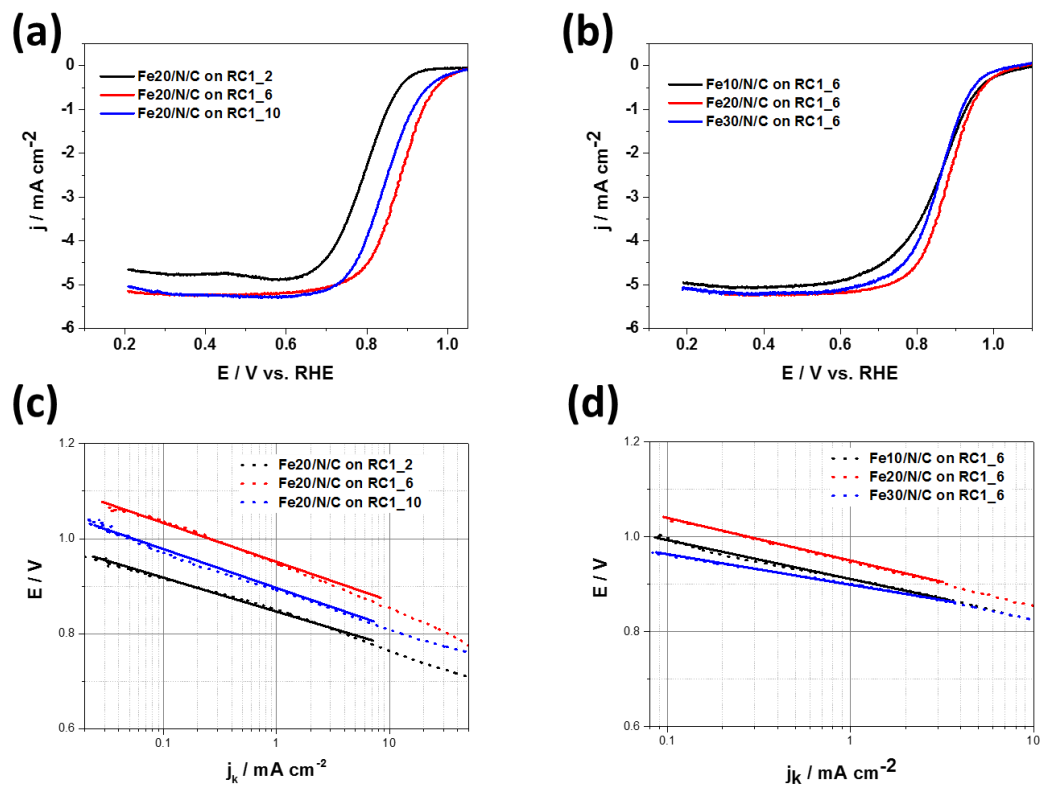


**Figure S1.** LSV results of (a) the Si-Fe/N/C with different carbon/KOH ratio and (b) different Fe content; (c, d) Tafel plots in O<sub>2</sub>-saturated 0.1 M KOH of the Si-Fe/N/C with different carbon/KOH ratio (a) and different Fe content (b) (scan rate = 10 mV s<sup>-1</sup>, rotation rate = 1600 rpm).

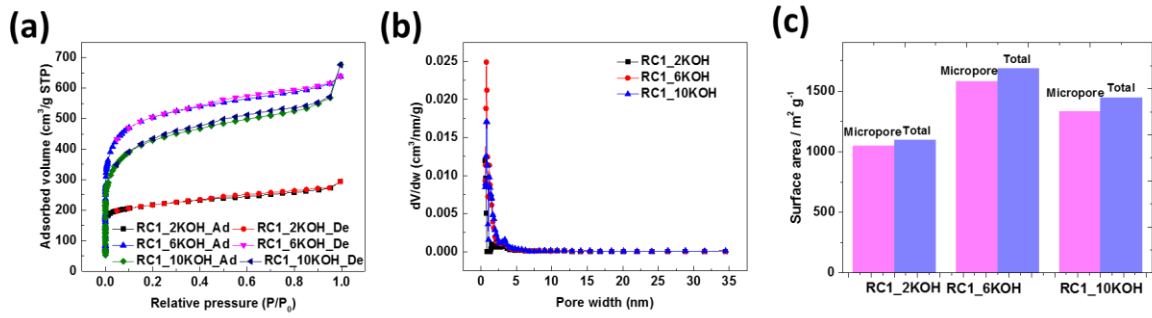


Figure S2. (a) N<sub>2</sub> adsorption/desorption and (b-c) pore width distribution of RC1<sub>x</sub> samples.

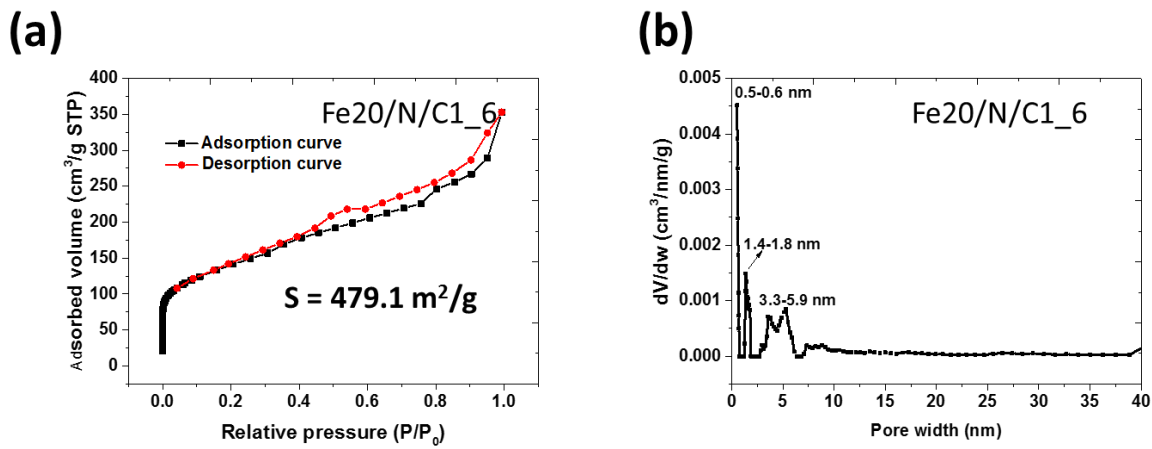
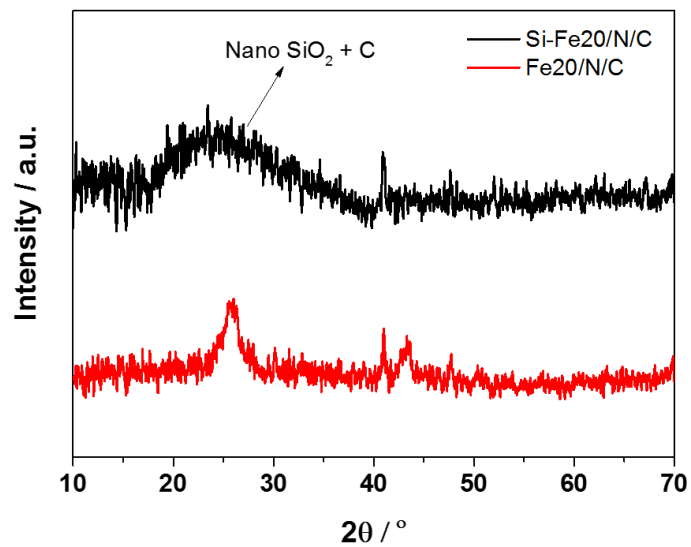
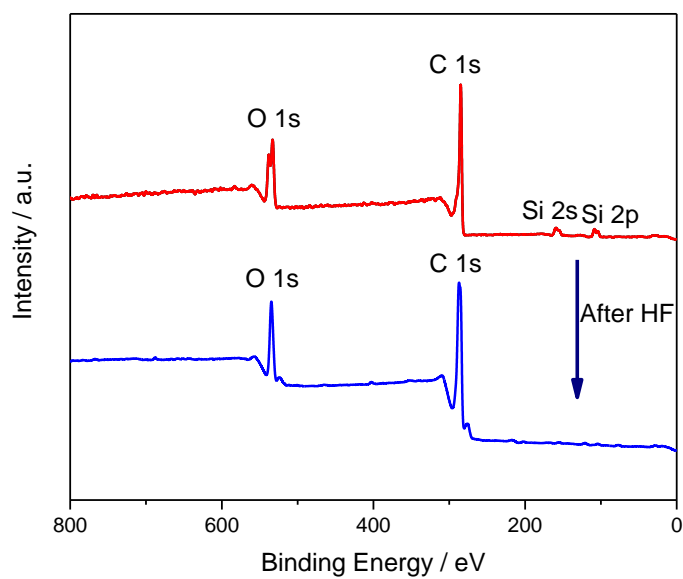


Figure S3. (a) N<sub>2</sub> adsorption/desorption and (b) pore width distribution of Fe20/N/C1<sub>6</sub> sample.



**Figure S4.** XRD spectra of Si-Fe20/N/C and Fe20/N/C.



**Figure S5.** XPS spectra of reed derived Si-RC1\_6 and RC1\_6 after removing Si.

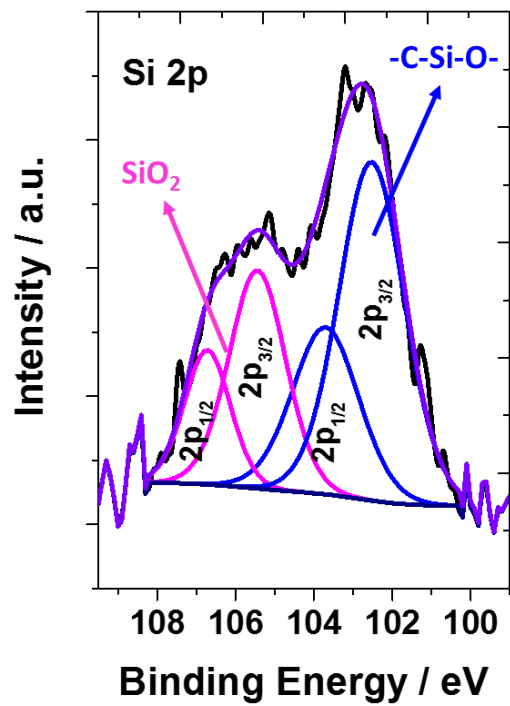


**Figure S6.** Core level Si 2p XPS spectrum of Si-Fe<sub>20</sub>/N/C1<sub>6</sub>.

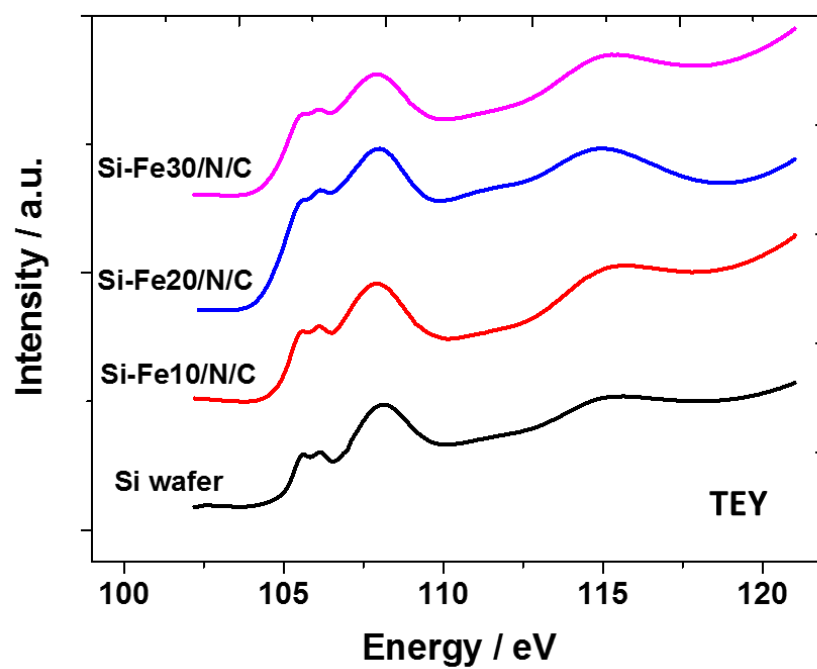


**Figure S7.** Silicon L-edge XANES for Si wafer and various Si-FeNC samples.

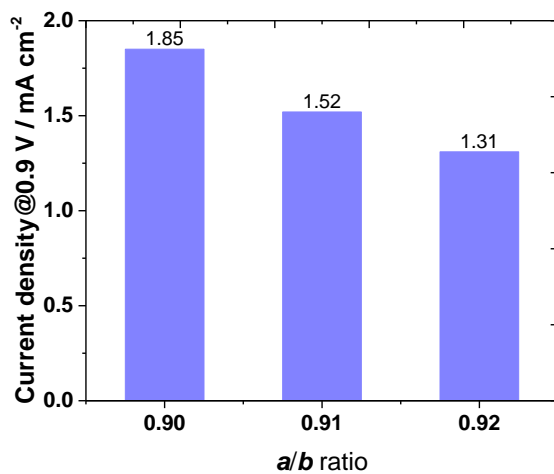


**Figure S8.** The relationship between the ORR activity and peak area ratios for peak *a* to peak *b* in Si L<sub>2,3</sub>-edge of Si-Fe/N/C samples.

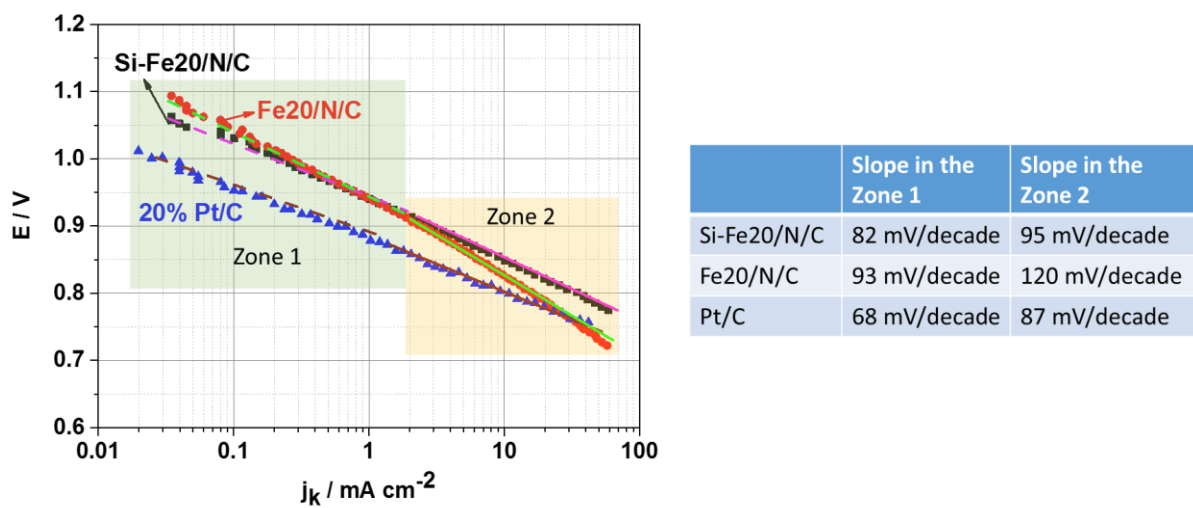


**Figure S9.** Tafel slope of Si-Fe20/N/C1\_6, Fe20/N/C1\_6 and commercial Pt/C in O<sub>2</sub>-saturated 0.1 M KOH at a scan rate of 10 mV s<sup>-1</sup>, rotation rate = 1600 rpm.

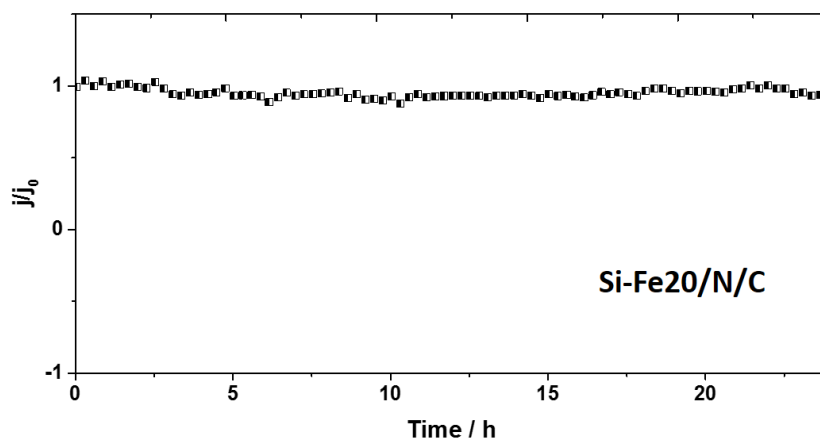


**Figure S10.** Long-term Chronoamperometric responses of Si-Fe20/N/C1\_6 in O<sub>2</sub>-saturated 0.1 M KOH without rotation.

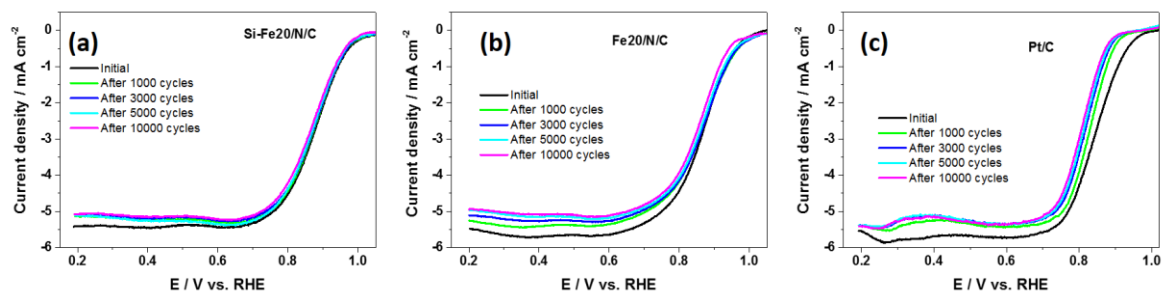


**Figure S11.** LSV curves of Si-Fe<sub>20</sub>/N/C<sub>1\_6</sub>, Fe<sub>20</sub>/N/C<sub>1\_6</sub> and commercial Pt/C after cycling between 0.6-1.0 V with different cycles in O<sub>2</sub>-saturated 0.1 M KOH at a scan rate of 10 mV s<sup>-1</sup>, rotation rate = 1600 rpm.

**Table S1.** N<sub>2</sub> adsorption/desorption analysis of KOH-activated porous samples

<b>N<sub>2</sub> adsorption/desorption (m<sup>2</sup>/g)</b>			
<b>Samples</b>	<b>Surface area (m<sup>2</sup>/g)</b>	<b>Surface area of micropore (m<sup>2</sup>/g)</b>	<b>Surface area of mesopore (m<sup>2</sup>/g)</b>
<b>RC1_2</b>	1097.6	1046.5 (95.3%)	51.1 (4.7%)
<b>RC1_6</b>	1763.3	1673.5 (89.8%)	89.8 (10.2%)
<b>RC1_10</b>	1445.1	1332.6 (92.2%)	88.5 (7.8%)

**Table S2.** N<sub>2</sub> adsorption/desorption analysis of Fe/N doped samples

<b>N<sub>2</sub> adsorption/desorption (m<sup>2</sup>/g)</b>			
<b>Samples</b>	<b>Surface area</b>	<b>Surface area of micropore (&lt;2.0 nm)</b>	<b>Surface area of mesopore (&gt;2.0 nm, &lt;35 nm)</b>
<b>Si-Fe10/N/C</b>	735.6	677 (92.0%)	58.6 (8.0%)
<b>Si-Fe20/N/C</b>	597.6	517 (86.5%)	80.6 (13.5%)
<b>Si-Fe30/N/C</b>	700.3	611.8 (87.4%)	88.5 (12.6%)
<b>Fe20/N/C</b>	596.3	402.4 (67.5%)	193.9 (32.5%)

**Table S3.** Integrated peak area ratios for peak *a* to peak *b* in Si L<sub>2,3</sub>-edge of Si-Fe/N/C samples.

<b>Samples</b>	<b>Ratio (a/b)</b>	<b>Current density @ 0.9 V</b>
<b>Si-Fe10/N/C</b>	0.91	1.52 mA/cm <sup>2</sup>
<b>Si-Fe20/N/C</b>	0.90	1.85 mA/cm <sup>2</sup>
<b>Si-Fe30/N/C</b>	0.92	1.31 mA/cm <sup>2</sup>

### 3.5 Transforming reed waste into a highly active metal-free catalyst for oxygen reduction reaction

Qiliang Wei, Mohamed Cherif, Gaixia Zhang, Ali Almesrati, Mingjie Wu, Yongfeng Hu, Vidal François, Shuhui Sun

To be submitted.

In this section, a high-activity metal-free catalyst for ORR was developed by using the waste reed stalk as the Si and C source, after the treatment with  $\text{NH}_3$ , the Si element in reed was demonstrated very active for ORR in alkaline media. The optimized Si-N-C sample shows an  $E_{\text{onset}}$  of  $\sim 1.00$  V and  $E_{1/2}$  of 0.89 V (vs. RHE), which can be rated as one of the best metal-free ORR catalysts among reported. It also displays better stability for ORR than commercial Pt/C in a half-cell environment. Moreover, this reed waste derived Si-N-C metal-free catalyst exhibits excellent performance as an air cathode for a Zn-air battery device. DFT calculation indicates that the Si and N sites (graphitic-N) in the carbon framework could promote the higher ORR activity.

*Contributions:* I performed most of the experimental synthesis, the electro-chemical measurements, and all characterizations. TEM measurements have been done by technicians. Mohamed Cherif and Ali Almesrati in Prof. Vidal François's group did the DFT simulation and wrote the corresponding DFT part in the manuscript. Mingjie Wu helped on the Zn-air battery test. I conducted the data analysis and the interpretation of results, as well as the manuscript writing, with the help of co-authors.

# Transforming reed waste into a highly active metal-free catalyst for oxygen reduction reaction

*Qiliang Wei,<sup>1</sup> Mohamed Cherif,<sup>1</sup> Gaixia Zhang,<sup>1,\*</sup> Ali Almesrati,<sup>1</sup> Mingjie Wu,<sup>1</sup> Yongfeng Hu,<sup>2</sup>  
Vidal François,<sup>1,\*</sup> Shuhui Sun<sup>1,\*</sup>*

<sup>1</sup>Énergie, Matériaux et Télécommunications, Institut National de la Recherche Scientifique (INRS), 1650 Boul. Lionel-Boulet, Varennes, Quebec J3X 1S2, Canada

<sup>2</sup>Canadian Light Source (CLS), 44 Innovation Boulevard, Saskatoon, SK, S7N 2V3, Canada.

**Abstract:** The disposal of bio-mass waste into valuable materials is of strategic importance to our future. Here, a simple and inexpensive metal-free catalyst was synthesised by employing the bio-waste reed as the single precursor for both carbon (C) and silicon (Si). Interestingly, after the treatment with NH<sub>3</sub>, the Si element in reed was demonstrated very active for oxygen reduction reaction (ORR) in alkaline media. The NH<sub>3</sub>-treatment extent has a big effect on its ORR performance. Impressively, the onset potential of the optimized sample reaches up to ~1.00 V (vs. reversible hydrogen electrode), the half-wave potential is 0.89 V, and it also shows longer term stability for ORR as compared to commercial Pt/C. Moreover, this reed waste derived Si-N-C metal-free catalyst exhibits excellent performance as an air cathode for a Zn-air battery device. The coexistence of Si and N is essential for the high ORR activity. DFT calculation corroborated this conclusion by indicating that the Si-N structure is essential for the high activity. These new findings will not only open an avenue for the rational design of highly active ORR electrocatalysts, but also symbolize an exciting area for sustainable and low-cost materials for advanced clean energy applications.

## Introduction

Oxygen reduction reaction (ORR) is one of the most extensively studied electrochemical processes occurring at the cathode of fuel cells and metal-air batteries.<sup>1-4</sup> Traditionally, platinum (Pt) has been regarded as the best ORR catalyst, however, as one of the scarcest noble metals on the Earth, its availability has become a major concern for all these electrochemical energy

storage and conversion (EESC) applications. In addition, Pt-based electrocatalysts are prone to agglomeration, which reduce their long-term ORR performance. Alternatively, low-cost electrocatalysts with comparable catalytic activities and stabilities to replace Pt is of prime importance for ORR, yet is still challenging. Nitrogen-doped carbon (NDC) materials have been of particular interest as metal-free electrocatalysts for ORR, due to the enhanced electric conductivity and electron-donor tendency.<sup>5-10</sup> Moreover, further improvement in the ORR activity was also demonstrated by the synergistic effect arising from the co-doping of a second heteroatom, such as S, P, B, F, Cl, Si, etc.<sup>11-22</sup> Among the second heteroatoms, S, P, and B are the most frequently studied doping elements, which could further break the electroneutrality of adjacent C atoms and create more charged sites favorable for O<sub>2</sub> adsorption and reduction. Recently, Si doping has also been proposed to improve the ORR activity of the carbon-based catalyst,<sup>18, 23, 24</sup> however, the performance of these reported metal-free catalysts are still far inferior to Pt/C and non-precious-metal catalysts (such as Fe/N/C), moreover, the active sites are not reliable or clear yet, due to the relative poor ORR activity. Additionally, biomass-derived carbon materials have aroused researchers' attention, from the point of view of economic processing and environmental protection. Therefore, finding new economical and renewable sources with simple and straightforward route to fabricate high performance metal-free catalysts to replace Pt/C for the ORR, as well as recognizing the active sites for ORR are still urgently required.

Reed (*Phragmites australis*), a typical member of the Poaceae family, is widely distributed worldwide<sup>25</sup> and outcompetes most of the other plants in its environment. So the overgrowing of reed lowers the local plant biodiversity and causes serious problems for many other hydrophyte wetland plants.<sup>26, 27</sup> Hence, developing uses for this potentially harmful resources is consistent with the global paradigm shifting towards green and sustainable development. It is known that Si exists in reed in a very favorable nanoscale arrangement. This sustainable Si source has been exploited for energy storage devices, such as lithium ion batteries<sup>28</sup> and supercapacitors<sup>29</sup>. Herein, we adopted waste reed stalk as C and Si precursor, after doping with N by an NH<sub>3</sub> treatment, the Si-N-C material exhibited excellent catalytic activity for ORR in 0.1 M KOH solution (it reaches a half-wave potential of 0.89 V vs. RHE), and excellent performance as an air electrode in a Zn-air battery. It can be rated as one of the best metal-free catalyst for ORR. First-principle calculations were performed to explain the high catalytic capability of the Si-N-C catalyst. This

may open a new path for rationally designing highly active ORR electrocatalysts from natural widely available waste.

## Results and discussion

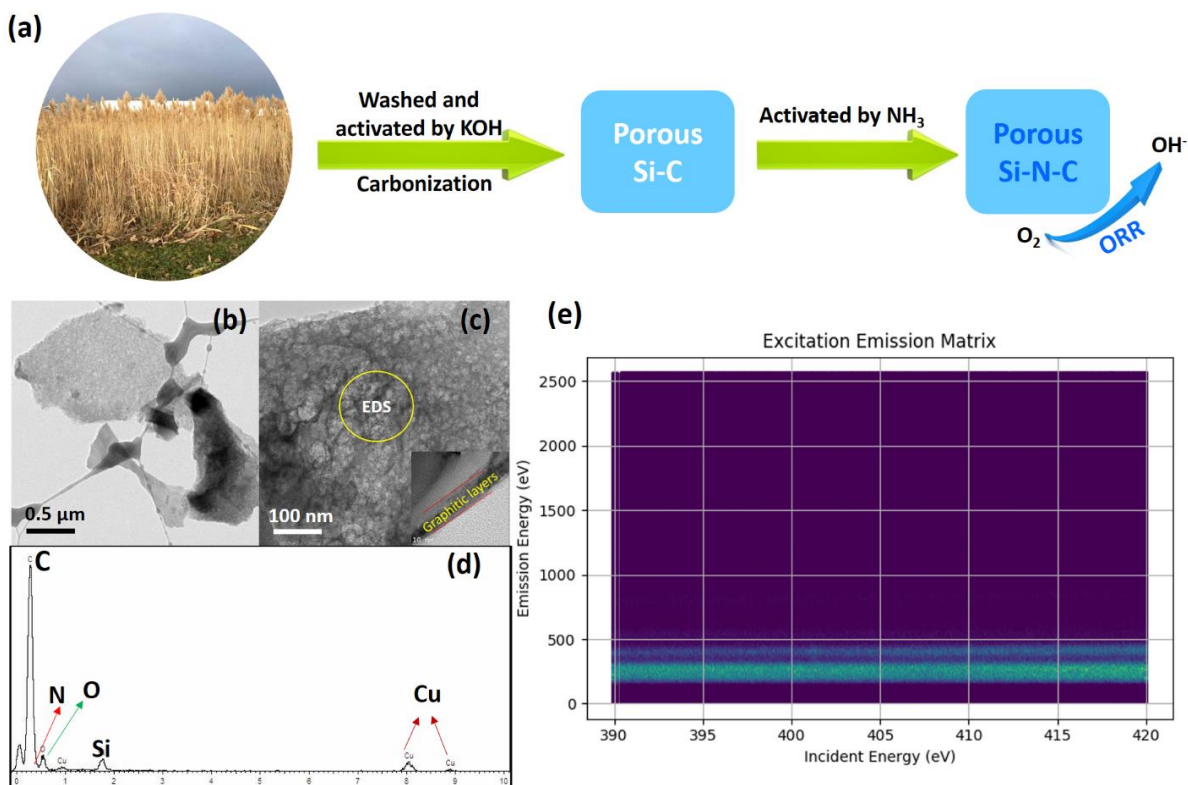


**Figure 1.** (a) Schematic procedure for the fabrication of porous Si-N-C from reed waste; (b-c) TEM images of porous Si-N-C-6 min; (d) EDS spectrum of the area in Figure 1b; (e) EEMS of Si-N-C-6 min.

The as-prepared (see Figure 1a and the section Materials in the SI) porous Si-C (before the NH<sub>3</sub> treatment) and porous Si-N-C catalysts were first investigated by transmission electron microscopy (TEM). The highly porous structure can be clearly observed for the Si-C sample from reed stalk after KOH-activation (Figure S1). The specimens of Si-N-C show a laminar structure consisting of thin cross-linked carbon nanosheets (Figure 1b), the high resolution TEM micrographs show the primarily defective microporous morphology with clear graphitic layers on the edge (inset of Figure 1c), the energy-dispersive X-ray spectroscopy (EDS) pattern indicates the existence of Si and C (Figure 1d), where the N peak is covered by C, but the existence of N can be confirmed by the blue emission line of excitation emission matrix spectrum (EEMS) shown in Figure 1e. By investigating the BET surface area of activated porous

Si-C and Si-N-C-*x* min samples, it can be seen that they all present a sharp uptake at low pressure and a smooth plateau at middle-to-high pressure, which is characteristic of micropore-dominated materials (Figure 2a and Figure S2a). The surface area of Si-N-C-*x* min (Figure 2c,  $\sim 1200 \text{ m}^2 \text{ g}^{-1}$ ) is a little lower than that of the porous Si-C sample before the  $\text{NH}_3$  treatment ( $\sim 1800 \text{ m}^2 \text{ g}^{-1}$ ) (Figure S2). This is caused by removing disordered carbon through the reaction between  $\text{NH}_3$  and the carbon matrix under high temperature.<sup>30</sup> Moreover, the duration of the  $\text{NH}_3$  treatment has little influence on the surface area of the Si-N-C samples, but longer treatment time leads to somewhat larger pore width, indicating that  $\text{NH}_3$  activation transforms part of the micropores into mesopores (Figure 2b and Table S1).

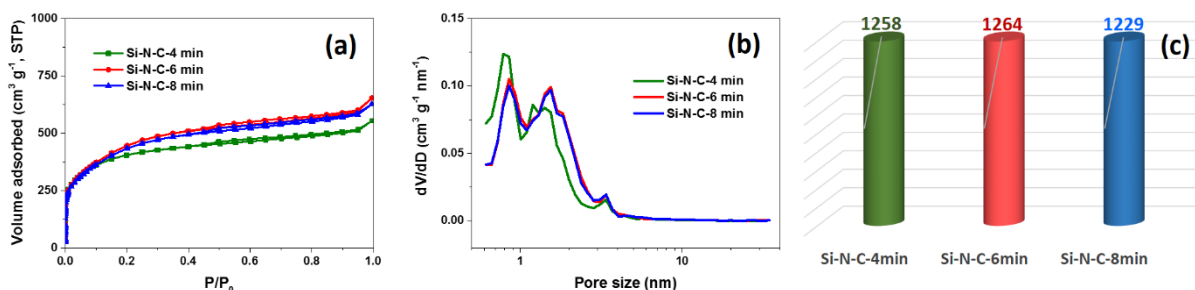


**Figure 2.** (a-b)  $\text{N}_2$ -adsorption/desorption isotherms of Si-N-C; (c) Surface area of Si-N-C-4 min, Si-N-C-6 min, and Si-N-C-8 min.

XPS analysis was carried out to investigate the elemental composition and chemical status evolution. The typical XPS survey spectrum (Figure 3a) indicates the existence of C, O, and Si in the Si-C samples derived from the natural reed stalks before the  $\text{NH}_3$  treatment. The appearance of the N peak around 400 eV in other Si-N-C-*x* min samples further confirms that nitrogen doping was successful. After an HF treatment, the Si element was removed successfully (see the N-C-6 min curve in Figure 3a). The high resolution C 1s XPS of Si-N-C sample (Figure S3) shows main peaks corresponding to the C–C and C=C bonds in the carbon basal plane, and strong C–O and C=O bonds resulting from carboxylic groups in the reed-based porous carbon samples. In addition, the C–N bond introduced by  $\text{NH}_3$  can be observed in the XPS spectra of the Si-N-C samples. According to the deconvoluted XPS spectra of N 1s shown in Figure 3c-e and Table S2, it can be seen that: (i) the oxygen content decreased with the longer  $\text{NH}_3$  activation time, (ii) the Si content doesn't change much during the  $\text{NH}_3$  activation, (iii) the nitrogen content first increased (from 4.04% for Si-N-C-4 min to 6.95% for Si-N-C-6 min) then decreased to

5.41% for Si-N-C-8 min. These observations indicate that during the  $\text{NH}_3$  activation process, with the doping of N into the carbon matrix, the  $\text{NH}_3$  was reacting with the oxygen species all the time, meanwhile, also eliminating nitrogen moieties after a certain time.<sup>31</sup> The N functionalities and their distribution were identified by the curve-fitting procedures, and the results are summarized in Figure 3f and Table S3. The N contents in pyridine, pyrrolic, and graphitic-N show slight changes, with higher graphitic-N for Si-N-C-6 min. These trends indicate that the types of N in the carbon network of graphene sheets can be slightly tuned by the  $\text{NH}_3$  activation treatment degree, but the N content reached a peak value after around 6 min treatment.

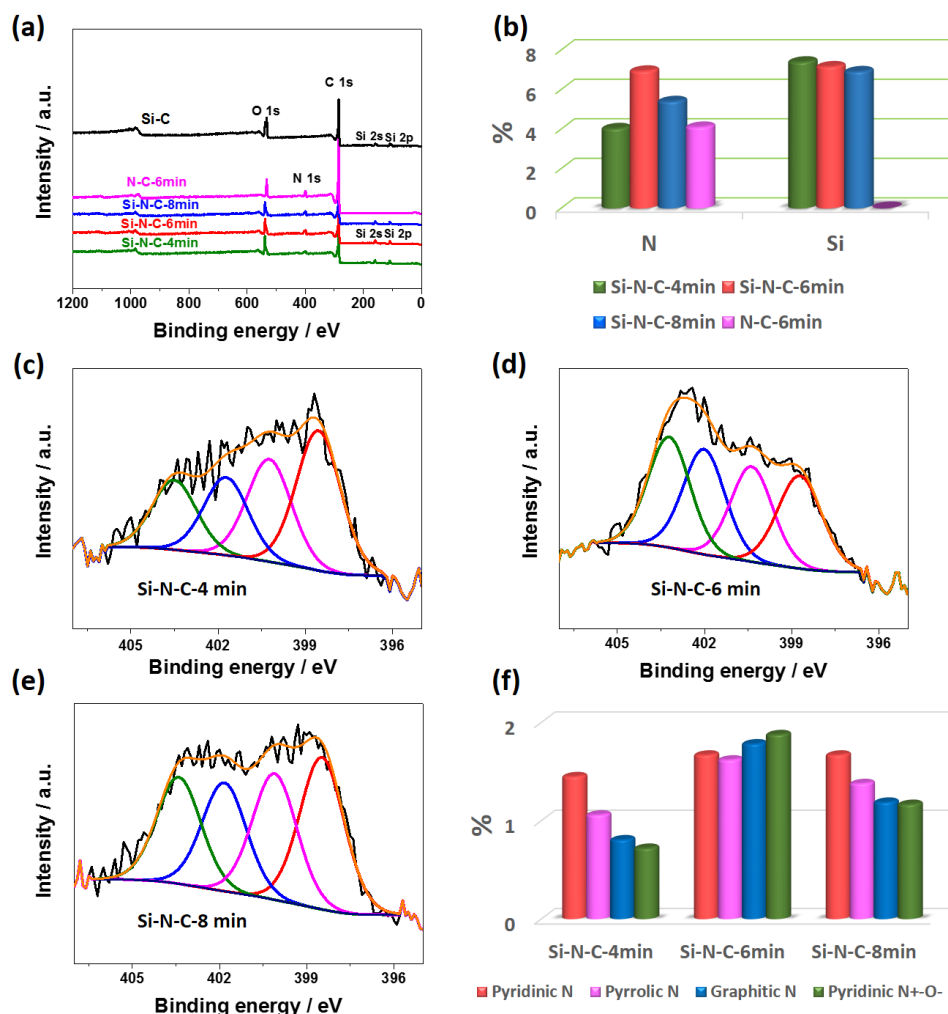


**Figure 3.** (a) XPS survey spectra of Si-N-C-*x* min, (b) Element N and Si content in different Si-N-C-*x* min samples, (c-e) core level N 1s XPS spectrum of Si-N-C-*x* min, (f) content of different N configurations in Si-N-C-4min, Si-N-C-*x* min.

To gain insight into the ORR activity, we examined the electrocatalytic properties of Si-N-C-*x* min and commercial Pt/C by employing cyclic voltammetry (CV) and rotation ring-disk electrode (RRDE) technique in a N<sub>2</sub>- and O<sub>2</sub>-saturated 0.1 M aqueous KOH electrolyte solution. As shown in Figure S4, the double layer capacitance of Si-C is higher than that of the Si-N-C-*x* min, which is consistent with the N<sub>2</sub> adsorption/desorption results (Figure 2). Under O<sub>2</sub> flow, well-defined characteristic ORR peaks can be observed for all Si-N-C-*x* min samples, among which, Si-N-C-6 min has more positive peak potential than the other samples, indicating a superior ORR activity. Figure 4a and Figure S5 is the LSV curves of these samples, it can be seen that the onset potential (here E<sub>onset</sub> is defined as the potential when catalytic current density reaches -0.20 mA cm<sup>-2</sup>) for Si-N-C-4 min, Si-N-C-6 min, Si-N-C-8 min and Pt/C was 0.93, 1.00, 0.92 and 0.96 V versus RHE, respectively; furthermore, since Si-N-C-6 min had a more positive half potential (E<sub>1/2</sub>) of 0.89 V, which was ~40 mV more positive than that of Pt/C, the ORR activity of the as-synthesized Si-N-C-6 min is superior to the other metal-free catalysts (Figure 4b). Moreover, even for a loading decreased to 0.16 mg cm<sup>-2</sup> for Si-N-C-6 min, the ORR activity can still stay a close level as Pt/C (Figure S7), indicating the excellent catalytic activity for ORR of the reed-derived Si-N-C-6min catalyst. The high ORR activity of Si-N-C-6 min is also supported by the Tafel plot as shown in Figure S8. The Si-C (without NH<sub>3</sub> treatment) and N-C-6 min show inferior activity (E<sub>onset</sub> = 0.82 V for Si-C, and 0.91 V for N-C-6min), indicating that both N and Si play an important roles for ORR. To disclose the reaction pathways of the as-prepared catalysts, the formed peroxide intermediate during the ORR process were calculated, as shown in Figure S6. The Si-N-C-6-min catalyst had a peroxide yield below 7.5% over the potential range of 0.1-0.8 V, suggesting its high efficiency to convert to OH<sup>-</sup>. Taking the porous structures and surface properties of prepared catalysts into consideration, such outstanding activity for Si-N-C-6-min is most probably related to the high content of N and the Si-N-C configuration, because other samples also possess large surface area and similar element composition. As the most active catalyst, Si-N-C-6-min was then subjected to accelerated durability test (ADT) to reveal its stability. After 5000 continuous cycles, E<sub>1/2</sub> of Si-N-C-6-min exhibits a slightly negative shift (Figure 4c), which outperforms the commercial Pt/C catalysts (33 mV, inset image of Figure 4c). These results suggest that the Si-N-C-6 min catalyst also has significantly better stability than Pt/C. To explore the potential application of Si-N-C-6 min catalyst for real energy devices, a Zn-air battery was assembled using Si-N-C-6 min as the air

cathode and a polished zinc plate as the anode filled with the 6 M KOH electrolyte, Figure 4d depicts the polarization curves and corresponding power density plots of a single Zn-air battery constructed with Si-N-C-6 min. One observes a maximum power density of  $\sim 100 \text{ mW cm}^{-2}$  which is comparable to many recently reported excellent catalysts.<sup>15, 32-35</sup> The galvanostatic discharge at  $20 \text{ mA cm}^{-2}$  reveals that the voltage delivered by the Zn-air batteries using the Si-N-C-6 min catalyst is 1.24 V (comparable with Pt/C, Figure 4e), while the specific capacity of the Si-N-C-6 min-based ZAB normalized to the mass of consumed Zn was estimated to be  $\sim 800 \text{ mAh g}^{-1}$ , corresponding to a gravimetric energy density of  $\sim 990 \text{ Wh kg}_{\text{Zn}}^{-1}$  at the discharge density of  $20 \text{ mA cm}^{-2}$  (Figure 4f). These results reveal that the reed waste derived Si-N-C-6 min catalyst has potential in metal-air batteries field.

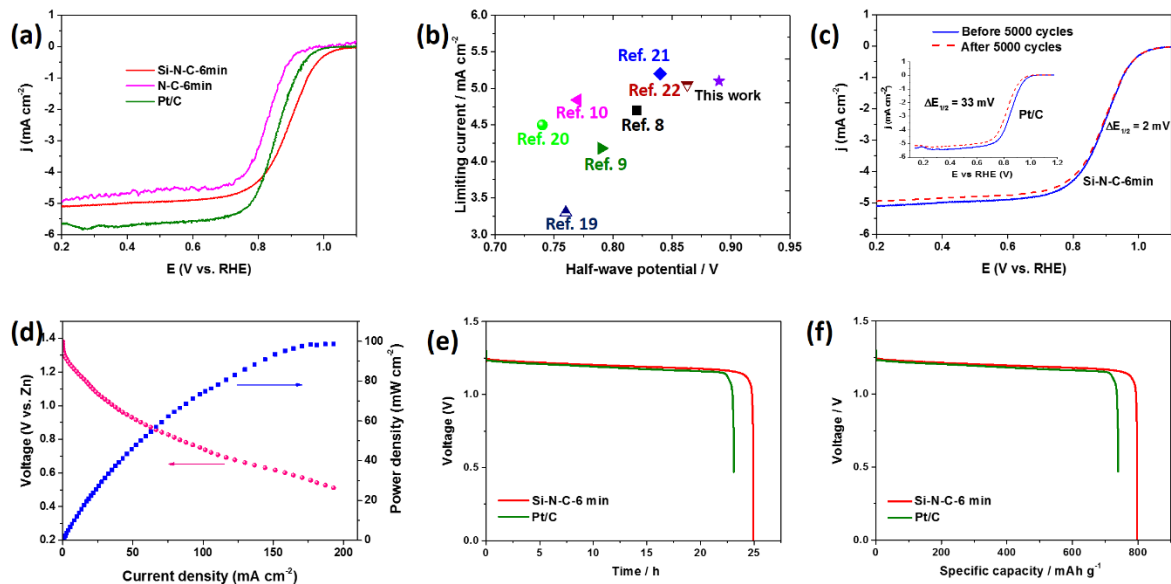


**Figure 4.** (a) LSV curves, (b) comparison of the limiting current as a function of the half-wave potential for recently reported metal-free electrocatalysts in  $\text{O}_2$ -saturated 0.1 M KOH at a scan rate of  $10 \text{ mV s}^{-1}$ , rotation rate = 1600 rpm, (c) RDE polarization curves of the studied catalyst and Pt/C (inset figure) before and after 5000 potential cycles in  $\text{O}_2$ -saturated 0.1 M KOH, (d) discharge polarization curves and corresponding power density plots in a two-electrode rechargeable Zn-air battery, (e) galvanostatic discharge curves of Zn-air batteries at  $20 \text{ mA cm}^{-2}$ , (f) long-term galvanostatic discharge curves at  $20 \text{ mA cm}^{-2}$  of Zn-air batteries until complete consumption of the Zn anode. The specific capacity was normalized to the mass of consumed Zn.

To explain the excellent catalytic activity of Si-N-C-6 min, the analysis of Si is necessary. Since the surface of Si is very sensitive and easily oxidized, XPS with a shallow detecting depth is not

suitable for the analysis of Si element. X-ray absorption fine structure (XAFS) spectroscopy was used to probe the chemical state of Si for the samples, measured in the TEY mode. TEY measurements of the Si K-edge has the detecting depth around 70 nm.<sup>36</sup> From Figure 5a, all samples have broad dominating characteristic peaks at 1848~1849 eV, featured as Si-C and Si-O. The first derivative spectra, defined as the inflection point of the XANES, was performed to determine if there is some chemical shifts of the absorption edge. The derivative of normalized TEY in Figure 5b indicates that there is a slight shift towards lower photon energy with longer treatment under ammonia. This indicates that with longer NH<sub>3</sub> treatment, transition from Si 1s electron to the p-featured orbitals becomes easier, mostly influenced by the N-doping effect. Apparently, with the treatment time of NH<sub>3</sub>, the shoulder of Si-N-C configuration peak becomes prominent.<sup>37</sup> Looking back to the ORR activity and XPS results, the explanation of why Si-N-C-6 min has the best performance for ORR becomes clear: although the normalized Si-N-C configuration peak for Si-N-C-8 min is even higher than Si-N-C-6 min, the lower N content in Si-N-C-8 min potentially reduce the active sites. Both Si and N are indispensable for the ORR activity, this can be supported by the density functional theory (DFT) calculation as following.

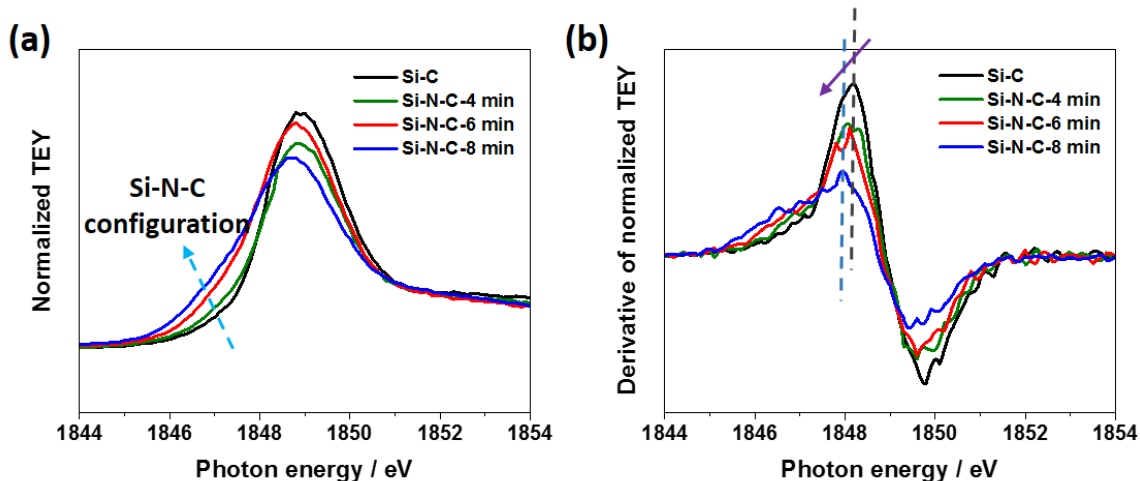


**Figure 5.** (a) Si K-edge X-ray absorption near-edge structure (XANES); (b) the corresponding derivative of the Si K-edge XANES.

### Density functional theory (DFT) calculations

We performed DFT calculations to (1) identify the catalytic sites in a graphene matrix doped with Si and/or N, and (2) understand the activity of such catalysts in alkaline media. The model

structure is made of graphene sheet in which two carbon atoms were replaced with Si and N atoms (Figure 6a). The first step of our calculations consisted in identifying the sites where O<sub>2</sub> would adsorb since this is the first step of the catalytic process. For doing so, we placed an O<sub>2</sub> molecule at different locations on the structures (on the top of C, Si and N atoms, between the bonds, and inside the cycles) and used DFT to optimize the atomic arrangement corresponding to the minimum energy of the system. We found (1) that the energy is always minimized when O<sub>2</sub> is on the top of the Si atom in the side-on position (parallel to the plane), and (2) that O<sub>2</sub> would not adsorb anywhere on the structure when Si and N are not in the same hexagonal cycle. Therefore, no adsorption occurs in absence of Si and/or N in the graphene structure or when Si and N are far apart. We identified adsorption of O<sub>2</sub> when its binding energy

$$E_b = E_{\text{Si/N/graph}+\text{O}_2} - E_{\text{Si/N/graph}} - E_{\text{O}_2} \quad (1)$$

is negative. In this expression  $E_{\text{Si/N/graph}}$  is the energy of the catalyst,  $E_{\text{O}_2}$  is the energy of the isolated O<sub>2</sub> molecule, while  $E_{\text{Si/N/graph}+\text{O}_2}$  is the energy of the catalyst including the O<sub>2</sub> molecule on its surface. The fact that  $E_b > 0$  in N-doped graphene (no Si) is in agreement with other calculations done in the same conditions (in aqueous environment, the binding energy of O<sub>2</sub> becomes slightly negative).<sup>38</sup> We have thus selected the 6 different C-N-Si arrangements shown in Figure 6a where O<sub>2</sub> would adsorb on the Si atom. The first 3 structures are periodic in the x-y plane while the 3 last structures are periodic only along the x direction. As seen in Table 1, the binding energies of O<sub>2</sub> ranges between -1.3 eV (structure 4) to -3.3 eV (structure 5).

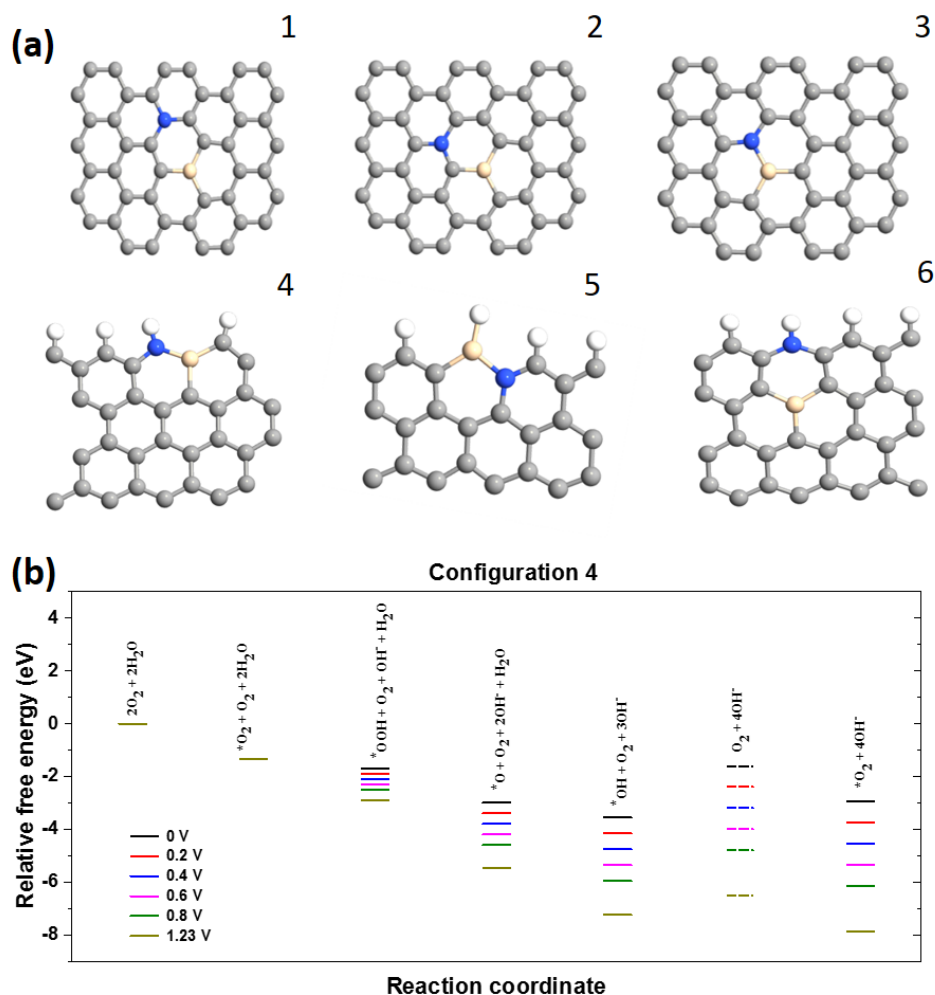


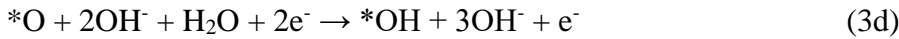
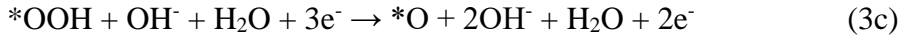
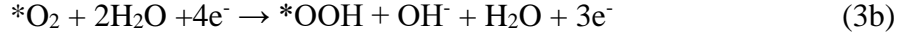
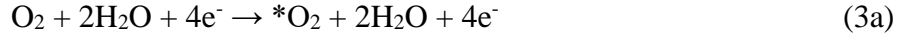
**Figure 6.** (a) Si- and N-doped graphene structures considered in our calculations. Legend: C: gray, N: blue, Si: yellow. (b) Relative free energy of the catalytic reaction of the structure 4 for different potentials  $U$ . The first 6 reaction coordinates correspond to those of the catalytic sequence (3a-3e) while the last one is the result of the reaction (5) replacing the reaction (3e).

We have calculated the relative formation energy of each structure to provide hints on the structures which are more likely to be found in the actual catalyst, by using the expression

$$\Delta E_f = E_{\text{Si/N/graph}} + 2E_C - (E_{\text{graph}} + E_N + E_{\text{Si}}) \quad (2)$$

where  $E_{\text{graph}}$  is the energy of the pristine graphene structure,  $E_C$  is the average energy of a carbon atom in the pristine graphene structure, while  $E_{\text{Si}}$  and  $E_N$  are the energy of an isolated Si and N atom, respectively. The relative formation energies for the 6 structures considered are shown in

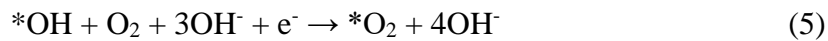
Table S4. One observes that the structures with a Si-N bond have the lowest formation energies in the two groups formed by the structures 1, 2, 3 and 4, 5, 6, respectively, and that the structure 4 has the lowest relative formation energy. The second step of our calculations consisted in estimating the relative free energies of the 4 electron catalytic reaction steps, assumed to be in alkaline media.<sup>38</sup>



where the prefix \* denotes adsorption of the species on the Si atom inside the graphene structure. The relative free energy for each reaction step is defined as

$$\Delta G = \Delta E + nU + \Delta E_{\text{water}} + \Delta ZPE - T\Delta S \quad (4)$$

In this expression,  $E$  is the total energy of the system,  $n$  is the number of  $\text{OH}^-$  ions,  $U$  is the external potential,  $E_{\text{water}}$  is the solvation energy, ZPE is the zero point energy, and TS is the entropy term. The energy of all neutral atomic structures was calculated through DFT while the energy of the  $\text{OH}^-$  ion is obtained from the thermodynamic balance of the whole catalytic process:  $E_{\text{O}_2} + 2E_{\text{H}_2\text{O}} - 4E_{\text{OH}^-} = 1.6 \text{ eV}$ . To keep the calculations tractable, we assumed as in a previous work that the three last terms of Equation (3) nearly cancel each other.<sup>39</sup> The relative free energy as a function of the reaction step for different potentials behaves qualitatively the same way for all structures considered. It is illustrated in Figure 6b for the structure 4, which has the lowest relative formation energy (Table S4). The reaction sequence (3a-3e) leads to the result that \*OH will poison the Si catalytic sites since the last step  $*\text{OH} + 3\text{OH}^- + \text{e}^- \rightarrow 4\text{OH}^-$  is uphill for  $U < 1.9 \text{ eV}$ . This result is similar to that of Yu et al. for N-doped graphene where the poison was rather \*O.<sup>38</sup> They assumed that  $\text{O}_2$  would somehow adsorb on a catalytic site by removing an \*O. In our case, the reaction



is exothermic for  $U \geq U_0 \sim 0.6$  V, as can be seen in Figure 6b, and the relative free energy becomes descending all the way, making the catalytic reaction thermodynamically possible. The results for all the 6 structures are shown in Figure S9 for comparison. The values of  $U_0$ , where the relative free energy becomes descending for the 6 structures considered, are displayed in Table S4. One observes that  $U_0 \sim 0.4$  V for structures 3 and 5 is in fair agreement with the experiments since one can see in Figure 4a that the limiting current being reached when  $E$  (V vs RHE)  $< 0.8$  V, meaning an overpotential  $U > 1.23 - 0.8 = 0.423$  V is needed to drive the reaction. In the case of structure 5, the reaction (5) is exothermic at  $U_0 = 0$ , but the relative free energy is uphill for the reaction 3b  $*\text{O}_2 + 2\text{H}_2\text{O} + 4\text{e}^- \rightarrow *\text{OOH} + \text{OH}^- + \text{H}_2\text{O} + 3\text{e}^-$  when  $U < 0.4$  V. In the case of the structure 6, the binding energy of  $*\text{OH}$  is very high and this structure seems to remain inactive for any useful potentials. In summary, these theoretically calculated results explain the most possible active sites and clarify the high ORR activity in the Si-N-C catalyst in this work.

## Conclusion

In summary, a high-activity metal-free catalyst for ORR was developed by using the waste reed stalk as the Si and C source, after the treatment with  $\text{NH}_3$ , the Si element in reed was demonstrated very active for ORR in alkaline media. The optimized Si-N-C sample shows an  $E_{\text{onset}}$  of  $\sim 1.00$  V and  $E_{1/2}$  of 0.89 V (vs. RHE), which is one of the best among reported metal-free ORR catalysts. It also displays better stability for ORR than commercial Pt/C in a half-cell environment. Moreover, this reed waste derived Si-N-C metal-free catalyst exhibits excellent performance as an air cathode for a Zn-air battery device. DFT calculation indicates that the Si and N sites (graphitic-N) in the carbon framework could promote the higher ORR activity. We believe that our work will give more insights to design more efficient catalysts for the clean energy related devices and bring a great significance to the sustainable development of energy.

## References

- [1] M. Lefèvre, E. Proietti, F. Jaouen and J.-P. Dodelet, *Science*, 2009, **324**, 71-74.
- [2] B. Wang, X. Wang, J. Zou, Y. Yan, S. Xie, G. Hu, Y. Li and A. Dong, *Nano Letters*, 2017, **17**, 2003-2009.
- [3] H. Pang, P. Gu, M. Zheng, Q. Zhao, X. Xiao and H. Xue, *Journal of Materials Chemistry A*, 2017.

- [4] Q. Wei, Y. Fu, G. Zhang and S. Sun, *Current Opinion in Electrochemistry*, 2017.
- [5] D. Guo, R. Shibuya, C. Akiba, S. Saji, T. Kondo and J. Nakamura, *Science*, 2016, **351**, 361-365.
- [6] P. Chen, L.-K. Wang, G. Wang, M.-R. Gao, J. Ge, W.-J. Yuan, Y.-H. Shen, A.-J. Xie and S.-H. Yu, *Energy & Environmental Science*, 2014, **7**, 4095-4103.
- [7] Q. Wei, X. Tong, G. Zhang, J. Qiao, Q. Gong and S. Sun, *Catalysts*, 2015, **5**, 1574-1602.
- [8] X. Li, Y. Fang, S. Zhao, J. Wu, F. Li, M. Tian, X. Long, J. Jin and J. Ma, *Journal of Materials Chemistry A*, 2016, **4**, 13133-13141.
- [9] L. Qin, R. Ding, H. Wang, J. Wu, C. Wang, C. Zhang, Y. Xu, L. Wang and B. Lv, *Nano Research*, 2017, **10**, 305-319.
- [10] B. Men, Y. Sun, M. Li, C. Hu, M. Zhang, L. Wang, Y. Tang, Y. Chen, P. Wan and J. Pan, *ACS Applied Materials & Interfaces*, 2016, **8**, 1415-1423.
- [11] S. Gao, H. Liu, K. Geng and X. Wei, *Nano Energy*, 2015, **12**, 785-793.
- [12] Z. Liu, H. Nie, Z. Yang, J. Zhang, Z. Jin, Y. Lu, Z. Xiao and S. Huang, *Nanoscale*, 2013, **5**, 3283-3288.
- [13] X. Wang, J. Wang, D. Wang, S. Dou, Z. Ma, J. Wu, L. Tao, A. Shen, C. Ouyang and Q. Liu, *Chemical Communications*, 2014, **50**, 4839-4842.
- [14] Y. Zhao, L. Yang, S. Chen, X. Wang, Y. Ma, Q. Wu, Y. Jiang, W. Qian and Z. Hu, *Journal of the American Chemical Society*, 2013, **135**, 1201-1204.
- [15] Y. Su, Z. Yao, F. Zhang, H. Wang, Z. Mics, E. Cánovas, M. Bonn, X. Zhuang and X. Feng, *Advanced Functional Materials*, 2016, **26**, 5893-5902.
- [16] C. Deng, H. Zhong, X. Li, L. Yao and H. Zhang, *Nanoscale*, 2016, **8**, 1580-1587.
- [17] Z. Liu, M. Li, F. Wang and Q.-D. Wang, *Journal of Power Sources*, 2016, **306**, 535-540.
- [18] Z. Liu, X. Fu, M. Li, F. Wang, Q. Wang, G. Kang and F. Peng, *Journal of Materials Chemistry A*, 2015, **3**, 3289-3293.
- [19] A. Mulyadi, Z. Zhang, M. Dutzer, W. Liu and Y. Deng, *Nano Energy*, 2017, **32**, 336-346.
- [20] S. Zhang, Y. Cai, H. He, Y. Zhang, R. Liu, H. Cao, M. Wang, J. Liu, G. Zhang and Y. Li, *Journal of Materials Chemistry A*, 2016, **4**, 4738-4744.
- [21] Y. Lv, L. Yang and D. Cao, *ACS applied materials & interfaces*, 2017, **9**, 32859-32867.
- [22] L. Zhao, X.-L. Sui, Q.-Y. Zhou, J.-Z. Li, J.-J. Zhang, G.-S. Huang and Z.-B. Wang, *Journal of Materials Chemistry A*, 2018, **6**, 6212-6219.

- [23] S. K. Ramasahayam and T. Viswanathan, *ChemistrySelect*, 2016, **1**, 3527-3534.
- [24] S. C. Abbas, K. Ding, Q. Liu, Y. Huang, Y. Bu, J. Wu, J. Lv, M. A. Ghausi and Y. Wang, *Journal of Materials Chemistry A*, 2016, **4**, 7924-7929.
- [25] E. Epstein, *Annals of Applied Biology*, 2009, **155**, 155-160.
- [26] K. Saltonstall, *Proceedings of the National Academy of Sciences*, 2002, **99**, 2445-2449.
- [27] Wikipedia, <https://en.wikipedia.org/wiki/Phragmites>, <https://en.wikipedia.org/wiki/Phragmites>).
- [28] J. Liu, P. Kopold, P. A. van Aken, J. Maier and Y. Yu, *Angewandte Chemie*, 2015, **127**, 9768-9772.
- [29] J. Zhao, Y. Zhang, T. Wang, P. Li, C. Wei and H. Pang, *Advanced Materials Interfaces*, 2015, **2**.
- [30] F. Jaouen and J.-P. Dodelet, *The Journal of Physical Chemistry C*, 2007, **111**, 5963-5970.
- [31] H.-W. Liang, X. Zhuang, S. Brüller, X. Feng and K. Müllen, *Nature Communications*, 2014, **5**.
- [32] P. Chen, T. Zhou, L. Xing, K. Xu, Y. Tong, H. Xie, L. Zhang, W. Yan, W. Chu and C. Wu, *Angewandte Chemie International Edition*, 2017, **56**, 610-614.
- [33] J. Zhang, Z. Zhao, Z. Xia and L. Dai, *Nature Nanotechnology*, 2015, **10**, 444-452.
- [34] L. Wang, C. Yang, S. Dou, S. Wang, J. Zhang, X. Gao, J. Ma and Y. Yu, *Electrochimica Acta*, 2016, **219**, 592-603.
- [35] M. G. Park, D. U. Lee, M. H. Seo, Z. P. Cano and Z. Chen, *Small*, 2016, **12**, 2707-2714.
- [36] M. Kasrai, W. N. Lennard, R. W. Brunner, G. M. Bancroft, J. A. Bardwell and K. H. Tan, *Applied Surface Science*, 1996, **99**, 303-312.
- [37] Y. F. Hu, H. Piao, J. Fronheiser and K. Matocha, *Journal of Electron Spectroscopy and Related Phenomena*, 2011, **184**, 245-248.
- [38] L. Yu, X. Pan, X. Cao, P. Hu and X. Bao, *Journal of Catalysis*, 2011, **282**, 183-190.
- [39] C. E. Szakacs, M. Lefèvre, U. I. Kramm, J.-P. Dodelet and F. Vidal, *Physical Chemistry Chemical Physics*, 2014, **16**, 13654-13661.

## Supporting Information

### **Transforming reed waste into a highly active metal-free catalyst for oxygen reduction reaction**

*Qiliang Wei,<sup>1</sup> Mohamed Cherif,<sup>1</sup> Gaixia Zhang,<sup>1,\*</sup> Ali Almesrati,<sup>1</sup> Mingjie Wu,<sup>1</sup> Yongfeng Hu,<sup>2</sup>  
Vidal François,<sup>1,\*</sup> Shuhui Sun<sup>1,\*</sup>*

<sup>1</sup>Énergie, Matériaux et Télécommunications, Institut National de la Recherche Scientifique (INRS), 1650 Boul. Lionel-Boulet, Varennes, Quebec J3X 1S2, Canada

<sup>2</sup>Canadian Light Source (CLS), 44 Innovation Boulevard, Saskatoon, SK, S7N 2V3, Canada.

## Experimental

### Materials

Hydrochloric acid (HCl, 32% in H<sub>2</sub>O), hydrofluoric acid (HF, 48-50%) and potassium hydroxide (KOH, 87.2%), were bought from Fisher Scientific; Reed stalk was obtained from a local farmland in Varennes (Quebec). All chemicals were used as received and solutions were prepared with deionized water (Millipore Milli-Q, 18.2 MΩ cm).

### Preparation of porous Si-N-C catalysts

The procedure of the preparation of porous Si-N-C catalysts from reed is summarized in Figure. 1a. Before carbonization, the reed was carefully cut into small pieces, washed with DI-water, and dried in oven at 80 °C for 2 days. The dry samples were pre-carbonized in a combustion boat at 800 °C for 1 h under Ar flow. Afterwards, the pre-carbonized materials were mixed with KOH sufficiently and heated in a homemade copper boat under Ar flow at 700 °C for 1 h (to obtain porous Si-C sample), followed by pyrolysis under ammonia atmosphere at 950 °C with different extent (in this work, we use 70 mg of each Si-C sample to undergo the NH<sub>3</sub> pyrolysis with 4 min, 6 min, and 8 min respectively, the samples are denoted as Si-N-C-*x* min, *x* = 4, 6, 8.). To investigate the role of Si, the Si-N-C sample was washed by HF (to remove the Si atoms), denoted as N-C-*x* min-HF.

### Physical characterizations

The morphological structures of the catalysts were investigated by transmission electron microscopy (TEM) and high-resolution TEM (HRTEM) (JEOL JEM-2100F, operated at 200 kV). The surface properties were analysed by X-Ray photoelectron spectroscopy (XPS, VG ESCALAB 220i-XL) equipped with a hemispherical analyser for a Twin Anode X-Ray Source. The C 1s peak (BE = 284.6 eV) was used as the reference line to accurately determine the positions of other spectral lines. The fine structure of the photoelectron lines was treated using Casa XPS software (2.3.15 Version). The surface areas of the catalysts were measured through N<sub>2</sub> sorption isotherms that were collected using Quantachrome Instruments Autosorb-1 at liquid nitrogen temperature (77.3 K). The surface areas were estimated from the Brunauer-Emmett-Teller (BET) equation and from the fitting of the N<sub>2</sub>-adsorption isotherms, with the Quenched

solid density functional theory (QSDFT) available in the AS1WIN software. QSDFT is the most advanced DFT method developed from 2006 for the pore size analysis of geometrically and chemically disordered micro-mesoporous carbons, which allows the calculation of pore size distributions from ca. 0.6 nm up to ca. 40 nm. It allows for a major improvement of the accuracy of DFT pore size distribution analyses of disordered carbon materials from low-temperature nitrogen adsorption isotherms because it takes into account the effects of surface roughness, anisotropy and heterogeneity explicitly.

The X-ray absorption near edge structure (XANES) measurements were performed at the Canadian Light Source (CLS) located at the University of Saskatchewan. The Si K-edge XANES were obtained at the soft X-ray micro characterization beamline (SXRMB). It can provide  $10^{11}$  photons/s at 100 mA with a resolution higher than 10000 ( $E/\Delta E$ ). The emission line of excitation emission matrix spectrum were obtained at the spherical grating monochromator (SGM) beamline 11ID-1.

### **Electrochemical measurements**

All electrochemical measurements were carried out in a three-electrode cell using a rotating ring disk electrode (RRDE, PINE Research Instrumentation) with a bipotentiostat (Pine, Model PGSTAT-72637) workstation at room temperature. A Pt wire and a Hg/HgO were used as the counter and reference electrodes, respectively. All potentials in this study refer to reversible hydrogen electrode (RHE). A RDE with glassy carbon (GC) disk electrode (5 mm in diameter) and a rotating ring-disk electrode (RRDE) with a Pt ring and a GC disk (5.61 mm diameter) were used as the substrate for the working electrodes. Before use, the GC electrodes in RDE/RRDE were polished using aqueous alumina suspension on felt polishing pads.

The catalyst suspension in this work was prepared as the following: 10 mg of catalyst was mixed in a glass vial with 95  $\mu\text{L}$  of 5 wt% Nafion solution and 350  $\mu\text{L}$  of ethanol, followed by sonication and agitation in a vortex mixer, alternatively, for a total of 1 h. Then 9  $\mu\text{L}$  of the catalyst suspension was dropped onto the GC electrode surface ( $\sim 0.8 \text{ mg cm}^{-2}$ ). For comparison, the 20 wt% Pt/C catalyst (E-ETK) was prepared through the same procedure with a loading amount of  $100 \mu\text{g/cm}^2$  (i.e.,  $20 \mu\text{g}_{\text{Pt}}/\text{cm}^2$ ). Before testing,  $\text{N}_2$  (or  $\text{O}_2$ ) was bubbled through the electrolyte for 30 min and the  $\text{N}_2$ - (or  $\text{O}_2$ ) was kept bubbling during the measurements, in order

to keep the N<sub>2</sub>- or O<sub>2</sub>-saturated in the solution. In 0.1 M KOH, the cyclic voltammetry (CV) profiles were recorded at 50 mV s<sup>-1</sup> and the linear sweep voltammograms (LSV) were recorded at 10 mV s<sup>-1</sup>, between 0-1.2 V (vs. RHE). All of the LSV curves were recorded with a positive going scan, after subtraction of the background current recorded in N<sub>2</sub>-saturated solution. For detecting peroxide formed at the disc electrode, the potential for the Pt ring electrode was set at 1.3 V (vs. RHE) and the voltammograms were recorded at 1600 rpm. The collection efficiency of the ring-disk electrode was N = 0.37. The peroxide yield (H<sub>2</sub>O<sub>2</sub>, %) and the electron transfer number (n) were calculated as follows:

$$\text{H}_2\text{O}_2\% = 200 \times (\text{I}_r/\text{N})/(\text{I}_d + \text{I}_r/\text{N})$$

$$n = 4 \times \text{I}_d / (\text{I}_d + \text{I}_r/\text{N})$$

Where I<sub>d</sub> is the disk current and I<sub>r</sub> is the ring current.

The stability of the catalysts was tested on fresh electrodes by chronoamperometry at 0.8 V (vs. RHE) for 5 h in O<sub>2</sub>-saturated 0.1 M KOH and at a rotation speed of 1600 rpm.

#### **Zn-air battery assembly and measurement:**

The Zn-air batteries were tested in home-built electrochemical cells, the electrolyte used was 6 M KOH solution. To prepare the air electrode, homogeneous catalyst ink consisting of Si-N-C catalyst, Nafion solution (5 wt%) and isopropanol was dropped onto a gas diffusion layer (GDL) with a catalyst loading of 0.9 mg cm<sup>-2</sup>, a polished zinc plate was used as the anode.

#### **Density function theory (DFT) calculation**

All DFT calculations were performed without symmetry restrictions, using the Vienna ab initio simulation package (VASP) code.<sup>S1, S2</sup> For these calculations, we used the parametrization of Perdew-Burke-Ernzerhof15 of the exchange-correlation functional<sup>S3</sup> within the generalized gradient approximation (GGA) formalism. The energy cut off was set to 400 eV, the Brillouin zone was sampled on (4×4×4) Gamma-Pack k-point grid, while the total energy convergence criterion was set to 10<sup>-6</sup> eV.

Figures:

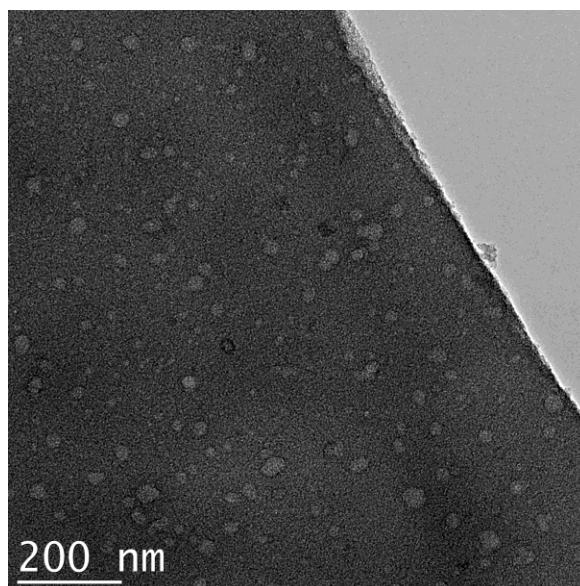


Figure S1. TEM image of porous Si-C from reed.

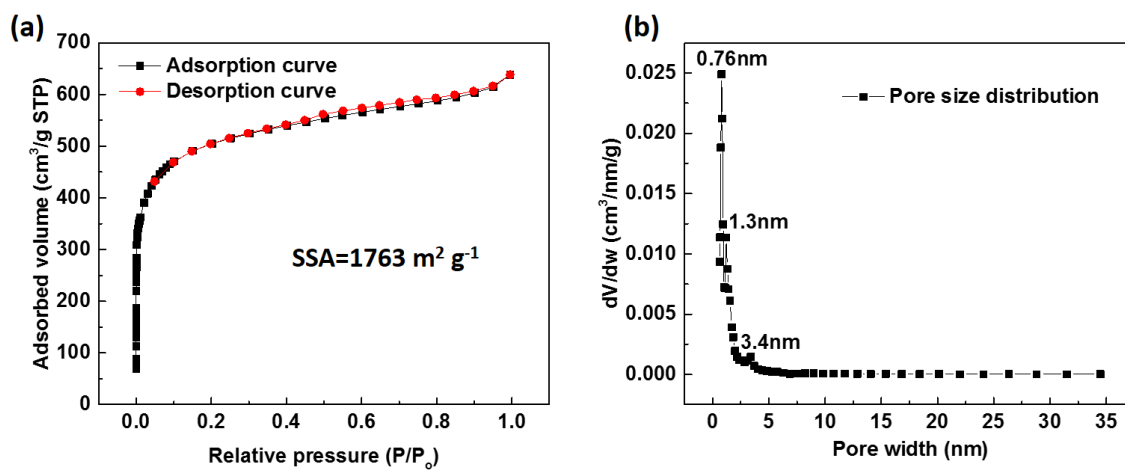
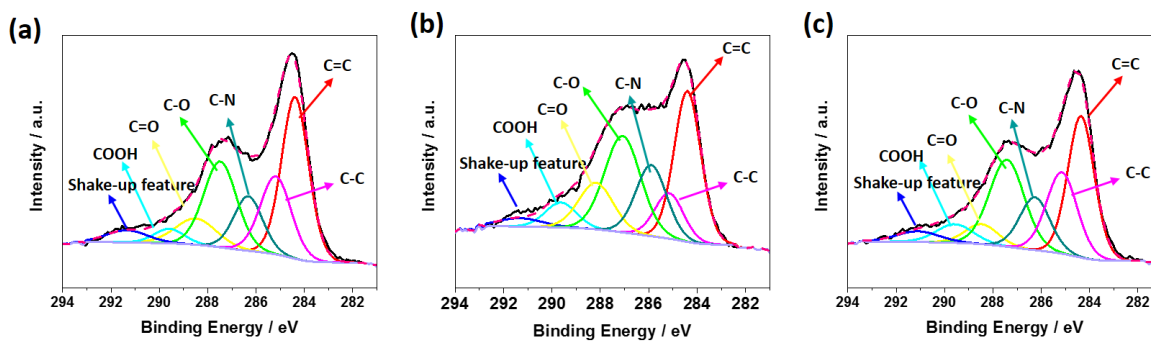
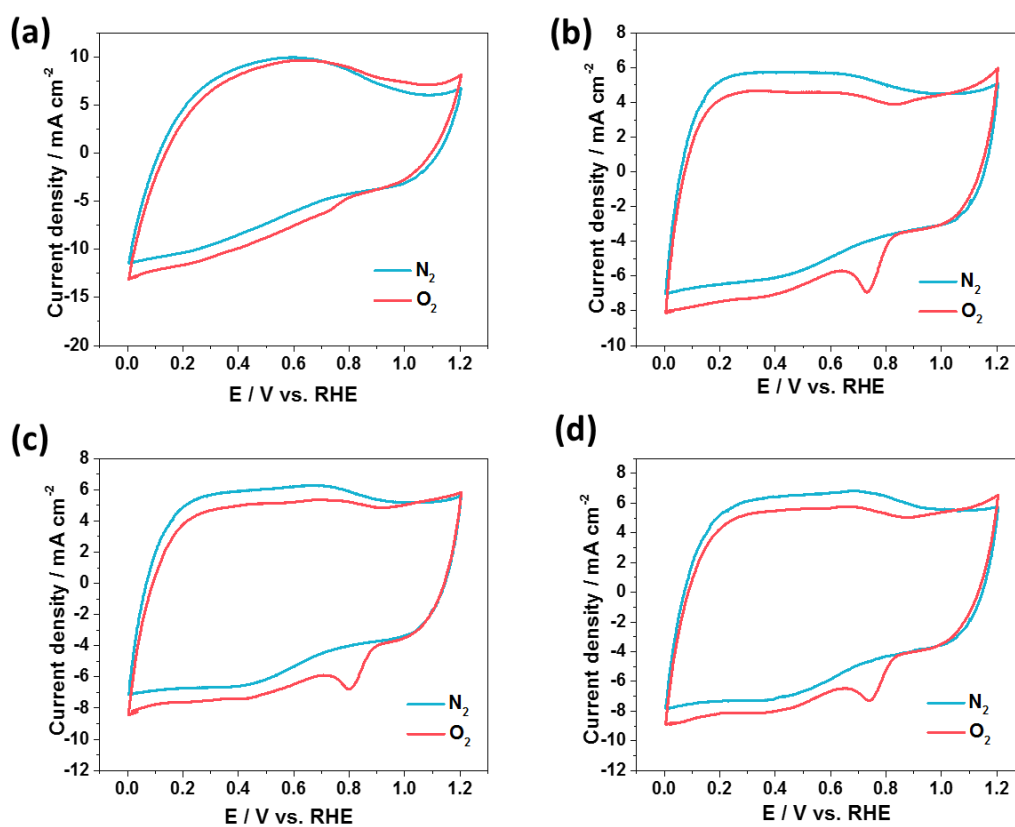


Figure S2. N<sub>2</sub>-adsorption/desorption isotherms (a) of porous Si-C from reed, and its pore size distribution (b).



**Figure S3.** The deconvoluted C 1s spectra of porous (a) Si-N-C-4 min, (b) Si-N-C-6 min, (c) Si-N-C-8 min.



**Figure S4.** Cyclic voltammograms of porous (a) Si-C, (b) Si-N-C-4 min, (c) Si-N-C-6 min, (d) Si-N-C-8 min.

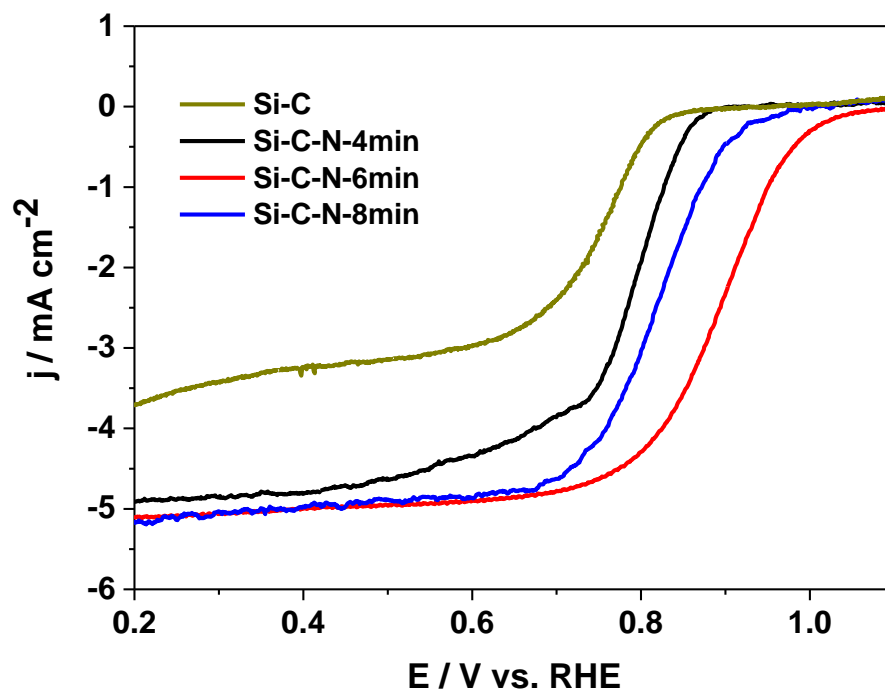


**Figure S5.** LSV curves of Si-C before activation and Si-N-C- $x$  min ( $x = 4, 6, 8$ ) in  $\text{O}_2$ -saturated 0.1 M KOH at a scan rate of  $10 \text{ mV s}^{-1}$ , rotation rate = 1600 rpm.

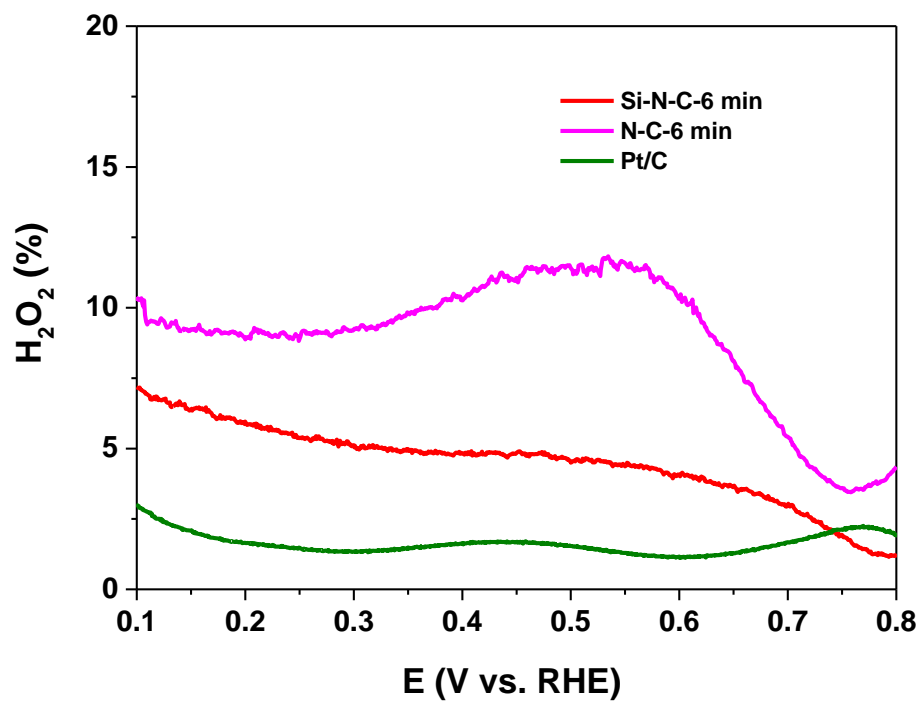


**Figure S6.** H<sub>2</sub>O<sub>2</sub> yield, of Si-C, Si-N-C-*x* min, Si-N-C-6 min-HF and commercial Pt/C in O<sub>2</sub>-saturated 0.1 M KOH at a scan rate of 10 mV s<sup>-1</sup>, rotation rate = 1600 rpm.

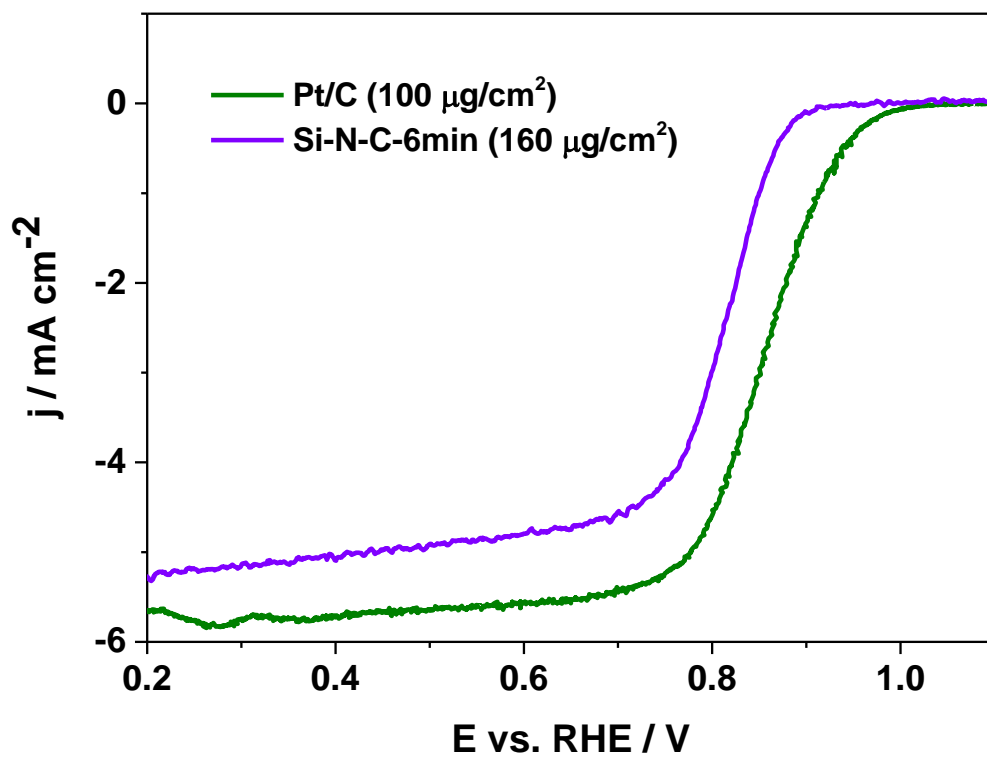


**Figure S7.** LSV curves of Si-N-C-6 min with a lower loading and commercial Pt/C in  $\text{O}_2$ -saturated 0.1 M KOH at a scan rate of  $10 \text{ mV s}^{-1}$ , rotation rate = 1600 rpm.

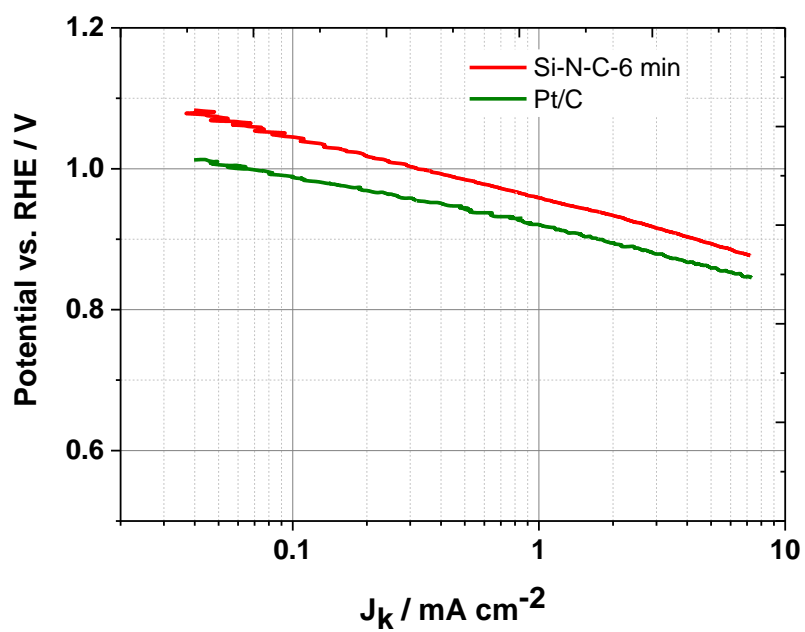


**Figure S8.** Tafel plots of Si-N-C-6 min and Pt/C in  $\text{O}_2$ -saturated 0.1 M KOH at a scan rate of  $10 \text{ mV s}^{-1}$ , rotation rate = 1600 rpm.

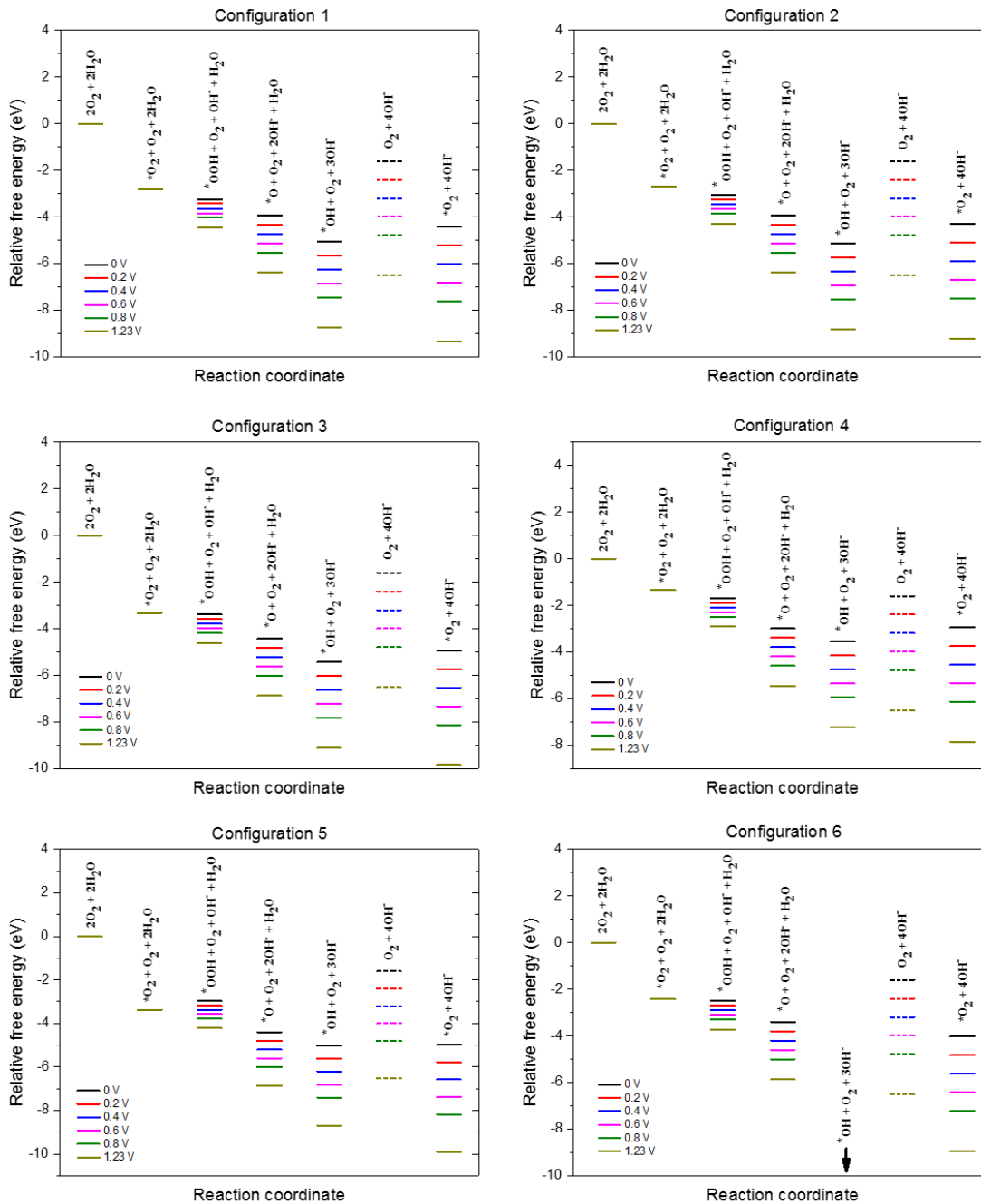


**Figure S9:** Relative free energy of the catalytic reaction of the 6 structures considered for different potentials  $U$ . The first 6 reaction coordinates correspond to those of the catalytic sequence (3a-3e) while the last one is the result of the reaction (5) replacing the reaction (3e).

**Table S1** N<sub>2</sub> adsorption/desorption analysis of selected samples

<b>Samples</b>	<b>Surface area (m<sup>2</sup>/g)</b>	<b>Surface area of micropore (m<sup>2</sup>/g)</b>	<b>Surface area of mesopore (m<sup>2</sup>/g)</b>	<b>Main pore width (nm)</b>	<b>Percentage of mesopores</b>
<b>Porous Si-C before NH<sub>3</sub> activation</b>	1763	1674	89	0.76, 1.3	5.0%
<b>Si-N-C-4 min</b>	1258	1164	94	0.80, 1.4	7.5%
<b>Si-N-C-6 min</b>	1264	1105	159	0.85, 1.5	12.6%
<b>Si-N-C-8 min</b>	1229	1075	154	0.85, 1.5	12.5%

**Table S2** Summary of element contents of the different Si-N-C catalysts

Samples	Elements content (at.%)			
	C	N	O	Si
Si-C	73.05	-	21.23	5.72
Si-N-C-4min	73.65	4.04	14.90	7.41
Si-N-C-6min	73.9	6.95	11.97	7.17
Si-N-C-8min	76.12	5.41	11.55	6.92
N-C-6min	89.21	4.11	6.68	-

**Table S3** Summary of different N configuration contents of different Si-N-C catalysts

Samples	Different N configuration content			
	Pyridinic N	Pyrolic N	Graphitic N	Pyridinic N <sup>+</sup> -O <sup>-</sup>
Si-N-C-4min	35.90	26.24	20.00	17.86
Si-N-C-6min	24.00	23.29	25.67	27.03
Si-N-C-8min	30.84	25.58	21.99	21.59
N-C-6min	31.89	46.35	8.08	13.68

**Table S4** Calculated binding energy  $E_b$  of  $O_2$  on the Si atom, relative formation energy  $\Delta E_f$  and threshold overpotential  $U_0$  producing a descending relative free energy, assuming the reaction (5), for the six structures considered.

Structure	$E_b$ (eV)	$\Delta E_f$ (eV)	$U_0$ (V)
1	-2.77	11.14	0.6
2	-2.73	11.12	0.8
3	-3.30	9.94	0.4
4	-1.33	6.72	0.6
5	-3.35	7.60	0.4
6	-2.47	8.75	$\infty$

## References

- [S1] G. Kresse and J. Hafner, *Physical Review B*, 1993, **47**, 558.  
[S2] G. Kresse and J. Furthmüller, *Computational materials science*, 1996, **6**, 15-50.  
[S3] J. P. Perdew, K. Burke and M. Ernzerhof, *Phys. Rev. Lett*, 1996, **77**, 3865-3868.

### 3.6 Highly-ordered microporous carbon nanospheres: a promising anode for high-performance sodium-ion batteries

Qiliang Wei, Yanqing Fu, Gaixia Zhang, Youling Wang, Xianyou Wang, Mohamed Mohamedi, Shuhui Sun

*RSC Adv.*, 2016, **6**, 84149-84154.

In this section, we prepared highly-ordered spherical microporous carbon (MPCs) for SIBs based on the SPRMs. The interlayer spacing of the MPC can be well tuned by simply adjusting the heat-treatment temperatures. The as-obtained carbon spheres treated at 700 °C (MPC-700) combine the features required for high-performance SIB electrode materials, such as a large interlayer spacing ( $\sim 0.457$  nm), high surface area, structural stability and plenty of micropores for Na insertion, which synergistically contribute to their impressive electrochemical properties. When applied as an anode for SIBs, the MPC-700 electrode exhibits a high reversible capacity, good cycling stability, and an excellent high-rate performance ( $\sim 160$  mA h g<sup>-1</sup> after 500 cycles at 1000 mA g<sup>-1</sup>), making it a promising candidate for SIB anodes.

*Contributions:* I performed most of the experimental synthesis of the microporous carbon, the electro-chemical measurements, and the characterizations. The TEM measurements have been done by technicians. Yanqing Fu helped test the SIB performance. Youling Wang helped on the Raman measurement. I conducted the data analysis and the interpretation of results, as well as the manuscript writing, with the help of co-authors.

# Highly-ordered microporous carbon nanospheres: a promising anode for high-performance sodium-ion batteries

*Qiliang Wei,<sup>1</sup> Yanqing Fu,<sup>2,1</sup> Gaixia Zhang,<sup>1</sup> Youling Wang,<sup>1</sup> Xianyou Wang,<sup>2,\*</sup> Mohamed Mohamedi,<sup>1</sup> and Shuhui Sun,<sup>1,\*</sup>*

<sup>1</sup>Institut National de la Recherche Scientifique-Énergie Matériaux et Télécommunications, Varennes, QC J3X 1S2, Canada.

<sup>2</sup>Key Laboratory of Environmentally Friendly Chemistry and Applications of Ministry of Education, Hunan Province Key Laboratory for Electrochemical Energy Storage and Conversion, School of Chemistry, Xiangtan University, Hunan, Xiangtan 411105, China.

Emails: [wxianyou@yahoo.com](mailto:wxianyou@yahoo.com) (X. Wang); [shuhui@emt.inrs.ca](mailto:shuhui@emt.inrs.ca) (S. Sun)

**Abstract:** Highly-ordered microporous carbon (MPC) nanospheres were prepared by a simple hydrothermal route based on soft template. The interlayer spacing of MPC was well tuned by simply adjusting the heat-treatment temperatures. The as-obtained carbon spheres treated at 700 °C (MPC-700) combine the features required for high-performance sodium-ion batteries (SIBs) electrode materials, such as large interlayer spacing (~0.457 nm), high surface area, structural stability and plentiful micropores for Na insertion, which synergistically contribute to their impressive electrochemical properties. When applied as an anode for SIBs, the MPC-700 electrode exhibits high reversible capacity, good cycling stability, and excellent high-rate performance (~160 mAh g<sup>-1</sup> after 500 cycles at 1000 mA g<sup>-1</sup>), making them promising candidates for SIB anodes.

**Keywords:** Sodium-ion batteries; Promising anodes; Microporous carbon; Controllable interlayer spacing; Soft template

## 1. Introduction

Sodium ion batteries (SIBs) are drawing increasing attention as a promising alternative to lithium ion batteries (LIBs) owing to their evident advantages such as the lower production cost, natural Na abundance and environmental benignity. [1-6] Nevertheless, the development of SIBs is

hampered by the lack of high-performance electrode materials. As a result, great efforts have been made to explore suitable electrode materials for SIBs. Recently, exciting progress on cathode material has been achieved by some groups. [7-15] However, the discovery of high performance anode materials is still more challenging. Among various candidates investigated, carbon-based materials such as hard carbon, [6, 16-19] carbon black, [20] carbon microspheres, [21-23] hollow carbon nanowires, [24] carbon nanofibers, [25, 26] carbon nanosheets, [27, 28] carbon nanotubes, [29] and porous carbon, [30-34] have been investigated as anode candidates for SIBs. It is well accepted that the large interlayer distance and disordered structure of hard carbon could facilitate  $\text{Na}^+$  insertion/extraction. [24, 35] For example, the initial capacities of  $300 \text{ mAh g}^{-1}$  and  $285 \text{ mAh g}^{-1}$  for hard carbon were reported by Stevens et al., and Alcántara et al., respectively, but only with limited cycles [17, 21]. Tang et al. [36] reported that polystyrene-templated hollow carbon microspheres possess large interlayer spacing ( $\sim 0.401 \text{ nm}$ ), leading to excellent performance for SIBs, i.e.  $160 \text{ mAh g}^{-1}$  at  $100 \text{ mA g}^{-1}$  over 100 cycles. Later, the carbon nanofibers reported by Cao et al. [24] and Luo et al. [25] displayed excellent cycling stability, while the rate capability is not very competitive. Moreover, it has been reported that the nanopores resulted from the randomly scattered graphene nanodomains in porous carbon can effectively store  $\text{Na}^+$ , facilitating fast kinetics and high capacity [17, 34, 37]. For example, the mesoporous carbon synthesized based on silica hard template exhibited significantly improved rate performance, exceeding  $100 \text{ mAh g}^{-1}$  even at high rates, [34] however, the charge/discharge was reported with only 40 cycles. What's more, the hard-templating method is well known for its tedious steps. This encourages us to explore simpler method to fabricate porous structures and to systematically study the effect of pore size and investigate whether further increasing the interlayer spacing in the porous structure will be more effective for Na-ion storage, and therefore benefit for a higher reversible capacity and better rate performance.

Herein, we report the use of highly ordered microporous carbon (MPC) spheres, synthesized based on soft-template, as a high-performance anode material for SIB. The highly-ordered MPC spheres are rich in micropores and possess large and tunable interlayer spacing, which provides a harmonious electrochemical environment that guarantees smooth Na-ion transfer and high charge storage capability. The results show that the MPCs after treatment of  $700 \text{ }^\circ\text{C}$  exhibit the best electrochemical performance, making them promising candidates for SIB anodes.

## 2. Experimental

### 2.1. Synthesis of highly-ordered MPC spheres

All the chemicals are analytical grade and used as received. The samples were prepared by a low-concentration hydrothermal route. [38, 39] Firstly, a tri-block copolymer Pluronic F127 (0.96 g,  $M_w \sim 12500$ , Sigma-Aldrich Cor.), acting as soft template, was dissolved in 15 mL DI water at room temperature by stirring for 30 min, then phenol (0.6 g), formaldehyde solution (2.1 mL), 1,10-phenanthroline (100 mg), and 0.1 M NaOH aqueous solution (15 mL) were mixed and stirred at 70 °C for another 30 min to obtain a low-molecular-weight phenolic resols. After that, the dissolved F127 solution was dropped to the phenolic resols slowly, and 2 hrs later, 50 mL of water was added and further stirred at 70 °C for 12-14 h. Afterwards, 15 mL of the as-prepared monomicelle solution and 22 mL of H<sub>2</sub>O was transferred into an autoclave (50 mL volume) for hydrothermal treatment at 130 °C for 20 h. In the end, the products were collected by centrifugation and washed with distilled water for several times, and then dried in an oven at 60 °C. The samples were first carbonized at 450 °C for 2 hrs and then further carbonized at different temperatures (550 °C, 700 °C, 850 °C and 1050 °C) for additional 2 hrs, thus, the corresponding samples were named as MPC-550, MPC-700, MPC-850 and MPC-1050, respectively.

### 2.2. Physical characterizations

The crystal structure of the as-prepared samples was characterized by X-ray diffraction (XRD, Bruker D8 Advanced Diffractometer, Cu K $\alpha$  radiation). The morphological structures were observed by transmission electron microscopy (TEM) and high-resolution TEM (HRTEM) (JEOL JEM-2100F, operated at 200 kV). The specific surface area of the as-prepared sample was determined by N<sub>2</sub> adsorption/desorption isotherm at 77 K (JW-BK112), and the pore size distribution was calculated by analyzing the adsorption branch of the N<sub>2</sub> isotherms using the quenched solid-state density functional theory (QSDFT) method. Raman spectroscopy (Renishaw Imaging Microscope Wire™) was performed using the 785 nm laser radiation with a circular polarization. The laser beam was focused onto the sample to a spot size of 1  $\mu$ m.

### 2.3. Electrochemical measurements

The button-type cells were assembled in an argon-filled glove box, where water and oxygen concentration were kept less than 5 ppm. The working electrodes were fabricated by mixing 70 wt% of active materials, 20 wt% of acetylene black and 10 wt% of polymer binder (polyvinylidene fluoride, PVDF), which were then pasted on copper foil followed by drying under vacuum at 110 °C for 10 h. The mass loading of active material on each disk is about 1.3 mg cm<sup>-2</sup>. Metal sodium was used as negative electrode; the electrolyte was 1 M NaClO<sub>4</sub> in propylene carbonate (PC) solution; the separator was glass microfiber filters (Whatman, GF/D). The galvanostatic charge-discharge measurements were performed using a Battery Testing System (Neware BTS-4008) at different current densities with a cut-off voltage window of 0-3.0 V. Cyclic Voltammetry (CV) tests were carried out on Autolab electrochemical workstation at a scan rate of 0.1 mV s<sup>-1</sup> with the potential interval 0-3.0 V. Electrochemical impedance spectroscopy (EIS) was employed to measure the assembled coin cell on Autolab electrochemical workstation by applying an AC amplitude of 5 mV over the frequency range from 10<sup>5</sup> to 0.01 Hz at an open circuit voltage (OCV: about 2.0 V vs. Na<sup>+</sup>/Na). All the electrochemical measurements were performed at room temperature.

## 2. Results and discussion

The morphologies of the as-synthesized materials were investigated by TEM. As shown in Figure 1a, the product MPC-700 is composed of homogeneous spheres with diameter in the range of 100-120 nm with highly ordered pores. The HRTEM image (Figure 1b) further demonstrates the rough surface and highly porous structure of the carbon sphere, which is favourable for Na<sup>+</sup> diffusion from various orientations and sufficient contact between active materials and electrolyte. [40] Figure 1c is the XRD patterns of MPC samples after different temperature treatment. For MPC-550, there is almost no obvious peaks appear, indicating its amorphous and disorder state which is probably caused by the low temperature treatment. From MPC-700 to MPC-1050, the (002) diffraction peak gradually shifts to higher angle, indicating that the spacing shrinkage between adjacent sheets occurs at higher temperature. According to Bragg equation, the interlayer spacing ( $d_{002}$ ) was calculated to be 0.457 nm for MPC-700, (versus 0.422 nm for MPC-850 and 0.403 nm for MPC-1050). More importantly, the interlayer spacing distance of MPC-700 in this work is larger than most reported carbon materials for SIBs.

[24-29, 33-41] The larger free space are expected to be favourable for the reversible storage of sodium considering the larger diameter of  $\text{Na}^+$  compared to that of  $\text{Li}^+$ . [36] The Raman spectrum of MPC-700 shows broad D and G bands at around 1313 and 1593  $\text{cm}^{-1}$ , respectively (Figure 1d). Notably, the MPC-700 sample exhibits very high peak intensity ratio of the D to G band ( $I_D/I_G = 1.51$ ), which is probably caused by the edge defects of the micropore structure. It has been reported that the edge defects could enhance the activity of the electrodes, [42-45] thus should be beneficial to the electrochemical performance.

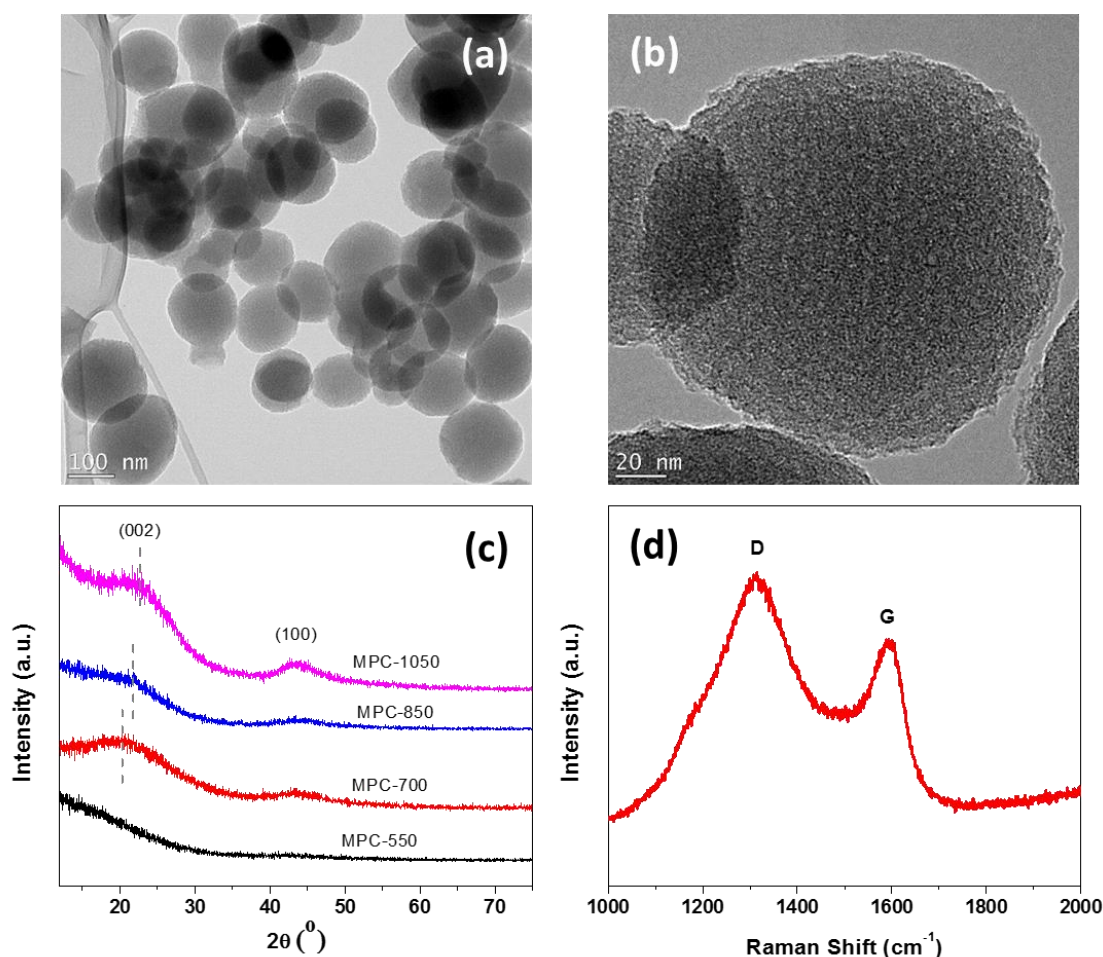


**Figure 1.** (a) TEM image and (b) HR-TEM image of MPC-700 spheres, (c) XRD pattern of MPC spheres at different treating temperature, (d) Raman spectrum of MPC-700.

The pore-size distribution and porous structure were analysed by nitrogen adsorption-desorption isotherms. Figure 2a presents the Type I isotherm with a sharp uptake at low pressure and a smooth plateau at middle-to-high pressure, which is characteristic of microporous

materials. [46] The specific surface area of MPC samples decreased as the increase of heat-treatment temperature (from 642.5 m<sup>2</sup> g<sup>-1</sup> for MPC-550, 580.1 m<sup>2</sup> g<sup>-1</sup> for MPC-700, 551.7 m<sup>2</sup> g<sup>-1</sup> for MPC-850, to 485.2 m<sup>2</sup> g<sup>-1</sup> for MPC-1050) (Figure 2a), this is probably caused by the shrinkage between adjacent sheets at higher temperatures as indicated in XRD (Figure 1c). As revealed by the QSDFT pore size distribution (Figure 2b), all samples possess plenty of micropores with size at around 0.6 nm and a small number of mesopores ranging between 2.0-3.0 nm. It has been reported that micropores with narrow pore-size distribution are beneficial for the reversible storage of Na<sup>+</sup>. [30]

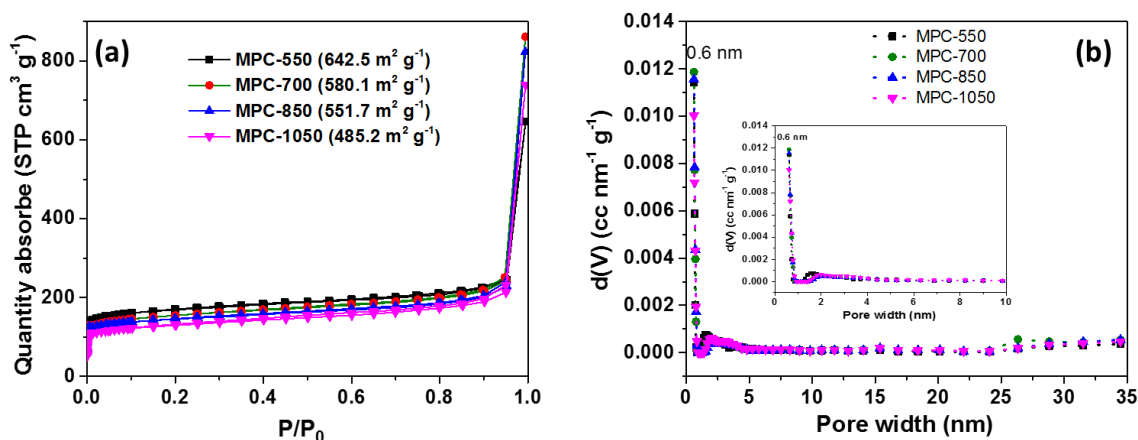


**Figure 2.** (a) N<sub>2</sub> sorption isotherm of MPC samples, (b) Pore-size distribution curves of MPC samples calculated by QSDFT.

CV and galvanostatic charge/discharge cycling were performed to investigate the Na<sup>+</sup> insertion/extraction properties (Figure 3). As shown in Figure 3a, in the first CV cycle, apparent cathodic peaks are observed at 0.8 V, 0.46 V and near 0 V for MPC-700. The peaks at around 0.8 V and 0.46 V come from the decomposition of electrolyte and formation of a solid electrolyte interphase (SEI). [45] The clear cathodic peak near 0 V is ascribed to Na<sup>+</sup> insertion into porous carbon. For the anodic processes, the main Na<sup>+</sup> extraction peak locates at around 0.08 V and the sodium removal occurs over a broad potential range (0.2 to 0.8 V), which is similarly to the previously reported work. [28, 36, 37] Moreover, it can be seen that the CV curves of the 3<sup>rd</sup> and 4<sup>th</sup> cycles almost overlap each other, indicating the excellent reversibility of Na<sup>+</sup> insertion/extraction in MPC-700.

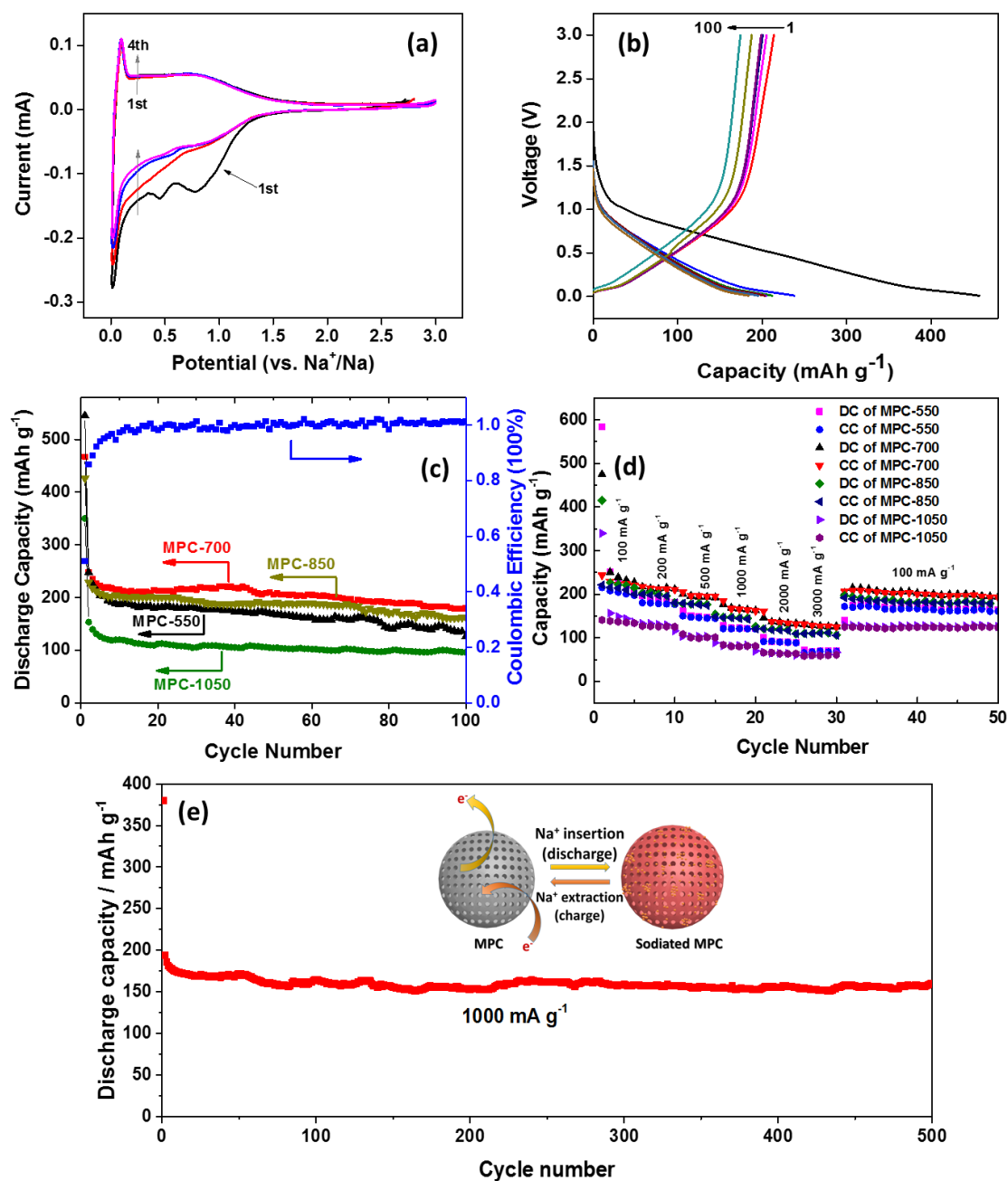


**Figure 3.** (a) CV curves of MPC-700 nanospheres with the first four cycles between 3 V and 0 V at a scan rate of  $0.1 \text{ mV s}^{-1}$ , (b) Galvanostatic charge/discharge profiles of MPC-700 at a current density of  $100 \text{ mA g}^{-1}$ , (c) Cycle performance of MPC samples at  $100 \text{ mA g}^{-1}$  and Coulombic efficiency of MPC-700, (d) Rate performance of MPC samples at variant rates (DC: discharge capacity; CC: charge capacity), (e) Long term cycle performance at  $1000 \text{ mA g}^{-1}$  for MPC-700 (inset is the scheme of the electrochemical process for MPCs).

As shown in Fig 3b, the first discharge/charge cycle of MPC-700 delivers specific discharge/charge capacity of 465 and 237 mAh g<sup>-1</sup>, respectively (with an initial coulombic efficiency of 51.0%), at 100 mA g<sup>-1</sup>. Similar to that reported in LIBs, the large irreversible capacity in the first cycle is an unavoidable phenomenon in porous carbonaceous electrodes. In addition to the electrolyte decomposition at the electrode/electrolyte interface and the formation of SEI films, the deep-seated micropores may also lead to irreversible sodium insertion/extraction in MPCs. [37, 47] This can be also verified with the CV of MPC-700 at the first scanning cycle. From Figure 3b and 3c, it can be seen that MPC-700 shows excellent capacity retention with a high reversible capacity of ~180 mAh g<sup>-1</sup> after 100 cycles at 100 mA g<sup>-1</sup>, the coulombic efficiency approaches to ~100% after several cycles. For comparison, after 100 cycles, MPC-550, MPC-850 and MPC-1050 maintain reversible capacities of 137, 162 and 98 mAh g<sup>-1</sup>, respectively, showing that 700 °C is an optimal heat-treatment temperature for the good performance of SIBs. It should be noted that the capacity of MPC-550 decreases faster than other three samples, this might be caused that with the highest surface area, the risk of secondary reactions involving electrolyte decomposition between electrode and electrolyte raises, this could cause a high level of irreversibility and poor cycle life. [48] While, the MPC-1050 shows much lower capacity which is probably ascribed to the smaller surface area and interlayer spacing. MPC-700 shows the best electrochemical performance among the four samples which can be attributed to the following: (i) its larger interlayer spacing of  $d_{002}$  (0.457 nm) favors the smooth reversible storage of sodium; (ii) the suitable porous structure with crystallographic defects (as shown in Figure 1b) serve as reservoirs for storage of sodium; (iii) an optimal balance between high surface area (for sufficient interface contact between the electrode and electrolyte) and good electrical conductivity (for electron transport).

Rate capability is another important index to evaluate the performance of SIBs. As shown in Figure 3d, the reversible capacities of MPC-700 sample are retained at 230, 210, 190, 165, 132, 125 mAh g<sup>-1</sup> at current densities of 100, 200, 500, 1000, 2000, 3000 mA g<sup>-1</sup>, respectively. Moreover, when the current density goes back to 100 mA g<sup>-1</sup>, the capacity recovers to 210 mAh g<sup>-1</sup>, which is higher than those of the other three samples at all different stages. It should be noted that for the MPC-550 sample, at the identical current densities, the capacities are 200, 180, 145, 119, 90 and 68 mAh g<sup>-1</sup>, respectively. At larger current densities, the capacity decreases dramatically, which can be ascribed to its poor conductivity due to the low treatment temperature.

While, when the treating temperature goes up to 850 and 1050 °C, although the performance retains relatively well at higher current densities, the capacity is lower due to the smaller surface area and interlayer spacing. Therefore, by combining the multifactor functioning effects, it can be concluded that the 700 °C is the optimal annealing temperature of MPC for use in SIBs. Furthermore, long term cycling of the MPC-700 at 1000 mA g<sup>-1</sup> exhibits a stable capacity of ~160 mAh g<sup>-1</sup> over 500 cycles (Figure 3e), indicating that the large interlayer distance guarantees the structural stability during the repeated sodiation/desodiation processes. To better understand the higher performance of the microporous spheres for SIBs, the EIS measurements of MPC samples (Figure 4) were carried out on cells comprising the samples as the working electrode vs. Na. Both of the Nyquist plots are similar to each other, composing of a broad depressed semicircle at high-medium frequency that is related to the ohmic resistance and charge transfer resistance ( $R_{ct}$ ), and an inclined straight line at low frequency that is associated with ionic diffusion impedance through the bulk of the active material. The  $R_{ct}$  of MPC-700 is about 26  $\Omega$  which is smaller than those for the other three MPC samples, indicating MPC-700 has much lower activation energy for Na<sup>+</sup> diffusion and undergoes a fast Faradaic reaction, conforming the excellent electrochemical properties.

The excellent electrochemical performance of MPC-700 is attributed to the specific characteristics of its unique spherical structure with plentiful micropores and suitable surface area. Firstly, thanks to the spherical shape, MPCs tend to form thin film electrodes without a preferred orientation, which is beneficial to homogeneous current low distribution within the electrode. [23] Secondly, the isotropic spherical structure is beneficial for high packing density and rate performance of the electrodes. [49] Thirdly, the large interlayer spacing of the disordered structure facilitates sodium ion transport and storage. Finally, suitable surface area provides more active sites for the Na<sup>+</sup> storage, meanwhile, it astricts secondary reactions involving electrolyte decomposition between electrode and electrolyte.

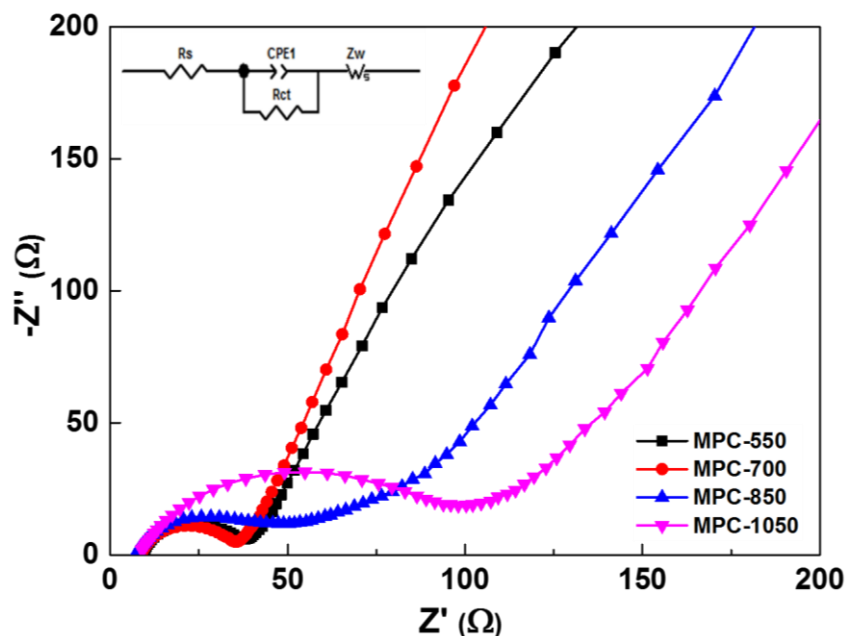


**Figure 4.** Impedance spectra of MPC samples (inset is the equivalent circuit).

### 3. Conclusions

In summary, we employed a simple soft-template method to fabricate highly-ordered spherical MPCs. The interlayer spacing and surface area can be tuned by simply adjusting the annealing temperature, which has large effects to the electrochemical performances. When used as anodes for SIBs, the synergistic effect of larger interlayer spacing, suitable surface area, and the numerous micropores in MPC-700 facilitates Na-ion transport and storage, contributing to excellent cycling stability and rate capability. Further optimization of such a promising electrode material can be conducted by adjusting their size, the ratio of micropores/mesopores and hetero-element doping (such as N, B, P, S...), which are believed to be effective strategies to boost the developments of new carbon materials for SIBs.

### Acknowledgments

This work is financially supported by the Natural Sciences and Engineering Research Council of Canada (NSERC), Institut National de la Recherche Scientifique (INRS), and Centre Québécois sur les Matériaux Fonctionnels (CQMF). Q. Wei gratefully acknowledges the scholarship from China Scholarship Council (CSC) and Fonds de Recherche du Québec-Nature et Technologies (FRQNT).

## References

- [1] J.M. Tarascon, *Nature Chem.*, 2010, **2**, 510-510.
- [2] B. Scrosati and J. Garche, *J. Power Sources*, 2010, **195**, 2419-2430.
- [3] N. Yabuuchi, K. Kubota, M. Dahbi and S. Komaba, *Chem. Rev.*, 2014, **114**, 11636-11682.
- [4] C.Y. Yu, J.S. Park, H.G. Jung, K.Y. Chung, D. Aurbach, Y.K. Sun and S.T. Myung, *Energy Environ. Sci.*, 2015, **8**, 2019-2026.
- [5] D. Kundu, E. Talaie, V. Duffort and L. F. Nazar, *Angew. Chem. Inter. Ed.*, 2015, **54**, 3431-3448.
- [6] S.W. Kim, D.H. Seo, X. Ma, G. Ceder and K. Kang, *Adv. Energy Mater.*, 2012, **2**, 710-721.
- [7] D. Kim, S.H. Kang, M. Slater, S. Rood, J.T. Vaughey, N. Karan, M. Balasubramanian and C.S. Johnson, *Adv. Energy Mater.*, 2011, **1**, 333-336.
- [8] Y. Yamada, T. Doi, I. Tanaka, S. Okada and J.I. Yamaki, *J. Power Sources*, 2011, **196**, 4837-4841.
- [9] P. Barpanda, T. Ye, S.I. Nishimura, S.C. Chung, Y. Yamada, M. Okubo, H. Zhou and A. Yamada, *Electrochem. Commun.*, 2012, **24**, 116-119.
- [10] J. Kang, S. Baek, V. Mathew, J. Gim, J. Song, H. Park, E. Chae, A.K. Rai and J. Kim, *J. Mater. Chem.*, 2012, **22**, 20857-20860.
- [11] D. Kim, E. Lee, M. Slater, W. Lu, S. Rood and C.S. Johnson, *Electrochem. Commun.*, 2012, **18**, 66-69.
- [12] J. Billaud, G. Singh, A. R. Armstrong, E. Gonzalo, V. Roddatis, M. Armand, T. Rojo and P. G. Bruce, *Energy Environ. Sci.*, 2014, **7**, 1387-1391.
- [13] J. Billaud, R.J. Clément, A.R. Armstrong, J. Canales-Vázquez, P. Rozier, C.P. Grey and P.G. Bruce, *J. Am. Chem. Soc.*, 2014, **136**, 17243-17248.
- [14] Y. You, X.L. Wu, Y.X. Yin and Y.G. Guo, *Energy Environ. Sci.*, 2014, **7**, 1643-1647.
- [15] J. Y. Hwang, S. M. Oh, S. T. Myung, K. Y. Chung, I. Belharouak and Y. K. Sun, *Nat. Commun.*, 2015, **6**, 6865.
- [16] S. Komaba, W. Murata, T. Ishikawa, N. Yabuuchi, T. Ozeki, T. Nakayama, A. Ogata, K. Gotoh and K. Fujiwara, *Adv. Funct. Mater.*, 2011, **21**, 3859-3867.
- [17] D. A. Stevens and J. R. Dahn, *J. Electrochem. Soc.*, 2000, **147**, 1271-1273.
- [18] A. Ponrouch, A.R. Goñi and M.R. Palacín, *Electrochem. Commun.*, 2013, **27**, 85-88.

- [19] C. Bommier, W. Luo, W.Y. Gao, A. Greaney, S. Ma and X. Ji, *Carbon*, 2014, 76, 165-174.
- [20] R. Alcántara, J.M. Jiménez-Mateos, P. Lavela and J.L. Tirado, *Electrochem. Commun.*, 2001, **3**, 639-642.
- [21] R. Alcántara, P. Lavela, G.F. Ortiz and J.L. Tirado, *Electrochem. Solid-State Lett.*, 2005, **8**, A222-A225.
- [22] V.G. Pol, E. Lee, D. Zhou, F. Dogan, J.M. Calderon-Moreno and C.S. Johnson, *Electrochim. Acta*, 2014, **127**, 61-67.
- [23] T. Chen, L. Pan, T. Lu, C. Fu, D.H.C. Chua and Z. Sun, *J. Mater. Chem. A*, 2014, **2**, 1263-1267.
- [24] Y. Cao, L. Xiao, M. L. Sushko, W. Wang, B. Schwenzer, J. Xiao, Z. Nie, L. V. Saraf, Z. Yang and J. Liu, *Nano Lett.*, 2012, **12**, 3783-3787.
- [25] W. Luo, J. Schardt, C. Bommier, B. Wang, J. Razink, J. Simonsen and X. Ji, *J. Mater. Chem. A*, 2013, **1**, 10662-10666.
- [26] W. Li, L. Zeng, Z. Yang, L. Gu, J. Wang, X. Liu, J. Cheng and Y. Yu, *Nanoscale*, 2014, **6**, 693-698.
- [27] H.G. Wang, Z. Wu, F.L. Meng, D.L. Ma, X.L. Huang, L.M. Wang and X.B. Zhang, *ChemSusChem*, 2013, **6**, 56-60.
- [28] F. Yang, Z. Zhang, K. Du, X. Zhao, W. Chen, Y. Lai and J. Li, *Carbon*, 2015, **91**, 88-95.
- [29] D. Li, L. Zhang, H. Chen, L.X. Ding, S. Wang and H. Wang, *Chem. Commun.*, 2015, **51**, 16045-16048.
- [30] Q. Qu, J. Yun, Z. Wan, H. Zheng, T. Gao, M. Shen, J. Shao and H. Zheng, *RSC Adv.*, 2014, **4**, 64692-64697.
- [31] Z. Wang, Y. Li and X. J. Lv, *RSC Adv.*, 2014, **4**, 62673-62677.
- [32] Y. Kado, Y. Soneda and N. Yoshizawa, *ECS Electrochem. Lett.*, 2015, **4**, A22-A23.
- [33] Z. Guan, H. Liu, B. Xu, X. Hao, Z. Wang and L. Chen, *J. Mater. Chem. A*, 2015, **3**, 7849-7854.
- [34] S. Wenzel, T. Hara, J. Janek and P. Adelhelm, *Energy Environ. Sci.*, 2011, **4**, 3342-3345.
- [35] E. Irisarri, A. Ponrouch and M.R. Palacin, *J. Electrochem. Soc.*, 2015, **162**, A2476-A2482.

- [36] K. Tang, L. Fu, R. J. White, L. Yu, M. M. Titirici, M. Antonietti and J. Maier, *Adv. Energy Mater.*, 2012, **2**, 873-877.
- [37] L. Fu, K. Tang, K. Song, P.A. van Aken, Y. Yu and J. Maier, *Nanoscale*, 2014, **6**, 1384-1389.
- [38] Y. Fang, D. Gu, Y. Zou, Z. Wu, F. Li, R. Che, Y. Deng, B. Tu and D. Zhao, *Angew. Chem. Inter. Ed.*, 2010, **49**, 7987-7991.
- [39] Y. Fang, Y. Lv, R. Che, H. Wu, X. Zhang, D. Gu, G. Zheng and D. Zhao, *J. Am. Chem. Soc.*, 2013, **135**, 1524-1530.
- [40] Z. Wang, L. Qie, L. Yuan, W. Zhang, X. Hu and Y. Huang, *Carbon*, 2013, **55**, 328-334.
- [41] D. Xu, C. Chen, J. Xie, B. Zhang, L. Miao, J. Cai, Y. Huang, L. Zhang, *Adv. Energy Mater.* 2016, **6**, 1501929.
- [42] Y. Xue, J. Liu, H. Chen, R. Wang, D. Li, J. Qu and L. Dai, *Angew. Chem. Inter. Ed.*, 2012, **51**, 12124-12127.
- [43] J. Xu, M. Wang, N.P. Wickramaratne, M. Jaroniec, S. Dou and L. Dai, *Adv. Mater.*, 2015, **27**, 2042-2048.
- [44] L. Ji, Z. Lin, A.J. Medford and X. Zhang, *Carbon*, 2009, **47**, 3346-3354.
- [45] X. Zhou and Y.G. Guo, *ChemElectroChem*, 2014, **1**, 83-86.
- [46] F. Su, C.K. Poh, J.S. Chen, et al., *Energy Environ. Sci.*, 2011, **4**, 717-724.
- [47] S.X. Wang, S. Chen, Q. Wei, X. Zhang, S.Y. Wong, S. Sun and X. Li, *Chem. Mater.*, 2014, **27**, 336-342.
- [48] Y.G. Guo, J.S. Hu, L.J. Wan, *Adv. Mater.*, 2008, **20**, 2878-2887.
- [49] M. Yoshio, H. Wang, K. Fukuda, *Angew. Chem. Inter. Ed.*, 2003, **115**, 4335-4338.

## CHAPTER 4 CONCLUSIONS AND PERSPECTIVES

### 4.1 Conclusions

The topic of this thesis is carbon-based non-precious catalyst materials for oxygen reduction reaction (ORR) and/or oxygen evolution reaction (OER) in energy conversion and storage devices, including PEM fuel cells and Zn-air batteries. In addition, we also employed the as-synthesized carbon materials for Na-ion batteries. Specifically, we have adopted three different types of carbon precursors (carbon spheres, MOFs and biomass reed) to fabricate non-precious catalysts and electrode materials for the above-mentioned applications.

The principle objective of this thesis work was to develop different methodologies to improve the activity and stability of the NPMCs (mainly Fe/N/C-based catalysts). Although Fe-N-C catalyst is the state-of-the-art of the NPMC, exploring new types of low-cost and highly efficient catalysts (e.g., metal-free catalyst) is also of significant importance to the development of next-generation energy conversion and storage devices. By using various advanced characterization techniques, each part of this thesis work lead to a better understanding of the factors that contribute to improved activity and stability (i.e., the relationship between structures and properties).

As there are several publications and six parts in this thesis, the conclusions shall be presented for each part individually, as the following.

(1) Motivated by the advantages of the spherical structures (including the abundant voids for the sufficient contact between the reactants and active sites; highly packed arrays; and high volume density), a series of 3D microporous Fe/N/C ORR catalysts were prepared by employing spherical SPRMs as the carbon host for impregnating FeAc and 1,10-Phen, followed by high temperature pyrolysis in Ar in NH<sub>3</sub> atmosphere, consequently. Through the systematic studies, we found that (i) the content of Fe precursor and pyrolysis time under NH<sub>3</sub> have distinct influence to the morphology and structure of the final Fe/N/C catalysts; (ii) the pyrolysis temperature in Ar, the BET surface area, and the content of Fe in the catalysts largely affect the ORR activity; (iii) the optimized Fe content of the Fe/N/C catalysts is around 5.5–8 wt% and the optimized porosity is with 450 m<sup>2</sup> g<sup>-1</sup> micropore with preferably higher value of mesopores; only

catalysts subjecting within these two ranges exhibit high activity. The Fe<sub>30</sub>NC-Ar700-NH<sub>3</sub>-45% catalyst shows an interconnected hollow and open spherical structure with optimized Fe content (~7 wt%), BET surface area (536.3 m<sup>2</sup> g<sup>-1</sup>, with 435.7 m<sup>2</sup> g<sup>-1</sup> of micropores and 100.6 m<sup>2</sup> g<sup>-1</sup> of mesopores with a R<sub>micro/meso</sub> of 4.33), and exhibits good ORR performances in both alkaline and acidic conditions. In alkaline solution, the 3D microporous Fe/N/C structure shows excellent activity and stability for ORR, as well as strong methanol tolerance, which indicating its promising potential application in alkaline fuel cells, methanol fuel cells, and metal-air batteries. Moreover, in acidic solution, Fe<sub>30</sub>NC-Ar700-NH<sub>3</sub>-45% also exhibits excellent stability and selectivity. Notably, the ORR process of Fe<sub>30</sub>NC-Ar700-NH<sub>3</sub>-45% catalyst in both alkaline and acidic media follows the direct 4e<sup>-</sup> transfer pathway, indicating a complete reduction of O<sub>2</sub> to water which is desired for fuel cells. All these characters make our Fe/N/C catalyst a very good non-noble-metal catalyst for ORR. This work provides more insights to fabricate highly efficient Fe/N/C catalysts in both acidic and alkaline electrolytes, which may boost the development of various fuel cells.

(2) Since the porous structure plays a key role in ORR performance of Fe/N/C, in the second work, we developed a straightforward yet highly efficient approach to adjust the pore structures of the Fe/N/C catalyst. Specifically, we used S as a pore promotor to fabricate hierarchical and highly porous Fe/N/C catalyst. We found out that the addition of S not only affords interpenetrating holes, leading to a large surface area and pore volume inside the architecture, but also helps the whole carbon framework to keep a perfect 3D spherical shape and uniformly dispersed Fe-N<sub>x</sub> active sites (this will help to increase the utilization of Fe and also increase the active sites). Moreover, the S-treatment could increase the degree of distortion of the local Fe-N<sub>4</sub> structure, which further improved the catalyst activity. Consequently, the optimal S-treated Fe/N/C catalyst shows a litchi-like spherical structure, large surface area (982.1 m<sup>2</sup> g<sup>-1</sup>) with a huge pore volume (1.01 cm<sup>3</sup> g<sup>-1</sup>), and excellent ORR activity. Importantly, it achieves an excellent power density (~250 mW cm<sup>-2</sup>, double than that of the untreated one) as an air cathode for a Zn-air battery device. This work may provide a new strategy to develop high performance carbon-based electrocatalysts for low cost metal-air batteries and other electrochemical energy conversion/storage applications.

(3) Another strategy to increase the porous structure was proved by introducing a second transition metal (e.g., Cu) to Fe/N/C. We found that compared with the Fe/N/C, the as-synthesized (Fe-Cu)/N/C possesses higher surface area in external pore area, longer Fe-N bond, and shows very similar ORR activity to Fe/N/C, but lower H<sub>2</sub>O<sub>2</sub> yield in the range of 0.3-0.8 V in a half-cell test. Importantly, when applied in a MEA in the H<sub>2</sub>-air PEMFC, the (Fe-Cu)/N/C catalyst demonstrates a higher power density (0.4 W cm<sup>-2</sup>) than that of the Fe/N/C (0.36 W cm<sup>-2</sup>), and an enhanced stability (i.e., an improvement of 3.7% of the current density under a potentiostatic testing after 40 h). Moreover, from the XPS and XAS analysis, it can be concluded that more porphyrin-like Fe<sup>II</sup>N<sub>4</sub>C<sub>12</sub> active sites exist in Fe/N/C, while FeN<sub>2+2</sub>/C modeled active sites are more prominent in (Fe-Cu)/N/C catalyst.

(4) From the point of view of economic processing and sustainability, finding new economical and renewable sources to fabricate high performance electrocatalysts are highly desired. Therefore, we used the biomass reed stalk as the C source to fabricate the Fe/N/C ORR catalyst. Interestingly, we found that the Si (contained in the reed) has been doped into the Fe/N/C structure during the fabrication process. The XANES, Raman and XPS measurements indicate that due to the participation of Si, the Si-Fe/N/C catalyst shows enhanced graphitic carbon structure with more nitrogen moieties coordinating with Fe. These features make Si-Fe/N/C catalyst possess good ORR activity, and importantly, better stability (with 94.8% retention of the current after 20000 s under a high voltage of 0.8 V) than the Fe/N/C counterpart (83.3%) and Pt/C (65.5%). Moreover, after 10,000 potential cycles in O<sub>2</sub>-saturated electrolyte, Si-Fe/N/C only shows ~12 mV of change vs. ~19 mV for Fe/N/C and ~40 mV for Pt/C. Si-Fe/N/C also shows higher tolerance toward methanol poisoning compared with Pt/C. Moreover, ORR on the Si-Fe/N/C catalyst follows the efficient 4e<sup>-</sup> pathway. Taking together, the newly developed Si-Fe/N/C catalyst shows good ORR performance and high stability and therefore holds great potential to replace commercial Pt/C in alkaline fuel cells and other applications. This is the first report to use the biomass reed as the raw materials to fabricate high performance ORR catalyst and has attracted much attention from the media (e.g., phys.org, lightsource.ca, hydrogen fuel news, etc.) We believe that this work will give more insights to design highly stable catalysts, based on more types of biomass materials, for clean energy related devices and will have significant economic and environment effects by making full use of biomass wastes.

(5) More interestingly, we found that even without metal Fe, the Si/N/C derived from reed is also very active for ORR in alkaline media, indicating the Si/N/C is a new type of cheap and efficient metal-free catalyst. The optimized Si-N-C sample shows excellent ORR activity, which is among the best reported metal-free ORR catalysts. It also displays better stability for ORR than the commercial Pt/C in a half-cell environment. Moreover, this reed waste derived Si-N-C metal-free catalyst exhibits excellent performance as an air cathode for a Zn-air battery device. DFT calculation indicates that the Si and N sites (graphitic-N) in the carbon framework could promote the ORR activity. We believe that our work will give more insights to design new type of metal-free catalysts for the clean energy related devices.

(6) Lastly, based on the discovery in the first part of the work (i.e., highly-ordered spherical MPCs), we found that the interlayer spacing and surface area of the MPCs can be tuned by simply adjusting the annealing temperature, which could be very useful for SIB applications. We found that when used as anodes for SIBs, the MPC-700 shows excellent cycling stability and rate capability because the synergistic effect of larger interlayer spacing, suitable surface area, and the numerous micropores could facilitate the Na-ion transport and storage. In future, further optimization of the pore size, the ratio of micropores/mesopores and hetero-element doping (such as N, B, P, S...) in MPC structure can be conducted, which is believed to be an effective strategy to boost the developments of new carbon materials for SIBs.

## 4.2 Perspectives

(1) For PEM fuel cells, major breakthroughs have been achieved over the last decade in the design of NPMCs for catalyzing the ORR, within the PEMFC technology and operate with overpotential requirements similar to those of conventional Pt catalysts. These catalysts are also more selective and therefore less sensitive to poisoning, which is a major asset for worldwide introduction of PEMFC technology if such innovative catalysts can be implemented in full devices while retaining other key specifications (i.e. power performance and durability). Still, significant progress has to be made in two directions. First, the electrochemical activities of such NPMCs are still lower than that of the Pt-based catalysts (in the acidic environment of the mainstream PEMFC). Closing the gap can be pursued by increasing the site density or the turnover frequency of the active sites for NPMCs. Additionally, specific optimization of the catalyst layer structures for such catalysts could help promoting the power density of the Pt-free H<sub>2</sub>/Air

PEMFCs, through a better control of the protons and product diffusion while avoiding the water flooding. The other direction, in which it is urgent to invest, is the stability of the NPMCs during representative drive cycles. The most efficient strategy would be systematically studying and making it clear of the relationships between the structure-performance-mechanism of the NPMCs, so that to guide the rational design of next-generation NPMCs.

(2) For Zn-air batteries, highly efficient and inexpensive bifunctional electrocatalysts that exhibit i) bifunctionality (requiring in-depth understanding of complex oxygen reduction and evolution processes in electrolytes), ii) versatility (requiring the function in a wide range of temperatures, voltages, and in both aqueous and non-aqueous electrolytes), and iii) scalability (ease of incorporation of catalysts into the air-electrode structure, enabling commercialization and widespread adoption). In addition, advanced in-situ or operando characterization methods are required for better understandings the reaction mechanism for both ORR and OER. Moreover, to create a comparable link between laboratory results and commercial applications, the catalysts must be studied under practical test conditions. Often, catalysts that show high activities in analytical three-electrode cells do not always perform well in single-cell devices that demand high current densities and operating temperatures with long lifetimes.

(3) For sodium-ion batteries, although great advancements have been achieved, many barriers still exist and the practical application of SIBs is still challenging. In terms of carbon anode materials, further exploration on Na-storage mechanism is highly desired. The low initial coulombic efficiency and rate capability of carbon materials should be improved. Few reported carbon materials could present an initial coulombic efficiency over 80% and most are below 70%, however, for practical applications, the higher initial coulombic efficiency over 90% is required. Therefore, the design of carbon materials with special micro/nanostructures containing rich reversible sodium storage active sites and shortened  $\text{Na}^+$  diffusion path is necessary. The optimized electrolyte and additive should be explored to tailor the formation of SEI film and improve the initial Coulombic efficiency. Reducing the processing cost and improving the Na storage capacity are crucial to the practical applications; therefore, the high-performance carbon materials produced through an effective method with cheap precursor and high yield are highly desired.

## References

- [1] S. Chu, Y. Cui, N. Liu, *The path towards sustainable energy*, Nature Materials, 2017, 16, 16.
- [2] M.Z. Jacobson, M.A. Delucchi, Z.A.F. Bauer, S.C. Goodman, W.E. Chapman, M.A. Cameron, C. Bozonnat, L. Chobadi, H.A. Clonts, P. Enevoldsen, *100% clean and renewable wind, water, and sunlight all-sector energy roadmaps for 139 countries of the world*, Joule, 2017, 1, 108-121.
- [3] Y. Tang, Y. Zhang, W. Li, B. Ma, X. Chen, *Rational material design for ultrafast rechargeable lithium-ion batteries*, Chemical Society Reviews, 2015, 44, 5926-5940.
- [4] Y. Zhao, X. Li, B. Yan, D. Xiong, D. Li, S. Lawes, X. Sun, *Recent Developments and Understanding of Novel Mixed Transition-Metal Oxides as Anodes in Lithium Ion Batteries*, Advanced Energy Materials, 2016, 6, 1502175.
- [5] Y. Fu, Q. Wei, G. Zhang, S. Sun, *Advanced Phosphorus-Based Materials for Lithium/Sodium-Ion Batteries: Recent Developments and Future Perspectives*, Advanced Energy Materials, 2018, 8, 1703058.
- [6] Z.P. Cano, D. Banham, S. Ye, A. Hintennach, J. Lu, M. Fowler, Z. Chen, *Batteries and fuel cells for emerging electric vehicle markets*, Nature Energy, 2018, 3, 279.
- [7] J.W. Choi, D. Aurbach, *Promise and reality of post-lithium-ion batteries with high energy densities*, Nature Reviews Materials, 2016, 1, 16013.
- [8] A. Tsutsumi, *Fuel cell/battery system*, 2013.
- [9] F. Jaouen, D. Jones, N. Coutard, V. Artero, P. Strasser, A. Kucernak, *Toward Platinum Group Metal-Free Catalysts for Hydrogen/Air Proton-Exchange Membrane Fuel Cells*, Johnson Matthey Technology Review, 2018, 62, 231-255.
- [10] Y. Li, J. Lu, *Metal-air batteries: will they be the future electrochemical energy storage device of choice?*, ACS Energy Letters, 2017, 2, 1370-1377.
- [11] D. Kundu, E. Talaie, V. Duffort, L.F. Nazar, *The emerging chemistry of sodium ion batteries for electrochemical energy storage*, Angewandte Chemie International Edition, 2015, 54, 3431-3448.
- [12] A.J. Appleby, E.B. Yeager, *Solid polymer electrolyte fuel cells (SPEFCs)*, Energy, 1986, 11, 137-152.

- [13] I.D. Raistrick, Modified gas diffusion electrode for proton exchange membrane fuel cells, pp. 172-177.
- [14] J. Zhang, Y. Tang, C. Song, J. Zhang, H. Wang, *PEM fuel cell open circuit voltage (OCV) in the temperature range of 23°C to 120°C*, Journal of Power Sources, 2006, 163, 532-537.
- [15] M. Lefevre, E. Proietti, F. Jaouen, J.P. Dodelet, *Iron-based catalysts with improved oxygen reduction activity in polymer electrolyte fuel cells*, Science, 2009, 324, 71-74.
- [16] E. Proietti, F. Jaouen, M. Lefevre, N. Larouche, J. Tian, J. Herranz, J.P. Dodelet, *Iron-based cathode catalyst with enhanced power density in polymer electrolyte membrane fuel cells*, Nature Communications, 2011, 2, 416.
- [17] M. Shao, Q. Chang, J.-P. Dodelet, R. Chenitz, *Recent advances in electrocatalysts for oxygen reduction reaction*, Chemical Reviews, 2016, 116, 3594-3657.
- [18] <http://sustainableskies.org/hydrogen-scooters-%E2%80%93-a-possible-power-source/pem-fuel-cell/>, 2012.
- [19] T. Agaesse, *Simulations of one and two-phase flows in porous microstructures, from tomographic images of gas diffusion layers of proton exchange membrane fuel cells*, 2016.
- [20] M. Asadi, B. Sayahpour, P. Abbasi, A.T. Ngo, K. Karis, J.R. Jokisaari, C. Liu, B. Narayanan, M. Gerard, P. Yasaei, *A lithium–oxygen battery with a long cycle life in an air-like atmosphere*, Nature, 2018, 555, 502.
- [21] M.A. Rahman, X. Wang, C. Wen, *High energy density metal-air batteries: a review*, Journal of The Electrochemical Society, 2013, 160, A1759-A1771.
- [22] J. Muldoon, C.B. Bucur, T. Gregory, *Quest for nonaqueous multivalent secondary batteries: magnesium and beyond*, Chemical Reviews, 2014, 114, 11683-11720.
- [23] J. Fu, Z.P. Cano, M.G. Park, A. Yu, M. Fowler, Z. Chen, *Electrically Rechargeable Zinc-Air Batteries: Progress, Challenges, and Perspectives*, Advanced Materials, 2017, 29.
- [24] A.J. Appleby, J. Jacquelin, J.P. Pompon, *Charge-Discharge Behavior of the CGE Circulating Zinc-Air Vehicle Battery*, SAE Technical Paper, 1977.
- [25] M.C. Cheiky, L.G. Danczyk, M.C. Wehrey, *Rechargeable zinc-air batteries in electric vehicle applications*, SAE Technical Paper, 1990.
- [26] M.C. Cheiky, L.G. Danczyk, R.L. Scheffler, *Zinc-Air Powered Electric Vehicle Systems Integration Issues*, SAE Technical Paper, 1991.

- [27] M.C. Cheiky, L.G. Danczyk, M.C. Wehrey, Second-generation Zinc-Air powered electric minivans, SAE Technical Paper, 1992.
- [28] J.R. Goldstein, B. Koretz, *Tests of a full-sized mechanically rechargeable zinc-air battery in an electric vehicle*, IEEE Aerospace and Electronic Systems Magazine, 1993, 8, 34-38.
- [29] J. Goldstein, I. Brown, B. Koretz, *New developments in the Electric Fuel Ltd. zinc/air system*, Journal of Power Sources, 1999, 80, 171-179.
- [30] Y. Nishi, *Lithium ion secondary batteries; past 10 years and the future*, Journal of Power Sources, 2001, 100, 101-106.
- [31] Q. Wei, Y. Fu, G. Zhang, S. Sun, *Rational design of carbon-based oxygen electrocatalysts for zinc-air batteries*, Current Opinion in Electrochemistry, 2017, 4, 45-59.
- [32] Q. Wei, X. Tong, G. Zhang, J. Qiao, Q. Gong, S. Sun, *Nitrogen-Doped Carbon Nanotube and Graphene Materials for Oxygen Reduction Reactions*, Catalysts, 2015, 5, 1574-1602.
- [33] W.R.P. Barros, Q. Wei, G. Zhang, S. Sun, M.R.V. Lanza, A.C. Tavares, *Oxygen reduction to hydrogen peroxide on Fe<sub>3</sub>O<sub>4</sub> nanoparticles supported on Printex carbon and Graphene*, Electrochimica Acta, 2015, 162, 263-270.
- [34] X. Ge, A. Sumboja, D. Wu, T. An, B. Li, F.W.T. Goh, T.S.A. Hor, Y. Zong, Z. Liu, *Oxygen reduction in alkaline media: from mechanisms to recent advances of catalysts*, Acs Catalysis, 2015, 5, 4643-4667.
- [35] N.-T. Suen, S.-F. Hung, Q. Quan, N. Zhang, Y.-J. Xu, H.M. Chen, *Electrocatalysis for the oxygen evolution reaction: recent development and future perspectives*, Chemical Society Reviews, 2017, 46, 337-365.
- [36] Y. Nie, L. Li, Z. Wei, *Recent advancements in Pt and Pt-free catalysts for oxygen reduction reaction*, Chemical Society Reviews, 2015, 44, 2168-2201.
- [37] P. Strasser, S. Koh, T. Anniyev, J. Greeley, K. More, C. Yu, Z. Liu, S. Kaya, D. Nordlund, H. Ogasawara, *Lattice-strain control of the activity in dealloyed core-shell fuel cell catalysts*, Nature Chemistry, 2010, 2, 454.
- [38] J.R. Kitchin, J.K. Nørskov, M.A. Barteau, J.G. Chen, *Modification of the surface electronic and chemical properties of Pt (111) by subsurface 3d transition metals*, The Journal of Chemical Physics, 2004, 120, 10240-10246.

- [39] V.R. Stamenkovic, B.S. Mun, M. Arenz, K.J.J. Mayrhofer, C.A. Lucas, G. Wang, P.N. Ross, N.M. Markovic, *Trends in electrocatalysis on extended and nanoscale Pt-bimetallic alloy surfaces*, Nature Materials, 2007, 6, 241.
- [40] N. Tian, Z.-Y. Zhou, S.-G. Sun, Y. Ding, Z.L. Wang, *Synthesis of tetrahedral platinum nanocrystals with high-index facets and high electro-oxidation activity*, Science, 2007, 316, 732-735.
- [41] V.R. Stamenkovic, B. Fowler, B.S. Mun, G. Wang, P.N. Ross, C.A. Lucas, N.M. Marković, *Improved oxygen reduction activity on Pt<sub>3</sub>Ni (111) via increased surface site availability*, Science, 2007, 315, 493-497.
- [42] J. Zhang, K. Sasaki, E. Sutter, R.R. Adzic, *Stabilization of platinum oxygen-reduction electrocatalysts using gold clusters*, Science, 2007, 315, 220-222.
- [43] S.J. Tauster, S.C. Fung, R.T.K. Baker, J.A. Horsley, *Strong interactions in supported-metal catalysts*, Science, 1981, 211, 1121-1125.
- [44] D. Banham, S. Ye, K. Pei, J.-i. Ozaki, T. Kishimoto, Y. Imashiro, *A review of the stability and durability of non-precious metal catalysts for the oxygen reduction reaction in proton exchange membrane fuel cells*, Journal of Power Sources, 2015, 285, 334-348.
- [45] M. Shen, C. Wei, K. Ai, L. Lu, *Transition metal–nitrogen–carbon nanostructured catalysts for the oxygen reduction reaction: From mechanistic insights to structural optimization*, Nano Research, 2017, 10, 1449-1470.
- [46] R. Jasinski, *A new fuel cell cathode catalyst*, Nature, 1964, 201, 1212.
- [47] E. Yeager, *Electrocatalysts for O<sub>2</sub> reduction*, Electrochimica Acta, 1984, 29, 1527-1537.
- [48] H. Liu, C. Song, Y. Tang, J. Zhang, J. Zhang, *High-surface-area CoTMPP/C synthesized by ultrasonic spray pyrolysis for PEM fuel cell electrocatalysts*, Electrochimica Acta, 2007, 52, 4532-4538.
- [49] D.H. Lee, W.J. Lee, W.J. Lee, S.O. Kim, Y.-H. Kim, *Theory, synthesis, and oxygen reduction catalysis of Fe-porphyrin-like carbon nanotube*, Physical Review Letters, 2011, 106, 175502.
- [50] D. Deng, L. Yu, X. Chen, G. Wang, L. Jin, X. Pan, J. Deng, G. Sun, X. Bao, *Iron encapsulated within pod-like carbon nanotubes for oxygen reduction reaction*, Angewandte Chemie International Edition, 2013, 125, 389-393.

- [51] Q. Shi, F. Peng, S. Liao, H. Wang, H. Yu, Z. Liu, B. Zhang, D. Su, *Sulfur and nitrogen co-doped carbon nanotubes for enhancing electrochemical oxygen reduction activity in acidic and alkaline media*, Journal of Materials Chemistry A, 2013, 1, 14853-14857.
- [52] Q. Wei, G. Zhang, X. Yang, R. Chenitz, D. Banham, L. Yang, S. Ye, S. Knights, S. Sun, *3D Porous Fe/N/C Spherical Nanostructures As High-Performance Electrocatalysts for Oxygen Reduction in Both Alkaline and Acidic Media*, ACS Appl Mater Interfaces, 2017, 9, 36944-36954.
- [53] P. Su, H. Xiao, J. Zhao, Y. Yao, Z. Shao, C. Li, Q. Yang, *Nitrogen-doped carbon nanotubes derived from Zn-Fe-ZIF nanospheres and their application as efficient oxygen reduction electrocatalysts with in situ generated iron species*, Chemical Science, 2013, 4, 2941-2946.
- [54] S.-A. Wohlgemuth, T.-P. Fellingner, P. Jäker, M. Antonietti, *Tunable nitrogen-doped carbon aerogels as sustainable electrocatalysts in the oxygen reduction reaction*, Journal of Materials Chemistry A, 2013, 1, 4002-4009.
- [55] H. Xiao, Z.-G. Shao, G. Zhang, Y. Gao, W. Lu, B. Yi, *Fe-N-carbon black for the oxygen reduction reaction in sulfuric acid*, Carbon, 2013, 57, 443-451.
- [56] G. Wu, K.L. More, C.M. Johnston, P. Zelenay, *High-performance electrocatalysts for oxygen reduction derived from polyaniline, iron, and cobalt*, Science, 2011, 332, 443-447.
- [57] P. Zhang, F. Sun, Z. Xiang, Z. Shen, J. Yun, D. Cao, *ZIF-derived in situ nitrogen-doped porous carbons as efficient metal-free electrocatalysts for oxygen reduction reaction*, Energy & Environmental Science, 2014, 7, 442-450.
- [58] Z.S. Wu, L. Chen, J. Liu, K. Parvez, H. Liang, J. Shu, H. Sachdev, R. Graf, X. Feng, K. Müllen, *High-Performance Electrocatalysts for Oxygen Reduction Derived from Cobalt Porphyrin-Based Conjugated Mesoporous Polymers*, Advanced Materials, 2014, 26, 1450-1455.
- [59] K. Ai, Y. Liu, C. Ruan, L. Lu, G. Lu, *Sp<sup>2</sup> C-dominant N-doped carbon sub-micrometer spheres with a tunable size: a versatile platform for highly efficient oxygen-reduction catalysts*, Advanced Materials, 2013, 25, 998-1003.
- [60] J.A.R. Van Veen, H.A. Colijn, J.F. Van Baar, *On the effect of a heat treatment on the structure of carbon-supported metalloporphyrins and phthalocyanines*, Electrochimica Acta, 1988, 33, 801-804.

- [61] D.A. Scherson, S.L. Gupta, C. Fierro, E.B. Yeager, M.E. Kordesch, J. Eldridge, R.W. Hoffman, J. Blue, *Cobalt tetramethoxyphenyl porphyrin—emission Mossbauer spectroscopy and O<sub>2</sub> reduction electrochemical studies*, *Electrochimica Acta*, 1983, 28, 1205-1209.
- [62] D. Scherson, A.A. Tanaka, S.L. Gupta, D. Tryk, C. Fierro, R. Holze, E.B. Yeager, R.P. Lattimer, *Transition metal macrocycles supported on high area carbon: Pyrolysis—mass spectrometry studies*, *Electrochimica Acta*, 1986, 31, 1247-1258.
- [63] J.-P. Dodelet, Oxygen reduction in PEM fuel cell conditions: heat-treated non-precious metal-N<sub>4</sub> macrocycles and beyond, *N<sub>4</sub>-Macrocyclic Metal Complexes*, Springer 2006, pp. 83-147.
- [64] U.I. Kramm, I. Abs-Wurmbach, I. Herrmann-Geppert, J. Radnik, S. Fiechter, P. Bogdanoff, *Influence of the electron-density of FeN<sub>4</sub>-centers towards the catalytic activity of pyrolyzed FeTMPPCl-based ORR-electrocatalysts*, *Journal of the Electrochemical Society*, 2011, 158, B69-B78.
- [65] U.I. Koslowski, I. Abs-Wurmbach, S. Fiechter, P. Bogdanoff, *Nature of the catalytic centers of porphyrin-based electrocatalysts for the ORR: a correlation of kinetic current density with the site density of Fe–N<sub>4</sub> centers*, *The Journal of Physical Chemistry C*, 2008, 112, 15356-15366.
- [66] S. Kattel, G. Wang, *A density functional theory study of oxygen reduction reaction on Me–N<sub>4</sub> (Me= Fe, Co, or Ni) clusters between graphitic pores*, *Journal of Materials Chemistry A*, 2013, 1, 10790-10797.
- [67] W.-J. Jiang, L. Gu, L. Li, Y. Zhang, X. Zhang, L.-J. Zhang, J.-Q. Wang, J.-S. Hu, Z. Wei, L.-J. Wan, *Understanding the high activity of Fe–N–C electrocatalysts in oxygen reduction: Fe/Fe<sub>3</sub>C nanoparticles boost the activity of Fe–N<sub>x</sub>*, *Journal of the American Chemical Society*, 2016, 138, 3570-3578.
- [68] S. Maldonado, K.J. Stevenson, *Direct preparation of carbon nanofiber electrodes via pyrolysis of iron (II) phthalocyanine: electrocatalytic aspects for oxygen reduction*, *The Journal of Physical Chemistry B*, 2004, 108, 11375-11383.
- [69] P.H. Matter, U.S. Ozkan, *Non-metal catalysts for dioxygen reduction in an acidic electrolyte*, *Catalysis Letters*, 2006, 109, 115-123.
- [70] P.H. Matter, E. Wang, J.-M.M. Millet, U.S. Ozkan, *Characterization of the iron phase in CN<sub>x</sub>-based oxygen reduction reaction catalysts*, *The Journal of Physical Chemistry C*, 2007, 111, 1444-1450.

- [71] U.I. Kramm, J. Herranz, N. Larouche, T.M. Arruda, M. Lefèvre, F. Jaouen, P. Bogdanoff, S. Fiechter, I. Abs-Wurmbach, S. Mukerjee, *Structure of the catalytic sites in Fe/N/C-catalysts for O<sub>2</sub>-reduction in PEM fuel cells*, *Physical Chemistry Chemical Physics*, 2012, 14, 11673-11688.
- [72] S. Liang, C. Hao, Y. Shi, *The Power of Single-Atom Catalysis*, *ChemCatChem*, 2015, 7, 2559-2567.
- [73] H. Zhang, G. Liu, L. Shi, J. Ye, *Single-Atom Catalysts: Emerging Multifunctional Materials in Heterogeneous Catalysis*, *Advanced Energy Materials*, 2018, 8, 1701343.
- [74] J.-C. Liu, Y.-G. Wang, J. Li, *Toward rational design of oxide-supported single-atom catalysts: atomic dispersion of gold on ceria*, *Journal of the American Chemical Society*, 2017, 139, 6190-6199.
- [75] Y. Chen, S. Ji, C. Chen, Q. Peng, D. Wang, Y. Li, *Single-atom catalysts: Synthetic strategies and electrochemical applications*, *Joule*, 2018, 2, 1242-1264.
- [76] Y. Gao, Z. Cai, X. Wu, Z. Lv, P. Wu, C. Cai, *Graphdiyne-Supported Single-Atom-Sized Fe Catalysts for the Oxygen Reduction Reaction: DFT Predictions and Experimental Validations*, *ACS Catalysis*, 2018.
- [77] H. Fei, J. Dong, M.J. Arellano-Jiménez, G. Ye, N.D. Kim, E.L.G. Samuel, Z. Peng, Z. Zhu, F. Qin, J. Bao, *Atomic cobalt on nitrogen-doped graphene for hydrogen generation*, *Nature Communications*, 2015, 6, 8668.
- [78] X.-F. Yang, A. Wang, B. Qiao, J. Li, J. Liu, T. Zhang, *Single-atom catalysts: a new frontier in heterogeneous catalysis*, *Accounts of Chemical Research*, 2013, 46, 1740-1748.
- [79] Y. Chen, S. Ji, Y. Wang, J. Dong, W. Chen, Z. Li, R. Shen, L. Zheng, Z. Zhuang, D. Wang, *Isolated single iron atoms anchored on N-doped porous carbon as an efficient electrocatalyst for the oxygen reduction reaction*, *Angewandte Chemie International Edition*, 2017, 56, 6937-6941.
- [80] H.T. Chung, D.A. Cullen, D. Higgins, B.T. Sneed, E.F. Holby, K.L. More, P. Zelenay, *Direct atomic-level insight into the active sites of a high-performance PGM-free ORR catalyst*, *Science*, 2017, 357, 479-484.
- [81] L. Yang, S. Jiang, Y. Zhao, L. Zhu, S. Chen, X. Wang, Q. Wu, J. Ma, Y. Ma, Z. Hu, *Boron-doped carbon nanotubes as metal-free electrocatalysts for the oxygen reduction reaction*, *Angewandte Chemie International Edition*, 2011, 50, 7132-7135.

- [82] Z.-H. Sheng, H.-L. Gao, W.-J. Bao, F.-B. Wang, X.-H. Xia, *Synthesis of boron doped graphene for oxygen reduction reaction in fuel cells*, Journal of Materials Chemistry, 2012, 22, 390-395.
- [83] H. Li, H. Liu, Z. Jong, W. Qu, D. Geng, X. Sun, H. Wang, *Nitrogen-doped carbon nanotubes with high activity for oxygen reduction in alkaline media*, International Journal of Hydrogen Energy, 2011, 36, 2258-2265.
- [84] Z. Luo, S. Lim, Z. Tian, J. Shang, L. Lai, B. MacDonald, C. Fu, Z. Shen, T. Yu, J. Lin, *Pyridinic N doped graphene: synthesis, electronic structure, and electrocatalytic property*, Journal of Materials Chemistry, 2011, 21, 8038.
- [85] R. Lv, T. Cui, M.-S. Jun, Q. Zhang, A. Cao, D.S. Su, Z. Zhang, S.-H. Yoon, J. Miyawaki, I. Mochida, F. Kang, *Open-Ended, N-Doped Carbon Nanotube-Graphene Hybrid Nanostructures as High-Performance Catalyst Support*, Advanced Functional Materials, 2011, 21, 999-1006.
- [86] T. Sharifi, G. Hu, X. Jia, T. Wagberg, *Formation of Active Sites for Oxygen Reduction Reactions by Transformation of Nitrogen Functionalities in Nitrogen-Doped Carbon Nanotubes*, ACS Nano, 2012, 6, 8904-8912.
- [87] W.-J. Jiang, J.-S. Hu, X. Zhang, Y. Jiang, B.-B. Yu, Z.-D. Wei, L.-J. Wan, *In situ nitrogen-doped nanoporous carbon nanocables as an efficient metal-free catalyst for oxygen reduction reaction*, Journal of Materials Chemistry A, 2014, 2, 10154.
- [88] Z. Ma, S. Dou, A. Shen, L. Tao, L. Dai, S. Wang, *Sulfur-doped graphene derived from cycled lithium-sulfur batteries as a metal-free electrocatalyst for the oxygen reduction reaction*, Angewandte Chemie International Edition, 2015, 54, 1888-1892.
- [89] Z. Yang, Z. Yao, G. Li, G. Fang, H. Nie, Z. Liu, X. Zhou, X.a. Chen, S. Huang, *Sulfur-doped graphene as an efficient metal-free cathode catalyst for oxygen reduction*, ACS Nano, 2011, 6, 205-211.
- [90] Z. Jin, H. Nie, Z. Yang, J. Zhang, Z. Liu, X. Xu, S. Huang, *Metal-free selenium doped carbon nanotube/graphene networks as a synergistically improved cathode catalyst for oxygen reduction reaction*, Nanoscale, 2012, 4, 6455-6460.
- [91] Z.W. Liu, F. Peng, H.J. Wang, H. Yu, W.X. Zheng, J. Yang, *Phosphorus-doped graphite layers with high electrocatalytic activity for the O<sub>2</sub> reduction in an alkaline medium*, Angewandte Chemie International Edition, 2011, 50, 3257-3261.

- [92] C. Zhang, N. Mahmood, H. Yin, F. Liu, Y. Hou, *Synthesis of phosphorus-doped graphene and its multifunctional applications for oxygen reduction reaction and lithium ion batteries*, *Advanced Materials*, 2013, 25, 4932-4937.
- [93] Z. Liu, X. Fu, M. Li, F. Wang, Q. Wang, G. Kang, F. Peng, *Novel silicon-doped, silicon and nitrogen-codoped carbon nanomaterials with high activity for the oxygen reduction reaction in alkaline medium*, *Journal of Materials Chemistry A*, 2015, 3, 3289-3293.
- [94] X. Sun, Y. Zhang, P. Song, J. Pan, L. Zhuang, W. Xu, W. Xing, *Fluorine-Doped Carbon Blacks: Highly Efficient Metal-Free Electrocatalysts for Oxygen Reduction Reaction*, *ACS Catalysis*, 2013, 3, 1726-1729.
- [95] S. Wang, E. Iyyamperumal, A. Roy, Y. Xue, D. Yu, L. Dai, *Vertically aligned BCN nanotubes as efficient metal-free electrocatalysts for the oxygen reduction reaction: a synergetic effect by co-doping with boron and nitrogen*, *Angewandte Chemie International Edition*, 2011, 50, 11756-11760.
- [96] C.H. Choi, S.H. Park, S.I. Woo, *Phosphorus–nitrogen dual doped carbon as an effective catalyst for oxygen reduction reaction in acidic media: effects of the amount of P-doping on the physical and electrochemical properties of carbon*, *Journal of Materials Chemistry*, 2012, 22, 12107.
- [97] H. Jiang, Y. Zhu, Q. Feng, Y. Su, X. Yang, C. Li, *Nitrogen and phosphorus dual-doped hierarchical porous carbon foams as efficient metal-free electrocatalysts for oxygen reduction reactions*, *Chemistry A European Journal*, 2014, 20, 3106-3112.
- [98] C. You, S. Liao, H. Li, S. Hou, H. Peng, X. Zeng, F. Liu, R. Zheng, Z. Fu, Y. Li, *Uniform nitrogen and sulfur co-doped carbon nanospheres as catalysts for the oxygen reduction reaction*, *Carbon*, 2014, 69, 294-301.
- [99] Y. Meng, D. Voiry, A. Goswami, X. Zou, X. Huang, M. Chhowalla, Z. Liu, T. Asefa, *N-, O-, and S-tridoped nanoporous carbons as selective catalysts for oxygen reduction and alcohol oxidation reactions*, *Journal of the American Chemical Society*, 2014, 136, 13554-13557.
- [100] Z. Liu, F. Wang, M. Li, Z.-H. Ni, *N, S and P-ternary doped carbon nano-pore/tube composites derived from natural chemicals in waste sweet osmanthus fruit with superior activity for oxygen reduction in acidic and alkaline media*, *RSC Advances*, 2016, 6, 37500-37505.
- [101] K. Gong, F. Du, Z. Xia, M. Durstock, L. Dai, *Nitrogen-doped carbon nanotube arrays with high electrocatalytic activity for oxygen reduction*, *Science*, 2009, 323, 760-764.

- [102] R.S. Lee, H.J. Kim, J.E. Fischer, A. Thess, R.E. Smalley, *Conductivity enhancement in single-walled carbon nanotube bundles doped with K and Br*, *Nature*, 1997, 388, 255.
- [103] R.A. Nistor, D.M. Newns, G.J. Martyna, *The role of chemistry in graphene doping for carbon-based electronics*, *ACS Nano*, 2011, 5, 3096-3103.
- [104] L. Zhao, R. He, K.T. Rim, T. Schiros, K.S. Kim, H. Zhou, C. Gutiérrez, S.P. Chockalingam, C.J. Arguello, L. Pálová, *Visualizing individual nitrogen dopants in monolayer graphene*, *Science*, 2011, 333, 999-1003.
- [105] L. Dai, *Functionalization of graphene for efficient energy conversion and storage*, *Accounts of Chemical Research*, 2012, 46, 31-42.
- [106] D.S. Su, J. Zhang, B. Frank, A. Thomas, X. Wang, J. Paraknowitsch, R. Schlögl, *Metal-free heterogeneous catalysis for sustainable chemistry*, *ChemSusChem: Chemistry & Sustainability Energy & Materials*, 2010, 3, 169-180.
- [107] D. Yu, E. Nagelli, F. Du, L. Dai, *Metal-free carbon nanomaterials become more active than metal catalysts and last longer*, *The Journal of Physical Chemistry Letters*, 2010, 1, 2165-2173.
- [108] L. Dai, Y. Xue, L. Qu, H.-J. Choi, J.-B. Baek, *Metal-free catalysts for oxygen reduction reaction*, *Chemical Reviews*, 2015, 115, 4823-4892.
- [109] C. Zhu, S. Dong, *Synthesis of graphene-supported noble metal hybrid nanostructures and their applications as advanced electrocatalysts for fuel cells*, *Nanoscale*, 2013, 5, 10765-10775.
- [110] Z.W. Liu, F. Peng, H.J. Wang, H. Yu, W.X. Zheng, J. Yang, *Phosphorus-doped graphite layers with high electrocatalytic activity for the O<sub>2</sub> reduction in an alkaline medium*, *Angewandte Chemie International Edition*, 2011, 50, 3257-3261.
- [111] L. Dai, D.W. Chang, J.B. Baek, W. Lu, *Carbon nanomaterials for advanced energy conversion and storage*, *Small*, 2012, 8, 1130-1166.
- [112] J. Shui, M. Wang, F. Du, L. Dai, *N-doped carbon nanomaterials are durable catalysts for oxygen reduction reaction in acidic fuel cells*, *Science Advances*, 2015, 1, e1400129.
- [113] K.A. Shah, B.A. Tali, *Synthesis of carbon nanotubes by catalytic chemical vapour deposition: A review on carbon sources, catalysts and substrates*, *Materials Science in Semiconductor Processing*, 2016, 41, 67-82.
- [114] M. Borghei, J. Lehtonen, L. Liu, O.J. Rojas, *Advanced Biomass-Derived Electrocatalysts for the Oxygen Reduction Reaction*, *Advanced Materials*, 2018, 30, 1703691.

- [115] E. De la Llave, V. Borgel, K.-J. Park, J.-Y. Hwang, Y.-K. Sun, P. Hartmann, F.-F. Chesneau, D. Aurbach, *Comparison between Na-Ion and Li-Ion cells: understanding the critical role of the cathodes stability and the anodes pretreatment on the cells behavior*, ACS Applied Materials & Interfaces, 2016, 8, 1867-1875.
- [116] M.D. Slater, D. Kim, E. Lee, C.S. Johnson, *Sodium-ion batteries*, Advanced Functional Materials, 2013, 23, 947-958.
- [117] P. Adelhelm, P. Hartmann, C.L. Bender, M. Busche, C. Eufinger, J. Janek, *From lithium to sodium: cell chemistry of room temperature sodium–air and sodium–sulfur batteries*, Journal of Nanotechnology, 2015, 6, 1016.
- [118] A.S. Nagelberg, W.L. Worrell, *A thermodynamic study of sodium-intercalated TaS<sub>2</sub> and TiS<sub>2</sub>*, Journal of Solid State Chemistry, 1979, 29, 345-354.
- [119] J.-J. Braconnier, C. Delmas, C. Fouassier, P. Hagenmuller, *Comportement electrochimique des phases Na<sub>x</sub>CoO<sub>2</sub>*, Materials Research Bulletin, 1980, 15, 1797-1804.
- [120] K. Kubota, S. Komaba, *Practical issues and future perspective for Na-ion batteries*, Journal of The Electrochemical Society, 2015, 162, A2538-A2550.
- [121] Y. Fu, Q. Wei, G. Zhang, S. Sun, *Advanced Phosphorus-Based Materials for Lithium/Sodium-Ion Batteries: Recent Developments and Future Perspectives*, Advanced Energy Materials, 2018, 1703058.
- [122] J.-Y. Hwang, S.-T. Myung, Y.-K. Sun, *Sodium-ion batteries: present and future*, Chemical Society Reviews, 2017, 46, 3529-3614.
- [123] E. Venere, *Sodium-ion batteries are potential power technology of future*, 2015.
- [124] H. Pan, Y.-S. Hu, L. Chen, *Room-temperature stationary sodium-ion batteries for large-scale electric energy storage*, Energy & Environmental Science, 2013, 6, 2338-2360.
- [125] P. Ge, M. Foulletier, *Electrochemical intercalation of sodium in graphite*, Solid State Ionics, 1988, 28, 1172-1175.
- [126] M.M. Doeff, Y. Ma, S.J. Visco, L.C. De Jonghe, *Electrochemical insertion of sodium into carbon*, Journal of The Electrochemical Society, 1993, 140, L169-L170.
- [127] X. Li, A. Dhanabalan, L. Gu, C. Wang, *Three-Dimensional Porous Core-Shell Sn@Carbon Composite Anodes for High-Performance Lithium-Ion Battery Applications*, Advanced Energy Materials, 2012, 2, 238-244.

- [128] A. Darwiche, C. Marino, M.T. Sougrati, B. Fraisse, L. Stievano, L. Monconduit, *Better cycling performances of bulk Sb in Na-ion batteries compared to Li-ion systems: an unexpected electrochemical mechanism*, Journal of the American Chemical Society, 2012, 134, 20805-20811.
- [129] Z. Liu, X.-Y. Yu, X.W.D. Lou, U. Paik, *Sb@C coaxial nanotubes as a superior long-life and high-rate anode for sodium ion batteries*, Energy & Environmental Science, 2016, 9, 2314-2318.
- [130] L. Baggetto, J.K. Keum, J.F. Browning, G.M. Veith, *Germanium as negative electrode material for sodium-ion batteries*, Electrochemistry Communications, 2013, 34, 41-44.
- [131] W.-J. Li, S.-L. Chou, J.-Z. Wang, H.-K. Liu, S.-X. Dou, *Simply mixed commercial red phosphorus and carbon nanotube composite with exceptionally reversible sodium-ion storage*, Nano Letters, 2013, 13, 5480-5484.
- [132] A. Nie, L.y. Gan, Y. Cheng, X. Tao, Y. Yuan, S. Sharifi-Asl, K. He, H. Asayesh-Ardakani, V. Vasiraju, J. Lu, *Ultrafast and Highly Reversible Sodium Storage in Zinc-Antimony Intermetallic Nanomaterials*, Advanced Functional Materials, 2016, 26, 543-552.
- [133] D. Su, H.-J. Ahn, G. Wang, *SnO<sub>2</sub>@ graphene nanocomposites as anode materials for Na-ion batteries with superior electrochemical performance*, Chemical Communications, 2013, 49, 3131-3133.
- [134] M. Hu, Y. Jiang, W. Sun, H. Wang, C. Jin, M. Yan, *Reversible conversion-alloying of Sb<sub>2</sub>O<sub>3</sub> as a high-capacity, high-rate, and durable anode for sodium ion batteries*, ACS Applied Materials & Interfaces, 2014, 6, 19449-19455.
- [135] S. Yuan, X.L. Huang, D.l. Ma, H.g. Wang, F.z. Meng, X.b. Zhang, *Engraving Copper Foil to Give Large-Scale Binder-Free Porous CuO Arrays for a High-Performance Sodium-Ion Battery Anode*, Advanced Materials, 2014, 26, 2273-2279.
- [136] N. Zhang, X. Han, Y. Liu, X. Hu, Q. Zhao, J. Chen, *3D Porous  $\gamma$ -Fe<sub>2</sub>O<sub>3</sub>@ C Nanocomposite as High-Performance Anode Material of Na-Ion Batteries*, Advanced Energy Materials, 2015, 5, 1401123.
- [137] Y. Liu, Z. Cheng, H. Sun, H. Arandiyani, J. Li, M. Ahmad, *Mesoporous Co<sub>3</sub>O<sub>4</sub> sheets/3D graphene networks nanohybrids for high-performance sodium-ion battery anode*, Journal of Power Sources, 2015, 273, 878-884.

- [138] Y. Zhang, C. Wang, H. Hou, G. Zou, X. Ji, *Nitrogen Doped/Carbon Tuning Yolk-Like TiO<sub>2</sub> and Its Remarkable Impact on Sodium Storage Performances*, *Advanced Energy Materials*, 2017, 7, 1600173.
- [139] Y. Liu, N. Zhang, C. Yu, L. Jiao, J. Chen, *MnFe<sub>2</sub>O<sub>4</sub>@C nanofibers as high-performance anode for sodium-ion batteries*, *Nano Letters*, 2016, 16, 3321-3328.
- [140] L. David, R. Bhandavat, G. Singh, *MoS<sub>2</sub>/graphene composite paper for sodium-ion battery electrodes*, *ACS Nano*, 2014, 8, 1759-1770.
- [141] J. Zhou, L. Wang, M. Yang, J. Wu, F. Chen, W. Huang, N. Han, H. Ye, F. Zhao, Y. Li, *Hierarchical VS<sub>2</sub> nanosheet assemblies: A universal host material for the reversible storage of alkali metal ions*, *Advanced Materials*, 2017, 29, 1702061.
- [142] B. Qu, C. Ma, G. Ji, C. Xu, J. Xu, Y.S. Meng, T. Wang, J.Y. Lee, *Layered SnS<sub>2</sub>-Reduced Graphene Oxide Composite—A High-Capacity, High-Rate, and Long-Cycle Life Sodium-Ion Battery Anode Material*, *Advanced materials*, 2014, 26, 3854-3859.
- [143] X. Xiong, G. Wang, Y. Lin, Y. Wang, X. Ou, F. Zheng, C. Yang, J.-H. Wang, M. Liu, *Enhancing sodium ion battery performance by strongly binding nanostructured Sb<sub>2</sub>S<sub>3</sub> on sulfur-doped graphene sheets*, *ACS Nano*, 2016, 10, 10953-10959.
- [144] W. Zhang, M. Dahbi, S. Amagasa, Y. Yamada, S. Komaba, *Iron phosphide as negative electrode material for Na-ion batteries*, *Electrochemistry Communications*, 2016, 69, 11-14.
- [145] H. Hou, X. Qiu, W. Wei, Y. Zhang, X. Ji, *Carbon Anode Materials for Advanced Sodium-Ion Batteries*, *Advanced Energy Materials*, 2017, 7, 1602898.
- [146] [https://commons.wikimedia.org/wiki/File:OSC\\_Microbio\\_02\\_03\\_ElMicSchem.jpg](https://commons.wikimedia.org/wiki/File:OSC_Microbio_02_03_ElMicSchem.jpg).
- [147] <https://wiki.anton-paar.com/en/x-ray-diffraction-xrd/>.
- [148] F. Dalton, *ECS Classics: Historical Origins of the Rotating Ring-Disk Electrode*, *The Electrochemical Society Interface*, 2016, 25, 50-59.
- [149] A. Frumkin, L. Nekrasov, B. Levich, J. Ivanov, *Die Anwendung der rotierenden Scheibenelektrode mit einem Ringe zur Untersuchung von Zwischenprodukten elektrochemischer Reaktionen*, *Journal of Electroanalytical Chemistry*, 1959, 1, 84-90.
- [150] L.N. Nekrasov, L. Müller, *The use of a rotating disc electrode with a ring in studying the cathode reduction of oxygen on platinum in alkaline solutions*, *Russian Academy of Sciences*, pp. 1107-1110.

- [151] W.J. Albery, M.L. Hitchman, W.J. Albery, *Ring-disc electrodes*, Clarendon Press Oxford 1971.
- [152] W.J. Albery, *Ring-disc electrodes. Part 1.—A new approach to the theory*, Transactions of the Faraday Society, 1966, 62, 1915-1919.
- [153] W.J. Albery, S. Bruckenstein, *Ring-disc electrodes. Part 2.—Theoretical and experimental collection efficiencies*, Transactions of the Faraday Society, 1966, 62, 1920-1931.
- [154] W.J. Albery, S. Bruckenstein, D.T. Napp, *Ring-disc electrodes. Part 3.—Current-voltage curves at the ring electrode with simultaneous currents at the disc electrode*, Transactions of the Faraday Society, 1966, 62, 1932-1937.
- [155] W.J. Albery, S. Bruckenstein, D.C. Johnson, *Ring-disc electrodes. Part 4.—Diffusion layer titration curves*, Transactions of the Faraday Society, 1966, 62, 1938-1945.
- [156] W.J. Albery, S. Bruckenstein, *Ring-disc electrodes. Part 5.—First-order kinetic collection efficiencies at the ring electrode*, Transactions of the Faraday Society, 1966, 62, 1946-1954.
- [157] U.A. Paulus, T.J. Schmidt, H.A. Gasteiger, R.J. Behm, *Oxygen reduction on a high-surface area Pt/Vulcan carbon catalyst: a thin-film rotating ring-disk electrode study*, Journal of Electroanalytical Chemistry, 2001, 495, 134-145.
- [158] <https://www.pineresearch.com/shop/knowledgebase/rotating-electrode-theory/>.

# RÉSUMÉ

## L'introduction

Aujourd'hui, la principale source d'énergie de la société repose toujours sur l'épuisement des combustibles fossiles [1]. Par conséquent, la réalisation d'un avenir énergétique sûr, économique, respectueux de l'environnement et durable est devenue l'un des plus grands défis scientifiques et sociétaux du XXI<sup>e</sup> siècle. Pour réduire notre dépendance aux combustibles fossiles, il est particulièrement urgent et important de développer des sources d'énergie renouvelables et durables, telles que l'énergie solaire, géothermique, hydraulique, marémotrice et éolienne [2]. Cependant, il est bien connu que ces sources d'énergie sont confrontées aux défis de l'imprévisibilité, de l'instabilité des capacités, de l'intermittence et du régionalisme. Pour utiliser de manière sûre et efficace ces énergies renouvelables, les dispositifs de stockage et de conversion d'énergie électrochimiques (SCEE) sont très prometteurs pour les applications à grande échelle. Parmi les nombreux SCEE, les batteries lithium-ion rechargeables (LIB selon anglais expression *Lithium-ion batteries*) sont devenues la source d'énergie la plus largement répandue dans la vie quotidienne, allant de l'électronique portable et véhicules électriques (VEs) aux réseaux intelligents à grande échelle [3-5]. Les dernières décennies ont constaté le progrès des LIB à partir de la performance et des coûts. Par exemple, l'énergie spécifique a augmenté de 90 Wh kg<sup>-1</sup><sub>cell</sub> dans les années 90 à plus de 250 Wh kg<sup>-1</sup><sub>cell</sub> à ce jour; entre-temps, le coût des packs LIB a diminué de plus de 1 000 \$ kW h<sup>-1</sup> à environ 250 \$ kW h<sup>-1</sup> [6], baissant les prix des VEs à un niveau raisonnable pour les consommateurs moyens. Cependant, avec le développement mondial rapide, les progrès de la technologie des LIB ne peuvent toujours pas répondre adéquatement à la demande croissante en permanence dans les applications énergétiques émergentes qui exigent généralement les densités de puissance et d'énergie plus élevées et une durée de vie plus longue, en particulier dans le segment des transports à longue distance. De plus, la source de lithium naturelle limitée avec sa répartition inégale (principalement en Amérique du Sud) dans la croûte terrestre et ses coûts de production élevés, ont également un impact négatif sur la satisfaction des besoins de stockage d'énergie à grande échelle dans notre société moderne. Des nouveaux systèmes électrochimiques sont donc activement recherchés [7].

La densité de puissance et la densité d'énergie sont les paramètres les plus importants pour évaluer les performances des dispositifs SCEE. Le diagramme de Ragone de la figure R1 décrit les densités de puissance et d'énergie caractéristiques de divers dispositifs de SECC. Par conséquent, les piles à combustible [9] et les batteries métal-air [10] ont suscité un grand intérêt des chercheurs parmi les dispositifs potentiels de SCEE, en raison de leur puissance théorique et densité d'énergie élevées. De plus, les performances électrochimiques, les piles à combustible à hydrogène et les batteries métal-air ont également l'avantage d'être écologiques, ce qui en fait les technologies les plus prometteuses et les plus attrayantes pour l'approvisionnement énergétique à venir. Le coût est également un facteur inéluctable des dispositifs de SCEE pour les applications les plus répandues. Compte tenu de la grande abondance et du faible coût du sodium ainsi que de son potentiel rédox très approprié [11], les cellules électrochimiques rechargeables à base de sodium sont également beaucoup plus prometteuses pour les applications de stockage d'énergie à grande échelle.

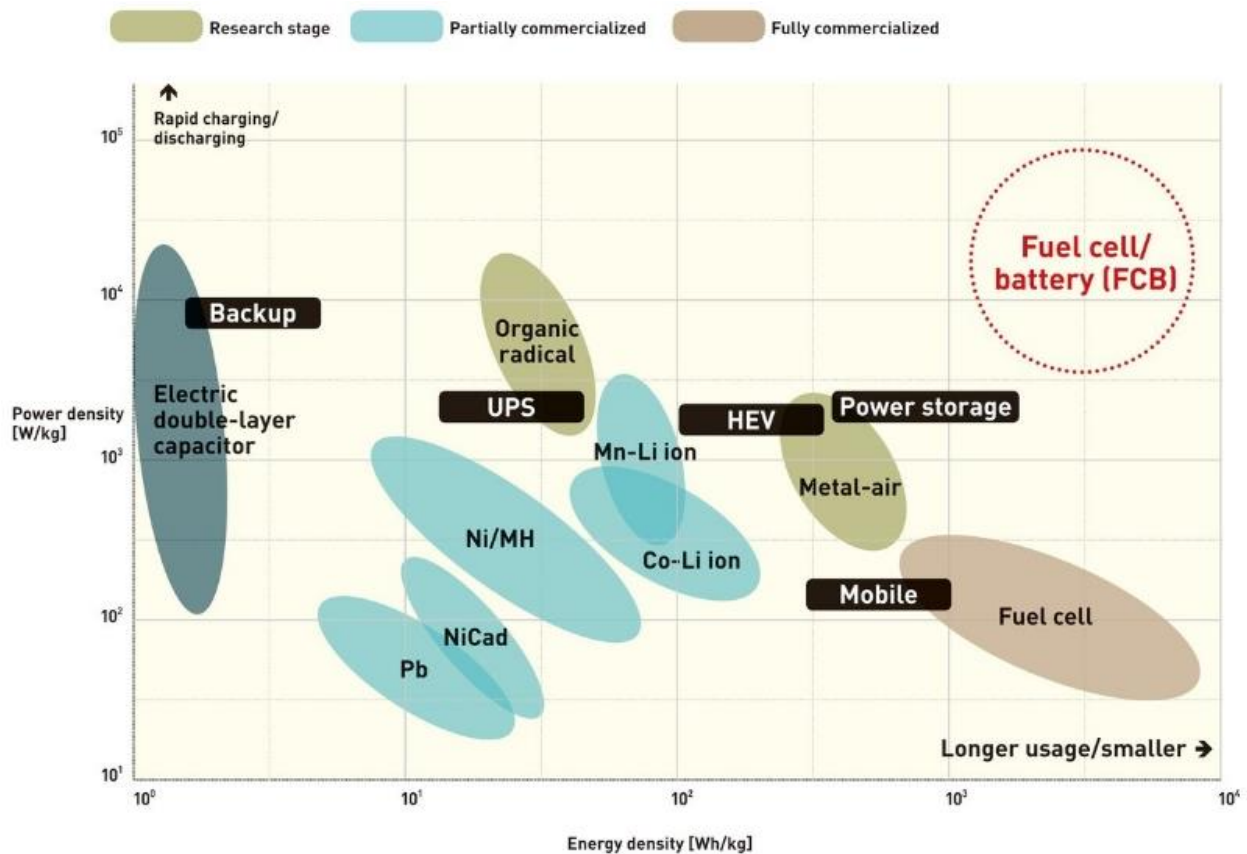


**Figure R1.** Diagramme de Ragone comparant les performances de divers appareils de SCEE (densité d'énergie vs densité de puissance) [8]

Du point de vue de la densité d'énergie et de la densité de puissance, récemment, la pile Zn-air (ZAB) et les piles à combustible à membrane échangeuse de protons (PEMFC selon expression anglais *proton exchange membrane fuel cells*) fonctionnant à l'hydrogène attirent une attention particulière du fait que l'oxygène de la cathode provient de l'air et est exclu du système, ce qui augmente considérablement les densités d'énergie. Dans ces dispositifs, un électrocatalyseur à l'oxygène efficace sur la cathode est extrêmement important pour le développement de ZAB et de PEMFC à haute performance. Jusqu'à présent, les catalyseurs de référence pour l'ORR (selon expression anglais *Oxygen Reduction Reaction*) sont des matériaux à base de métaux nobles ; mais, le prix élevé et la rareté empêchent leur vaste portée commerciale. Par conséquent, la mise au point de catalyseurs hautement efficaces à base de métaux non précieux (NPMC selon expression anglais *non-precious-metal catalysts*) afin de ralentir l'ORR en cathode est un problème essentiel pour les batteries métal-air et les piles à combustible. Dans cette thèse, les travaux réalisés se concentrent sur le développement de la synthèse de différents électrocatalyseurs d'ORR à base de carbone et de leurs applications dans les batteries Zn-air et les PEMFC. De plus, nous avons également fabriqué des sphères de carbone microporeux hautement ordonné (MPC selon anglais expression *microporous carbon*) et les avons appliquées en tant qu'anodes à haute performance pour SIB (selon anglais expression *Sodium-ion batteries*).

### **Objectif de la thèse**

Des batteries et des piles à combustible avec l'amélioration d'énergie spécifique, de densité d'énergie, de coûts, de sécurité et de réseau de compatibilité sont nécessaires pour électrifier les secteurs des transports à longue distance, à faible coût et à forte utilisation. Le problème technologique majeur de ces technologies réside dans la mise au point de catalyseurs à base de métaux non précieux destinés à remplacer le catalyseur coûteux et rare à base de platine servant à ralentir l'ORR en cathode. Pour les SIB, la réduction des coûts de traitement et l'amélioration de la capacité de stockage de Na sont essentielles à l'application pratique. Les matériaux carbonés en hautes performances produits par une méthode de synthèse efficace avec précurseur pas cher et avec un rendement élevé sont tout à fait exploitables.

Objectif I: Etudier et concevoir des NPMCs très actifs et stables pour l'ORR.

Objectif II: Amélioration des performances des piles à combustible et des piles métal-air basées sur les électrocatalyseurs à l'oxygène conçus au niveau des cathodes.

Objectif III: Développer l'anode avec faibles coûts et hautes performances pour les batteries Na-ion.

## Résultats

Dans la première partie de la thèse, nous avons fabriqué des monomicelles phénoliques sphériques de resol-F127 (SPRMs en anglais expression *spherical phenolic resol-F127 monomicelles*) par une simple voie hydrothermale basée sur un modèle souple. Une série de catalyseurs de microporeux en 3D Fe/ N/C ORR a ensuite été préparée en utilisant des SPRMs en tant qu'hôte carbone pour imprégner FeAc et 1,10-Phen, suivies d'une pyrolyse à haute température dans Ar et dans une atmosphère de NH<sub>3</sub>. Au cours des études systématiques, nous avons constaté que (i) la teneur en précurseur de Fe et le temps de pyrolyse sous NH<sub>3</sub> avaient une influence distincte sur la morphologie et la structure des catalyseurs Fe/N/C finaux; (ii) la température de pyrolyse en Ar, la surface BET et la teneur en Fe des catalyseurs affectent largement l'activité d'ORR; (iii) la teneur en Fe optimisée des catalyseurs Fe/N/C est d'environ 5,5 à 8% en poids et la porosité optimisée est de 450 m<sup>2</sup> g<sup>-1</sup> micropore avec de préférence une valeur plus élevée de mésopores, seuls les catalyseurs situés dans ces deux plages présentent des activités. Le 3D Fe/N/C optimisé présente de bonnes performances d'ORR en conditions alcalines et acides. En solution alcaline, il présente un potentiel de demi-onde de 0,87 V, une excellente stabilité même dans une solution saturée en O<sub>2</sub> et une forte tolérance au méthanol. De plus, en solution acide, il présente également une stabilité et une sélectivité excellentes. Tout ceci fait de la nanostructure Fe/N/C poreuse en 3D un excellent candidat pour le catalyseur ORR à base de métal non précieux dans les batteries métal-air et les piles à combustible.

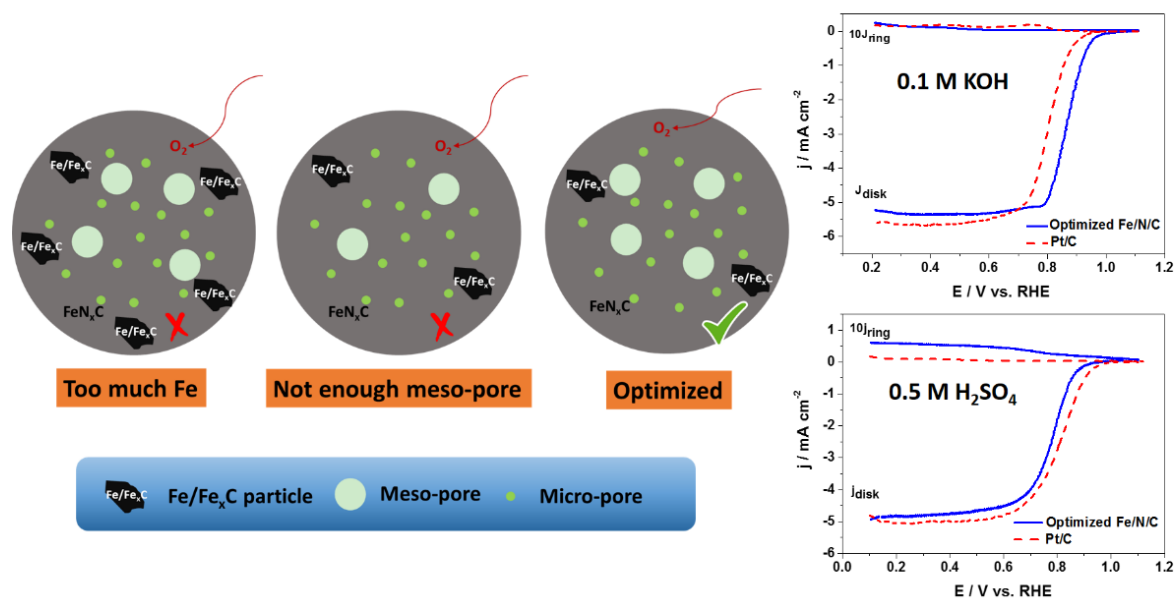


**Figure R2.** Images schématiques de la microstructure optimale des catalyseurs 3D Fe/N/C développés à base de SPRMs; et leur performance d'activité d'ORR en milieu acide / alcalin.

L'article traitant ces résultats décrits dans ce chapitre est le suivant

**Q. Wei, G. Zhang, X. Yang, et al.** 3D porous Fe/N/C spherical nanostructures as high-performance electrocatalysts for oxygen reduction in both alkaline and acidic media. *ACS Appl. Mater. Interfaces*, 2017, **9**, 36944-36954.

Dans la deuxième partie de la thèse, nous avons développé une approche simple mais très efficace, basée sur l'utilisation de S en tant que promoteur et de SPRMs en tant qu'hôte carbone, pour fabriquer un catalyseur Fe/N/C poreux hiérarchique de type litchi. L'ajout de S permet non seulement de créer des trous s'interpénétrant, générant une grande surface et un volume de pores plus important dans l'architecture, mais aide également l'ensemble de la structure en carbone à conserver une forme sphérique 3D parfaite et des sites actifs Fe-N<sub>x</sub> uniformément dispersés une large mesure; de plus, un degré de distorsion plus élevé de la structure locale Fe-N<sub>4</sub> a été observé pour l'échantillon Fe/N/C traité au S. En conséquence, le catalyseur Fe/N/C optimal traité au S présente une structure sphérique de type litchi, une grande surface spécifique (982,1 m<sup>2</sup> g<sup>-1</sup>) avec un volume de pores énorme (1,01 cm<sup>3</sup> g<sup>-1</sup>) et une excellente activité ORR/OER. Il est important

de noter qu'elle réalise une performance supérieure ( $250 \text{ mW cm}^{-2}$ , soit deux fois la densité de puissance par rapport à celle qui n'est pas traitée) comme une cathode à air pour un dispositif de batterie Zn-air. Ces travaux pourraient fournir une nouvelle stratégie pour développer des électrocatalyseurs à base de carbone en haute performance destinés aux batteries métal-air à faible coût et aux autres applications de conversion/stockage d'énergie électrochimique.

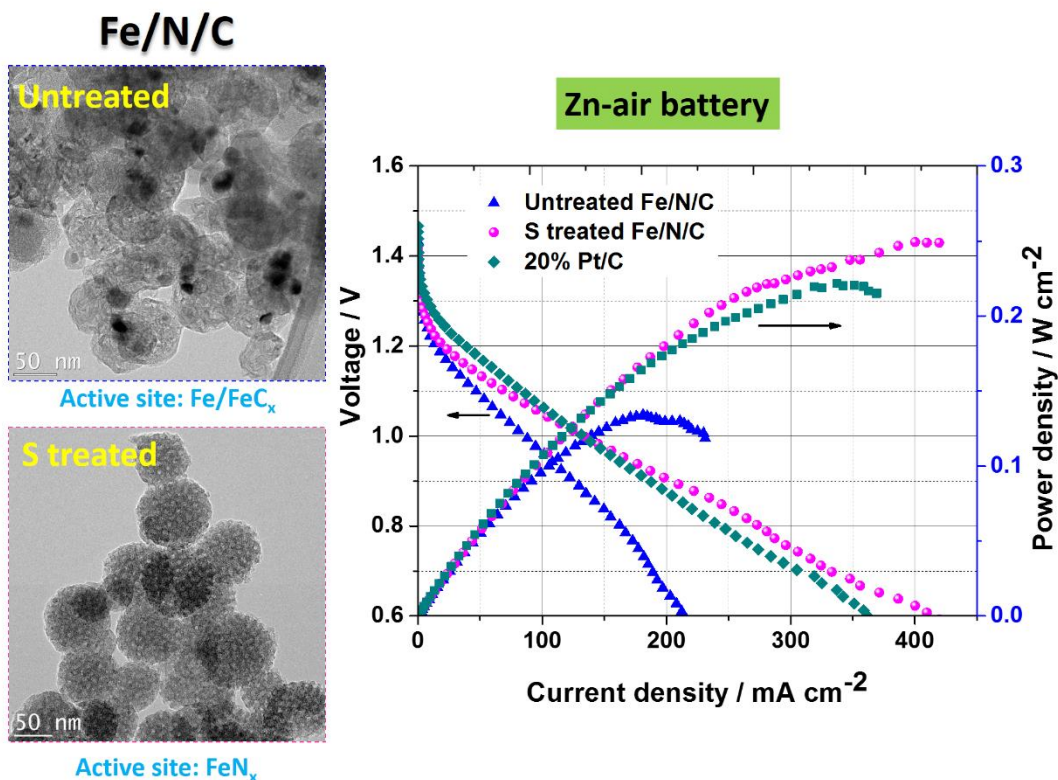


**Figure R3.** Morphologie des catalyseurs Fe/N/C non traités et traités au S et leurs courbes polarisation/densité de puissance dans un dispositif à batterie Zn-air.

L'article traitant ces résultats décrits dans ce chapitre est le suivant

**Q. Wei, G. Zhang, X. Yang, et al.** Litchi-like porous Fe/N/C spheres with atomically dispersed FeN<sub>x</sub> promoted by sulfur as highly efficient oxygen electrocatalysts for Zn–air batteries. *J. Mater. Chem. A*, 2018, **6**, 4605–4610.

Dans la troisième partie de la thèse, inspirée par la structure centrée sur le métal de l'enzyme à fonctionnement d'ORR dans la vie et par les effets synergiques entre les métaux de transition,

nous avons préparé un mélange hautement poreux (Fe-Cu)/N/C à base de MOF. Nous avons constaté que, comparé au Fe/N/C, le synthétiseur (Fe-Cu)/N/C possède une surface spécifique plus élevée, une liaison Fe-N plus longue et un rendement en H<sub>2</sub>O<sub>2</sub> plus faible dans la plage de 0,3-0,8 V dans test de demi-cellules. De manière importante, lorsqu'il est appliqué dans un MEA dans la PEMFC H<sub>2</sub>-Air, le catalyseur (Fe-Cu)/N/C présente une densité de puissance supérieure de 0,4 W cm<sup>-2</sup> à celle de Fe/N/C (0,36 W cm<sup>-2</sup>), et une stabilité accrue, c'est-à-dire qu'une amélioration de 3,7 % de la densité de courant sous un test potentiostatique à 0,6 V après 40 h.

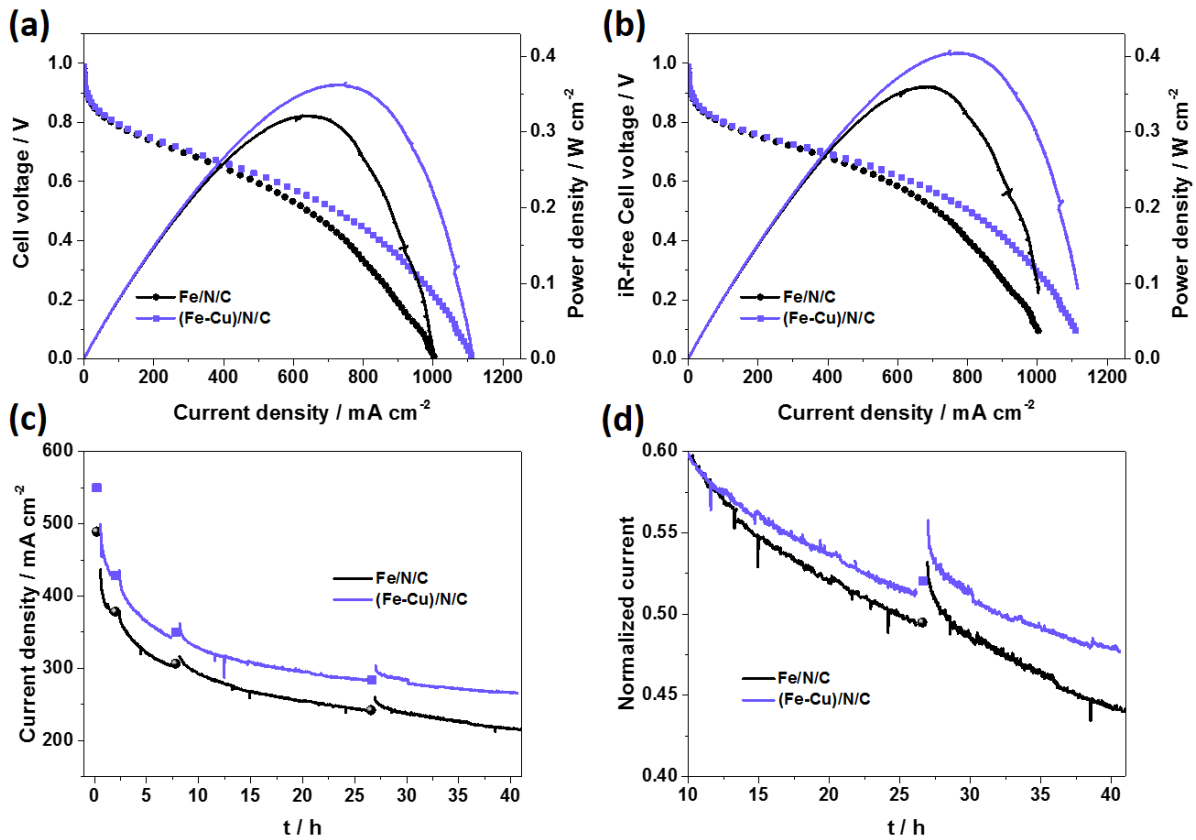


**Figure R4.** (a) Diagrammes de polarisation et de densité de puissance pour PEMFC H<sub>2</sub>-air avec (Fe-Cu)/N/C et Fe/N/C en tant que catalyseur de cathode à 80 °C. (b) i-R corrigé de (a). (c) Courbes de chronoampérométrie montrant la décroissance de la densité de courant à 0,6 V pour PEMFC H<sub>2</sub>-air. (d) La stabilité normalisée, chaque courbe est normalisée à sa densité de courant initiale à 0,6 V dans (c). La contre-pression est de 1 bar ; débit: 0,3 slpm; Zone active MEA: 1,14 cm<sup>2</sup>; Membrane NRE 211; charge cathodique: 4,0 mg cm<sup>-2</sup>; catalyseur anodique: Pt/C (45,4%, TKK) avec 0,5 mg<sub>Pt</sub> cm<sup>-2</sup>.

L'article traitant ces résultats décrits dans ce chapitre est le suivant

***Q. Wei, X. Yang, G. Zhang, et al.*** Bio-inspired nonprecious bimetallic (Fe-Cu)/N/C catalyst for oxygen reduction in proton exchange membrane fuel cells. être soumis.

Dans la quatrième partie de la thèse, nous avons développé un catalyseur efficace d'ORR qui est le Fe/N/C contenant du Si en utilisant les déchets de la tige de roseaux en tant que la source de Si et de C. En raison de la participation de Si dans le processus de dopage Fe/N, le catalyseur Si-Fe/N/C possède une structure de carbone graphitique améliorée avec plus de fractions d'azote se coordonnant avec Fe. Ces caractéristiques font que le catalyseur Si-Fe/N/C présente une bonne activité d'ORR et, surtout, que Si-Fe/N/C présente une meilleure stabilité (avec une rétention du courant de 94,8% après 20 000 secondes sous une tension élevée de 0,8 V) que la contrepartie qui est le Fe/N/C (83,3%) et Pt/C (65,5%); et seulement environ 12 mV de variation à 3 mA cm<sup>-2</sup> pour Si-Fe/N/C après 10 000 cycles de potentiel sous électrolyte saturé en O<sub>2</sub> (vs -19 mV pour Fe/N/C et -40 mV pour Pt/C), ainsi qu'une tolérance plus élevée au méthanol par rapport au Pt/C. En réunissant notre catalyseur développé de Si-Fe/N/C en remplacement du Pt/C du commerce pourrait offrir une possibilité dans les piles à combustible alcalines et d'autres applications offrant de bonnes performances d'ORR et une grande stabilité. Nous pensons que ces travaux permettront de mieux concevoir des catalyseurs hautement stables pour les dispositifs liés à l'énergie propre et auront des effets économiques et environnementaux importants en exploitant pleinement les déchets de biomasse.

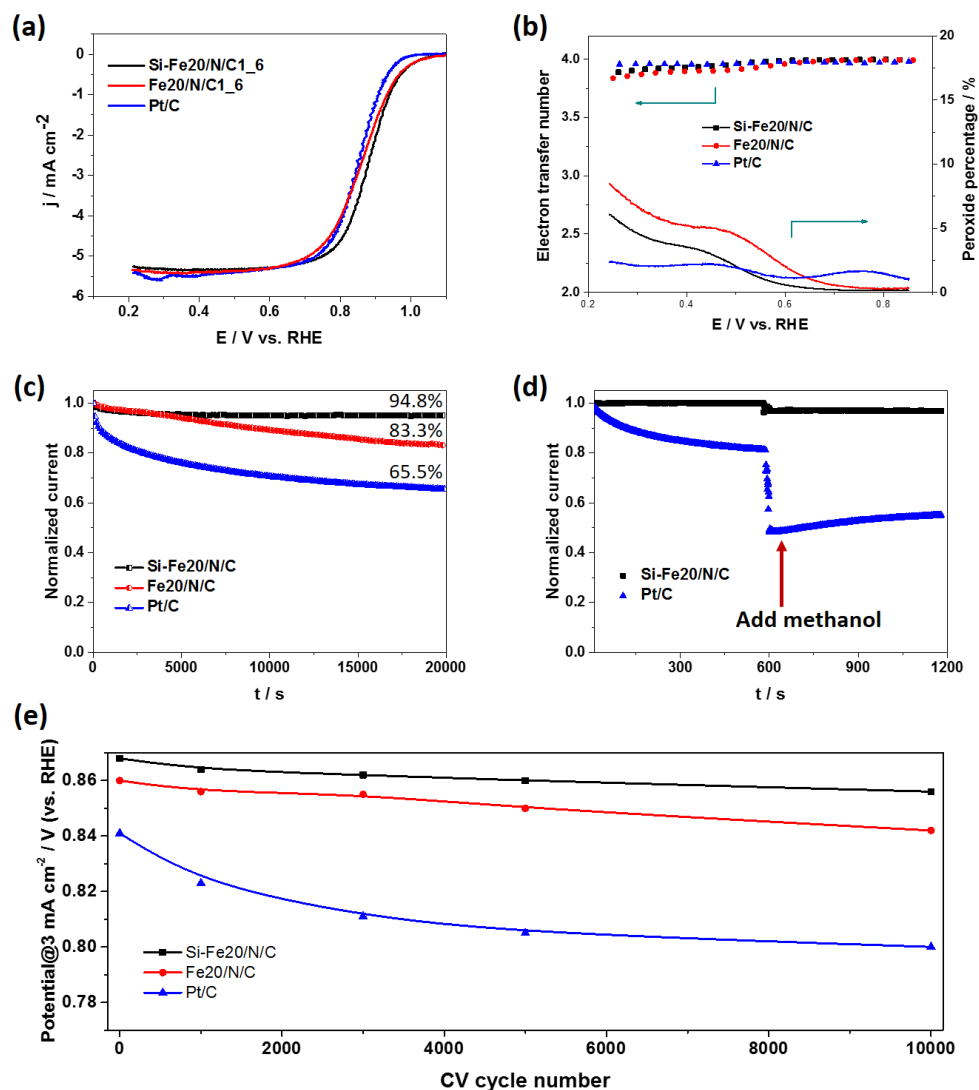


**Figure R5.** (a) courbes LSV, (b) numéro de transfert d'électrons ( $n$ ) et sélectivité en  $\text{H}_2\text{O}_2$  de Si-Fe20/N/C1\_6, Fe20/N/C1\_6 et Pt / C du commerce dans KOH de 0,1 M saturé en  $\text{O}_2$  à une vitesse de balayage de  $10 \text{ mV s}^{-1}$ , taux de rotation = 1600 tr/min. (c) Réponses chronoampérométriques (à 0,8 V vs. RHE) de Si-Fe20/N/C1\_6, Fe20/N/C1\_6 et de catalyseurs commerciaux Pt/C dans KOH de 0,1 M saturé en  $\text{O}_2$  avec une vitesse de rotation de 1600 tr/min, (d) Les réponses chronoampérométriques des catalyseurs Si-Fe20/N/C1\_6 et Pt/C montrent l'effet de l'ajout de 4 ml de méthanol dans la solution de 100 ml de KOH de 0,1 M saturée en  $\text{O}_2$ . (e) Potentiel à  $3 \text{ mA cm}^{-2}$  de Si-Fe20/N/C1\_6, Fe20/N/C1\_6 et Pt/C du commerce en fonction du nombre de cycles potentiels dans un électrolyte saturé en  $\text{O}_2$ .

L'article traitant ces résultats décrits dans ce chapitre est le suivant

**Q. Wei, X. Yang, G. Zhang, et al.** An active and robust Si-Fe/N/C catalyst derived from waste reed for oxygen reduction. *Appl. Catal., B.*, 2018, 237, 85-93.

Dans la cinquième partie de la thèse, un catalyseur sans activité de métal à haute activité pour l'ORR a été développé en utilisant les déchets de la tige de roseaux comme la source de Si et de C, après le traitement avec  $\text{NH}_3$ , l'élément Si dans l'anche a été démontré très actif pour l'ORR en milieu alcalin. L'échantillon optimisé de Si-N-C montre un  $E_{\text{onset}}$  de  $\sim 1,00$  V et un  $E_{1/2}$  de 0,89 V (vs RHE), qui est l'un des meilleurs parmi les catalyseurs d'ORR sans métal signalés. Il présente également une meilleure stabilité pour l'ORR que le Pt/C commercial dans un environnement demi-cellulaire. De plus, ce catalyseur de Si-N-C sans métal dérivé de déchets des roseaux présente des performances excellentes en tant qu'une cathode à air pour un dispositif de batterie au Zn-air. Le calcul de la TFD indique que les sites de Si et de N (graphitique-N) dans le cadre du carbone pourraient promouvoir une activité d'ORR plus élevée. Nous pensons que nos travaux donneront plus des idées pour concevoir des catalyseurs plus efficaces pour les dispositifs liés à l'énergie propre et apporteront une grande importance au développement durable de l'énergie.

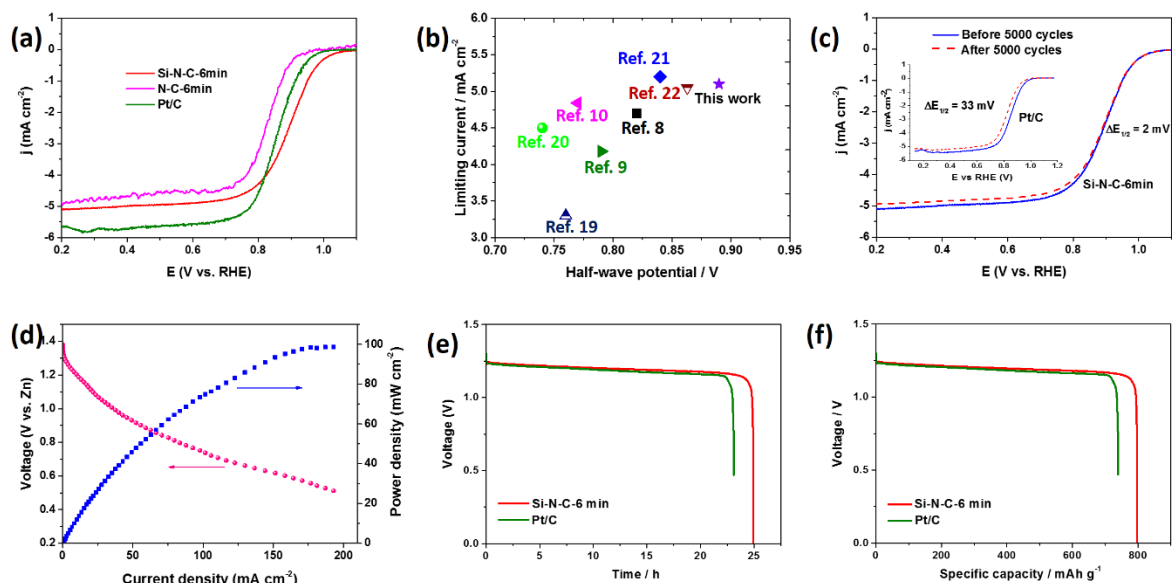


**Figure R6.** (a) courbes LSV, (b) comparaison du courant limite en fonction du potentiel de demi-onde pour les électrocatalyseurs sans métal récemment signalés dans KOH de 0,1 M saturé en  $\text{O}_2$  à une vitesse de balayage de  $10 \text{ mV s}^{-1}$ , vitesse de rotation = 1600 tr/min, (c) courbes de polarisation de RDE du catalyseur étudié et Pt/C (figure en médaillon) avant et après 5000 cycles de potentiel dans 0,1 M KOH saturé en  $\text{O}_2$ , (d) courbes de polarisation déchargée et les diagrammes de densité de puissance correspondantes dans batterie rechargeable à deux électrodes à Zn-air, (e) courbes de décharge galvanostatique de batteries Zn-air à  $20 \text{ mA cm}^{-2}$ , (f) courbes de décharge

galvanostatique à long terme à 20 mA cm<sup>-2</sup> de batteries Zn-air jusqu'à la consommation complète de l'anode de Zn. La capacité spécifique a été normalisée à la masse de Zn consommée.

L'article traitant ces résultats décrits dans ce chapitre est le suivant

*Q. Wei, M. Cherif, et al.* Transforming reed waste into a highly active metal-free catalyst for oxygen reduction reaction. être soumis.

Dans la dernière partie de la thèse, basée sur les SPRMs, nous avons préparé des MPC sphériques hautement ordonnés pour les modules SIB. L'espacement entre les couches du MPC a été bien réglé en ajustant simplement le traitement thermique par température. Les sphères de carbone ainsi obtenues traitées à 700 °C (MPC-700) associent les caractéristiques requises pour les matériaux d'électrodes de SIB en hautes performances, telles qu'un grand espacement d'intercouche (~0,457 nm), une grande surface spécifique, une stabilité structurelle et de nombreux micropores pour l'insertion de Na, qui contribuent de manière synergique à leurs propriétés électrochimiques impressionnantes. Appliquée comme anode pour les modules SIB, l'électrode MPC-700 présente une grande capacité réversible, une bonne stabilité des cycles et une excellente performance à débit élevé (160 mA h g<sup>-1</sup> après 500 cycles à 1000 mA g<sup>-1</sup>), ce qui en fait un candidat prometteur pour les anodes de SIB.

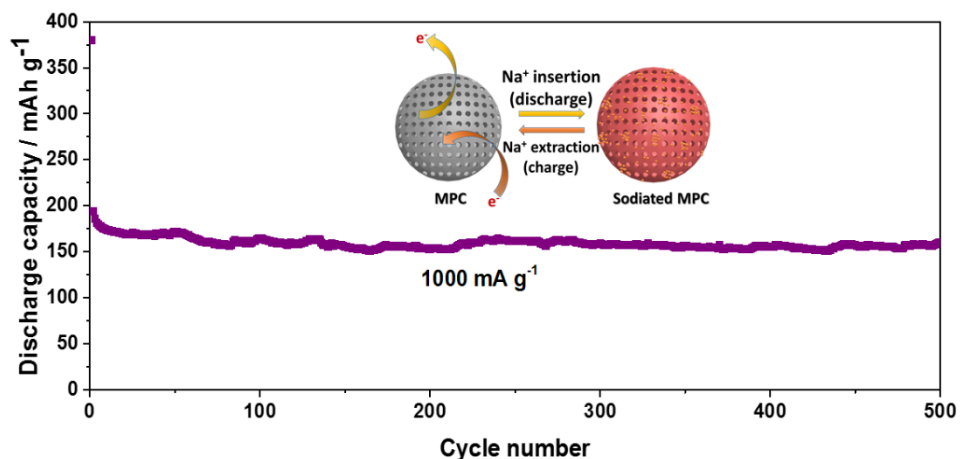


**Figure R7.** Performance du cycle à long terme à 1000 mA g<sup>-1</sup> pour le MPC-700 et schéma du processus électrochimique pour les MPC.

L'article traitant ces résultats décrits dans ce chapitre est le suivant

**Q. Wei, Y. Fu, G. Zhang, et al.** Highly-ordered microporous carbon nanospheres: a promising anode for high-performance sodium-ion batteries. *RSC Adv.*, 2016, **6**, 84149-84154.